DEVELOPMENT OF MONITORING SYSTEMS USING FIBER OPTIC SENSORS

Yoshinobu OSHIMA

March 2003

Development of Monitoring Systems Using Fiber Optic Sensors

by

Yoshinobu Oshima

March 2003

A dissertation submitted to
Graduate school of engineering, Kyoto University
in partial fulfillment of requirements for the degree of

Doctor of Engineering

ABSTRUCT

Monitoring plays an important roll to keep various structures such as bridge, dam and tunnel in sound condition and to prolong their life. Monitoring is also essential for safe construction such as cut slope and underground excavation. In this study, an innovative monitoring system is developed together with the development of strain and displacement transducer on the basis of fiber optic sensor. This newly developed system is tested in laboratory and a construction site and it is found that this system can be applicable for various practical purposes. The followings are main conclusions obtained in this study.

Fiber Optic Gauge (FOG) is developed as a strain gauge module based on Fiber Bragg Grating (FBG) sensor and the mechanical characteristics are clarified by the tensile and bending test together with the temperature sensitivity test. Clarification of the strain and temperature sensitivity extends the application of FOG to a wider range of temperature.

Fiber Optic Displacement Device (FODD) is developed on the basis of FBG sensor attached to vinyl chloride pipe. FBG sensors are installed in the several sections in the pipe with three sensors in each section. This installation of FBG sensors enables FODD to measure displacement and its direction. Interpolation of spline and polynomial is applied to obtain continuous displacement. It is found that a good displacement measurement can be attained by a constant interval allocation of FBG sensors and application of spline method particularly when displacement is not monotonous.

It is also clarified the influence of the source voltage during the measurement and the local curvature of the data transmission optical fiber.

Strain and displacement monitoring system is established on the basis of the various fundamental considerations. This proposed monitoring system is found to be applicable for a longer period of monitoring and for remote-controlled measurement.

This monitoring system is expected to be applied for various structures for their safety control.

ACKNOWLEDGMENTS

My special thanks go to my supervisor, Professor Koichi ONO, for giving me the opportunity to research this exciting topic and encouraging me to think deeper about the subject. I appreciate all his support, advice, and guidance; I learn a great deal from him and am honored to be his first student in Kyoto University.

My next thanks go to Professor Yuzo ONISHI for generously advising me to complete my dissertation. My thanks also go to Professor Toyoaki MIYAGAWA for continuously guiding me through my dissertation and generously sharing this knowledge and expertise.

I would also like to thank the associate Professor Kunitomo SUGIURA for his excellent teaching, continuous support and guidance. My study would not be nearly as successful without any of his contribution.

My research was strongly supported by FODD section of E.E. industrial and academic research collaboration (E.E. Sangaku renkei kenkyu Kai). I acknowledge the helpful advice from the members of this group, especially Mr. T. GOTO and Mr. Y. MAEDA, NTT InfraNet Co., Ltd.; Mr. S. SAKAMOTO, Oyou Keisoku Co., Ltd.; Mr. M. TAGUCHI, Ohtori consultant Co., Ltd.; Mr. T. KANASUGI, K.D.S. Co., Ltd.; Mr. S. KAITORI, Mr. H. TASHIRO, Mr. K. FURUKAWA, and Mr. K. IIMA, Konoike construction Co., Ltd.; Mr. N. WAKAHARA, Konishi bond Co., Ltd.; Mr. M. KISHIDA, Sekisui chemical Co., Ltd.; and, Mr. Y. OHOKA, and Dr. M. CHO, Toua Grout Co. Ltd.

I also wish to express appreciation to Mr. H. OKANO, Mr. T. OZAWA, and Mr. H. TAKASAKI, Tokyo Sokki Co., Ltd., as well as Mr. W. FUNAKOSHI, and Dr. Y. KOBAYASHI, Nichizotech Co., Ltd., who gave valuable advice on fiber optic sensors and the monitoring.

In this study, a series of experiments were carried out on the specimens carefully fabricated by Hitachi Cable Co., Ltd. under guidance of Mr. T. KUMAGAI.

I am thankful to Dr. G. LEE as well as Dr. M. TONG for giving me the opportunity to stay the state university of New York at Buffalo to finish my dissertation. I am also thankful to Dr. Y. KITANE and Dr. M. YAMAGUCHI, for helping my stay in Buffalo and encouraging me to finish my dissertation. Thanks to them, I had a comfortable time in Buffalo to concentrate on my research.

I also wish to express appreciation to the members of BUD research association; Mr. T. FUMOTO, Mr. K. HIBINO, Mr. M. INOUE, Dr. Y. MIKATA, and Dr. T YAMAMOTO.

My deep thanks also go to my juniors and friends, especially my colleagues, Mr. Chiwei Lu, and Mr. Pongthon THARACHAI, for their support to complete my dissertation.

Lastly I express my deepest appreciation to my parents for helping my life and giving the opportunity to continue the study.

TABLE OF CONTENTS

Chapter 1 Introduction 1

1.1 General remarks on monitoring system 1
1.2 Overview of state-of-the art on optical fiber sensors for structural monitoring 3
1.2.1 Optical fiber sensors 3
1.2.2 Fiber Bragg Grating sensors 12
1.3 Objectives and scopes 18

Chapter 2 Development of a strain module based on FBG sensors 21

2.1 General remarks 21
2.2 Fundamental scheme of the proposed module 22
2.3 Calibration test 23
2.3.1 Tension test 23
2.3.2 Bending test 26
2.3.3 Temperature test 29
2.4 Numerical analysis 30
2.4.1 Transmission Matrix (T-matrix) method 31
2.4.2 Evaluation of typical strain distributions using T-matrix 34
2.4.3 Evaluation of the module using finite element analysis 41
2.4.4 Evaluation of the strain distributions in the tension and bending tests 53
2.4.5 Summary 56
2.5 Temperature-independent strain module 56
2.5.1 Target of this section 56
2.5.2 Material selection 57
2.5.3 Dimensions 60
2.5.4 Strain sensitivity 63
2.6 Summary of Chapter 2 66

Chapter 3 Development of a displacement transducer based on FBG sensors 69

3.1 General remarks 69
3.2 Principle of fiber optic displacement device 69
3.3 Displacement transformation procedure 73
3.3.1 Double integration 73
3.3.2 Spline interpolation 73
3.3.3 Polynomial interpolation 74
3.4 Evaluation of the transformation procedure using virtual measurement 75
3.4.1 Target of this section 75
3.4.2 Analytical model 75
3.4.3 Results and discussion 78
3.4.4 Summary 91
3.5 Fundamental test for FODD 92
3.5.1 Element test 92
3.5.2 Measurement test on FBG sensor 95
3.5.3 FODD unit test 95
3.6 Site test 100
3.6.1 Test setup 100
3.6.2 Results and discussion 104
3.7 Summary of Chapter 3 106

Chapter 4 Monitoring system configuration 109

4.1 General remarks 109
4.2 Fabry-Perot tunable filter demodulation system (FBG-IS) 110
4.3 Environment test on FBG-IS unit 112
4.3.1 Test setup 112
4.3.2 Results and discussion 112
4.4 Stability evaluation against transmission loss 114
4.4.1 Test setup 114
4.4.2 Results and discussion 114
4.5 Multiplexing loss evaluation 119
4.5.1 Target of this section 119

4.5.2 Test setup 119
4.5.3 Results and discussion 121
4.6 Bonding test 123
4.6.1 Target of this section 123
4.6.2 Test setup 124
4.6.3 Results and discussion 124
4.7 System configuration for monitoring 127
4.7.1 Target of this section 127
4.7.2 Maximum number of multiplexing 127
4.7.3 Optical loss calculation 128
4.7.4 System configuration 130
4.8 Summary of Chapter 4 132

Chapter 5 Application study 133

5.1 General remarks 133
5.2 Application for open cut excavation control 133
5.2.1 Measurement plan for open cut excavation 133
5.2.2 Site 133
5.2.3 System configuration 140
5.2.4 Construction procedure control using the monitoring system 141
5.2.5 Measurement results and discussions 146
5.2.6 System configuration for land-sliding control 151
5.2.7 Summary 153
5.3 Application for pipeline control 153
5.3.1 Target of this section 153
5.3.2 Finite deformation analysis 154
5.3.3 Safety conditions for the pipeline in permafrost area 158
5.3.4 Requirements for pipeline monitoring in permafrost area 160
5.3.5 Summary 163
5.4 Summary of Chapter 5 164

Chapter 6 Conclusion 167

References 171

Appendixes

A. Fundamentals of optic fiber technology A-1
A.1 Structure of an optical fiber A-1
A.2 Concept of wave mode A-1
A.3 Optical transmission loss A-4

B. Bragg Grating Reflection B-1
B.1 Bragg grating reflection B-1
B.2 Temperature and strain sensitivity B-9

C. Optical Fiber Sensor Multiplexing Techniques C-1
C.1 Multiplexing techniques C-1

Chapter 1 Introduction

1.1 General remarks on monitoring system

How many years can structures survive? Even though engineers have made tremendous efforts for a reasonable answer to this question, it is still difficult, even impossible, to solve because of the obscure mechanisms of structural deterioration: for instance, increasing traffic and the axle loads of heavy vehicles or other environmental agencies have contributed to the deterioration of the structures. Moreover, the number of deteriorated or aged structures has increased rapidly.

To predict their life or even retrofit their deterioration, the damage must be monitored and detected. Thus the proper and frequent monitoring of the structures is important and necessary in Japan and other developed nations. From the prehistoric times, visual monitoring has played the main role in monitoring, because it is a simple and fundamental technique to evaluate the safety of structures. Although visual inspections have dominated monitoring procedures, the current trend is for new technologies such as optical fiber technology to be effectively applied in monitoring the structures.

At present, various physical quantities such as strain, stress, displacement, or load can be measured using strain gauges or strain gauge-based transducers. The most common contact strain gauge available in civil engineering is the electrical resistive gauge. Resistive strain gauge technology is highly developed, and the gauges exhibit excellent sensitivity. But they have unique stability (drift) characteristics versus temperature and hysteresis caused by the temperature cycling, which may be problematic (Berthod, 1997). Furthermore, these gauges have corrosion or durability problems because of their metal and electric properties. Thus resistive gauges are not adequate for long-term and long-distance monitoring.

Even for ground-deformation monitoring, a borehole inclinometer and extensometer are also based on the resistive gauge, which causes a durability problem as well. Especially the inclinometer requires manual operation that limits continuous and remote measurement because it takes much time and labor for one measurement. Surveying is also a simple method to measure ground deformation, but it also requires manual operation. Additionally, the number of sensors needed to monitor the whole structure requires significant wiring. Because these systems use resistive strain gauge or need manual operation, they commonly have difficulty in accomplishing long-term monitoring and in building a central control system. However, sensors designed for ground monitoring applications should survive under hostile environments on earth and will monitor the movement of the slope widely, continuously, and over long period of time, so as to detect them quickly. Consequently, durability in transducer technology is one of the main challenges for installing permanent ground monitoring systems. Recently GPS and other topographic surveys have been applied to the geo monitoring (Fukuoka et al., 1997). Furthermore, CCD (Charge Coupled Device) camera systems have been recently proposed (Kimura et al., 1999). These systems can detect the position of the targets installed on the slope without manual operation, but obstacles such as snow or dust should be removed between the camera and the targets.

In contrast, "smart sensors" open up the possibility of building durable monitoring systems and central control systems for civil structures, including ground monitoring. Smart sensors indicate an advanced sensor that uses other than the electrical resistive principle such as optical fiber sensors, Piezo sensors, and advanced metal sensors. Because of their precision and accessibility, Piezo sensors and some advanced metal sensors, have been studied mainly in mechanical engineering (Srinivasan et al., 2001; Banks et al., 1996; Inman et al., 2000; Dignath et al., 2000). In civil engineering, however, the use of PZT or metal sensors might be restricted because of their small dynamic range and fragility. Unlike metallic sensors, optic fiber sensors are attractive and considered the leading technology in forming monitoring and safety control systems because of their numerous advantages such as flexibility, small size, negligible weight, resistance to harsh environments, and immunity to electromagnetic interference.

Thus in this study, optical fiber sensors are adopted to build the monitoring

system not only for the structures, but for the geo disastrous monitoring.

1.2 Overview of the state-of-art on fiber optic sensors for structural monitoring

1.2.1 Fiber optic sensors

Optical fibers have been developed mainly in the telecommunication field in recent years. But the ability of the fiber to measure strains and temperature is found at the end of the 1970s as a side effect of noise detection. Later, fibers attracted civil engineers as one of the fundamental technologies for developing smart structures and safety control systems. Optical fiber sensors can be divided into a number of groups, or categories.

First of all, two important groups, intrinsic sensors and extrinsic sensors, should be distinguished (see **Fig. 1-1**). Both sensors use optical fibers as media to transfer the light between sensing heads and detection systems. But in an intrinsic sensor, the sensing element is also the optical fiber itself (**Fig. 1-1a**). In contrast, the sensor heads of extrinsic sensors are devices that convert physical phenomena into the state of light (**Fig. 1-1b**).

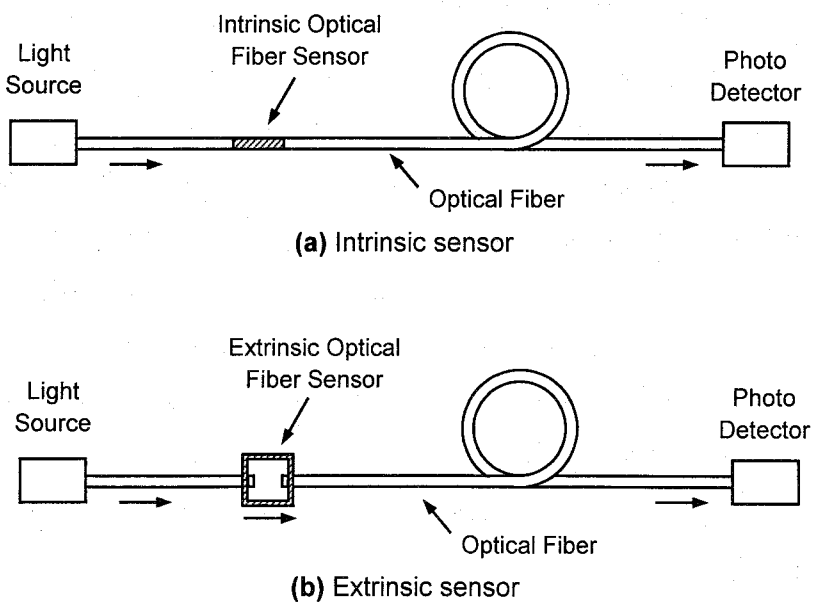

Fig. 1-1 Intrinsic and extrinsic optical fiber sensors

For chemical sensing, such as pH, oxygen, carbon dioxide, ammonia, and iron sensing, mainly extrinsic sensors are employed in direct or indirect detection (Dakin et al., 1997; Wolfbeis, 1997). On the other hand, intrinsic optical fiber sensors can measure strains, temperatures, pressures, etc. They can be classified according to the transduction mechanism (Measures, 2001):

- Intensiometric
- Interferometric
- Polarimetric/ Modalmetric
- Spectrometric.

Table 1-1 shows the classification of intrinsic optical fiber sensors. Although the most important optical fiber sensors are FBG (Fiber Bragg Grating) sensor, FFP (Fiber Fabry-Perot) sensor and B-OTDR (Brillouin Optical Time Domain Reflectometry), the other sensors should be referred to because sometimes they become important for special uses. In the following listing, the sensor mechanisms and applications are described according to the sensor mechanism. Especially FBG sensors are described in detail in the next section because they are positively used in this study.

(1) Intensiometric fiber optic sensors

Intensiometric sensors depend upon a variation of the light power transmitted through a multimode fiber. These sensors require only the intensity of the light power telling the amount of strain or other physical information. The simplest form of this sensor detects the absence or presence of the light within the fiber. If some damage or fracture occurs within the fiber, the incident light cannot pass through the fiber. In this sensor, the location can be detected by the traveling time of a pulse light that is emitted at the end and reflected at the fracture. This technique is known as the Optical Time Domain Reflectometry (OTDR) technique, which can also be applied to other optical fiber sensors. Unfortunately, this system is expensive because of the pulse detection control.

A microbend sensor, one of the representative sensors among intensiometric sensors, is based on the loss mechanism of bended fibers (see **Appendix A**). As

Table 1-1 Representative intrinsic optical fiber sensors

Sensor type or sensor name	Measured information	Measurement principle	Accuracy	Fiber type	Notes
OSMOS	displacement	Microbend loss	0.02mm~	multi mode	gauge length of 2, 5, 10m
SOFO	displacement	Michelson interferometer	2μm~	single mode	gauge length of 20cm to 10m
FFP (EFPI, ILFE)	strain	Fabry-Perot interferometer	1μ~	single mode	gauge length of 5~20mm
B-OTDR	strain	Brillouin scattering	±100μ	single mode	spatial resolution of 1.0m~
R-OTDR	temperature	Raman scattering	±0.5°C~	multi mode	spatial resolution of 0.25m~
FBG	strain	Bragg grating reflection	±4μ	single mode	gauge length of 10mm

shown in **Fig. 1-2**, this sensor converts the power decay into the pressure or strain information of the bending part. Fields et al. (1980) originally demonstrated this mechanism, and Berthold (1997) evaluated this sensor experimentally, with a displacement resolution of about 2×10^{-7}mm. Furthermore, OSMOS (Optical Strand Monitoring System) is a microbend sensor commercially produced by OSMOS Deha-com BV (France). OSMOS measures the distance of the optical strand, which consists of two anchors and twisted optical fiber, as shown in **Fig 1-3**. When the strand is elongated or shortened, the fiber will be bent according to the length of two

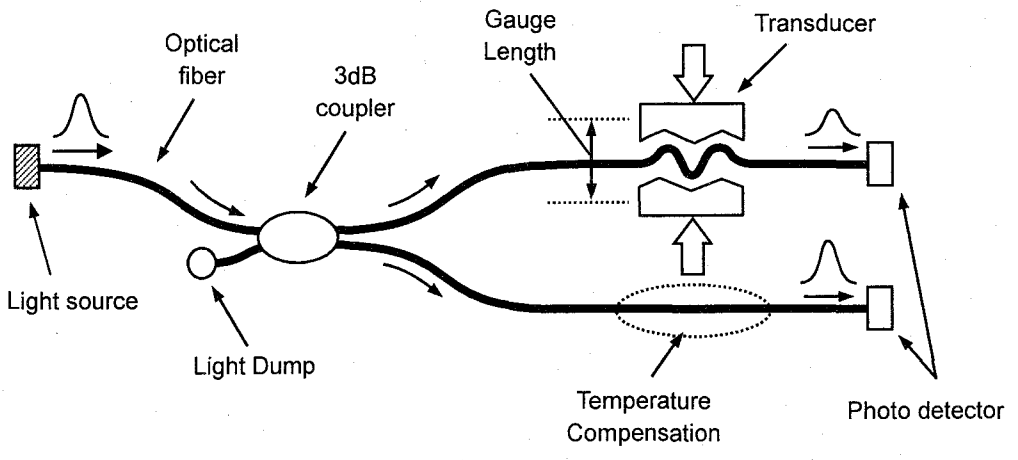

Fig. 1-2 Mechanism of a microbend sensor

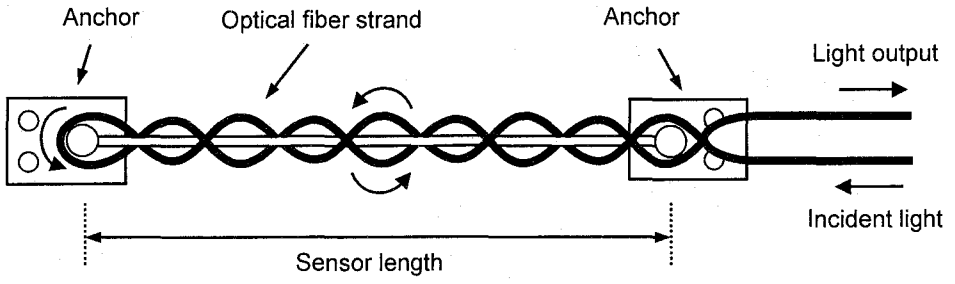

Fig. 1-3 Mechanism of OSMOS

anchors. This sensor can measure the displacement with a resolution of 0.02mm for the gauge length of 2, 5 or 10m (Hasui, 2002).

But intensiometric fiber optic sensors in general have restricted sensitivity, measurement range, and accuracy since the source power or the light intensity is not stable.

(2) Interferometric fiber optic sensors

Interferometric sensors respond to changes in the phase of a light-wave propagating along a single-mode optical fiber. The Michelson fiber optic interferometer is one of the simplest to understand and easiest to build for laboratory experiments. As shown in **Fig. 1-4**, the essential difference in phase between the sensing and referencing fiber represents the extension of the sensing fiber. The sensing arm which is fixed on the structure, responds to the changes of the structure, while the reference arm is free over the structure. Thus the phase difference corresponds to the displacement that can be detected by the Michelson interferometer. In this mechanism, the temperature compensation is achieved by the presence of reference fiber, which acts as a dummy gauge. One of the commercialized sensors using this mechanism is SOFO (Inaudi, 2001). SOFO can measure the displacement with a resolution of 2μm for gauge length of 20cm to 10m, and has been used in many applications for real structural monitoring: Venoge Bridge

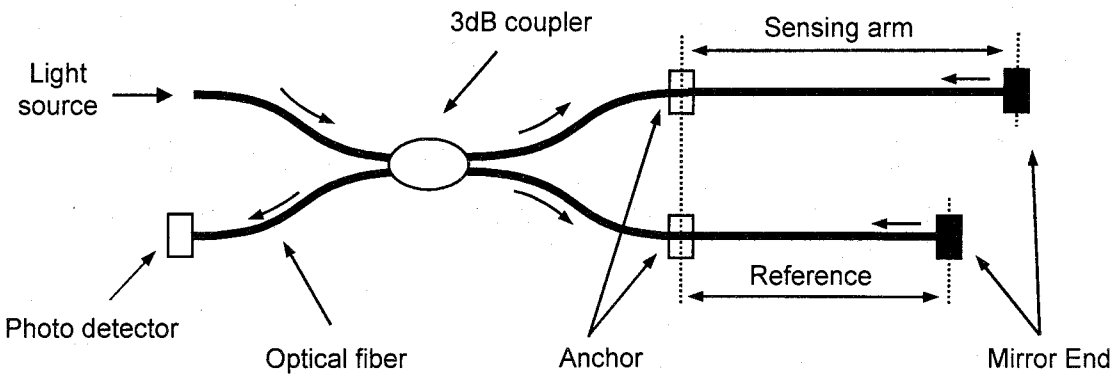

Fig. 1-4 Displacement sensor based on Michelson interferometer

in Switzerland (1996) with 30 sensors, Versoix Highway Bridge in Switzerland (1997) with 100 sensors, Moesa Railway Bridge in Switzerland (1997) with 30 long gauge-length sensors, the Schiffenen shell-mass Dam in Switzerland (1997), etc. (Inaudi et al., 1997; Vurpillot, 1997; Kronenberg et al., 1997; Glisic, 1999; Measures, 2001).

Another important interferometric sensor is Fiber Fabry-Perot (FFP). As illustrated in **Fig. 1-5**, the FFP sensor comprises the cavity or splicing mirrors in the fiber. The distance between two ends of the fibers is the sensing length in this system, which forms a Fabry-Perot interferometer. There are three types of FFP sensors: extrinsic Fabry-Perot Interferometer (EFPI), intrinsic fiber Fabry-Perot sensor (FFP) and in-line fiber etalon (ILFE).

The EFPI sensor is fabricated by fusion-splicing a glass tube onto a cleaved optical fiber (**Fig. 1-5a**). The EFPI has the advantage of no transverse coupling, and can therefore evaluate more directly the axial component of strain in a host material. Moreover, this sensor has low sensitivity toward temperature because of the presence of the air gap and the temperature compensation attained by the glass tube. But this extrinsic sensor is larger than the other two sensors, which is a disadvantage for embedding the materials. Compared to intrinsic FFP sensors, the EFPI cavity must be kept small to avoid significant loss of light from diffraction. This size limits the strain range. But the low-coherent white light interferometer method enables EFPI to measure strain with an accuracy of 0.25μ when the strain length and

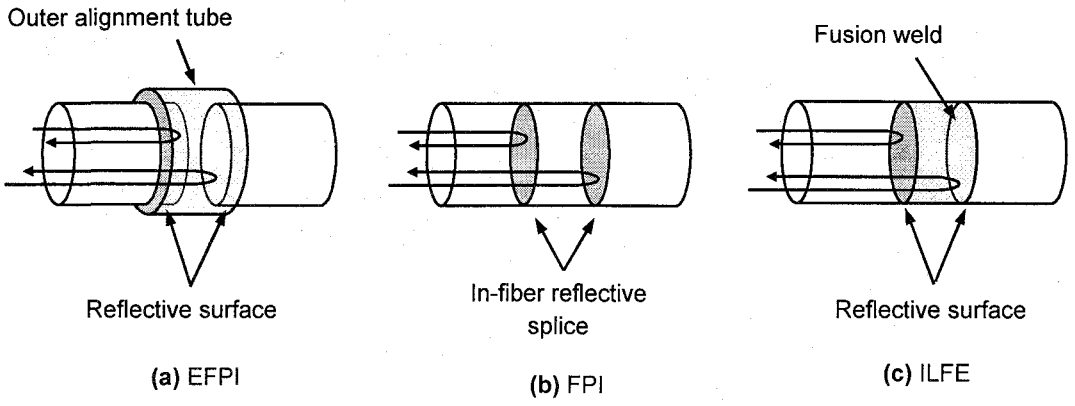

Fig. 1-5 Three types of FFP sensors

range is set to 1mm and 1000μ, respectively (Belleville and Duplain, 1993; Measure, 2001). Note that if sensor length is set to 10mm, the strain range of 10,000□ can be attained. One of the representative applications of EFPI is reported by Morin et al. (1996). Fifty-four EFPI sensors are installed on the propeller blade of a Polar class icebreaker ship. The sensor length of EFPI installed in this application is 10mm, with a resolution and range of 2μ and ±4000μ, respectively. Finally, however, of a total of 55 sensors installed in the blade, 53 sensors are found to be functional (Morin et al., 1996).

Unlike the EFPI, the FFP and ILFE sensors are formed within the fiber, which means they can be easily embedded in the materials (Varis et al., 1990; Marcus, 1988). Within the sensing part, the FFP sensor has two reflective fusion sections of a single-mode fiber (**Fig. 1-5b**), while a hollow-core fiber is spliced between the ends of the fiber of the ILFE (**Fig. 1-5c**). These two sensors are elegantly designed but difficult to fabricate. In addition, the mechanical integrity and robustness of these sensors might be inferior to the EFPI (Tuck et al., 2002). The cavity of an intrinsic FFP sensor can be made large, making it possible to achieve a strain resolution of a few μ with a 20 mm gauge length at a sampling rate of 10^5μ/sec (Mason et al., 1992).

Another remarkable intrinsic FFP sensor is attained by using twin Bragg Grating to form a Fabry-Perot interferometer. In this FBG-FP approach, an identical pair of fiber Bragg gratings are formed in the optical fiber with a predetermined separation (**Fig. 1-6**). This approach also enables sensor multiplexing, for which the reflectivity must be less than 0.13% if 30 such FBG-FP sensors will be used along a single fiber (Measures, 2001). Dakin et al. (1997) reported that a strain resolution of ~1μ is expected in measurement time ~1s, by using low-coherence interferometry. Furthermore, using a broadband light source would permit a sensor length of less than 5mm.

(3) Polarimetric and modalmetric fiber optic sensors

The polarimetric sensor can measure host temperature or strain by detecting the state of polarization of the fiber, using a highly birefringent optical fiber that produces the change of polarization; the length of this birefringent fiber can be determined by detecting the intensity of polarized light. Based on this principle, a hydrostatic pressure and temperature sensor is proposed experimentally (Measures, 2001). But the need for polarization-maintaining optical fiber and polarization-insensitive

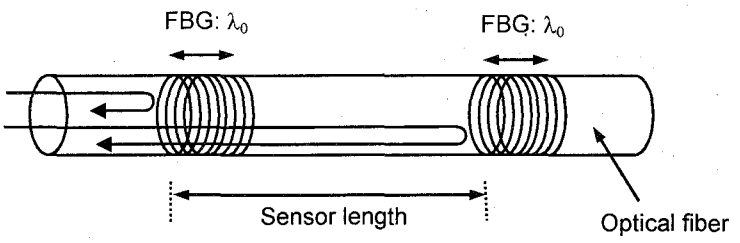

Fig. 1-6 Mechanism of an FBG-FP sensor

couplers has considerably limited the use of this kind of sensor.

The modalmetric sensor contains two-mode and single-mode fiber. In this sensor, the two-mode fiber is employed as a sensing fiber, where the spatial variation in the transverse mode light is converted into a non-linear relation between the signal and the strain in the host structure. However, the difficulty and inaccuracy of manufacture has diminished interest in this sensor, and almost no application has been reported so far (Measures, 2001).

(4) Spectrometric fiber optic sensors

Spectrometric sensors are sophisticated optical fiber sensors that are based on the spectrum of reflected light. These sensors employ both the intensity and the wavelength information of the reflected light. The spectrometric sensors can be classified into two main sensors: backscattering-based sensors and FBG (Fiber Bragg Grating) sensor.

Backscattering-based sensors can make a distributed measurement with the OTDR technique. The backscattering contains Rayleigh, Raman and Brillouin scattering, each of which can be applied to a sensor (see **Appendix A**).

A Rayleigh scattering-based OTDR sensor is the simplest temperature sensor because the wavelength of the scattering light is identical to that of incident light, and the intensity of the scattering increases with temperature. But since Rayleigh scattering has small power, the specific optical fiber (high Rayleigh scattering sensitivity) is required for temperature sensing (Hartog, 1983).

Raman scattering comprises Stokes (higher energy) and Anti-Stokes (lower energy) emissions, as shown in **Fig. A-9**. The temperature sensor is achieved by

Anti-Stokes detection because only Anti-Stokes emission responds to the temperature shift. Systems capable of operation over several kilometers of fiber length with about 1°C resolution and 3 to 10m spatial resolutions have been demonstrated (Dakin, 1995). Moreover, based on the temperature measurement, many advanced applications of this sensor including gas leakage detection have been reported (Vogel et al, 2001).

Brillouin scattering in optical fibers arise due to the interaction of light with phonons (quantized acoustic waves), as shown in **Fig. A-10**. The frequency of the Brillouin scattering light depends on the strain and temperature of the optical fiber. When the Brillouin scattering light frequency is detected with the OTDR technique, the distributed strain sensor is achieved. However, the Brillouin frequency shift is very much smaller than experienced in Raman or Rayleigh scattering, which causes difficulties in measurement such as low accuracy or resolution. In the 1990s, the strain accuracy of 100μ with 1m spatial resolution is reported (Kurashima et al., 1997). After that, Bao et al. (2001) improved the sensing system for Brillouin OTDR (B-OTDR), achieving the strain accuracy of $\pm$10μ with a spatial resolution of 0.5m. Another advantage of B-OTDR, unlike Raman scattering based sensor, is the ability to separately detect the strain and temperature. This simultaneous measurement is possible because the Brillouin scattering coefficient and the Brillouin frequency shift are independent of each other with respect to the temperature and strain change (Horiguchi et al., 1997). Of this distributed sensor, a number of field applications have been attempted. Kumagai et al. (2000) developed the B-OTDR based-concrete, embedded-sensor, by covering the fiber with fiber reinforced plastic (FRP) to overcome the weakness of the fiber during the construction. However, the accuracy and resolution of B-OTDR is not so high as FBG or traditional resistive gauges. Wu et al. (2002) improved the resolution of B-OTDR by looping the fiber, especially in the sensing area, to detect cracks in concrete structures. As for the steel structures, Miki et al. (2000) applied B-OTDR to the steel bridge. In the geo technical field, various applications are challenged, including falling rock detection, tunnel monitoring, embankment monitoring, ground anchor monitoring, etc (Wakabayashi et al, 2002; Okumura et al, 2002; Matsushita et al, 2002; K. Kojima et al, 2002). Note that these geotechnical applications have been demonstrated mainly by Japanese engineers. Finally, the problems of the accuracy and resolution may restrict progress in using

scattering based sensors.

1.2.2 Fiber Bragg Grating sensor

On the other hand, Fiber Bragg Grating sensor is one of the most promising sensors, although it can measure the strain or temperature at only predetermined points, not distributed points. As shown in **Fig. 1-7**, a fiber Bragg grating is a periodic, refractive index perturbation which is formed in the core of an optical fiber by exposure to an intense UV interference pattern (see **Appendix B**).

Naturally, the accuracy of this sensor depends on the demodulation system, but a wavelength resolution of about 1pm is required at a wavelength of 1.3μm corresponding to a temperature change of 0.1°C, or a strain of 1 μ. In addition, FBG sensors can be arrayed in one fiber using multiplexing methods such as wavelength, time, or coherence division (see **Appendix C**). However, their number or dynamic range also depends on the multiplexing method and demodulation system. For instance, an FFP tunable filter demodulation system can give a resolution of 4μ and identify 31 sensors in one fiber. Tremendous applications of this sensor have been reported up to now, but the technical challenges tend to focus on the following four targets:

- simultaneous strain and temperature measurement
- embedment into composite materials
- multiaxis or distributed strain measurement
- applications using FBG.

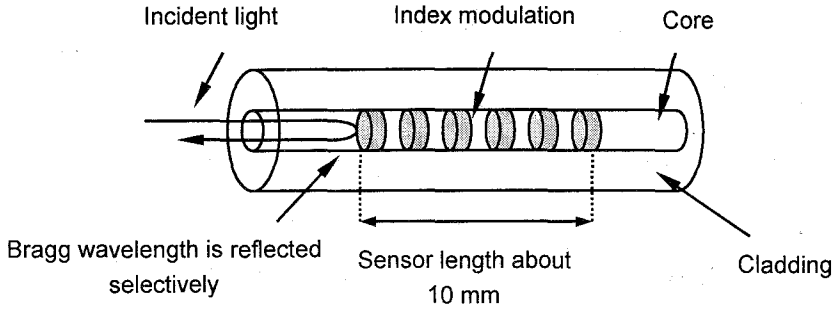

Fig. 1-7 Structure of an FBG sensor

(1) Simultaneous strain and temperature

Simultaneous strain and temperature measurement, or temperature compensation, can be attained by several methods including combinations of FBGs, FBG and FP combination, long-period gratings (LPG), use of Brillouin scattering or polarization-maintaining fiber, etc.

The use of two FBG sensors is one of the simplest methods of simultaneous measurement. Lo and Sirks (1997) demonstrated that one half of an FBG is bonded to its host structure, leaving the other half free of mechanical strain (**Fig. 1-8**). The section of the FBG that is bonded suffers both strain and temperature, while the free section suffers only the temperature change. The authors recommend that the one Bragg wavelength should be slightly different from the other so as to clearly separate the two peaks.

Another way is the combination of EFPI and FBG sensors, where FBG is used for temperature and strain discrimination, and EFPI acts as a strain sensor. Rao et al. (2001a and 2001b) employed chirped FBG for the temperature compensation, experimentally achieving a strain accuracy of ±20μ with a temperature accuracy of ±2.0°C.

The Fabry-Perot sensor formed by twin FBG sensors, FBG-FP sensor, can also achieve the compensation, by detecting both FBG spectrum and interferometric length of FP. Jin and Sirkis (1997) showed that their FBG-FP sensor agreed with conventional strain and temperature gauges to within 5μ and 0.5°C, respectively, for a sensor length of 10mm.

Polarization-maintaining fiber can simultaneously measure the sensitivity for

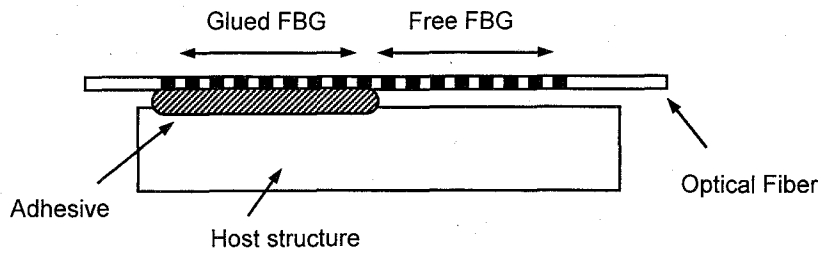

Fig. 1-8 Temperature compensation method in FBG sensors

strain and temperature of slow and fast axes of the birefringent fiber (Ishikawa, 2000).

As for LPG sensors, the multi peaks with different temperature and strain sensitivity enables a temperature and strain separation, and a minimum detectable strain and temperature remains about 30μ and 0.6°C due to its nonlinearity (Bhatia et al., 1997). Additionally, LPG and FBG combinations are also demonstrated a strain and temperature resolution of ±9μ and ±1.5°C, respectively, over a range from 290 to 1270μ and 25.0 to 50.0°C (Patrick et al. 1996).

As described in the B-OTDR sensor, the Brillouin scattering shift is also a function of both temperature and strain. Thus it takes for granted that the combination of FBG and Brillouin scattering enables temperature and strain discrimination, a mechanism shown experimentally by Davis and Kersey (1996).

Moreover, temperature-independent sensors can be attained by chirped grating (Xu et al., 1995), who demonstrated a strain resolution of 4.4μ over the range of 4066μ by using tapered fiber. Tanaka et al. (2002) proposed temperature compensated strain modules using FRP plate; using the difference of elastic moduli and thermal expansion coefficients between two different FRP plates, temperature compensation is achieved.

Though other principles including use of second-order diffraction peaks of FBG have been reported (Lopez-Higuera et al., 2001), the goal of recent research tends to upgrade the accuracy of the discrimination by using the described principles. But most of them have not been tested in the practical application.

(2) Embedment into composite material

Incorporating FBG sensors into composite material is an attractive target for aerospace engineers. An excellent review of the various issues associated with the embedded sensors in FRP can be seen in the book by Measures (2001). According to this book, a number of research projects have been done on the influence of embedded sensors. These projects focused on tensile, transverse, compressive, and shear strength as well as fatigue, etc.

N. Takeda et al. (2001) have made outstanding progress with embedded sensors, using small-diameter FBG sensors. In order to diminish the influence of the fiber on the structure, the developed sensor has a core and cladding diameter of 6.5μm and 40 μm, respectively. The proposed sensors include a 10mm normal FBG sensor,

LPG sensor and 40mm chirped FBG sensor for temperature compensation or distributed sensing. As a result, the authors reported that the sensor can detect the delamination of layers, cracks, and stress distributions of FRP structures (S. Kojima et al., 2002; S. Takeda et al., 2002; N. Taleda, 2002; Mizutani et al., 2002). Though this topic is quite attractive, the application may be restricted due to the high cost of FRP material for civil engineering use.

(3) Multi-axial measurement

Multi-axial strain measurement can be attained using polarization-maintaining (PM) fiber (e.g., birefringent fiber), since the two orthogonal polarization modes in PM fiber are reflected at different wavelengths. This topic has also attracted researchers, who have been reported some progresses (Menendez and Guemes, 2000; Doyle and Fernando, 2000; Black et al., 2002); however, some practical problems such as high cost have been left (Bosia et al., 2002).

A rosette gauge, a kind of multi-axis measurement that uses four FBG sensors is proposed by Matrat et al. (2001): one sensor should be required for the temperature compensation, while the other three sensors can decide two principal strains and shear strain. But in this gauge the strain distribution becomes complicated with the temperature compensation since four sensors need four layers. The authors proposed a three-layer rosette without temperature compensation, and by far, the strain response of this rosette agreed with that of conventional gauge within 5% errors (Matrat and Levin, 2002). Note that these rosette gauges, embedded into composite materials, cannot be installed on the surface of the host structures.

Finally, although the multiplex measurement can be attained in principle, the difficulties limit their practical use.

(4) Applications

On the other hand, a number of practical applications or transducers based on the FBG sensors have been reported recently, including bridge monitoring, geo-structure monitoring and geo-intended transducers.

As for the bride monitoring, FBG sensors are installed within the concrete structure beside the reinforcement bars or within the tension cables of the cable-stayed bridge (Nellen et al., 1999; Kodindouma et al., 1996). Preliminary to these applications, fundamental tests are also carried out for elemental specimens

such as simple beams or FRP rods to confirm the accuracy of the sensors, which showed good agreement with the conventional instruments (Davis et al., 1997; Kodindouma and Idriss, 1996). Jones et al. (1998), using 16 FBG sensors, demonstrates the mapping system for the out-of-plane deformation of a cantilever subject to single-point load. This experiment is a challenge to evaluate the whole structure with information from the local sensors. Kodindouma at al. (1996) report a parallel and serial multiplexed network of 48 FBG sensors to measure the strain distribution of a quarter-scale test bridge with a 12.25m span. The authors attach 13 FBG sensors to rebars in both longitudinal and transverse directions, while 15 FBG sensors are attached to I-beams. The sensors monitored the dead load as well as the live load provided by a hydraulic jack. This research leads to practical monitoring with the bridge to offer the damage detections. The I-10 Bridge in North America is one of the retrofitting in-service bridges with fiber optical monitoring systems (Idriss et al., 1998). An array of 32 FBG sensors is installed in the bridge so as to monitor the strain of the concrete girders at various locations.

For monitoring geo disasters, various transducers have been developed using FBG or B-OTDR because they have high durability and wide monitoring range. Yoshida et al. (2002) developed the borehole inclinometer for ground deformation. This inclinometer, installed within the casing-tube, has several 1m units connected to each other with a hinge plate and two sensing tubes (**Fig.1-9**). Of the two tubes, only one tube contains FBG; the other is used for fiber transmission. Whereas this

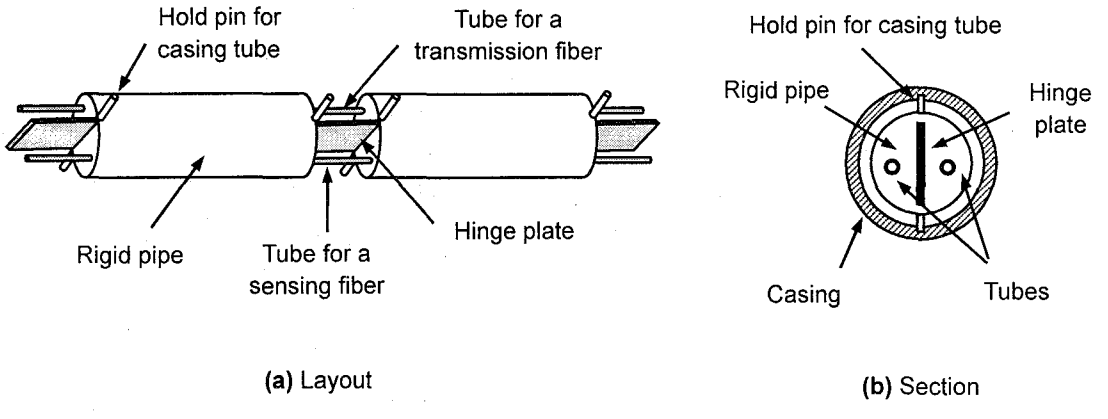

Fig. 1-9 Inclinometer based on FBG sensors proposed by Yoshida et al. (2002)

proposal is excellent, the results of this in-situ experiment are not calibrated by the other instruments, and the temperature influence must be large since they use only one FBG sensor for one section, precluding compensating the temperature with this system. Sato et al. (2001) proposed a ground strain measurement system that can measure dynamic strain using bronze plate. Though this system showed high accuracy compared with conventional instruments, more improvements are required for practical applications. Chang et al. (2000) proposed soil pressure meter usingFBG sensors. Because of the disc shape of the bulkhead, the sensor is installed circumferentially so that the sensor's spectrum of the sensor shows one clear peak.

All the above transducers, unfortunately, cannot compensate the temperature. When FBG sensors are applied to the practical measurement, temperature compensation must be done. Tokyo Measuring Instruments Laboratory Co. Ltd. and NTT advanced technology Co. Ltd. have commercially produced the transducers based on FBG sensors which have compensation mechanism within the transducers (Yamaga et al., 2002). They compensate the temperature mechanically using bimetal plate and demonstrated high stability in the field, as shown in **Fig. 1-10**.

Other practical applications such as landslide, tunnel, rock bolt, and dam monitoring have been reported, some of which have been used successfully. Especially for geo disastrous monitoring, a number of systems using FBG or B-OTDR are proposed (Yamanabe et al., 2001), but are still undergoing testing.

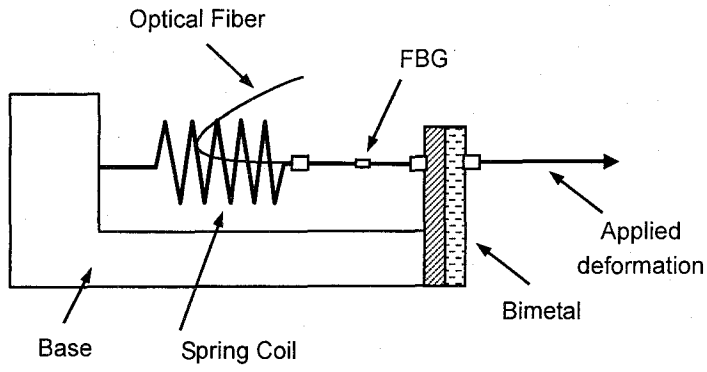

Fig. 1-10 Displacement transducer with temperature compensation mechanism proposed by Yamaga et al. (2002)

1.3 Objectives and Scopes

The purpose of this study is to develop and evaluate monitoring systems using optical fiber sensors.

This study consists of 3 steps: in the first step, the author focuses on developing the transducers for strain or displacement measurement, based on the optical fiber sensors. In this step, the feasibility of the fiber-optic-sensor-based transducers is evaluated both empirically and analytically. The practical problems associated with the proposed sensors are also evaluated. Then the all-purpose sensing system using optical fiber sensors, including the proposed transducers, is developed in the second step. Finally, in the third step, the developed sensing system is applied to the geo structures so as to confirm the monitoring system.

As discussed in Chapter 2, a strain gauge module using FBG sensors is developed for the steel structures. Fundamental experiments including bending, tension, and temperature tests are carried out. Additionally, numerical analyses are conducted with FEM and T-matrix methods, to discover the relationship between the strain distribution and the reflection spectrum.

For the geo monitoring, Chapter 3 describes the development of a displacement transducer using FBG sensors. Since the sensor installation arrangement onto the transducer, as well as the curvature distribution of ground, determines the accuracy of the measurement, the influence of the sensor position on the accuracy is evaluated by numerical analysis. Additionally, preliminary tests such as bending and site tests are carried out.

In Chapter 4, the all-purpose sensing system is configured on the basis of optical fiber sensors. In this monitoring system, FFP tunable filter demodulation is adopted and evaluated against the harsh environment.

In Chapter 5, based on the results in chapters 2 to 4, a monitoring system using the deformation transducer and strain module is configured and applied to the excavation control. Though these transducers are developed for the geo disasters, this experiment holds importance since this system can be applied to the geo disasters without major changes. Finally, a pipeline monitoring system based on the proposed system is designed. In this application, the monitoring conditions are evaluated by FEM analysis considering the buckling and inner pressure, as well as

the sensor requirements for long-distance monitoring.

Chapter 6 reviews the several conclusions that can be drawn from this study.

Chapter 2 Development of a strain module based on FBG sensors

2.1 General remarks

To identify the state of structures, strain is one of the most important physical properties. The monitoring of strain in structures has been traditionally performed by resistive gauges. However, resistive gauges have some problems since they use electrical resistance and wires that tend to be corroded. Moreover, lightning-storm damage, such as thunder, is quite serious for resistive gauges as opposed to optical fiber sensors. Thus, though the resistive gauges are considered by practitioners to be reliable and stable, optical fiber sensors are thought to be ideal for long term monitoring because of their high durability. As discussed in Chapter 1, FBG sensors can be the best for strain measurement as well as structural monitoring. However, when FBG sensors are used for measurement with only a primal jacket such as polyimide coating, much attention is required to handle them. The reason is that the optical fiber, made of silica, can be easily broken by small curvature bending, and the sensing part is weaker than the normal part by exposure to the ultraviolet lasers. In general, the strength of the optical fiber depends on the coverage; for example, the naked fiber has tension strength of 0.35GPa. The transmission part of the optical fiber can be protected by a coating such as nylon or acryl, but the sensing part cannot be covered because of the high sensitivity, and still remains weak. In addition to this weak point, if non-uniform strain distribution is developed in the sensing part of the FBG sensor, the spectrum of FBG contains multi-peaks that may cause measurement errors.

Therefore, in this section, to protect the sensing part of the FBG sensor, a strain measurement module is developed and evaluated. Fundamental tests such as tension, bending and temperature tests are conducted to evaluate the basic

properties of it. Moreover, numerical analyses are carried out to evaluate the influence of the strain distribution on the FBG spectrum as well as the performance of the proposed module. Note that this module is intended to be applied to steel structures and installed with bolts to host structure instead of adhesives due to their higher durability.

2.2 Fundamental scheme of the proposed module

The outline and detailed dimensions of the proposed module are shown in **Fig. 2-1** and **Fig. 2-2**, respectively. In this module, H-shaped aluminum plate is used for the

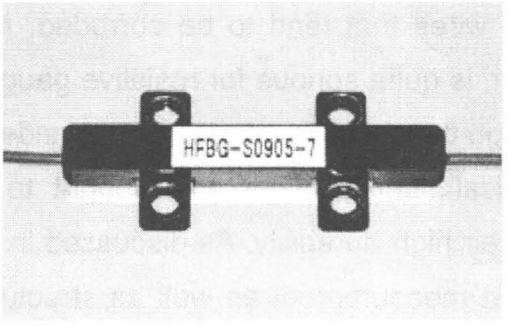

Fig. 2-1 Picture of the proposed module

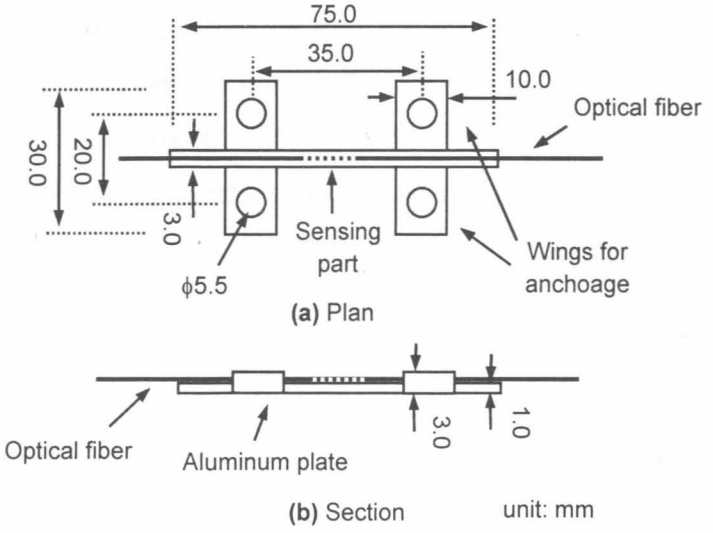

Fig. 2-2 The outline of the proposed module

base. On the center of the base, the FBG sensor is installed and protected by a plastic case, while the base is fixed to the host structure with 4 bolts at the four wings. The sensing part is attached to the base with adhesive (Epo-tech 353ND) and covered by a plastic case. The optical fiber (except for the sensing part) has nylon coating for protection that can be connected to the other fibers with FC connectors.

2.3 Calibration test

2.3.1 Tension test

(1) Test setup

To evaluate the stain sensitivity of the module to the tension force, two tension tests are carried out. As shown in **Fig. 2-3**, two aluminum plates are attached to the module with bolts and pulled by the universal testing machine, introducing tension force to the module. First, the tension force is applied up to 588.0N (60.0kgf) with an increment of 98.0N (10.0kgf), then unloaded at once, to evaluate behavior under a higher stress level. Secondly, in order to estimate the linearity or restoring behavior under a lower stress level, the module is loaded up to 98.0N (10.0kgf), then unloaded, with an increment of 19.6N (2.0kgf). Note that in every test a resistive strain gauge is mounted on the center of the back side of the base. The measurement system used in this test is shown in **Fig. 2-4**.

(2) Results and discussion

Fig. 2-5 illustrates the relationship between applied stress and strains obtained by the Bragg wavelength shift as well as by the resistive gauge. The applied stress here denotes the applied force divided by the module section. In this figure, the triangle indicates the value of the gauge; the rectangle indicates the value of the FBG sensor. In addition, a line represents the initial tangent of the FBG sensor. This figure shows that, until the applied stress reached around 95MPa corresponding to 1560μ, the values of FBG agreed well with that of the gauge and that the stress-strain relationships by both sensors are linear. However, both relationships become nonlinear at a higher stress level such as 95MPa, which can be attributed to the nonlinearity of the base aluminum. At a higher stress level, the difference between the

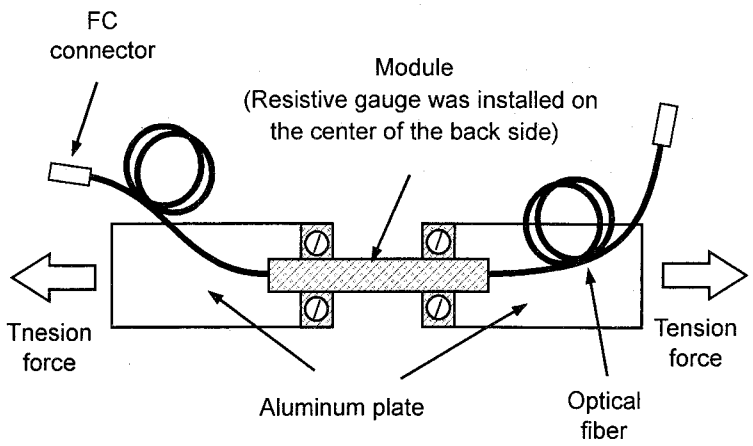

Fig. 2-3 Tension test setup

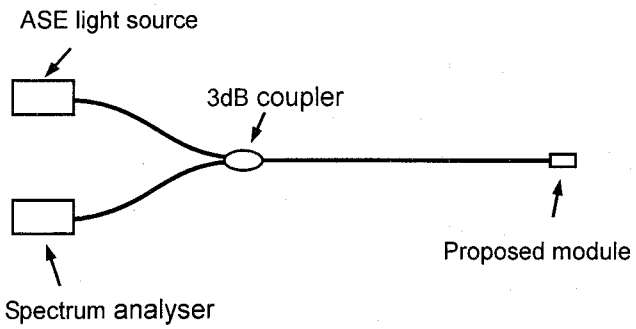

Fig. 2-4 Measurement system used in the test

values of gauge and FBG increase as the applied stress increases. Finally, residual strains by both sensors are also different. These differences may be attributed to the bending moment caused by the bolt anchorage and by the eccentricity due to the thickness of the wing: if such a bending moment occurs, strain by the FBG sensor at the top surface can become larger than strain by the resistive gauge at the bottom because of some strain gradients of the section.

On the other hand, **Fig. 2-6** shows the spectra of reflected light from Bragg grating. In general, when the grating is subjected to strain gradient, a peak of the spectrum splits into multiple peaks that may cause some errors in detecting the peak wavelength, i.e., Bragg wavelength. From this figure, multiple peaks appear in the spectrum at 588N and that of the residual strain, which means some strain gradient

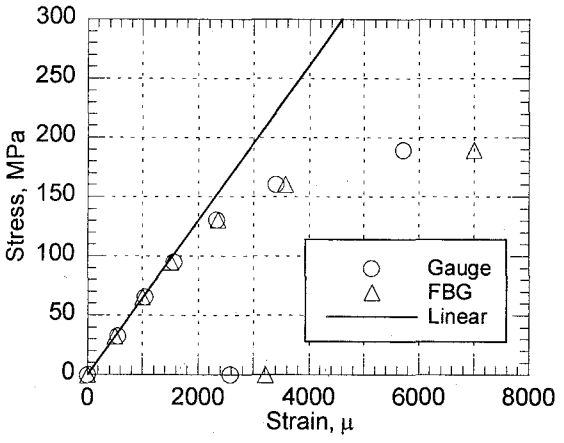

Fig. 2-5 Strain-stress curve in the tension test

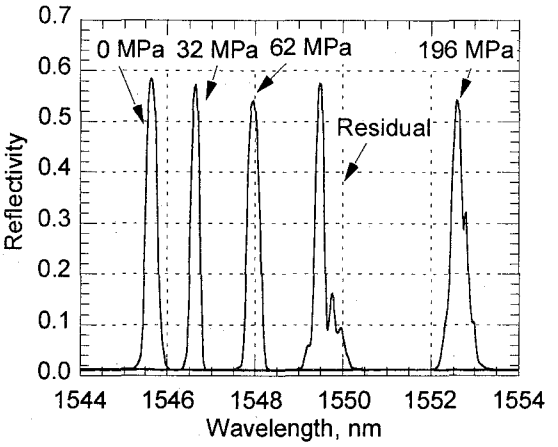

Fig. 2-6 Spectra in the tension test

along the fiber. Though these spectra contain multi peaks, the largest peak may denote almost the average of the strain distribution at a lower strain gradient.

Next, the results of tension tests at a lower stress level are discussed. Note that in this lower test, the same specimen is employed as in the higher test, thus the aluminum base is already deformed plastically by the former test. Consequently, the spectrum of this specimen initially contained multiple peaks. **Fig. 2-7** demonstrates the relationship between stress and strain at a lower stress level. In this figure, L. and LU. denote the loading and unloading process, respectively. During the loading process, the stress-strain curves by both instruments are almost linear and in agreement. In contrast, during the unloading process, though each stress-strain curve is linear, the slope of the curve by gauge becomes smaller than that by the FBG. It may be attributed to the fact that some bending moment may occur to the module during unloading process. Note the elastic modulus acquired by loading test is 66.3GPa, which is almost identical to that of aluminum-magnesium alloy (Al-Mg 5052), 69.0GPa.

Fig. 2-8 shows the spectra of the reflected light at the beginning, maximum load, and the end of the unloading. These spectra had almost similar forms and each peak can be identified clearly, which means that the test is carried out in the elastic regime. Note that they are not exactly similar to each other since some bending occurred, giving rise to a small strain gradient along the fiber, especially during unloading process.

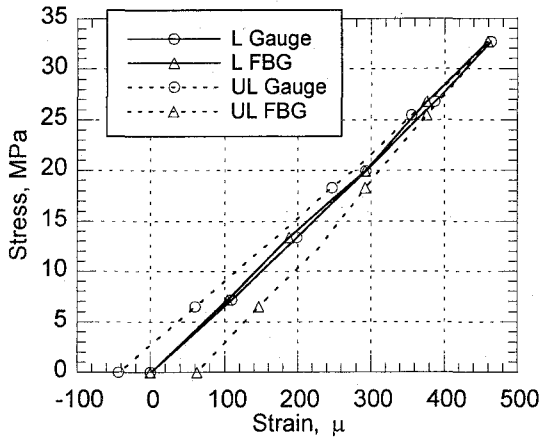

Fig. 2-7 Strain-stress curve in the tension test (at a lower level)

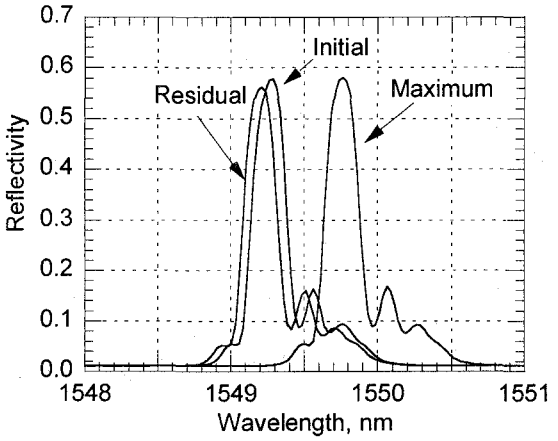

Fig. 2-8 Spectra in the tension test (at a lower level)

As a result, provided that the use of the proposed module is restricted in the elastic regime, it can be applied to the strain measurement up to about 2000μ. Note that the optical fiber itself behaves elastically until failure and the failure strain is about 5000μ. When the module experiences a small-strain gradient, the wavelength corresponding to the spectrum peak may indicate approximately the mean value of the strain distribution along the sensing fiber. However, in contrast to a small-strain gradient, when it experiences a larger-strain gradient, multiple peaks of the spectrum may occur and the largest peak may not indicate the mean value of the strain gradient. Therefore, for practical use of the proposed module, users must pay attention to controlling the module in order not to generate the strain gradient at the sensing part.

2.3.2 Bending test

(1) Test setup

As shown in **Fig. 2-9**, a four point bending test is conducted on the steel plate, on whose center the proposed module is installed. The locations of resistive gauges and the module are shown in **Fig. 2-10**. In this test, a gauge value indicates the mean value of 10 resistive gauges located in the uniform bending span. The load is applied up to about 50% of the yielding load of the steel plate, and then released step by step so that the steel behaved elastically. The system used in this test is the same as that in the tension test.

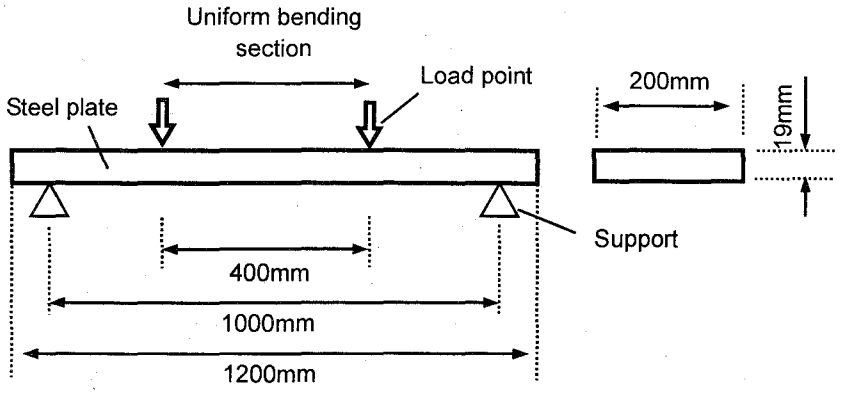

Fig. 2-9 Setup of the bending test

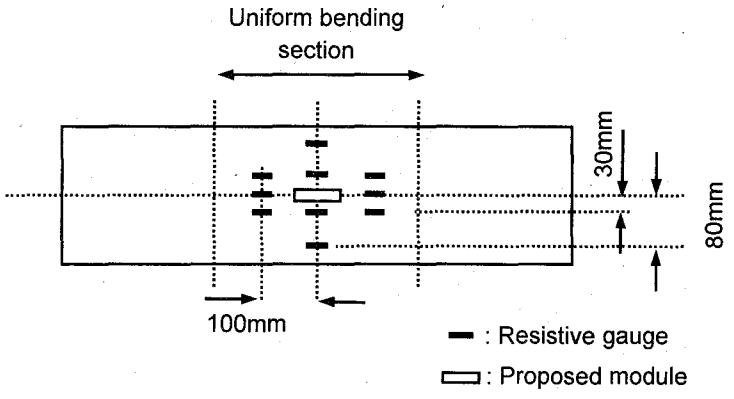

Fig. 2-10 Sensor locations in the bending test

(2) Results and discussion

Fig. 2-11 illustrates the relationships between the applied load and the strain by the resistive gauge and the FBG sensor, respectively. For both instruments, these relationships are almost linear while the slope of the FBG is larger than that of the gauge. Let us assume that the module is perfectly attached to the plate, allowing us to ignore the stiffness change due to this attachment. Therefore, the strain output at the module position should be 1.11 times as large as that at the surface of the plate, because the thickness of the plate and module are 19.0mm and 1.0mm, respectively.

However, the strain ratio obtained in this test by fitting a line to all data is 1.19.

This value is larger than the assumption, which may be attributed to the module's not being perfectly attached to the plate because of the bolts' anchorage, which can give rise to some play or bending. Moreover, it is difficult to determine the ratio by conducting the calibration test because the play of the bolts may depend on the installation. This problem can be overcome by welding or other installation methods to fix perfectly the position.

The spectra of the reflected light at the beginning and maximum load of this test are shown in **Fig. 2-12**. Note that these spectra contained more multi-peaks than those of the tension test, because before the bending test, the module is excessively deformed to remain in non-uniform plastic deformation. Moreover, the reflectivity of the spectra is smaller than those in the former test because the decrease of the uniform part of the grating caused lower reflectivity. From this figure, though the spectra include many peaks, they have similar form, and the peak shift can be detected clearly. It can be said that during this test the stain of the sensor developed uniformly.

As a result, this bending test shows that the strain at the steel surface by the gauge and the module have some constant relationship. However, this constant cannot be determined by calibration testing since this constant depends on uncertain phenomena, requiring perfect attachment or other mechanisms for unmoved installation such as welding so as to yield the unique constant.

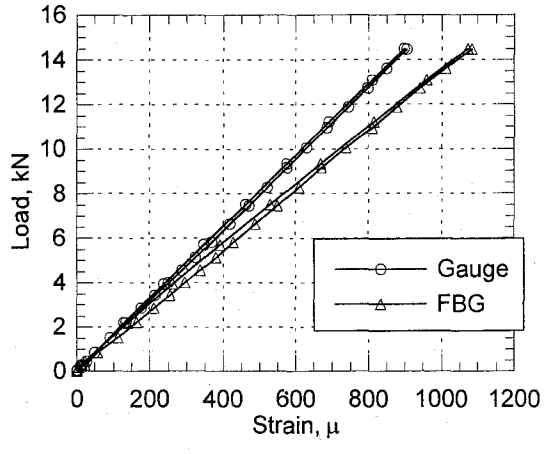

Fig. 2-11 Strain-stress curve in the bending test

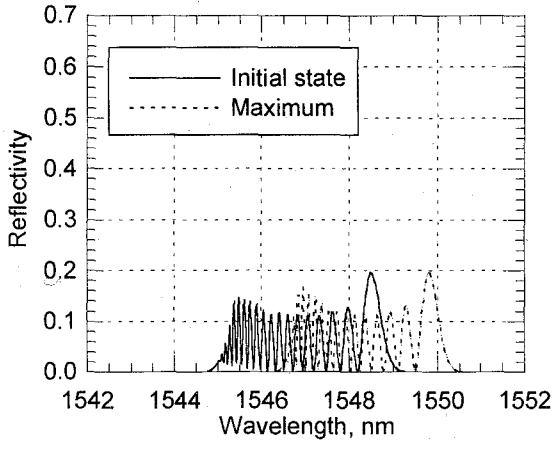

Fig. 2-12 Spectra in the bending test

2.3.3 Temperature test

(1) Test setup

To evaluate the temperature property of the module, a temperature test is conducted and the relationship between temperature and wavelength is obtained. The module is heated step-by-step at 17, 30, 50 and 70°C in the environmental test machine without any constraint and mechanical load.

(2) Results and discussion

The relationship between temperature and peak wavelength (**Fig. 2-13**) is linear, and the sensitivity of the peak shift to the temperature becomes 0.0224nm/°C by linear regression. By substituting this value into equation (B.50) in **Appendix B**, the apparent temperature strain, $\Delta\varepsilon$, can be given by

$$\Delta\varepsilon = \frac{\Delta\lambda}{\lambda S_\varepsilon}. \tag{2.1}$$

where $\Delta\lambda$ is the obtained wavelength shift, λ is a representative wavelength, and $S\varepsilon$ is the temperature coefficient.

Thus, by substituting 0.024nm for $\Delta\lambda$, 1530nm for λ, and 0.78 for S_ε, the apparent temperature strain becomes 18.77m/°C. Note that the representative wavelength of 1503nm denotes the wavelength corresponding to 50°C, the mean value between -20 and 80°C, since the sensitivity should be considered at temperatures ranging from -20 to 80°C.

Next, when the FBG sensor is installed on the host (temperature coefficient of α_H), using equation (B.50) the temperature apparent strain of the FBG sensor can be expressed by

$$\Delta\varepsilon = \alpha_H - \alpha_F + \frac{S_T}{S_\varepsilon}. \tag{2.2}$$

where α_F and α_H are the thermal coefficient of optical fiber and host structure, respectively, and S_T and $S\varepsilon$ are the temperature and strain coefficient, respectively.

Now assuming that these coefficients can be expressed by those at a wavelength

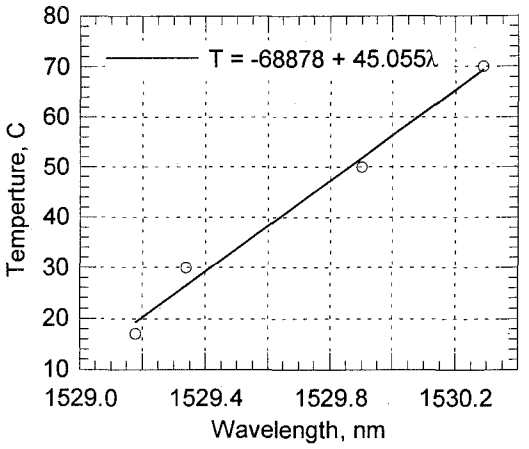

Fig. 2-13 Temperature-wavelength curve in the temperature test

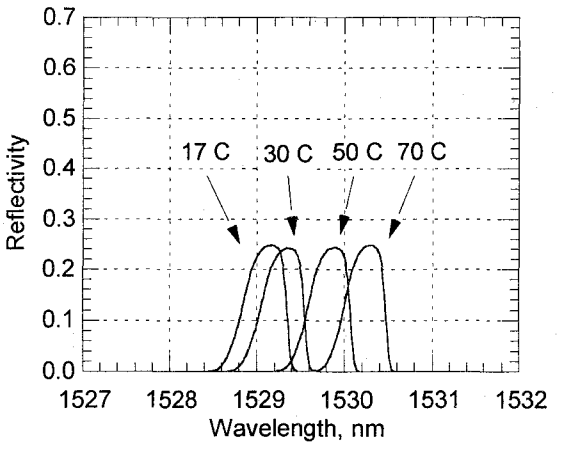

Fig. 2-14 Spectra in the temperature test

of 1550nm, such that α_F = 0.5×10^{-6}/°C, S_T = 6.7×10^{-6}/°C and S_ε = 0.78×10^{-6}, then the apparent strain becomes 10.69×10^{-6}/°C. On the other hand, the thermal coefficient obtained by the material test becomes 11.8×10^{-6}/°C, which is close to the above value. Thus, it can be said that the FBG is perfectly attached to the base plate, giving smooth transition of the strain from the base to the FBG.

Fig. 2-14 shows the spectra at each temperature level, with each spectrum clearly sharp and an almost similar form. Moreover, each bandwidth of the spectrum is small. These facts denote that the uniform strain developed because of the temperature change. Note that the specimen used in this temperature test is different from that used in the former test, and not initially deformed.

As a result, the temperature sensitivity of the proposed module is found to be 18.77×10^{-6}/°C. Because this sensitivity is relatively large, temperature compensation must be required for practical applications such as in situ monitoring.

2.4 Numerical analysis

First, to evaluate the measurement errors caused by the FBG demodulation system, the spectra of the FBG sensors subject to typical non-uniform strain distributions are evaluated by the T-matrix method. Discussions are held, especially about the difference between the mean values of strain distribution and the strain corresponding

to the peak wavelength shift in the spectrum. Secondarily, for evaluating the proposed module, an evaluation is made of the sensitivity of Bragg wavelength shift to the applied strain and of the spectra of FBG installed on the module subject to tension, compression, and bending; this evaluation can be divided into two phases. In the phase I analysis, in order to obtain the strain distribution of the module, FEM analysis using FEM code *ABAQUS* is carried out. Then as a phase II analysis, the spectra of the strain distributions obtained in the phase I analysis are evaluated by T-matrix method.

2.4.1 Transmission matrix (T-matrix) method

T-matrix (transmission matrix) formalism offers a numerical way to analyze the response of the non-uniform grating structure proposed by Yamada and Sakuda (1987). For structural sensing, Huang et al. (1995) evaluated this method and applied it to various non-uniform gratings. The following expressions forming T-matrix are mainly based on their literature.

We now consider two counter-propagating waves guided within the core-forming uniform Bragg grating of length ΔL with uniform pitch length Λ, as shown in **Fig. 2-15**. The electric fields of the backward and forward waves in this uniform grating can be expressed by

$$E_f(z,t) = A_f \exp[i(\omega t - \beta z)] \tag{2.3}$$

and

$$E_b(z,t) = A_b \exp[i(\omega t + \beta z)] \tag{2.4}$$

respectively, where A_b and A_f is the complex amplitudes, ω is the angular frequency, and β is the propagation constant of the two waves.

According to Yariv and Nakamura (1977), these amplitudes obey the coupled-mode equations; i.e.:

$$\frac{dA_f}{dz} = -i\bar{k}A_b \exp(2iz\Delta\beta) \tag{2.5}$$

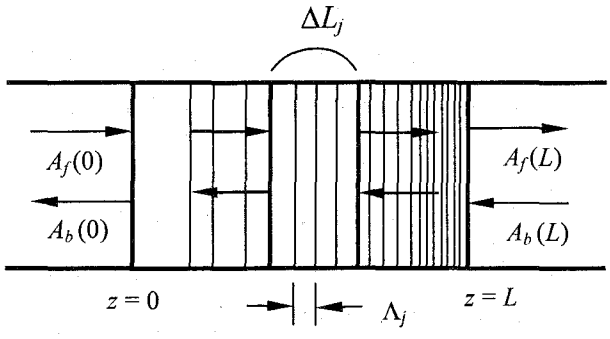

Fig. 2-15 Sub-gratings assumed in T-matrix method

and

$$\frac{dA_b}{dz} = ikA_f \exp(2iz\Delta\beta) \tag{2.6}$$

over $0 < z < \Delta L$, where $\Delta\beta = \beta - \beta_0 = 2n\pi/\lambda - \pi/\Lambda$ is the differential propagation constant, n is the average effective index of refraction in the grating, and κ is the coupling coefficient.

Note that β_0 is the propagation constant of which wavelength meets the Bragg condition; i.e., $\lambda = 2n\Lambda$ and $\bar{\kappa}$ denotes the conjugate complex of κ. For a uniform grating with sinusoidal modulation of the refractive index, n and κ can be expressed as

$$n(z) = n + \Delta n \cos\left(\frac{2\pi}{\Lambda}\right) \tag{2.7}$$

and

$$k = \frac{\pi\Delta n}{\lambda}, \tag{2.8}$$

respectively. Based on the boundary conditions of $A_b(0) = B_0$ and $A_f(\Delta L) = A_L$, the closed form solutions can be obtained by equations (2.5) and (2.6). Therefore, using

these solutions and $A_b(\Delta L)$ and $A_f(0)$ obtained by substituting $z = 0$ and $z = \Delta L$ into these solutions, Huang et al. (1995) showed the T-matrix relationship,

$$\begin{Bmatrix} A_b(0) \\ A_f(0) \end{Bmatrix} = \begin{bmatrix} T_{11} & T_{12} \\ T_{21} & T_{22} \end{bmatrix} \begin{Bmatrix} A_b(\Delta L) \\ A_f(\Delta L) \end{Bmatrix} \tag{2.9}$$

where

$$T_{11} = \overline{T}_{22} = \frac{\Delta\beta \sinh(\gamma\Delta L) + i\gamma \cosh(\gamma\Delta L)}{i\gamma} e^{-i\beta_0 \Delta L}$$

$$T_{12} = \overline{T}_{21} = \frac{\kappa \sinh(\gamma\Delta L)}{i\gamma} e^{i\beta_0 \Delta L} \tag{2.10}$$

and

$$\gamma = \sqrt{|\kappa|^2 - \Delta\beta^2}\,. \tag{2.11}$$

For non-uniform analysis, the amplitudes through the whole grating with length L can be obtained by dividing the grating into N sub-gratings with length, ΔL_1, ..., ΔL_N, each of which can be treated as a uniform grating with its own T-matrix. Now we can derive the T-matrix for the whole grating expressed as

$$\begin{Bmatrix} A_b(0) \\ A_f(0) \end{Bmatrix} = [T_1][T_2]..[T_N] \begin{Bmatrix} A_b(L) \\ A_f(L) \end{Bmatrix} \tag{2.12}$$

where T_i indicates T-matrix for ith grating.

Because there is no backward input wave, assuming the first and last amplitude is set to 0 and non-zero value A_w, respectively, we obtain the amplitude spectral reflectivity $R(\lambda)$ given by

$$R(\lambda) = \left| \frac{A_b(0,\lambda)}{A_f(0,\lambda)} \right|^2 . \tag{2.13}$$

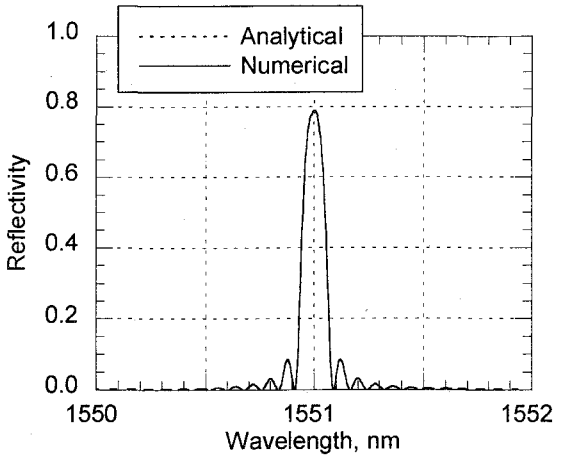

Fig. 2-16 Spectra of uniform grating by numerical and analytical methods

Note that A_w is the common factor of both the amplitudes that is obviously cancelled out.

For calibration of this method, the spectrum is obtained for uniform strain distribution. **Fig. 2-16** shows the spectra of uniform grating by T-matrix method and analytical method using equation (B.31) and (B.38). From this figure, one can see that both spectra agreed well with each other. Additionally, as for several non-uniform distributions, the results by T-matrix method agreed well with those reported by Huang et al. (1995). Thus, this method can be reliable and applied to the following evaluations.

2.4.2 Evaluation of typical strain distributions using T-matrix

Huang et al. (1995) showed that the spectrum of the reflected light from the non-uniform grating contained multi-peaks. As for resistive gauges, when they are subject to strain gradient, their outputs indicate the average of the gradient. However, for FBG sensors subjected to a strain gradient, the shift of the largest peak may not indicate the average strain. Thus in this section, the relationship between the largest peak in spectrum and the mean strain value is evaluated by the T-matrix method.

Now let us assume the strain distribution along the sensing fiber as shown in **Fig. 2-17** to **Fig. 2-22**. In these figures, Case 1-1 to Case1-8; i.e., series 1, indicate linear distribution, Case 2-1 to Case 2-8; i.e., series 2, indicate quadric distribution and Case

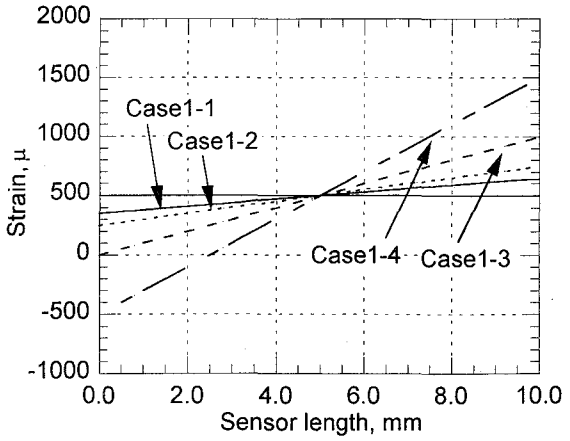

Fig. 2-17 Linear distribution 1

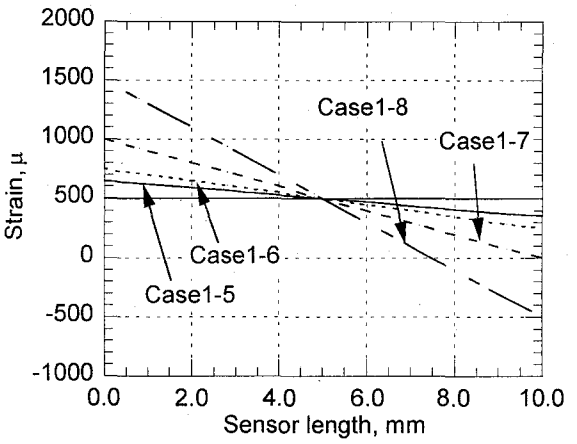

Fig. 2-18 Linear distribution 2

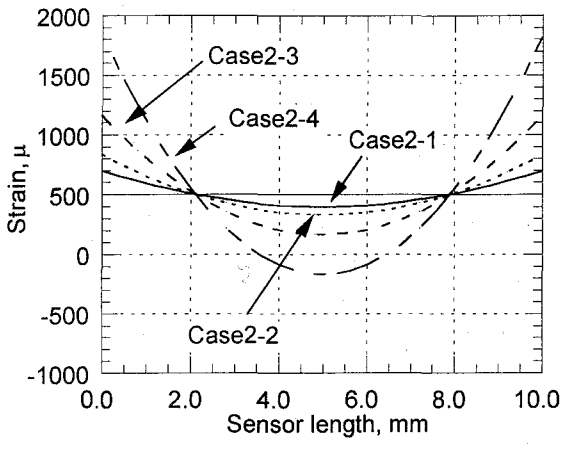

Fig. 2-19 Quadric distribution 1

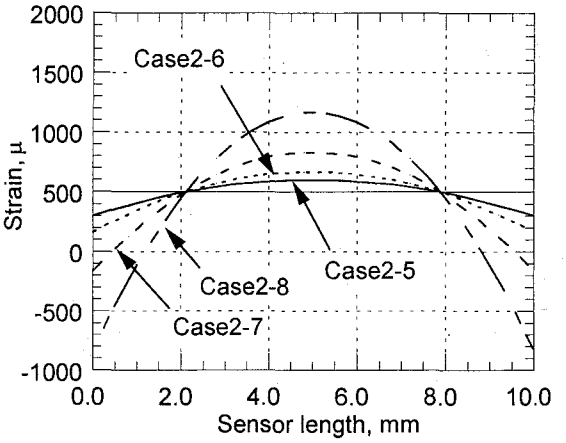

Fig. 2-20 Quadric distribution 2

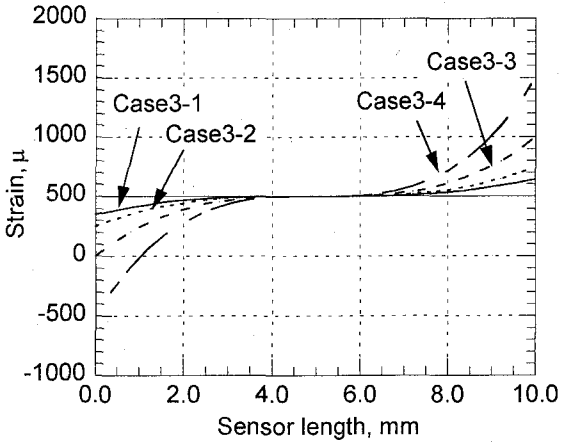

Fig. 2-21 Cubic distribution 1

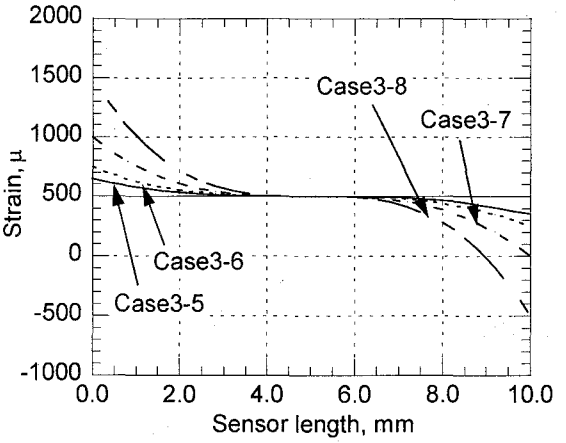

Fig. 2-22 Cubic distribution 2

3-1 to Case 3-8; i.e., series 3, indicate cubic distribution. These distributions can be expressed as the following equations:

for case1-1 to case1-8

$$\varepsilon(z)=\frac{1}{L}(\varepsilon_1-\varepsilon_2)z+\varepsilon_2 \tag{2.14}$$

for case2-1 to case2-8

$$\varepsilon(z)=\frac{4}{L^2}(\varepsilon_1-\varepsilon_2)\left(z-\frac{L}{2}\right)^2+\varepsilon_2 \tag{2.15}$$

for case3-1 to case3-8

$$\varepsilon(z)=\frac{4}{L^3}(\varepsilon_1-\varepsilon_2)\left(z-\frac{L}{2}\right)^3+\frac{\varepsilon_2+\varepsilon_1}{2} \tag{2.16}$$

where ε_1 and ε_2 are the maximum and minimum strain, respectively. Then the grating period is given by

$$\Lambda(z)=\Lambda_0+\alpha\varepsilon(z) \tag{2.17}$$

where ε is strain and α is the coefficient that is given by

$$\alpha=\frac{1}{2nS_\varepsilon}=4.0\times10^{-4}\ mm \tag{2.18}$$

where n is the refractive index and S_ε is the sensitivity coefficient (see **Appendix B**).

Table 2-1 shows the minimum and maximum strain in each case. Note that ε_1 and ε_2 are determined so that the average strain of ε_0 becomes 500μ for all cases. Note also that β denotes the ratio of the difference between the maximum and minimum strain to the average strain defined as the following equation.

Table 2-1 Parameters of the assumed distribution

Case	Degree of polynomial	ε_1 μ	ε_2 μ	ε_0 μ	β
NON	0	500	500	500	0.0
1-1	1	650	350	500	0.6
1-2		750	250	500	1.0
1-3		1000	0	500	2.0
1-4		1500	-500	500	4.0
1-5		350	650	500	-0.6
1-6		250	750	500	-1.0
1-7		0	1000	500	-2.0
1-8		-500	1500	500	-4.0
2-1	2	700	400	500	0.6
2-2		833.3	333.3	500	1.0
2-3		1166.7	166.7	500	2.0
2-4		1833.3	-166.7	500	4.0
2-5		300	600	500	-0.6
2-6		166.7	666.7	500	-1.0
2-7		-166.7	833.3	500	-2.0
2-8		-833.3	1166.7	500	-4.0
3-1	3	650	350	500	0.6
3-2		750	250	500	1.0
3-3		1000	0	500	2.0
3-4		1500	-500	500	4.0
3-5		350	650	500	-0.6
3-6		250	750	500	-1.0
3-7		0	1000	500	-2.0
3-8		-500	1500	500	-4.0

$$\beta = \frac{\varepsilon_2 - \varepsilon_1}{\varepsilon_0}. \qquad (2.19)$$

In this analysis the initial period is set to 517.0nm, and the number of grating division and length are assumed to be 2000 and 10mm, respectively, while the refractive index and fluctuation amplitude of this grating are set to 1.5 and 7.0×10^{-5}, respectively. **Fig. 2-23** shows the spectra of Case 1-1 to Case 1-4. From this figure, it is found that the peak of the spectrum split is caused by the linear gradient of the strain and that the number of the peak increases as the gradient increases. Additionally, the reflectivity decreases as the gradient increases. But these spectra are symmetric and the center wavelength of all cases corresponded to the mean strain value. **Fig. 2-24** shows the spectra of Case 1-5 to Case 1-8. From these two figures, the spectrum of Case 1-1, 1-2, 1-3, and 1-4 are identical to those of Case 1-5, 1-6, 1-7, and 1-8, respectively. It is also found that in series 1, if the gradient is small such as in Case 1-1, the peak clearly indicates the mean value of the strain distribution, but as the gradient increases, the peak becomes unclear and shifted. **Fig. 2-25** and **Fig. 2-26** show the spectra of Case 2-1 to Case 2-4 and Case 2-5 to Case 2-8, respectively. In Case 2-1 to Case 2-4, the peak split and the largest peak shifted to the large wavelength as the gradient change increases.

On the other hand, in Case 2-5 to Case 2-8, the largest peak shifted to small wavelength. In all cases of series 2, even small gradient change made some multi-peaks and caused peak shift from the average. But in series 3, even though the reflectivity decreases as the gradient change increases, all the spectra have the single peak that exactly corresponds to the average strain, as shown in **Fig. 2-27** and **Fig. 2-28**. This result may be attributed to the fact that in series 3, the area having the strain close to the average is comparatively long, and this flat area resulted in a clear peak in the spectrum. Note that if the gradient of the distribution is large, the reflectivity becomes low since the area corresponding to each Bragg wavelength become short. **Fig. 2-29** illustrates the relationship between γ and β of Case1-1 to 1-4, Case 2-1 to 2-4 and Case 3-1 to 3-4, where γ is the ratio of the strain corresponding to the peak wavelength to the average strain. From this figure, γ at β = 0.5 of linear distribution, i.e., case1-1, remains 1 while as β increases γ increases proportionally. For quadric distribution, γ increases linearly as β increases. In contrast to these

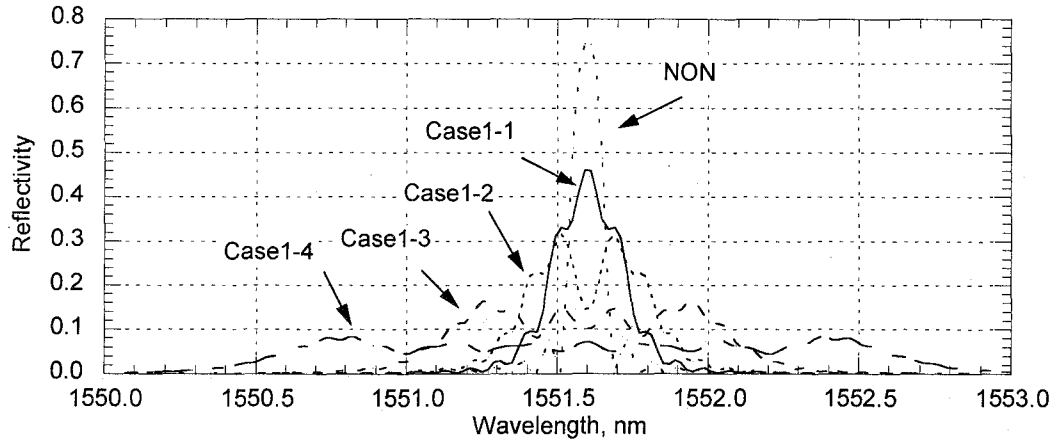

Fig. 2-23 Spectra of Case 1-1 to Case 1-4

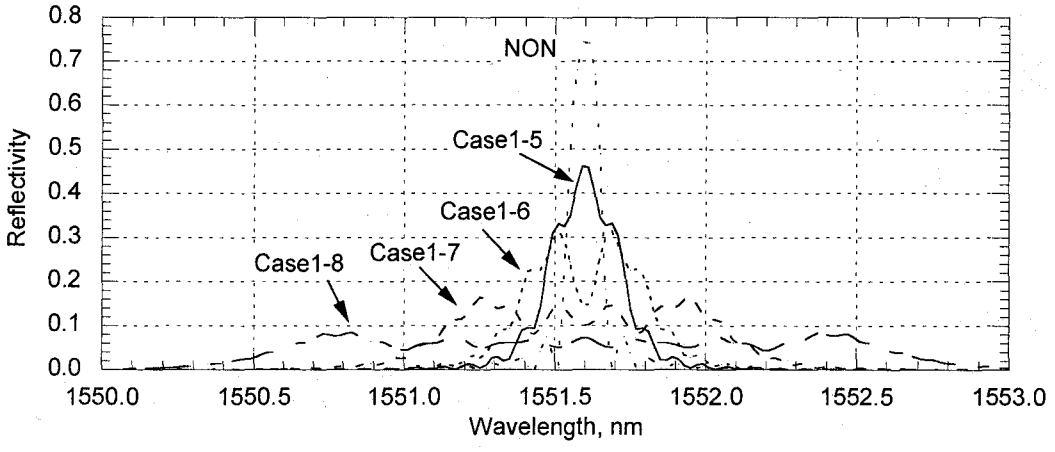

Fig. 2-24 Spectra of Case 1-5 to Case 1-8

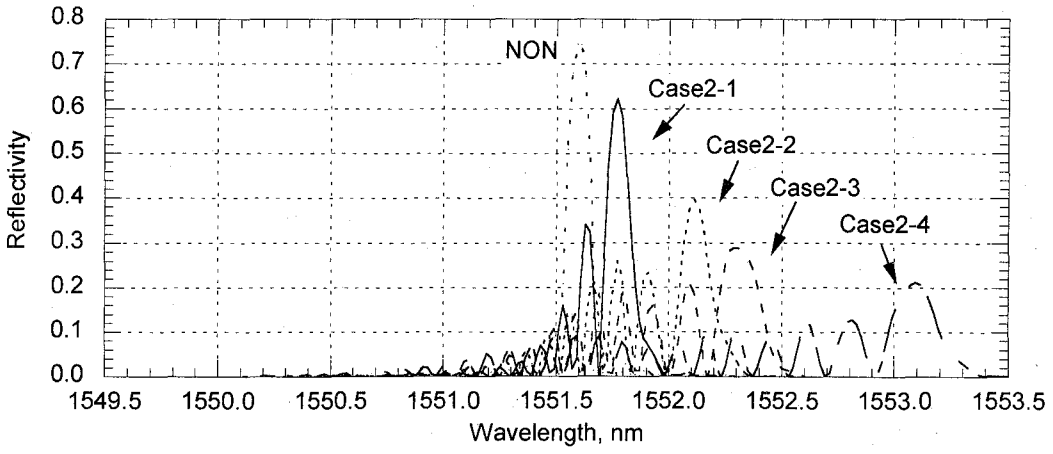

Fig. 2-25 Spectra of Case 2-1 to Case 2-4

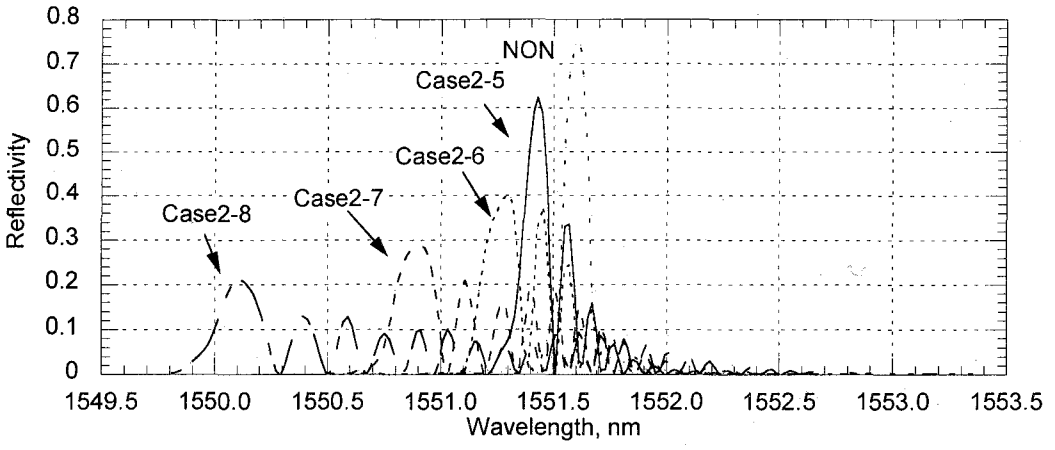

Fig. 2-26 Spectra of Case 2-5 to Case 2-8

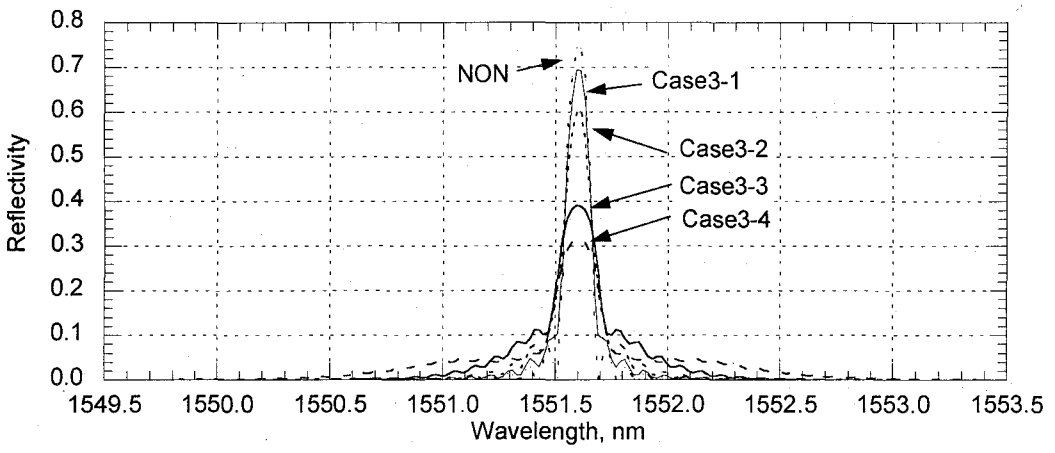

Fig. 2-27 Spectra of Case 3-1 to Case 3-4

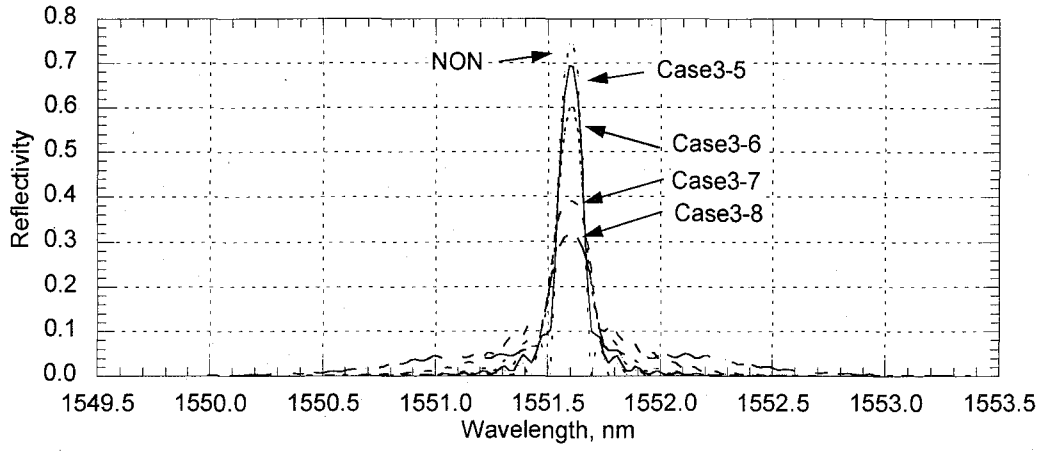

Fig. 2-28 Spectra of Case 3-5 to Case 3-8

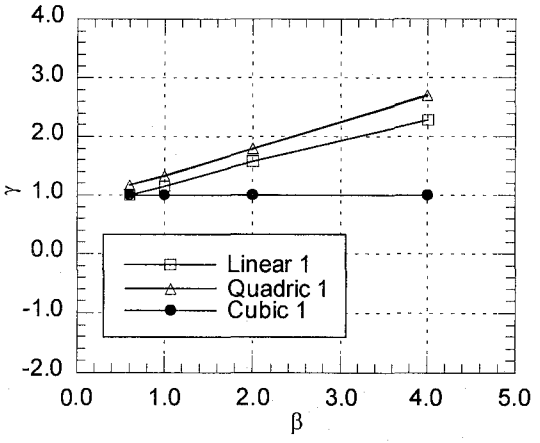

Fig. 2-29 Relationship between γ and β (1: positive β)

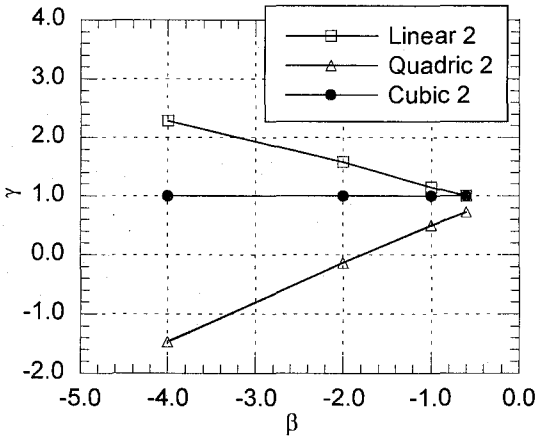

Fig. 2-30 Relationship between γ and β (2: negative β)

distributions, for cubic distribution, γ is 1 for all β.

Fig. 2-30 shows the relationship between γ and β of Case1-5 to 1-8, Case 2-5 to 2-8, and Case 3-5 to 3-8. All cases in **Fig. 2-30** except series 2 showed the same results as in **Fig. 2-29**, but series 2 in **Fig. 2-30** has values opposite to those in **Fig. 2-29**. This difference may be attributed to the point-symmetric distribution of series 1 and 3 with respect to (5.0, ε_0), while series 2 had a line-symmetric distribution with respect to the center line.

From these figures, one can see that as the gradient or gradient change of the distribution increases, the bandwidth of the spectrum becomes large and the reflectivity becomes low for all cases. It can also be said that the peak wavelength does not always correspond to the average of strain distribution; the difference between the peak and the average may increase as the gradient increases.

2.4.3 Evaluation of the module using finite element analysis

Fig. 2-31 shows the finite element model for the proposed module. In this model, an aluminum body is modeled as 8-node 3D structural solids, but the fiber is modeled as 2-node truss elements in order to estimate strains of the sensing area. Although the optic fiber is assumed to be elastic material, the solid element is assumed to be elastic plastic material in which Mises yield surfaces are used with associated plastic flow. The stress-strain relationship for this model is assumed to be a bi-linear, and the

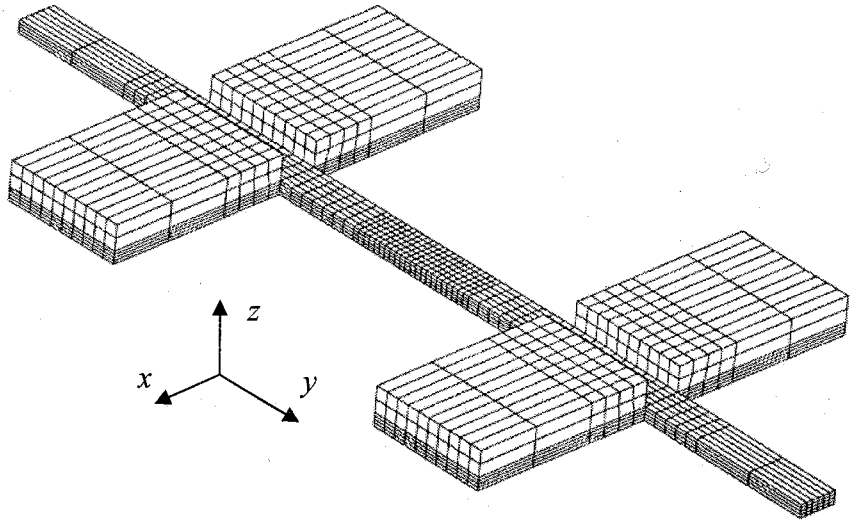

Fig. 2-31 FEM model for the proposed module

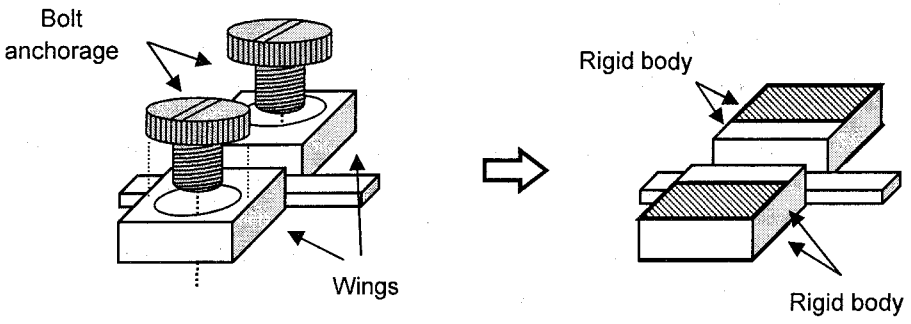

Fig. 2-32 Rigid body for bolt anchorage modeling

assumed properties of the aluminum and the fiber are shown in **Table 2-2**. The fiber is divided into 20 elements, each of which has a length of 0.5mm and has constant strain within each element. The gauge values are obtained by averaging the strains in the four elements located on the center of the backside. Rigid elements are used to simulate the bolt anchorage, as shown in **Fig. 2-32**. Two rigid elements in the wing behave similarly according to the node at the center of the wing.

As for boundary conditions, eight types of conditions are assumed for this model. As shown in **Table 2-3**, through all the conditions, the rigid bodies are constrained in

Table 2-2 Assumed properties of the module

Material	Aluminum	Fiber
Elastic modulus	6.63×10^4 (N/mm^2)	7.31×10^4 (N/mm^2)
Poisson's ratio	0.345	0.17
Yield stress σ_y	195.0 (N/mm^2)	-
Tensile strength σ_u	250.0 (N/mm^2)	-
ε_u	0.03	-

Table 2-3 Parameters of the assumed cases

Case	Type	Boundary condition				
		Sym.*	x-rot.* [rad]	y-rot. [rad]	z-rot. [rad]	y-disp.* [mm]
T1	Tension	A	○	○	○	+0.35
T2	Tension	B	○	○	–	+0.35
T3	Tension	C	○	–	○	+0.35
T4	Tension	D	○	–	–	+0.35
T5	Tension	E	–	○	○	+0.35
T6	Tension	F	–	○	–	+0.35
T7	Tension	G	–	–	○	+0.35
T8	Tension	H	–	–	–	+0.35
C1	Compression	A	○	○	○	-0.35
C2	Compression	B	○	○	–	-0.35
C3	Compression	C	○	–	○	-0.35
C4	Compression	D	○	–	–	-0.35
C5	Compression	E	–	○	○	-0.35
C6	Compression	F	–	○	–	-0.35
C7	Compression	G	–	–	○	-0.35
C8	Compression	H	–	–	–	-0.35

*sym.: symbol; rot.: rotation; disp.: displacement.

the x and z direction and pulled in the y direction. In conditions of A, B, C, and D, the rigid bodies are fixed in the x-axial rotation; in conditions E, F, G, and H, the rigid bodies are constrained in the x-axial rotation. Tension and compression forces are applied to this model by giving the displacement; given displacement of 0.35 is determined so that the strain on the top of the module becomes 10000μ.

Additionally, in order to evaluate the influence of the fiber's attachment-length, four attachment-lengths, 10.0, 15.0, 23.0, and 31.0mm, are assumed for Case T-1. Note that for all cases of sensitivity and spectrum evaluation the attachment-length is set to 15.0mm.

(1) Influence of the attachment-length

First, the strain distributions along the attachment-area at the applied strain of 100μ and 5025μ are shown in **Fig. 2-33** and **Fig. 2-34**, respectively. Note that the sensing area ranges from 0.0mm to 10.0mm. At a lower strain level, i.e., 100μ, when the optical fiber is attached over distances of 10.0 and 15.0mm, the strains decrease from both of the ends over a distance of about 2.5mm. However, when the fiber is attached over distances of 23.0 and 31.0mm, the strain distributions of both cases dropped at a position of -5.0mm and 25.0mm, respectively. This difference may be attributed to the fact that at a position of -5.0 and 25.0mm, the strain distribution changed considerably since at these positions the wings are connected to the main body. A similar result can also be seen at a higher strain level, i.e., 5025μ, but the strain values within the sensing area are much different: for the attachment-length of 10.0 and 15.0mm, the strain values increase with the applied strain, while for the attachment-length of 23.0 and 31.0mm, the strain values agreed with each other, and slightly gained at a position of -5.0 and 25.0mm. This may be attributed to the elastic modulus of the optical fiber sensor, which is larger than that of the aluminum. **Fig. 2-35** shows the relationship between the applied strain and reaction force of the module. From this figure, one can see that the stiffness of the module is different, especially after yielding, according to the attachment-length. This may also be attributed to the fiber's elastic modulus, which remained linear after the aluminum base reached the yielding point. Note that even though the stiffness is changed due to the optical fiber, the module can be used if it is calibrated.

Thus, considering that the attached fiber may cause the stiffness change, the influence of the end may range over 2.5mm from the end and should be canceled out

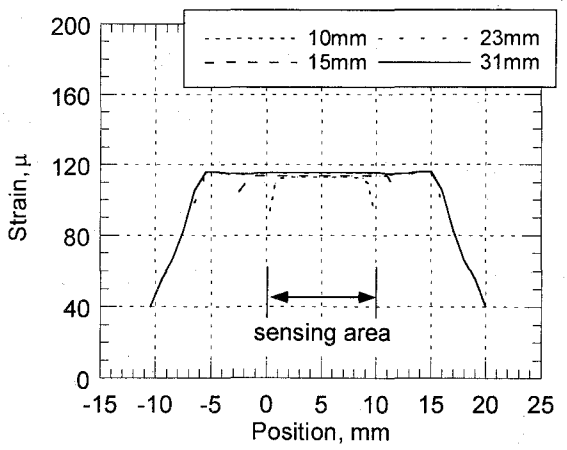

Fig. 2-33 Strain distributions at 100μ

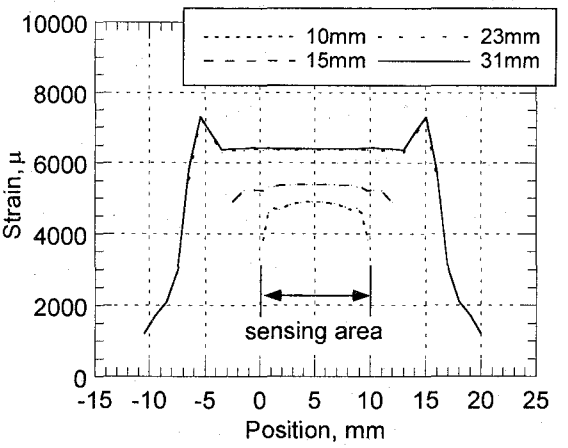

Fig. 2-34 Strain distributions at 5025μ

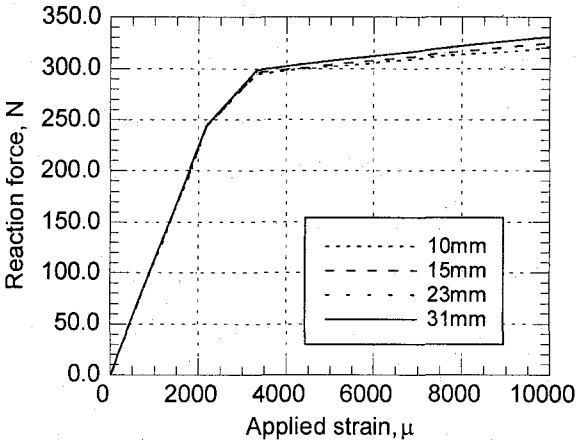

Fig. 2-35 The relationship between the applied strain and the reaction force

by enlarging the attaching length of the fiber about 5.0mm beyond the sensing length.

(2) Tension and compression

Fig. 2-36 to **Fig. 2-39** show the relationship between the applied and the output strain with boundary conditions A, B, C, and D. In these figures, "Peak" denotes the output strain obtained by a wavelength shift of the highest peak in the spectrum, while "Ave." denotes the average strain of the fiber over the sensing area; "Exact" denotes the exact correspondence, and "Gauge" denotes the average strain in the center of the buck side. Note that the applied strain is defined as the applied displacement divided by the sensor length of 35mm. These figures are rearranged according to the

boundary conditions A to E for easy comprehension.

From these figures, the curves of conditions A and C are almost identical, while those of conditions B and D are almost identical. Those set of conditions are different in the constraint of z-axial rotation. It is found also from this figure that the z-axial rotation may cause the different sensitivity. Naturally, rotation about the z-axis may occur because the module is anchored by the bolts and, if the clamp force decreases, the bolts may permit this rotation.

Fig. 2-40 and shows the relationship between the applied and the output strain with a boundary condition E. It is clear from these figures that the output strains are much smaller than the applied strain. A similar result can be seen in the other conditions of F, G and H. This small sensitivity may be attributed to the fact that the position of the applied displacement is different from the center of the section, and the x-axial rotation easily yields the y-axial displacement under these conditions. Thus the x-axial rotation must be constrained because it may much influence the sensitivity. However, a large x-axial rotation cannot occur since if the module rotates about the x-axis, it is constrained by touching the host structure.

Fig. 2-41 illustrates the ratios of the initial gradient of "Peak", "Ave.", and "Gauge" curves to the exact line for all conditions. From this figure, it is clear that for conditions A to D the ratios of "Peak" and "Gauge" coincidentally agreed with each other, and are about 0.97 times smaller than that of "Ave.", while the ratios of conditions E to H are much smaller than those of conditions A to D. Additionally, the ratios of "Gauge" under conditions E to H are negative, which indicates that the module is bent by the applied displacement.

Fig. 2-42 to **Fig. 2-45** show the strain distributions in tension and compression procedures with conditions A to D, but focusing on the two distributions at a lower and higher strain level, i.e., 913μ and 10000μ, or -913μ and -10000μ. From these figures, it is found that at a low strain level, the distributions in tension with boundary conditions B and D agreed with each other while those with conditions A and C agreed with each other; the latter group is about 1.2 times larger than the former. At a higher strain level, the distributions with B and D are still larger than the others as seen in tension. Thus it can be said that the constraint of z-axial rotation caused the increase of strain. As for compression, at a lower strain level the curves of conditions B and D are about 1.2 times larger than the others, as in tension. But the trend of these curves

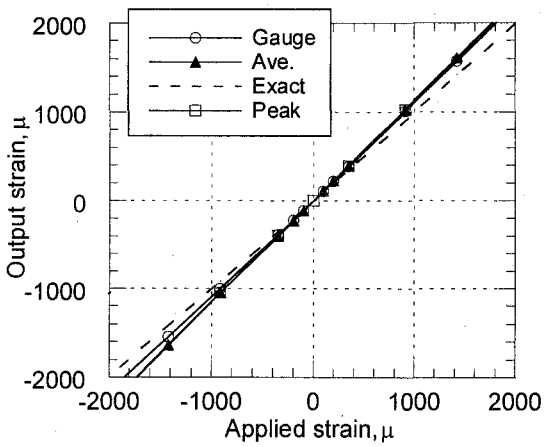

Fig. 2-36 Applied-Output strain relation :Case T1 and Case C1 (condition A)

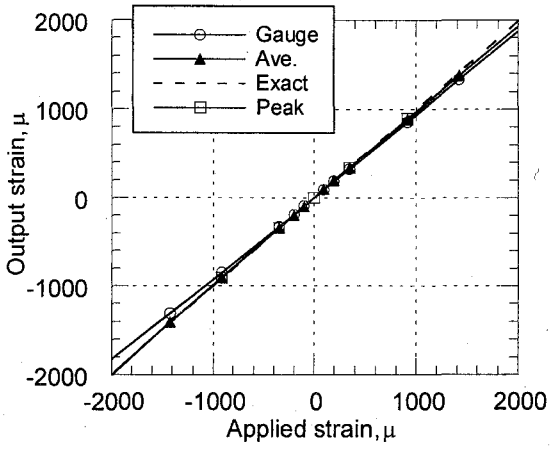

Fig. 2-37 Applied-Output strain relation :Case T2 and Case C2 (condition B)

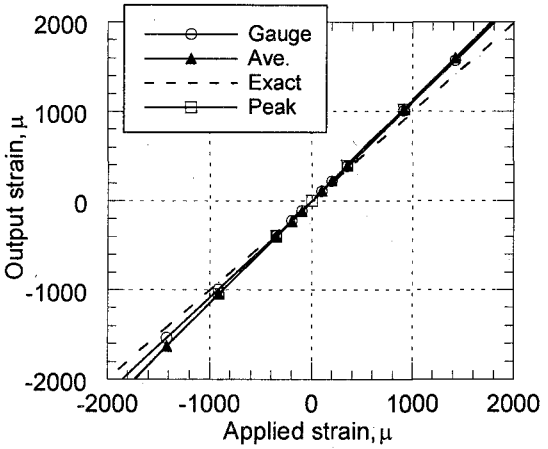

Fig. 2-38 Applied-Output strain relation :Case T3 and Case C3 (condition C)

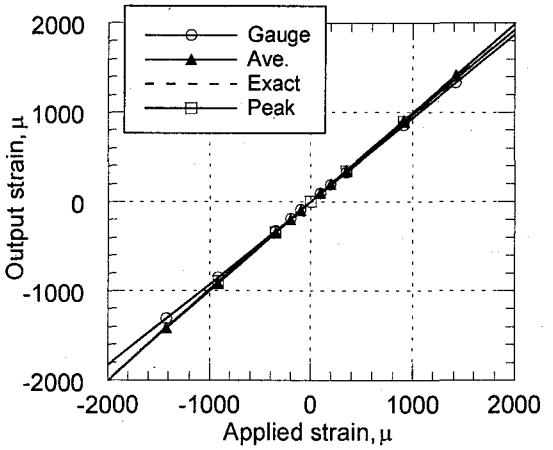

Fig. 2-39 Applied-Output strain relation :Case T4 and Case C4 (condition D)

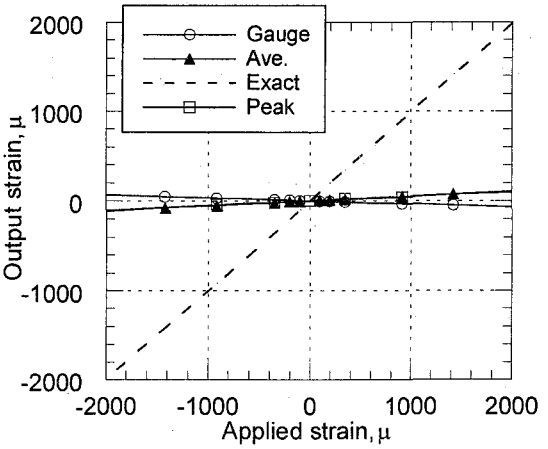

Fig. 2-40 Applied-Output strain relation :Case T5 and Case C5 (condition E)

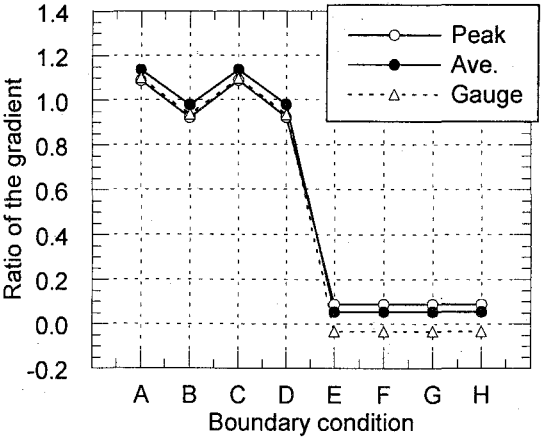

Fig. 2-41 Ratios of the initial gradient of output strain to that of the exact line

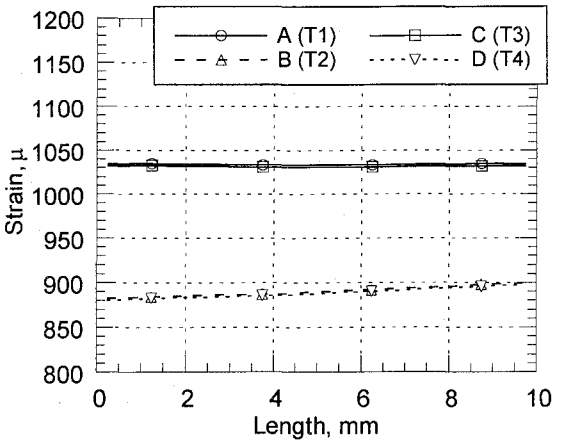

Fig. 2-42 Strain distribution of Case T1 to T4 at a lower strain level

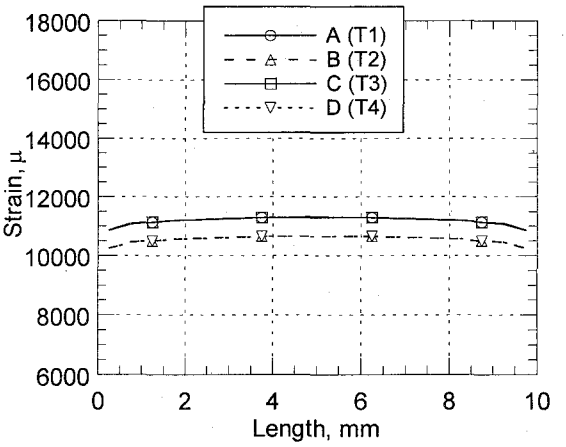

Fig. 2-43 Strain distribution of Case T1 to T4 at a higher strain level

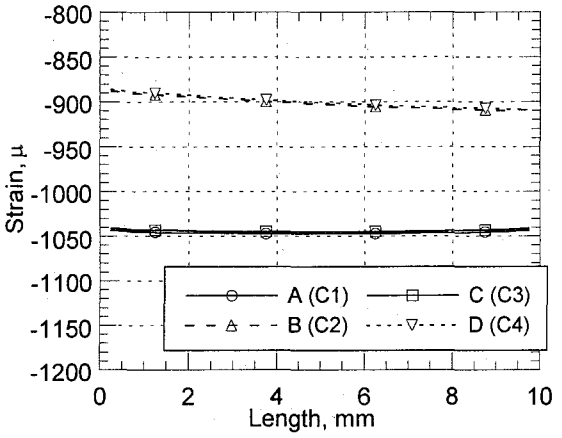

Fig. 2-44 Strain distribution of Case C1 to C4 at a lower strain level

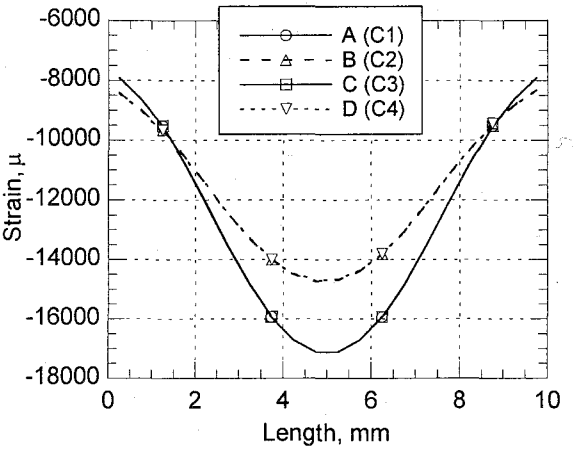

Fig. 2-45 Strain distribution of Case C1 to C4 at a higher strain level

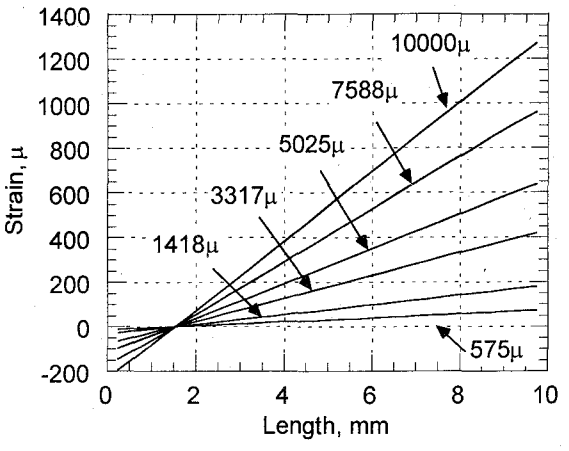

Fig. 2-46 Strain distribution of Case T5

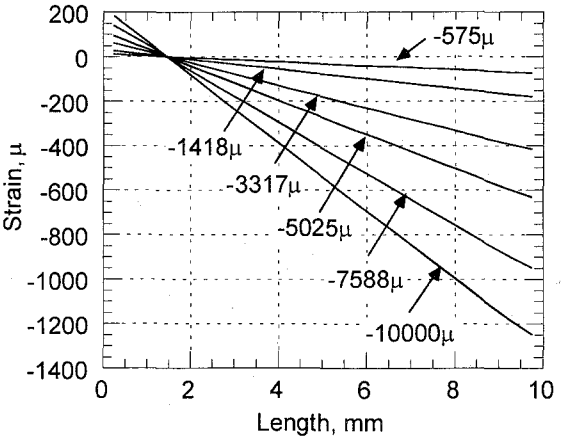

Fig. 2-47 Strain distribution of Case C5

is slightly different at a higher strain level. At a higher level, the distributions formed also downward convex shape and those values of B and D are larger than those of the others around the center, but they are close to each other around both the section ends. However, it can be said that the constraint of z-axial rotation caused the decrease of strain in both tension and compression. Additionally non-uniform distributions may be attributed to the eccentricity of the module; because the wings of the module are 3mm high while the main body is 1mm, this difference may develop the eccentricity. In comparison with tension and compression, compression developed a large gradient change, which may be caused by the local buckling.

As for the cases with conditions E to H, strain distributions become linear, which is much smaller than those with conditions A to D. **Fig. 2-46** and **Fig. 2-47** shows the strain distributions with the condition of E. One can see that all distributions are linear and the gradient developed as the applied strain increases. A similar result can be seen in the other cases in both tension and compression. This means that the x-axial rotation of the wing yielded bending moment in the main body.

The spectra corresponding to the strain distribution in Case T1 to T4 are shown in **Fig. 2-48** to **Fig. 2-51**, respectively. From these figures, it is found that the peak of the spectrum split and the reflectivity decreases as the applied displacement increases. In these cases, multi-peaks came out on the right side of the spectrum because of the upward convex strain distribution. **Fig. 2-52** to **Fig. 2-55** illustrate the spectra of Case C1 to C4. A similar trend to the tension can be seen in these cases, i.e., the compression, but the spectrum contained more peaks and the reflectivity decreases faster than that in tension and the multi-peaks generated from the left side of the spectrum.

On the other hand, the spectra of Case T5 and Case C5 are shown in **Fig. 2-56** and **Fig. 2-57**. Note that the horizontal axis in these figures is focused on the neighborhood around the Bragg wave length, ranging from 1549.0nm to 1552.0nm or from 1550.0nm to 1553.0nm. It is clear that the reflectivity decreases and the spectra become wider as the applied strain increases. A similar spectrum is obtained in the other cases with conditions F, G and H. These spectra are similar to those in **Fig. 2-23** and **Fig. 2-24**, indicating that the strain distribution is linear as can be seen in **Fig. 2-46** and **Fig. 2-47**.

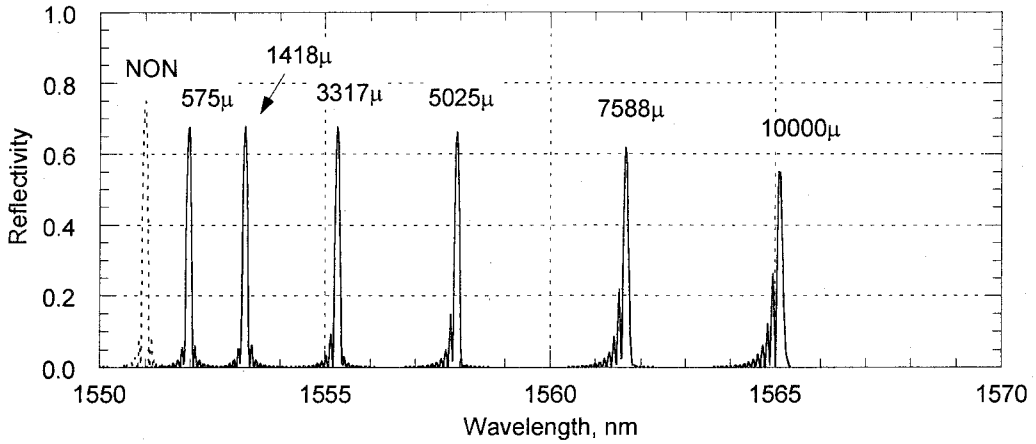

Fig. 2-48 Spectra of Case T1

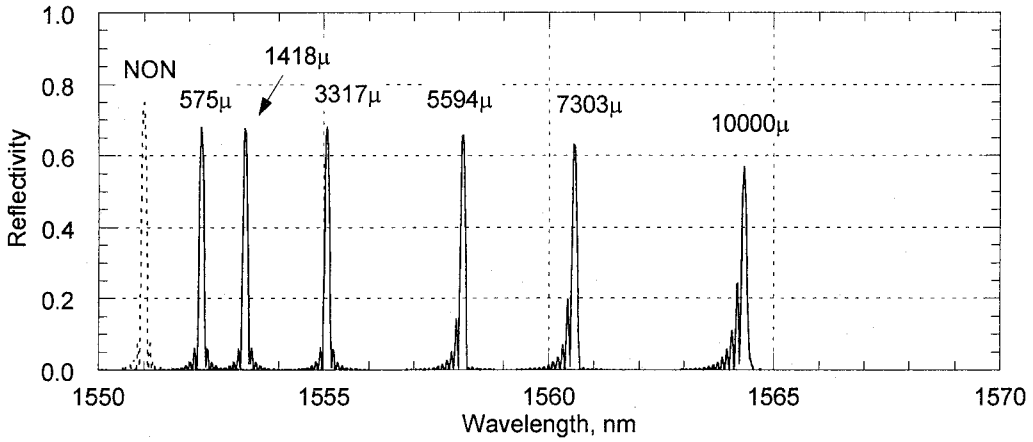

Fig. 2-49 Spectra of Case T2

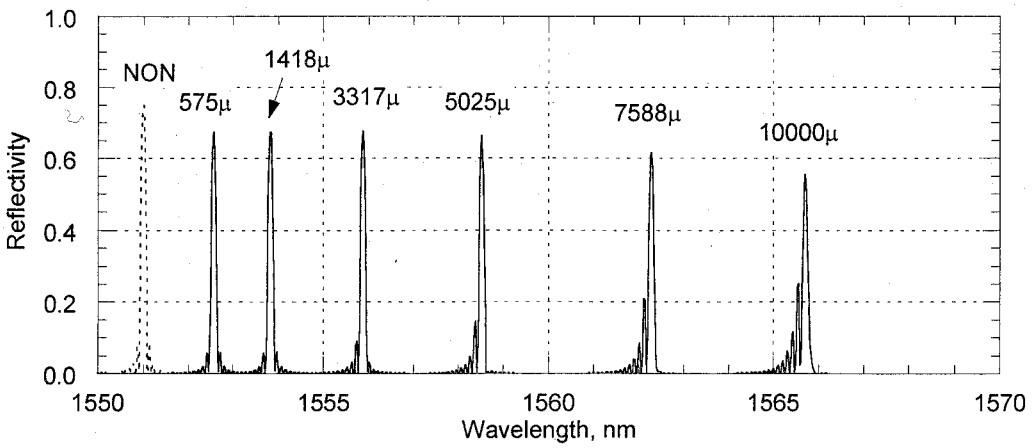

Fig. 2-50 Spectra of Case T3

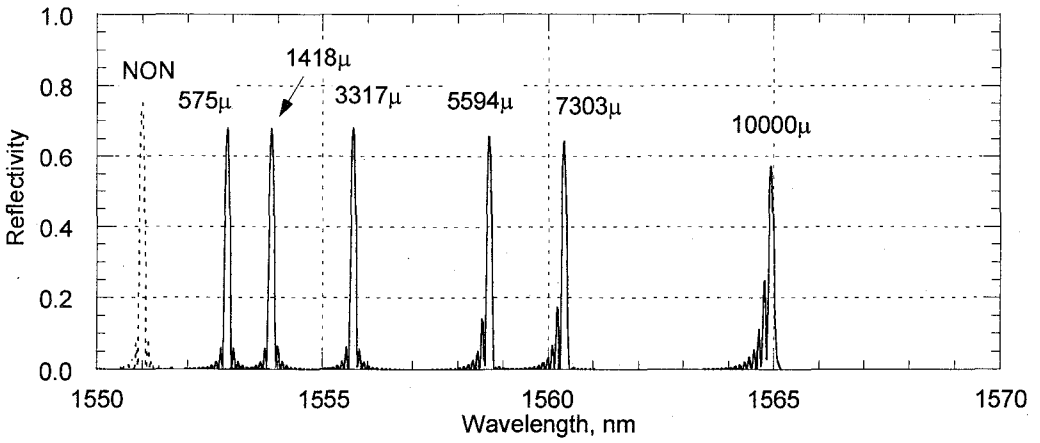

Fig. 2-51 Spectra of Case T4

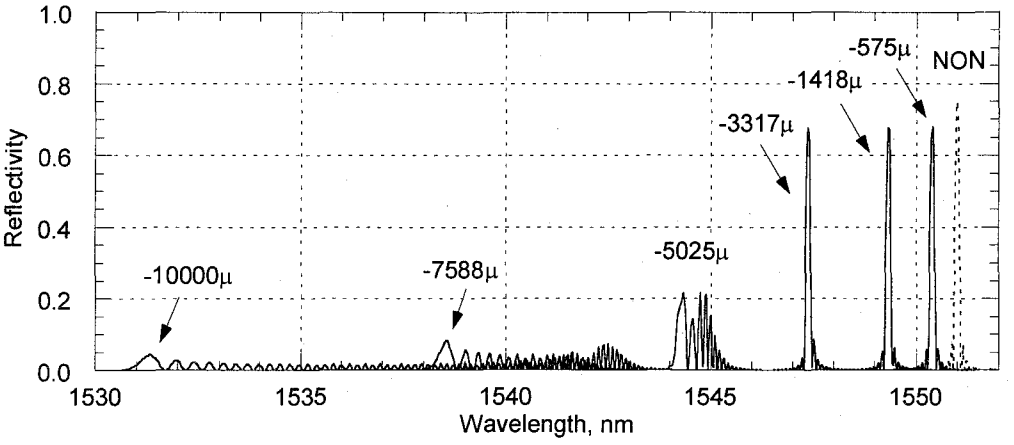

Fig. 2-52 Spectra of Case C1

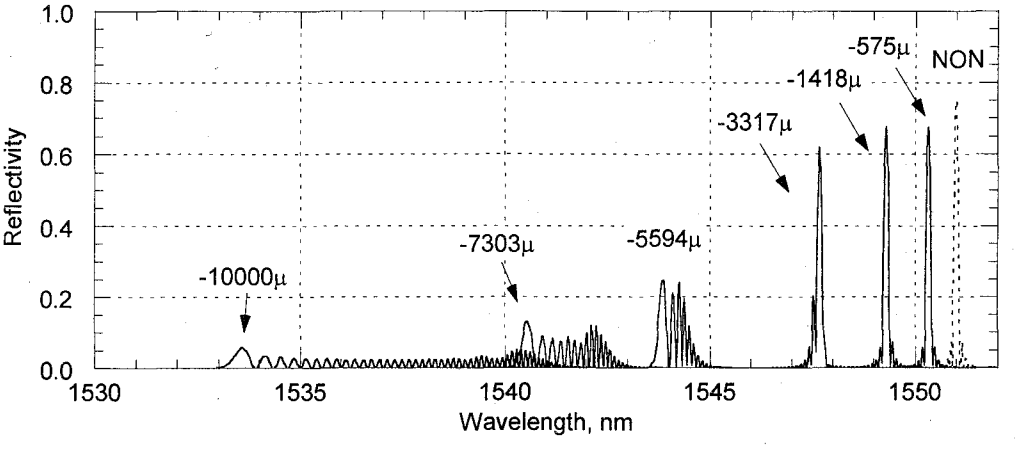

Fig. 2-53 Spectra of Case C2

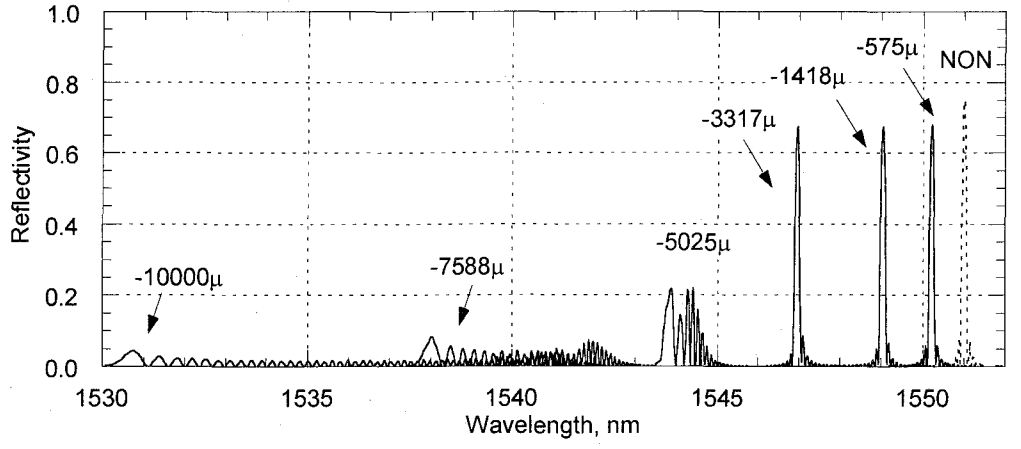

Fig. 2-54 Spectra of Case C3

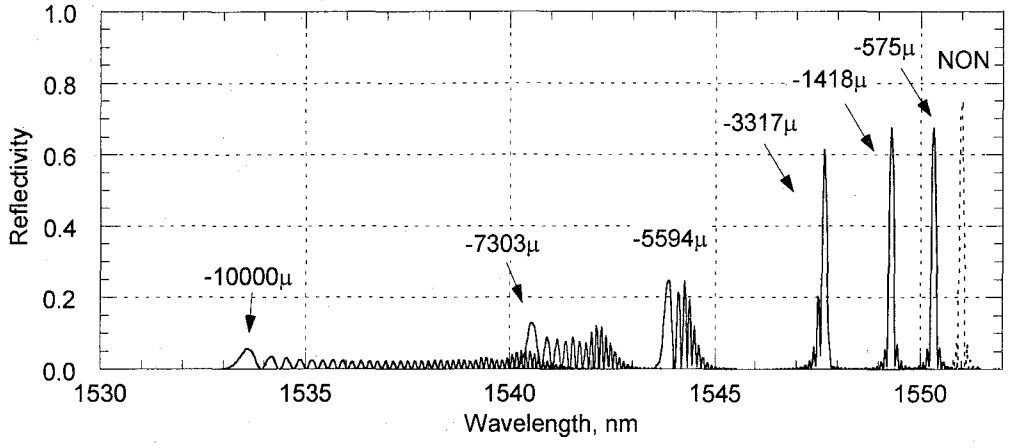

Fig. 2-55 Spectra of Case C4

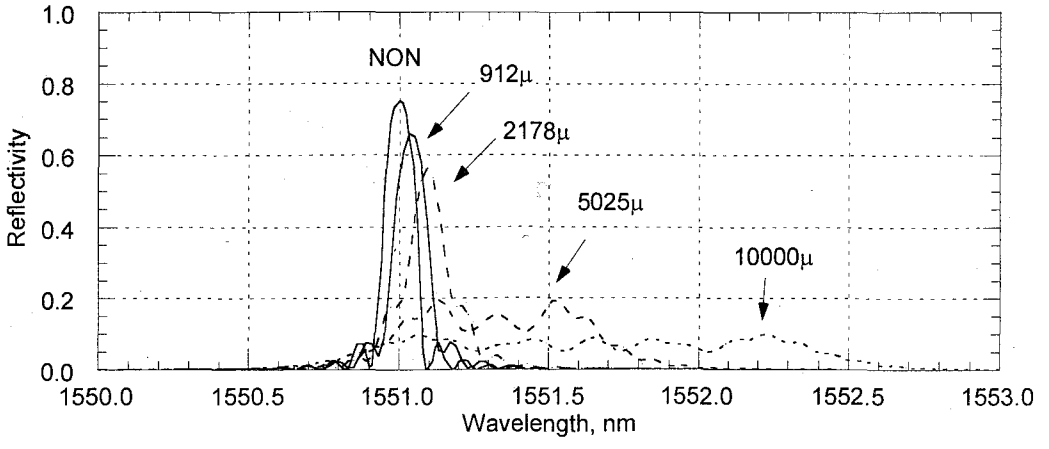

Fig. 2-56 Spectra of Case T5

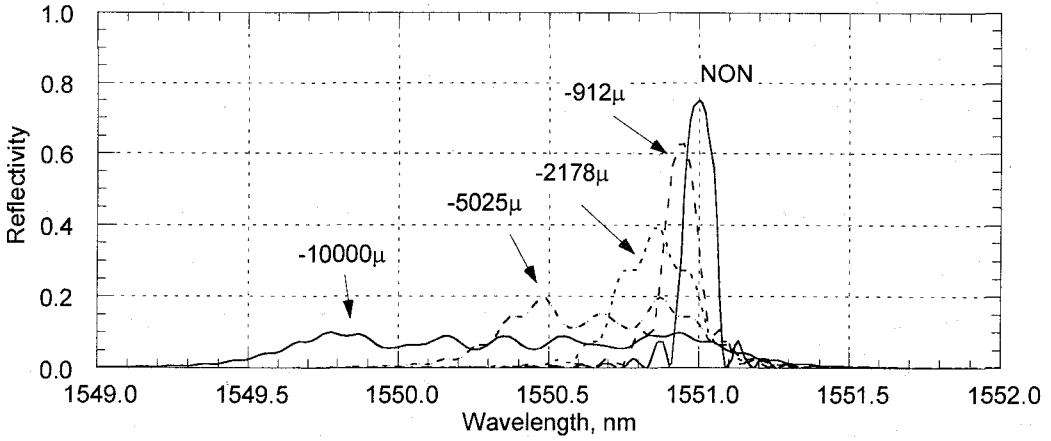

Fig. 2-57 Spectra of Case C5

Finally, it is found that when the module is pulled or pushed, the x-axial rotation should be perfectly constrained; otherwise, the sensitivity of output strain significantly decreases. Additionally, even though the x-axial rotation is perfectly fixed, the z-axial rotation may influence the sensitivity, which may occur due to the bolt anchorage.

2.4.5 Evaluation of the strain distributions in the tension and bending tests

The spectra in the tension and bending test have multi-peaks. These spectra may be caused by some bending and tension occurring in the sensing area. Thus to evaluate the spectra obtained in the tests, the strain distributions for the tension and bending test are assumed. Unfortunately, since one spectrum has several strain distributions, the assumed distributions may not simulate the conducted tests. But this assumption is one possibility since any distribution may happen during the tests.

(1) Strain distribution in the tension test

The spectrum in the tension test at the maximum load includes multi-peaks that may be caused by bending. Since in the obtained spectra only few multi-peaks developed in the right side, the gradient of the strain distribution can be small. Additionally, the strain distribution can be expressed as a simply-increasing or decreasing function, because the deflection may be caused by the eccentricity as well as the bolt action. Thus herein a quadric distribution is assumed for the tension test, which yields

asymmetric spectrum. Note that the peak of the assumed quadric function is set at the origin so that the function simply increase or decrease. The assumed function is determined as follows:

The largest peak in the obtained spectrum at the maximum load is 1552.59nm. Now assuming a uniform strain distribution for the sensing area, the grating period at the maximum load becomes 517.53nm. Furthermore, the second peak is at 1552.70nm, which corresponds to 517.56mm, and the difference between the first and second peak is 0.03nm. Considering the center position of the assumed distribution, the distribution has the peak value of 517.53nm at the origin and increases by 0.09nm (=0.03nm x 3), as shown in **Fig. 2-58**.

Fig. 2-59 shows the spectra of the assumed distribution and that obtained in the tension test, whose reflectivity are normalized so that the largest reflectivity becomes 1.0. Although the width of the assumed distribution is slightly smaller than that obtained in the test, the trend of the spectrum agrees with each other. This difference may be caused by the fact the assumed refractive index is different from the actual one and the actual distribution is not exactly quadric. The assumed distribution can be caused by several actions. But it can be said that some bending action results in this non-uniform distribution.

(2) Strain distribution in the bending test

The initial spectrum of the bending test has several peaks as opposed to the tension test. These multi-peaks may be caused by the relatively high bending moment that is locally applied to the module. The assumed distribution is determined as follows: the largest peak of the initial spectrum in the test is at 1548.49nm. Thus, the quadric distribution is determined for this spectrum so that the average of the distribution is 516.17nm (corresponding to 1548.49nm), as shown in **Fig. 2-60**. Note that the difference between the top and the bottom of the given distribution is a third of the difference between the first and second peaks.

The spectra of the bending test and the assumed distribution are shown in **Fig. 2-61**. The total width of the spectrum agrees with each other, but at a shorter wavelength the reflectivity of the assumed distribution is smaller than that of the test. The reflectivity at a shorter wavelength may increase by increasing the gradient of the distribution around the end because the reflectivity depends on the length of the grating period. Therefore, though the spectra do not agree well with each other, it can

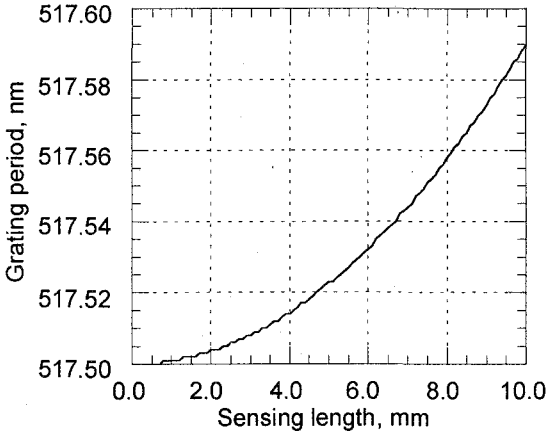

Fig. 2-58 Assumed distribution for the tension test

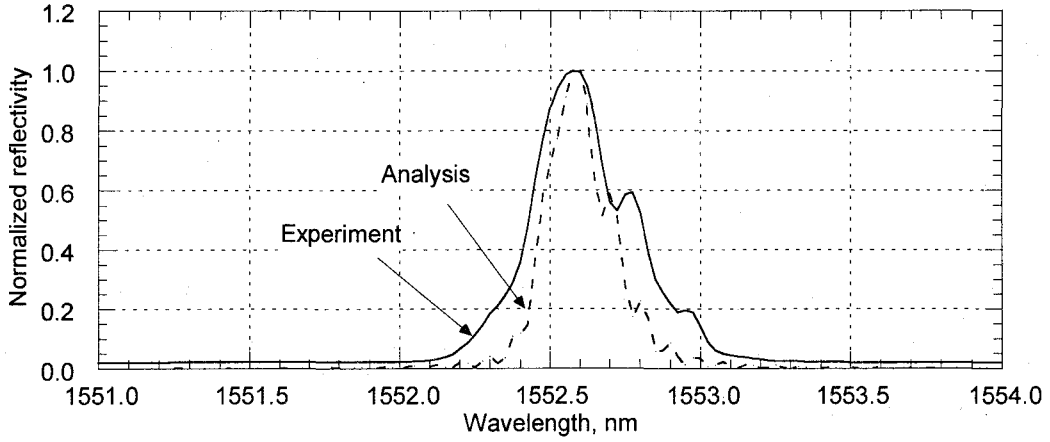

Fig. 2-59 Spectra of the assumed distribution and the tension test

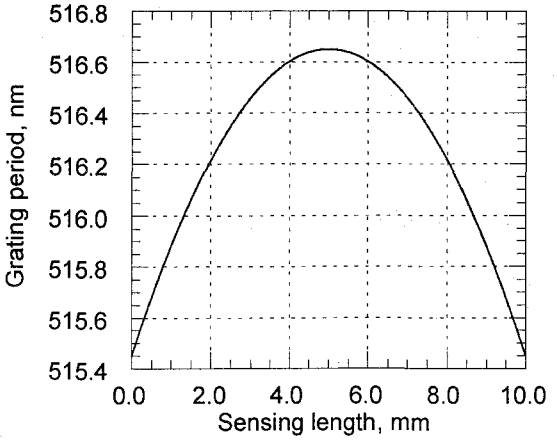

Fig. 2-60 Assumed distribution for the bending test

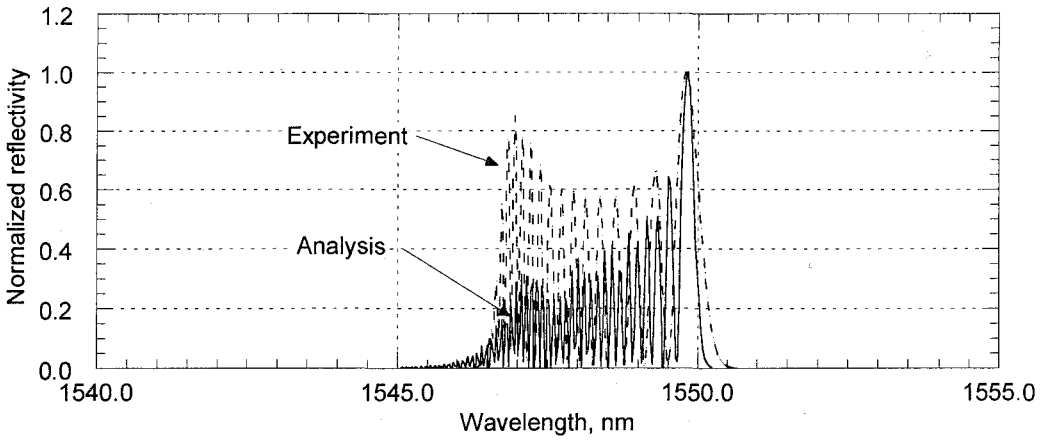

Fig. 2-61 Spectra of the assumed distribution and the bending test

be said that the multi-peaks in the obtained spectra in the being test may be caused by quite large gradient as shown in **Fig. 2-61**.

2.4.5 Summary

Finally, it can be said that the peak wavelength does not always correspond to the average of strain distribution, and the difference between the peak and the average may increase as the gradient increase.

Moreover, the sensitivity of the module strongly depends on the z-axial rotation; the non-uniform distribution may occur also because of the pure tension force. Thus the module should be modified so that it has no geometrical eccentricity and the z-axial rotation is constrained perfectly for constant sensitivity.

2.5 Temperature-independent strain module

2.5.1 Target of this section

To measure strains of the host structure, FBG sensors require some temperature compensations because of the high sensitivity to temperature. Even the proposed module is found to have a high temperature-sensitivity; thus, the temperature effect

should be compensated. The use of two FBG sensors is the simplest way for the compensation, but requires a wide dynamic range of the spectrum, which results in decreaseing admissible strain range. The mechanical compensation may be the best solution so far because the other mechanisms impose a costly burden on the interrogation system. Therefore, we proposed the two-metal-combination (**Fig. 2-62**), which produces negative temperature expansion. Because the dimensions of this model are also related to the compensation mechanism, the dimensions should be decided according to the type of applying materials. Moreover, due to the three-dimensional effect, such as Poisson, the dimensions should be decided by three-dimensional model. Accordingly in the following section, after the dimensions are temporarily decided by the one-dimensional mechanism, parametric analysis using FEM is conducted to select the dimensions and to evaluate the strain sensitivity.

2.5.2 Material selection

Fig. 2-63 shows the proposed module, which has two struts and regulating members, and four wings for welding to be fixed on the host structure. Note that the wings are made of steel for welding anchorage.

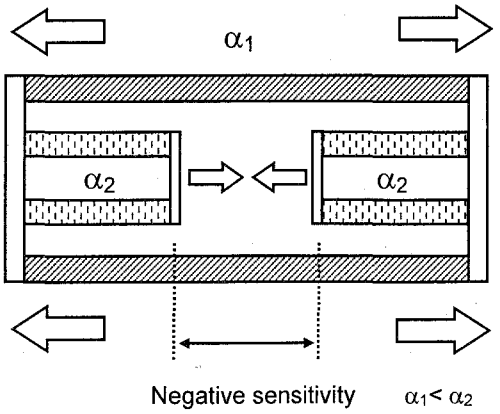

Fig. 2-62 Two-metal combination for negative sensitivity

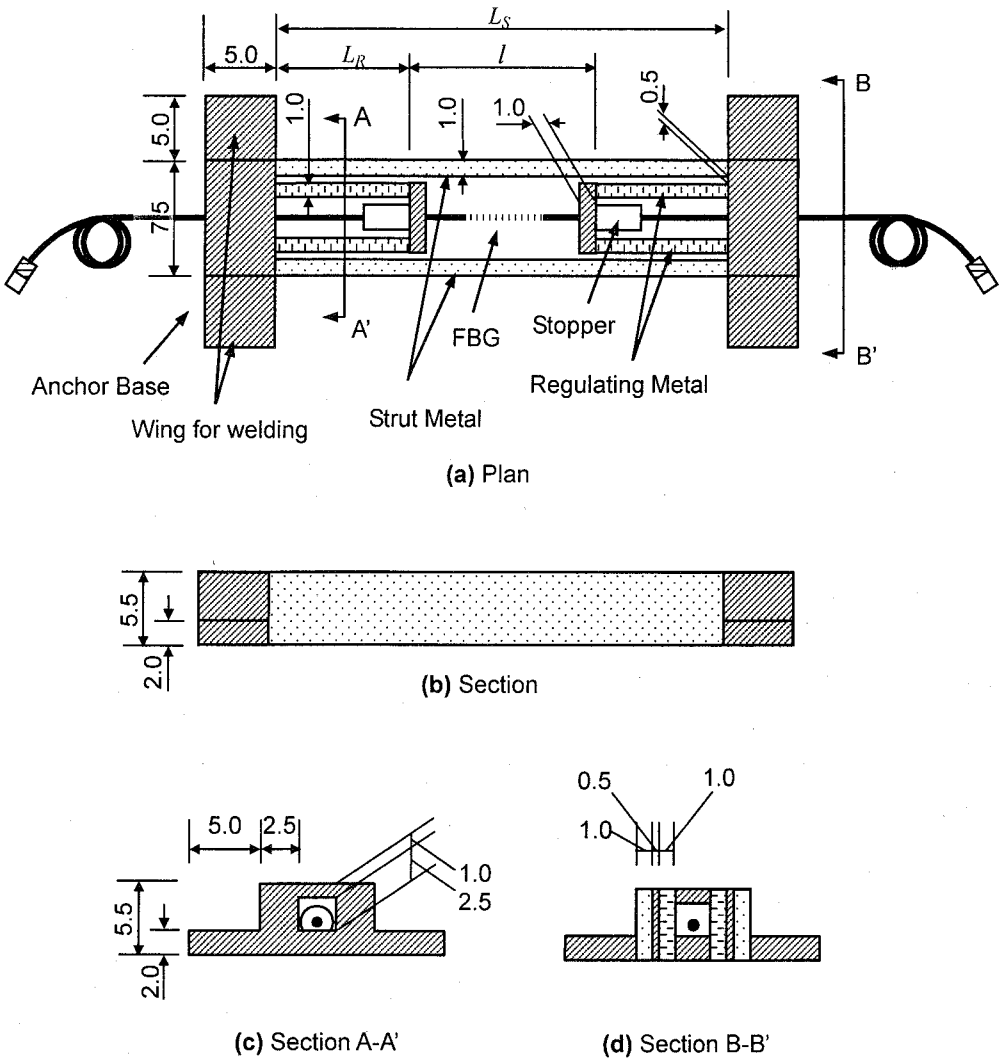

Fig. 2-63 Detailed dimension of the new module

Now, the distance between the regulating metals, l, is related to the strut length, L_S, and the regulating length, L_R, and given by

$$l = L_S - 2L_R . \tag{2.20}$$

Assuming that the proposed module experiences a small change in temperature, ΔT, the mechanical strain between the regulating metals, ε_m, can be defined by the following equation:

$$\varepsilon_m = \left(\frac{L_S}{l} \alpha_s - \frac{2L_R}{l} \alpha_R \right) \Delta T \tag{2.21}$$

where α_S and α_R are the thermal expansion coefficient of the strut and regulating metal, respectively.

To compensate the thermal effect, the mechanical strain should be equal to the apparent thermal strain of FBG, ε_0 , i.e.,

$$\varepsilon_0 = s_1 \Delta T = \varepsilon_m \tag{2.22}$$

where s_1 is the temperature sensitivity of FBG and this yields

$$s_1 = \frac{L_S}{l} \alpha_S - \frac{2L_R}{l} \alpha_R . \tag{2.23}$$

Note that for the negative thermal sensitivity, α_R must be larger than α_S, i.e.,

$$\alpha_S < \alpha_R . \tag{2.24}$$

Let the play for the anchorage of the optical fiber be 10mm; the sensing length, l, should then be larger than 20mm because the grating length is 10mm, i.e.,

$$20 \le l . \tag{2.25}$$

Additionally, the strut length should be minimized for the high strain sensitivity. Using the above conditions, we can now determine L_S and L_R, which are given by

$$L_S = 20 \frac{\alpha_S - s_1}{\alpha_S - \alpha_R} . \tag{2.26}$$

$$L_R = 10 \frac{\alpha_R - s_1}{\alpha_S - \alpha_R} \tag{2.27}$$

Now let the strut and regulating material be selected within **Table 2-4**, giving the possible combination of strut and regulating metal can in **Table 2-5**.

Fig. 2-64 shows the minimum L_S and the corresponding L_R for each case, which can be acquired by substituting 8.59×10^{-6} °C into s_1. Considering that the elastic modulus of the optic fiber (7.31×10^{-4} N/mm^2) is much larger than that of lead, it is found that Case 4 is the optimum combination for the proposed module. As initial dimensions, L_S, L_R, and l are set to 34.0, 6.6, and 20.8mm, respectively. Letting L_S be 34.0mm, finite element analysis is conducted by varying L_R to find the optimum dimensions which produce temperature independence. In practice for compression measurement, some pretension may be required for the fiber. But in this analysis, this consideration is ignored since deformation due to the pre-tension is thought to be independent of the thermal expansion.

2.5.3 Dimensions

A Finite Element Model is built up to determine the dimensions, as shown in **Fig. 2-65**. The model consisted of 3D structural solids for the main body, truss elements for the fiber and rigid elements for the wings. The metals are assumed to be tri-linear material and their properties are shown in **Table 2-6**. The term ε_2 in the table indicates the strain corresponding to the tensile strength, which is decided so that ε_2 is the center value between 2% and the coefficient of extension. In this analysis, L_R varied from 6.6 to 12.0mm, and a temperature change of 20°C is given to each model without any external load. During this analysis, two of the wings on the one side are

Table 2-4 Properties of the candidate metals

type	expansion coefficient μ/°C	elastic modulus ×10^4 N/mm^2
zinc	30.2	10.84
lead	28.9	1.61
Aluminum	23.1	7.03
tin	22.0	4.99
bronze	17.0	12.0

Table 2-5 Combination of the metals

Case	Strut metal	Regulating metal
1	lead	Zinc
2	Aluminum	Zinc
3	tin	Zinc
4	bronze	Zinc
5	Aluminum	lead
6	tin	lead
7	bronze	lead
8	tin	Aluminum
9	bronze	Aluminum
10	bronze	tin

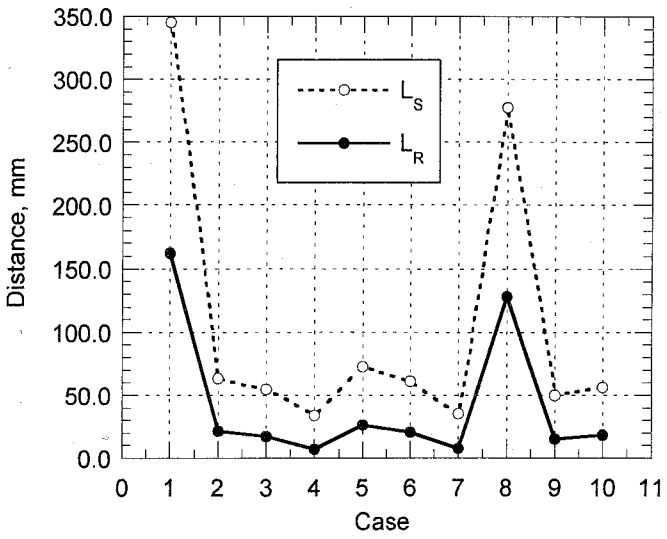

Fig. 2-64 Minimum L_S and the corresponding L_R

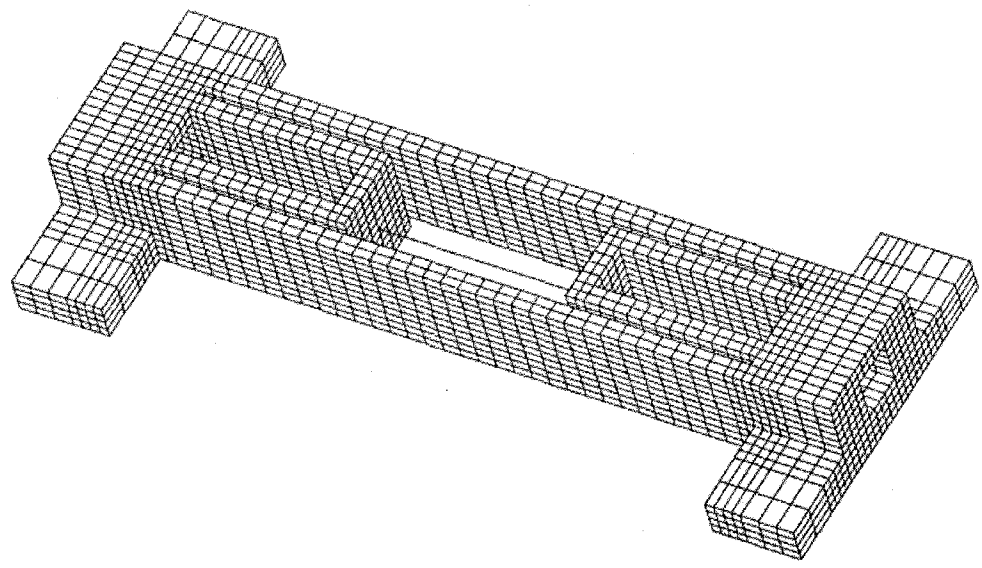

Fig. 2-65 FEM model for the new module

Table 2-6 Assumed properties of the metal

Material	Bronze	Zinc	Steel	Fiber
Elastic modulus N/mm^2	1.20×10^5	1.084×10^5	2.10×10^5	0.73×10^5
Poisson	0.38	0.249	0.3	0.17
Yield stress N/mm^2	165.0	178.0	240.0	-
Tensile strength N/mm^2	295.0	274.0	350.0	-
ε_2	0.06	0.035	0.293	-

fixed while the others are free. Note that the increment of L_R is assumed to be 0.01mm because of the working accuracy.

The relationship between the length of regulating metal and the strain of the fiber is shown in **Fig. 2-66**. The solid horizontal line indicates the value of -8.69μ, which can compensate the temperature reaction of the FBG sensor. It is found that this relationship is almost linear, and the optimum length can be around 9.74 to 9.75. Thus, considering the working accuracy, 9.75mm is adopted for the optimum length. When the length is set to 9.75mm, the temperature sensitivity becomes 0.1μ/°C. Note that the sensitivity of the length to the strain becomes about 83μ/mm, which is quite high:

for instance, the length error of only 0.1mm will increase the output by 8.3μ. Therefore, though the length can be set to 9.75mm, a very careful operation is required to make the module.

Finally, it can be said that the temperature sensitivity of the module is 0.1μ/°C for the optimum length of 9.75mm.

2.5.4 Strain sensitivity

For strain sensitivity evaluation, forced displacements are given to this finite element model. The model clumped at the four wings is shifted horizontally in both the negative and positive axial direction by 0.00345, 0.01745, 0.0345, 0.069 and 0.138mm so that the positive and negative strain of the fiber developed up to 100, 500, 1000, 2000, and 4000μ, respectively. In this process, the temperature is set to be constant.

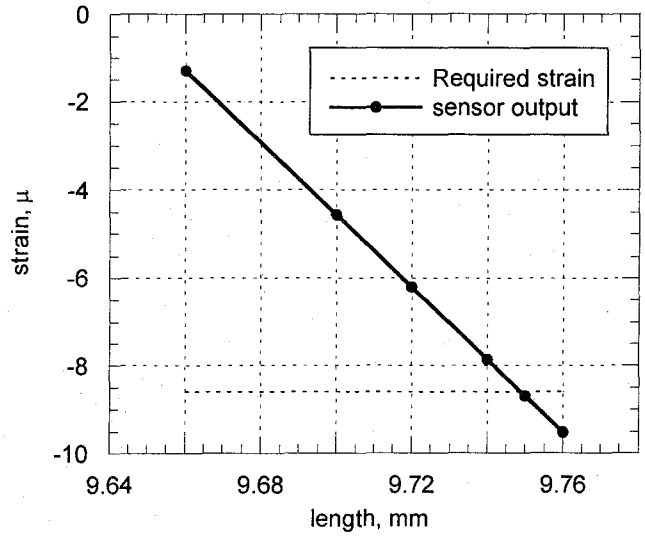

Fig. 2-66 Relationship between the length of regulating metal and the output strain

Fig. 2-67 and **Fig. 2-68** show the typical deformation of the module. As for compression, the strut is bent due to the buckling. In contrast, for tension, the module is slightly bent from the eccentricity: the regulating metals are rotated to some extent, thus the sensing length l might be affected by this rotation, which must be overcome for the practical application. **Fig. 2-69** illustrates the relationship between the assumed strain and the estimated strain by FEM. In this figure, the dotted line denotes the initial tangent line of the estimated strain, while the solid line denotes the assumed strain. At a higher strain for both tension and compression, the output strain becomes slightly nonlinear. Let the use of the module be restricted within elastic behavior; the range of the module can be roughly -2000μ to 2000μ. The ratio of the dotted line slope to the solid line slope is about 1.705, and this ratio can be adopted as a calibration coefficient for the tension or compression measurement. This fact suggests that if the model is formed in practice, some calibration is required.

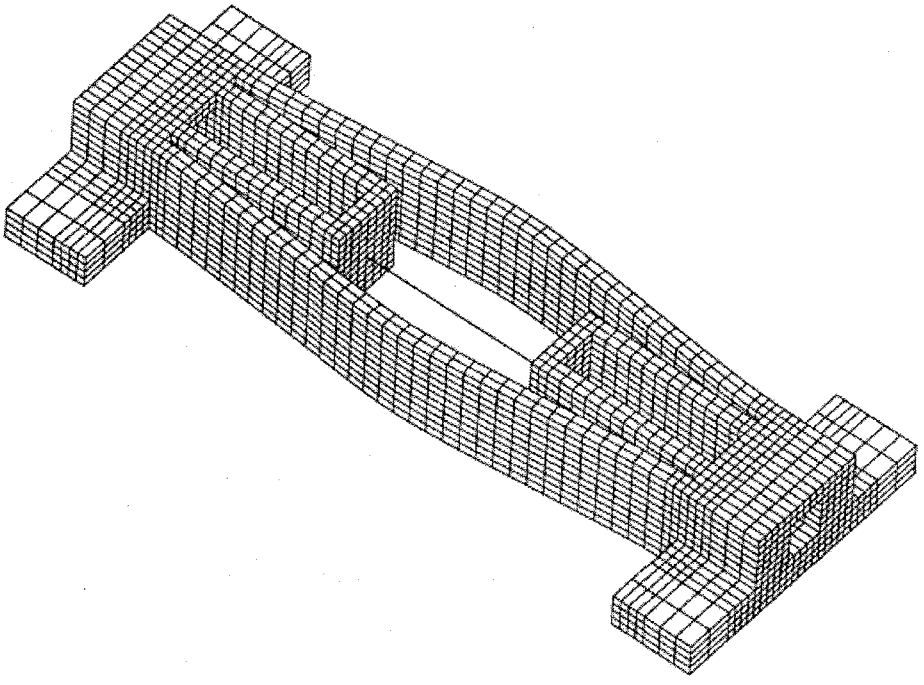

Fig. 2-67 Deformation developed by compression force

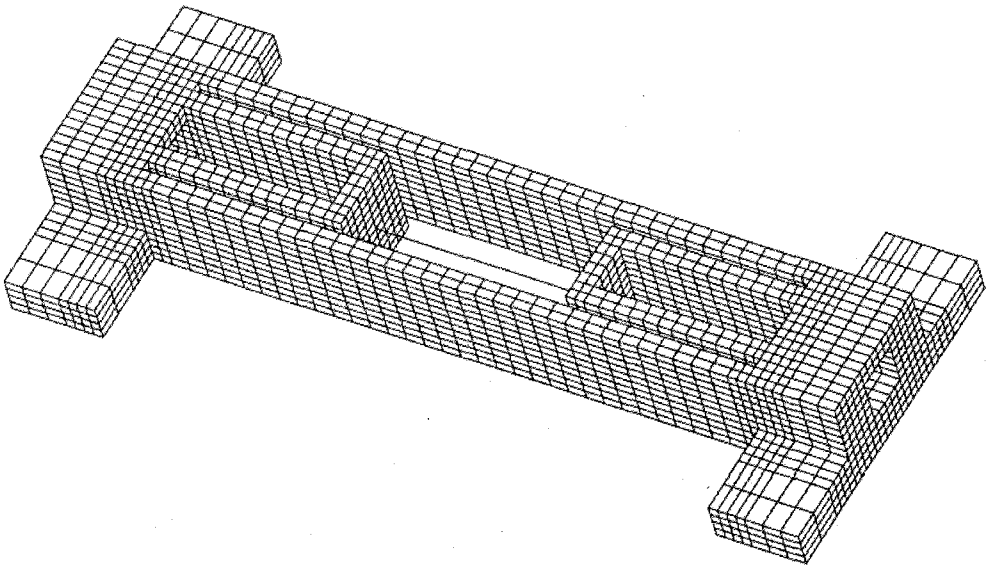

Fig. 2-68 Deformation developed by tension force

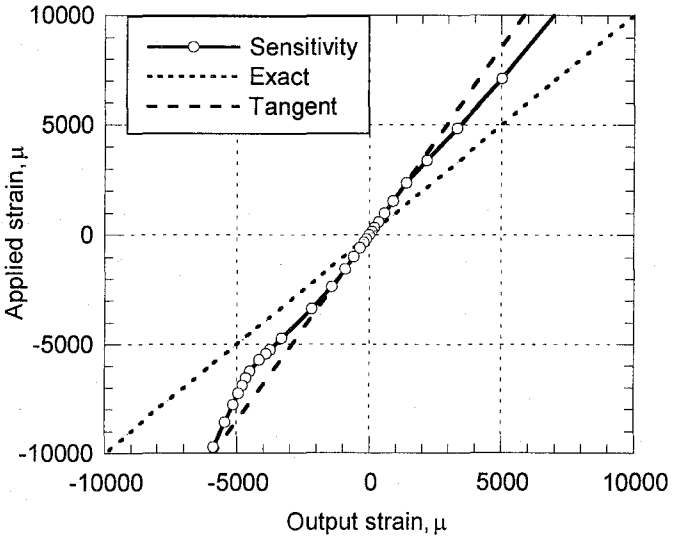

Fig. 2-69 Relation between applied and output strain

2.6 Summary of Chapter 2

The proposed module is evaluated experimentally and analytically. As a result of the tension test, the proposed module showed elastic behavior within a strain of about 2000μ. But in this test, some bending may have occurred because of the incomplete bolt anchorage, thereby developing a non-uniform strain gradient along the fiber and causing multi-peak spectrum. It can be said that once some excessive force is applied to the module beyond the elastic regime to develop a non-uniform strain gradient, the module maintains the deformation history, which affects measurement stability. Therefore, the proposed module should be applied to the strain measurement within its elastic regime, i.e., up to around 2000μ.

In the bending test, although the output of FBG and the strain of the host structure obtained by the gauge are found to be proportional to the applied load, these two values did not agree with each other. Because of uncertain factors such as bolt anchorage, the ratio of these two values cannot be determined. Thus, at the least, some complete anchorage, such as welding should be required so as to determine the calibration coefficient.

Temperature sensitivity is obtained by the temperature test. As a result, the wavelength shift is proportional to the temperature change, and the sensitivity is found to be 18.77×10^{-6} /°C. However, because this sensitivity is quite large, temperature compensation must be required in case of practical applications such as in situ monitoring.

To evaluate the FBG spectrum subject to a non-uniform gradient including linear, quadric, and cubic distributions are assumed and converted into the spectrum by the T-matrix method. Consequently, as the gradient of the distribution increases, the bandwidth of the spectrum increases and the reflectivity decreases. Moreover, it is found that the peak wavelength does not always correspond to the average of the strain distribution and the difference between the peak and the average may increase as the gradient increase.

FEM analysis is conducted to obtain the strain distribution of the module subject to tension, compression, and bending. The spectra of FBG on the module are also obtained by the T-matrix method. As a result, it can be said that the sensitivity of the module strongly depends on the z-axial rotation, and non-uniform distribution may

occur due to the pure tension force. Thus the module should be modified so that it has no geometrical eccentricity and the z-axial rotation is perfectly constrained for constant sensitivity.

Finally a temperature independent module is proposed in order to overcome the problems associated with the old module: high temperature sensitivity and vulnerability to the deformation history. This new module is analytically evaluated. Consequently, the mechanism of the new module can compensate the temperature effect, but the sensitivity of the module length to the output strain is found to be quite high. Thus, high fabrication accuracy should be required for accurate compensation. Moreover, the output of FBG did not agree with the applied strain, but there is a linear relationship between them. Thus, some calibration testing should be used for this new module, even if it is attached to the host by welding.

Chapter 3 Development of a displacement transducer based on FBG sensors

3.1 General remarks

This chapter discusses the development and evaluation of a ground deformation transducer using FBG sensors, named FODD (Fiber Optic Displacement Device). Designed for long term monitoring, the proposed transducer uses vinyl chloride pipe for the main body and optical fiber for the sensor. Moreover, the FODD opens up the possibility of controlling the geo disasters such as land sliding as well as construction procedures by monitoring them continuously and remotely.

In the following sections, in order to evaluate the accuracy of FODD, the displacement estimation is conducted using spline interpolation and polynomial approximation for the fitting, assuming 8 curvature distributions and 10 sensor arrangements for the 20m FODD. Moreover, elemental testing is conducted on the pipe with the FBG sensor and also FODD unit.

3.2 Principle of Fiber Optic Displacement Device

The FODD is intended to measure the ground deformation using fiber optic sensors. **Fig. 3-1** is an outline of FODD, which consists of vinyl chloride pipe (its elastic modulus is about 3.0×10^3MPa in general) and three cables of optical fiber sensors. The parallel optical fibers are installed on the pipe at an angle interval of 120°; each has FBG sensors along the fiber at the same section. Each optical fiber is glued with epoxy resin within the small trench on the surface at a depth of 3mm and a width of 2mm. When the pipe is bent, the pipe's displacement can be estimated by the strain distributions measured by FBG sensors with some boundary conditions. Moreover,

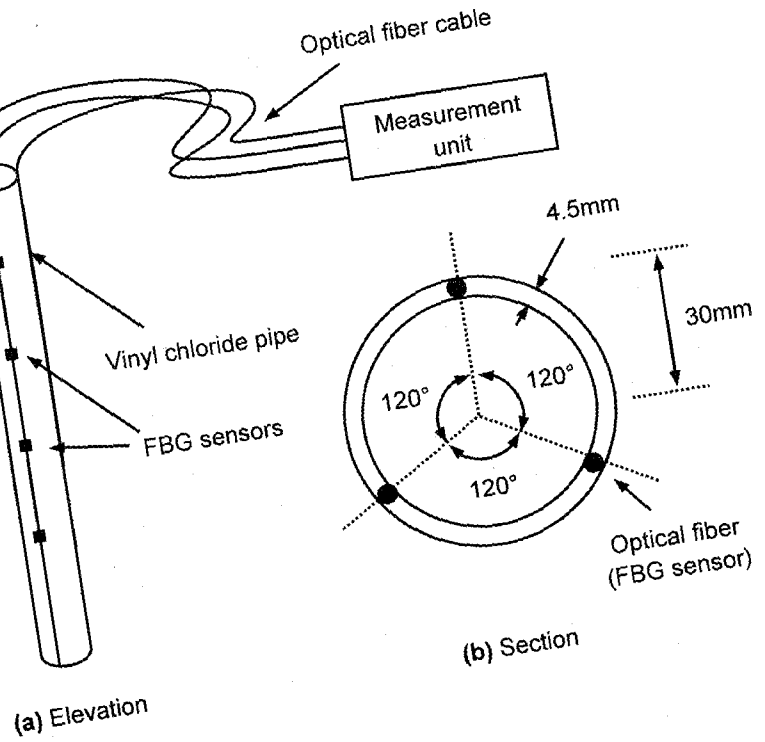

Fig. 3-1 Outline of FODD system

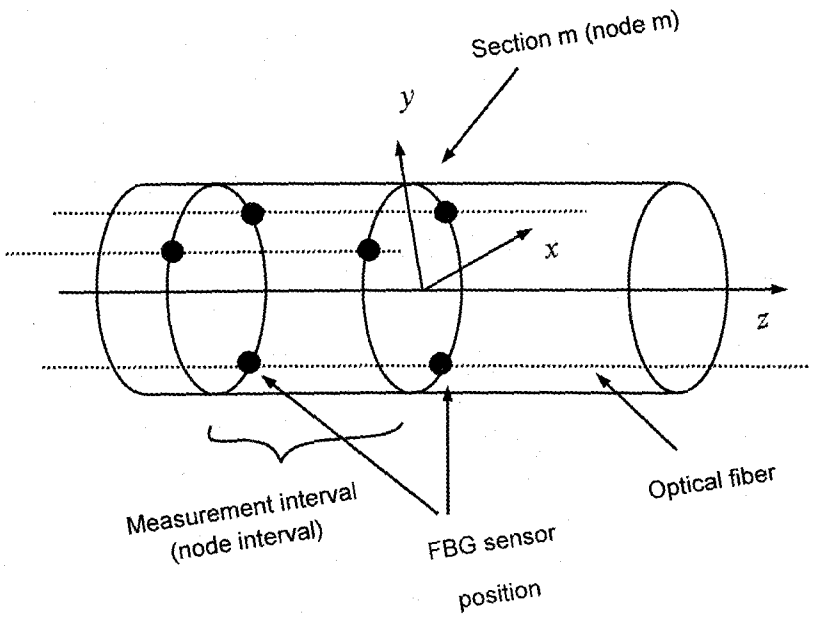

Fig. 3-2 Local coordinates in FODD

two-dimensional displacements can be obtained because FODD used three strain values on each section as follows: Now let the coordinate be set as shown in **Fig. 3-2**, and assuming the Euler-Bernoulli hypothesis on the pipe section, the strain at the arbitrary location in the section z, $\varepsilon(x, y, z)$, can be given by

$$\varepsilon(x,y,z)=\varepsilon_0(z)+x\cdot\varphi_x(z)+y\cdot\varphi_y(z) \tag{3.1}$$

where $\varepsilon_0(z)$ is the axial strain and, $\varphi_x(z)$ and $\varphi_y(z)$ are the curvatures about the x and y axes, respectively. Now on the section z, equation (3.1) contains three unknowns, $\varepsilon_0(z)$, $\varphi_x(z)$, and $\varphi_y(z)$, which can be determined by the three strains in the section, ε_1, ε_2 and ε_3, obtained by the three FBG sensors, respectively. Then let the coordinate of the ith measurement point be (x_i, y_i, z_m), the two curvatures can be expressed as

$$\begin{Bmatrix}\varphi_x(z_m)\\ \varphi_y(z_m)\end{Bmatrix}=\frac{1}{\Delta}\begin{bmatrix}y_1-y_3 & -y_1+y_2\\ -x_1+x_3 & x_1-x_2\end{bmatrix}\begin{Bmatrix}\varepsilon_1-\varepsilon_2\\ \varepsilon_1-\varepsilon_3\end{Bmatrix} \tag{3.2}$$

where

$$\Delta=(x_1-x_2)(y_1-y_3)-(x_1-x_3)(y_1-y_2). \tag{3.3}$$

Finally by double integrations of each curvature, the displacements in the direction of x and y, $u_x(z)$ and $u_y(z)$, can be given by

$$u_x(z)=-\iint\varphi_x(z)dzdz+C_1z+C_2 \tag{3.4}$$

$$u_y(z)=-\iint\varphi_y(z)dzdz+C_3z+C_4. \tag{3.5}$$

Note that constants of integrals in the equations, C_1 to C_4, can be determined by the boundary conditions. These conditions can be obtained by assuming that FODD is clumped at the boundary between the movable and unmovable ground layers detected by soil exploration, or by giving the angle and displacement of FODD at the ground surface. Note also that temperature compensation is not needed in this

system, because the displacement can be acquired by strain differences that will cancel out the temperature-induced strains, assuming that the temperature is constant in the section.

In addition, due to its workability and easy installation, FODD should be separated into unit parts having a length of 4m. Thus FODD naturally includes joints between the units, as shown in **Fig. 3-3**. On the one surface of the triangle tube within the joint,

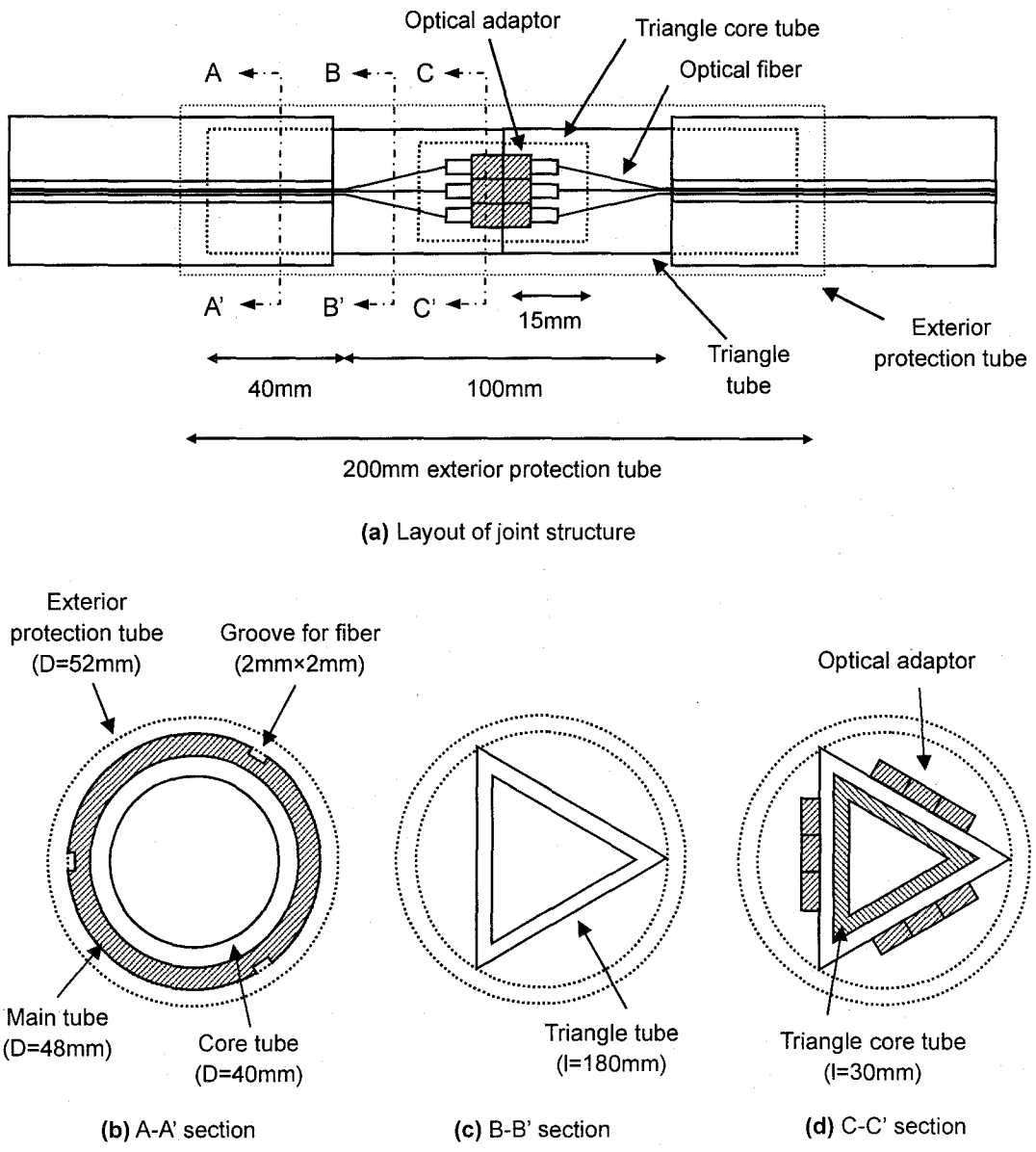

Fig. 3-3 Joint structure of FODD

at most three optical fibers can be connected with MU connectors. Note that this joint structure may become a weak point because the light connection is based on the mechanical attachment, which is easily interrupted by small particles, or the connection misalignment leads to the loss of light power.

3.3 Displacement transformation procedure

3.3.1 Double integration

In the FODD system, the double integrations of the quasi-distributed curvature functions must be done because the curvatures are obtained at several pre-determined positions. Therefore, we first fitted the curvature data to some continuous functions, and then performed double integrations of the fitted functions. In this research, two continuous functions, spline and polynomial functions, are adopted for the fittings. As show in the following sections, these two functions are adopted and evaluated.

3.3.2 Spline interpolation

Assuming linear soil pressure distributions applying to FODD, cubic polynomials should be used for spline functions since the bending moment, i.e., curvature distribution of FODD, can be expressed using cubic functions. Thus in this research, cubic functions are used for the fittings, and the two slopes at both ends are given as the boundary conditions. These slopes can be determined by differentiating the cubic polynomials having four measurement points from the end, respectively. In addition, errors in the measurement values should be compensated before they are fitted. In this research, the moving average method smoothed the obtained data, defined as following equations:

$$\overline{\varphi}_i = \omega_{i,i-1}\varphi_{i-1} + \omega_{i,i}\varphi_i + \omega_{i,i+1}\varphi_{i+1} \tag{3.6}$$

where

$\overline{\varphi_i}$: Optimum value corresponding to ith measurement value

φ_i : ith measurement value

$\omega_{i,j}$: Weight of jth measurement value for ith optimum value.

Note that the weight is determined according to the distance from the neighboring measurement points, defined as follows:

$$\omega_{i,j} = \begin{cases} 0.25 \times \left(\hat{h}/h_j\right) & (i \neq j) \\ 1 - \omega_{i,j-1} - \omega_{i,j+1} & (i = j) \end{cases} \tag{3.7}$$

where h_j is the distance between ith and jth measurement points and $\hat{h}$ is the minimum distance of the intervals.

3.3.3 Polynomial approximation

When a polynomial function is applied to the fitting of m values, at most an m-1 degree polynomial can be determined using the least square method (LSM). However, using LSM, the optimum degree can not be determined although the optimum coefficients can be obtained for the given degree. Thus in this research AIC (Akaike's Information Criteria: Akaike, H., 1974) is adopted to determine the optimum degree, given by

$$\mathrm{AIC} = m \cdot \ln(S) + 2n \tag{3.8}$$

where n is degree of the function, m is the number of the measurement points, and S is the residual error sum of squares. According to this theory, the optimum degree can be obtained when the AIC reaches minimum value.

3.4 Evaluation of the transformation procedure using virtual measurement

3.4.1 Target of this section

Assuming that FODD clumped at the end satisfies the small deformation theory, the accuracy of the displacement estimation simply depends on that of the curvature estimation as well as sensor arrangements. Therefore, herein assuming several curvature distributions and sensor arrangements, the displacement estimation using two fitting methods is evaluated. Note that this assessment can not be generalized because the assumed curvature is limited. However, considering that the curvature of the ground deformation also can not be generalized, this assessment may lead the preferable algorithm and arrangement.

3.4.2 Analytical model

Now assuming FODD is perfectly clumped at the end, let the measurement depth, L, be 20.0m, and the maximum displacement due to the assumed curvature, δ, be 0.5 or 1.0m, respectively. The curvature distributions are assumed to form one to three triangles within each section, and the measurement values are given by adding random errors to the exact values of the distributions. Note that the error amplitude is set to $\pm 1.33 \times 10^{-4}$ 1/m, which is equal to the FBG accuracy of $\pm 4.0\mu$ m/m in curvature expression of the FODD section. Note also that the assumed distributions are determined so that maximum displacement becomes 0.5 or 1.0m, and all triangles in each distribution has identical height. **Fig. 3-4** shows the assumed curvature distributions and the exact solutions of displacement, respectively.

On the other hand, the measurement points arranged in FODD are located uniformly or non-uniformly as shown in **Table 3-1**. Note that "node" herein means the section position of FODD which includes three FBG sensors and gives one curvature value using these three FBG sensors. In this figure, φ_{max} indicates the maximum curvature of each assumed distribution.

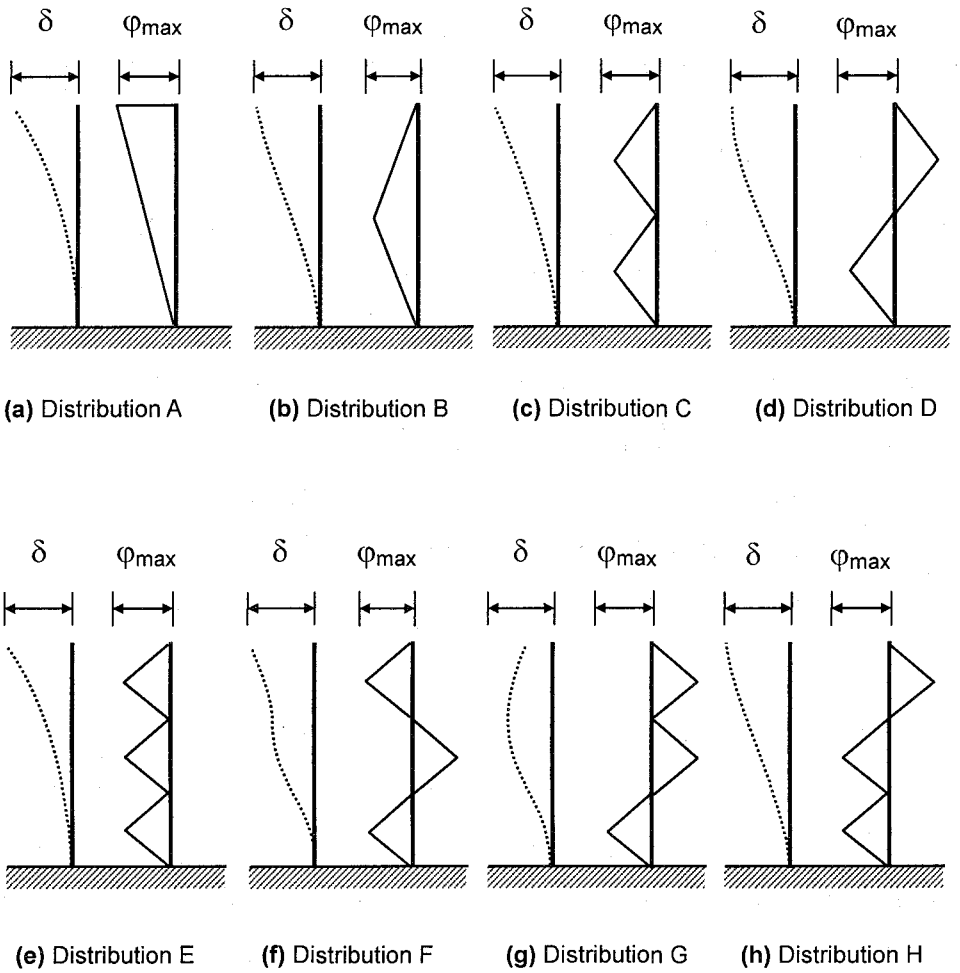

Fig. 3-4 Curvature distribution and displacement

In this research to evaluate the closeness of the estimation to the exact value, the standard deviation, σ, is introduced as given by

$$\sigma = \sqrt{\sum_{i=0}^{M} \frac{(h(z_i) - f(z_i))^2}{M}} \tag{3.9}$$

where z_i is the position of the ith node when total length is divided into M sections, $h(z_i)$ is the value of the exact solution at x_i and $f(x_i)$ is the estimated value at x_i. In this research, when these values are small, the model is considered to have high accuracy. **Table 3-2** shows the maximum curvature and the ratio of the assumed error to the maximum curvature. The largest maximum curvature among the assumed distributions is found in D, which has a ratio of 0.29%, while the smallest one is found

Table 3-1 Sensor arrangement

Arrangement	Number of nodes	Divisions (intervals)
a	3	2 uniform sections (10.0m)
b	4	3 uniform sections (6.6m)
c	6	5 uniform sections (4.0m)
d	11	10 uniform sections (2.0m)
e	21	20 uniform sections (1.0m)
f	41	40 uniform sections (0.5m)
b 01*	4	3 non-uniform sections
b 10*	4	(10.0m, 5.0m)
c 03*	6	5 non-uniform sections
c 30*	6	(10.0m, 0.25m)

* In these cases the total area is divided into 2 identical sections, and then one of them is divided into two or four sections. A suffix in the name denotes the number of nodes located in the former and latter equivalent section. For example, in c30, the former section is divided into 4 identical sections.

Table 3-2 Maximum curvature and error ratio

distribution	Maximum curvature $\times 10^{-2}$ (1/m)		Ratio to the assumed error of 1.33×10^{-4} (1/m)	
	δ=1.0m	δ=0.5m	δ=1.0m	δ=0.5m
A	1.50	0.75	0.89%	1.77%
B	1.00	0.50	1.33%	2.66%
C	1.00	0.50	1.33%	2.66%
D	2.00	1.00	0.67%	1.33%
E	1.00	0.50	1.33%	2.66%
F	3.00	1.50	0.44%	0.89%
G	4.50	2.25	0.29%	0.59%
H	1.29	0.64	1.03%	2.06%

in B, C and E, which have a ratio of 0.66%. Note that if the error of 1.33×10^{-4}1/m is simply distributed, the standard deviation becomes 1.19×10^{-2}m.

In addition, if the stable area of the ground is not clear in advance surveying, the origin of the FODD coordinate can not be located on the boundary between the stable and unstable area. Thus we also evaluate the errors caused by incorrect boundary conditions with sensor arrangement of e and f for distribution E.

3.4.3 Results and discussion

(1) Evaluation of the proposed algorithms

First of all, to evaluate the proposed algorithms, the displacements of the cases with uniform sensor-arrangements are estimated by simply interpolating linear lines between the given curvatures. Note that since an integral is required twice to obtain the displacement, the lines interpolating the curvatures are integrated and interpolated with the lines that are also integrated.

Fig. 3-5 and **Fig. 3-6** show the ratio of the standard deviation by the linear interpolation, σ_0, to that by spline interpolation, σ_S, and polynomial approximation, σ_P, respectively, when the maximum displacement is 0.5m. Note that if the value is below 1.0, the proposed algorithm gives higher accuracy than the linear interpolation. These figures indicate that both algorithms may give smaller deviations than the linear interpolation, especially at a larger node.

As for the maximum displacement of 1.0m, as shown in **Fig. 3-7**, the ratios of the standard deviation by the linear interpolation to that by spline interpolation are below 1.0 except at a lower node, such as 3 and 4. Even at these nodes, the ratios are around 1.0. Thus the spline interpolation can give relatively higher accuracy than the linear interpolation. However, for the polynomial approximation, the ratios are generally higher than 1.0 at the maximum displacement of 1.0m, as shown in **Fig. 3-8**. This may be attributed to the fact that the given curvature-distributions have linear lines that is close to the linear interpolation and the polynomial yields some fluctuation leading to the errors.

Finally, comparing to the linear interpolation, the spline interpolation can give a relatively higher accuracy to estimate the displacement.

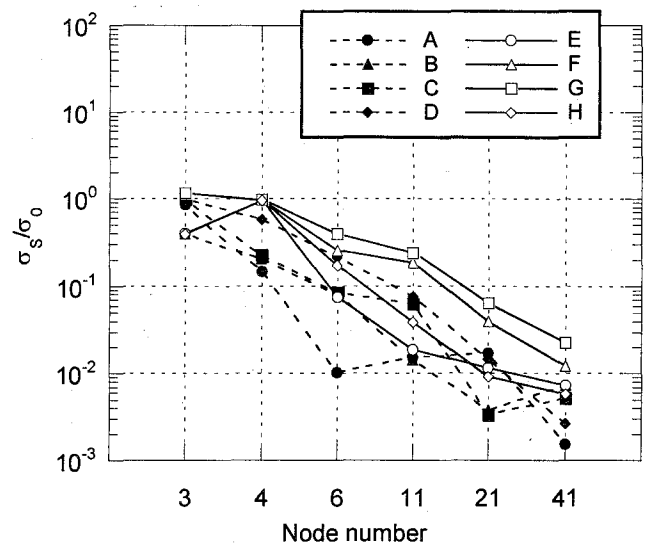

Fig. 3-5 Ratios of the standard deviation by the linear interpolation to that by the spline interpolation at δ = 0.5m with uniform arrangement

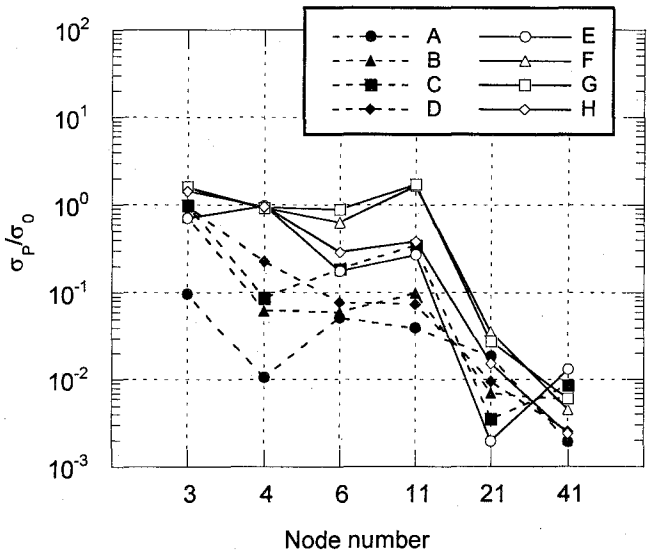

Fig. 3-6 Ratios of the standard deviation by the linear interpolation to that by the polynomial approximation at δ = 0.5m with uniform arrangement

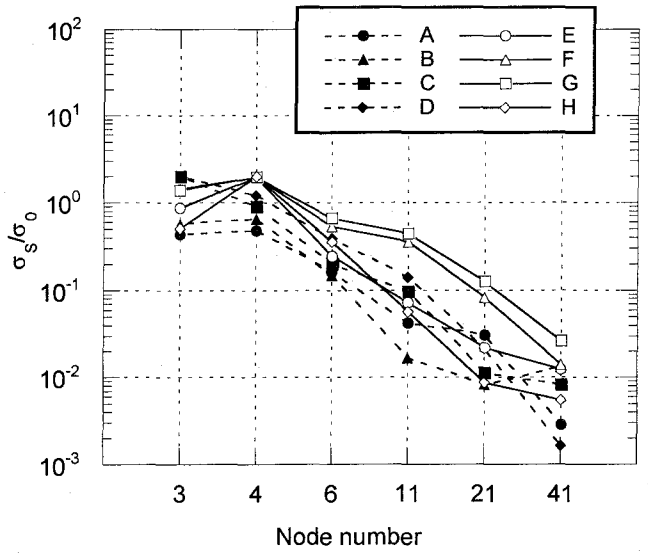

Fig. 3-7 Ratios of the standard deviation by the linear interpolation to that by the spline interpolation at δ = 1.0m with uniform arrangement

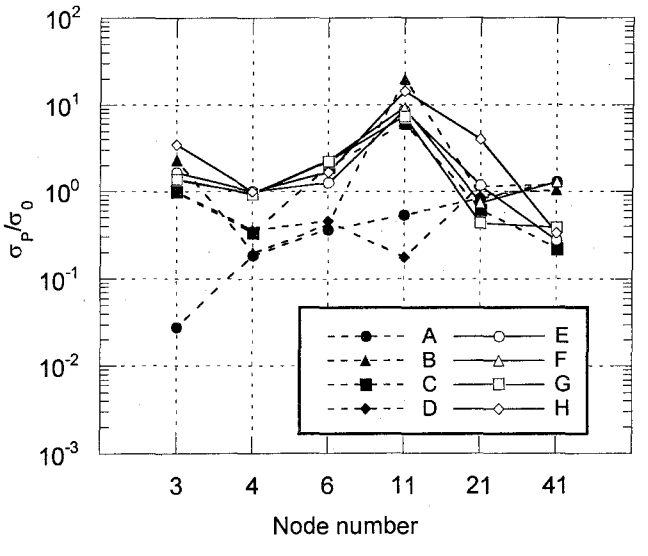

Fig. 3-8 Ratios of the standard deviation by the linear interpolation to that by the polynomial approximation at δ = 1.0m with uniform arrangement

(2) Effect of the number of nodes

Since the nodes are set uniformly in arrangement of a to f, the effect of the number of nodes is evaluated using their results. In this evaluation, the sensor arrangement will be identified by the number of the node they include, not by the alphabet symbols.

Fig. 3-9 illustrates the standard deviation by spline interpolation when the maximum displacement is 0.5m. Note that the data are smoothed once before they are integrated. From this figure, the deviations for all distributions roughly decrease as the number of the node increases. In addition, the deviations for distributions F and G are larger than those for the other distributions due to their larger maximum curvature. However, the values for distributions E and H at 3 nodes are smaller than those at 4 nodes. These values may attribute to the ill node location: when three nodes are arranged uniformly for the distribution of E and H, the nodes are located at the valleys of the triangles and can not give enough information to estimate the whole distribution. In contrast at 3 nodes, the second node can give the information of the whole distribution that is coincidently close to the exact distribution, due to their small curvatures.

Fig. 3-10 illustrates the standard deviation by spline interpolation at δ = 1.0m. This figure shows a trend similar to those at δ = 0.5m. But generally, the deviations at δ = 1.0m are about twice as large as those at δ = 0.5m, meaning that the increase in maximum displacement may cause the increase in error if the accuracy is defined as σ. Note that if accuracy is defined as the ratio of σ to δ, the accuracy may increase as the maximum displacement increases.

On the other hand, **Fig. 3-11** shows the standard deviations by polynomial approximation when the maximum displacement is 0.5m, while **Fig. 3-12** shows those when the displacement is 1.0m. From these figures, like spline, twofold maximum displacement resulted in almost twofold errors in the estimation. From 3 to 11 nodes, an increase in node did not drastically improve the accuracies, for all distributions. Especially for distributions E and H, the deviations at 4 nodes are larger than those at 3 nodes, and for distributions F and G, the deviations at 11 nodes are larger than those at 4 and 6 nodes. These deviations may be attributed to the polynomial characteristics: polynomial functions tend to vibrate around the section end as the degree increases. On the other hand, AIC determined the optimum degree when the function is simply close to the given data. Thus, even though the function is simply

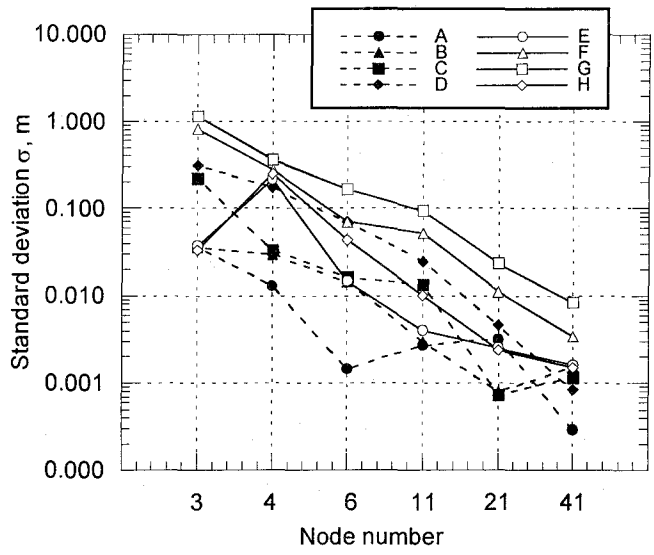

Fig. 3-9 Standard deviation by spline interpolation at δ = 0.5m with uniform arrangement

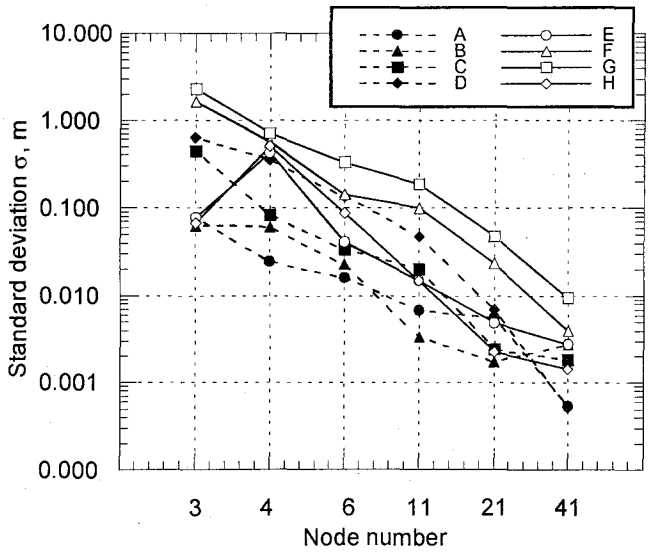

Fig. 3-10 Standard deviation by spline interpolation at δ = 1.0m with uniform arrangement

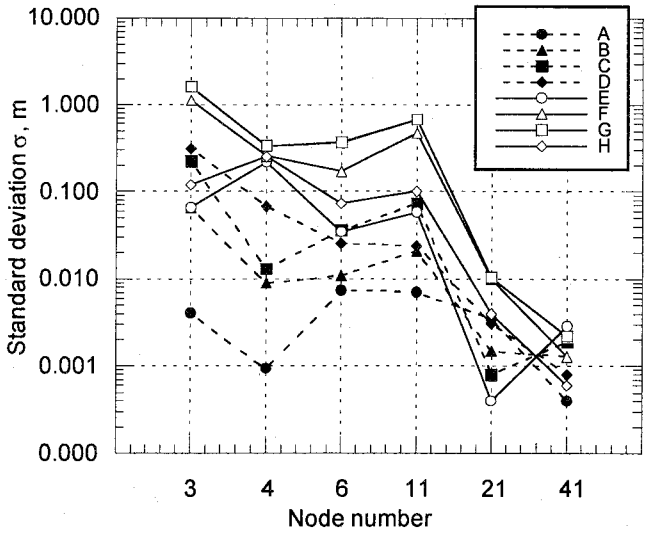

Fig. 3-11 Standard deviation by polynomial interpolation at δ = 0.5m with uniform arrangement

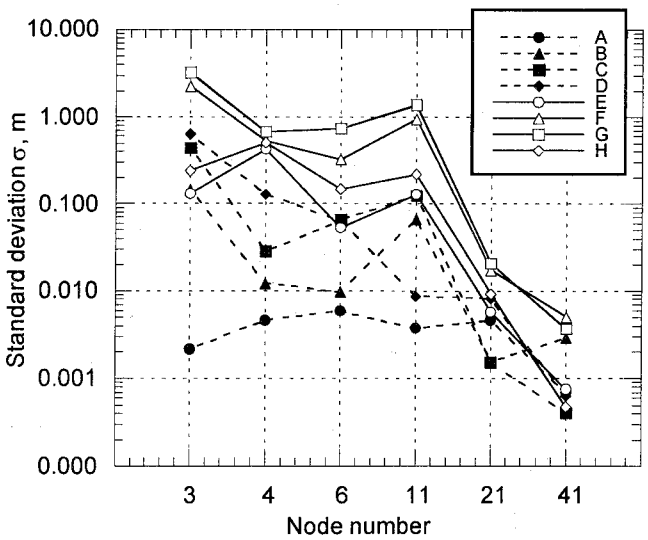

Fig. 3-12 Standard deviation by polynomial interpolation at δ = 1.0m with uniform arrangement

close to the data except around the ends, the function could be recognized by the AIC as an optimum one. For instance, as for distribution F at 11 nodes, the optimum degree is 10 by AIC, but the 10th degree polynomial shows rapid changes around the section ends. This change may cause the total error since the estimated function should be integrated from the origin and the errors accumulated during the integral.

Next, **Fig. 3-13** and **Fig. 3-14** show the ratios of the standard deviation by polynomial, σ_P, to that by spline, σ_S, i.e., σ_P/σ_S, at δ = 0.5 and δ = 1.0m, respectively. Note that the ratio is expressed as logarithms. Thus, for instance, if the value is positive, the accuracy by spline is higher than that of polynomial. From these figures, for all cases at 11 nodes, the accuracy by polynomial is much worse than that of spline. This may be caused by the polynomial characteristics, as mentioned before. When the node is 3, 4 or 6, if the distribution is complicated, i.e., E, F, G, or H, the accuracy by spline is higher than that of polynomial. In contrast when the node is 41 for all distribution, the accuracy by polynomial is relatively higher than that by spline. For the other cases, there is no significant difference between the two algorithms.

Considering that the spline tends to increase accuracy as the node increases as opposed to polynomial, the spline interpolation with many sensors may be preferable for random distribution.

(3) Effect of the sensor arrangement

As for the sensor arrangement of b10, b01, c03, and c30, the standard deviations by spline interpolation at δ = 0.5 and 1.0m are shown in **Fig. 3-15** and **Fig. 3-16**, respectively, while those by polynomial approximation are shown in **Fig. 3-17** and **Fig. 3-18**, respectively. In these figures, the uniform arrangement of b and c which have the same number of nodes as b10 and b01, or c30 and c03, are also plotted. Note in the following discussion that the former section indicates one of the identical sections which includes the origin when the total sections are divided into two identical sections.

From these figures, regardless of calculation algorithms, it is found that the accuracies of uniform arrangement are higher than those of non-uniform arrangement. The arrangement with nodes in the former section, i.e., b10 and c30, gave higher accuracy than those without nodes, i.e., b01 and c03, respectively. Moreover, comparing the b10 and c03 arrangements, the accuracy of b10, which has fewer nodes but has a node in the former section, is higher than that of c03, which has no

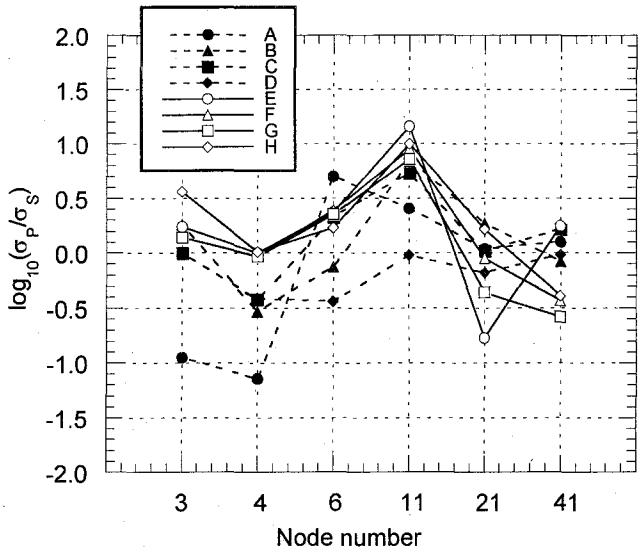

Fig. 3-13 Ratio of standard deviation, σ_P/σ_S, at δ = 0.5m with uniform arrangement

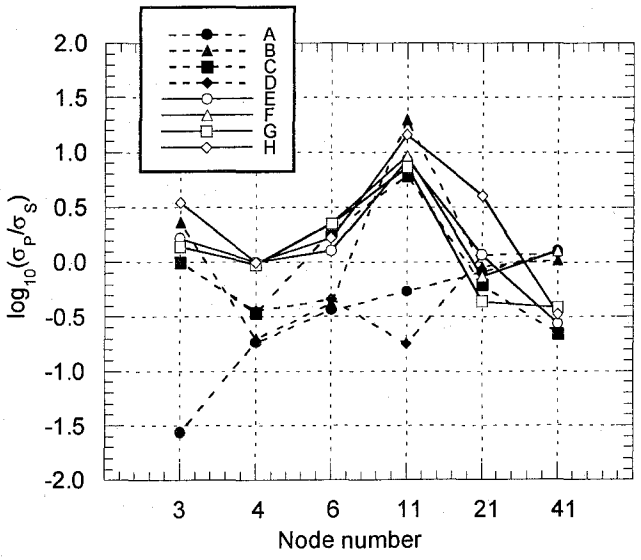

Fig. 3-14 Ratio of standard deviation, σ_P/σ_S, at δ = 1.0m with uniform arrangement

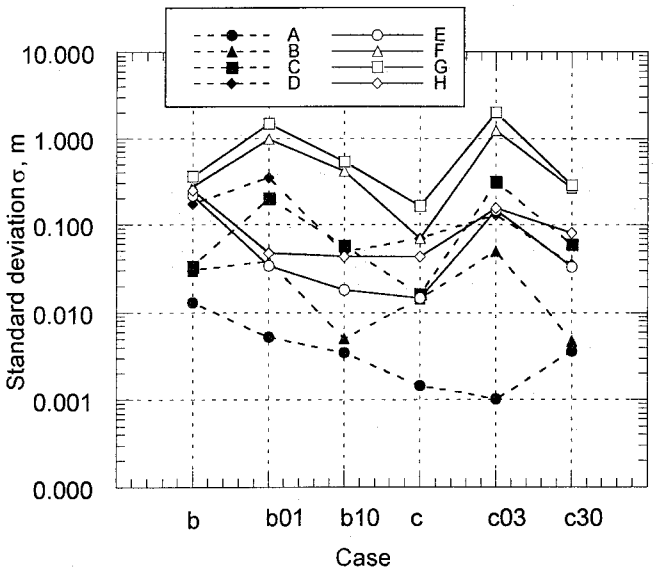

Fig. 3-15 Standard deviation by spline interpolation at δ = 0.5m with non-uniform arrangement

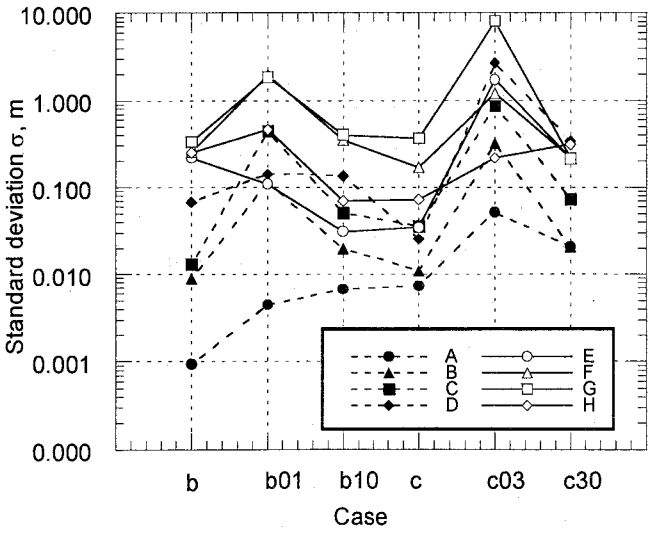

Fig. 3-16 Standard deviation by spline interpolation at δ = 1.0m with non-uniform arrangement

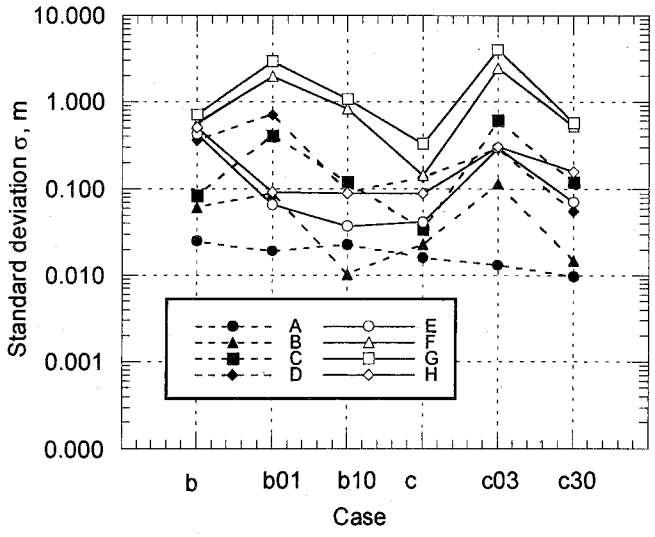

Fig. 3-17 Standard deviation by polynomial interpolation at δ = 0.5m with non-uniform arrangement

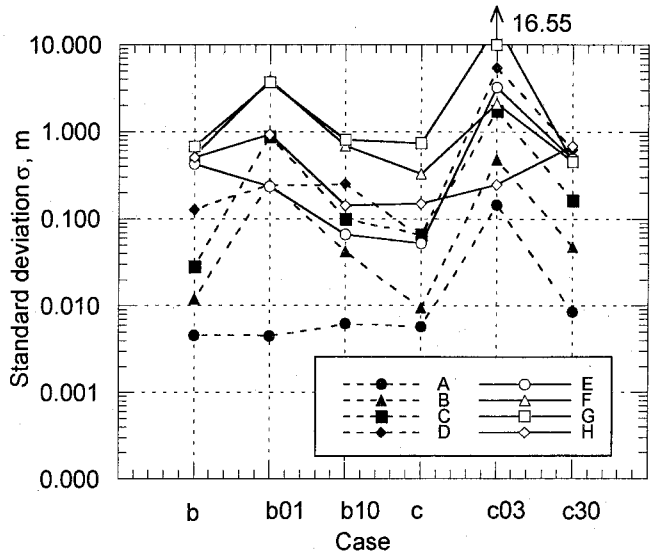

Fig. 3-18 Standard deviation by polynomial interpolation at δ = 1.0m with non-uniform arrangement

node in the former section. This may be attributed to the fact that the estimation for the curvature in the former section significantly depends on the information in the latter section for b01 and c03 since no information can be extracted in the former section in these cases. Consequently, the errors in the former section may cause the drift of the curvature estimation in the latter section.

On the other hand, the ratios of the standard deviation by spline to those by polynomial at δ = 0.5 and 1.0m are shown in **Fig. 3-19** and **Fig. 3-20**, respectively. Note that in these figures the ratios are plotted in the logarithms. From these figures, for complicated distributions such as E, F, G, and H at both the maximum displacements, the accuracy by spline is higher than that by polynomial. Especially in the c03 arrangement, which contains no node in the former section, the accuracy by spline is quite higher.

Therefore, if the nodes are arranged non-uniformly, the accuracy by estimation may increase by installing more nodes in the former section and also using the spline interpolation for the displacement transformation. However, for almost all cases, uniform arrangement gave higher accuracy than non-uniform arrangement. Thus uniform arrangement may be preferable if possible.

(3) Effect of the ill boundary assumption

In order to evaluate the effect of the ill boundary assumption, the clumped end is assumed to be located 0.5m or 1.0m shallower than the origin. Then the deformations are obtained by integrating the curvatures from those shallower points to the end. Note that in this evaluation, 21 and 41 uniform arrangements are set for distribution E. Note also that the nodes in the arrangements decreases by 1 or 2 due to the decrease of total section when the boundary is assumed to be shallower than the origin.

Fig. 3-21 and **Fig. 3-22** shows the deviations by spline and polynomial when the maximum displacement is 0.5m and 1.0m, respectively. In these figures, L and P represent spline interpolation and polynomial approximation, respectively, and the number that follows denotes the number of the node. From **Fig. 3-21**, it is found that regardless of the integral algorithms when the maximum displacement is 0.5m, the ill assumption of 0.5m resulted in a small increase in the accuracy of the cases with fewer nodes, i.e., 21, while in the cases with more nodes, i.e., 41, the ill assumption of 0.5m caused a large decrease in accuracy. In contrast, the ill assumption of 1.0m caused a decrease in the accuracy down to 0.01m for all cases. This decrease may

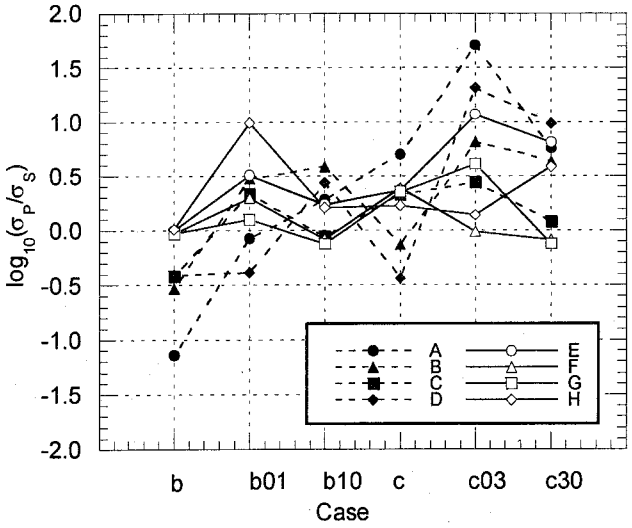

Fig. 3-19 Ratio of standard deviation, σ_P/σ_S, at δ = 0.5m with non-uniform arrangement

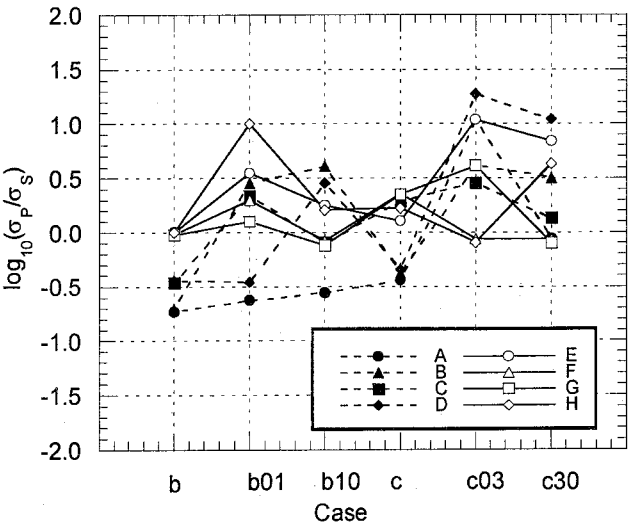

Fig. 3-20 Ratio of standard deviation, σ_P/σ_S, at δ = 1.0m with non-uniform arrangement

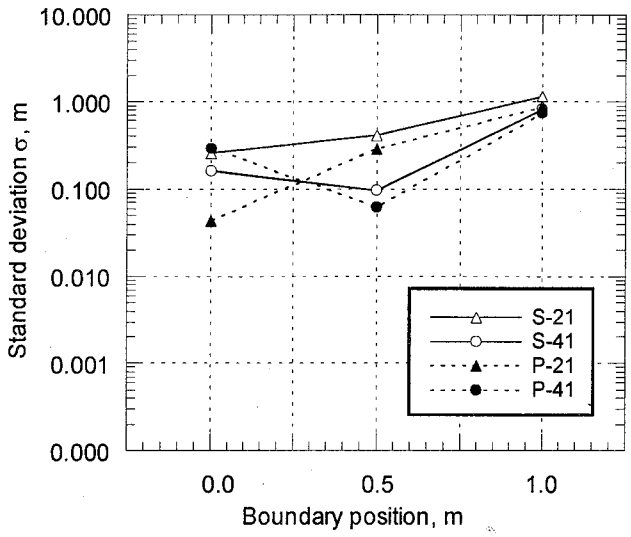

Fig. 3-21 Standard deviation at δ = 0.5m with ill assumption

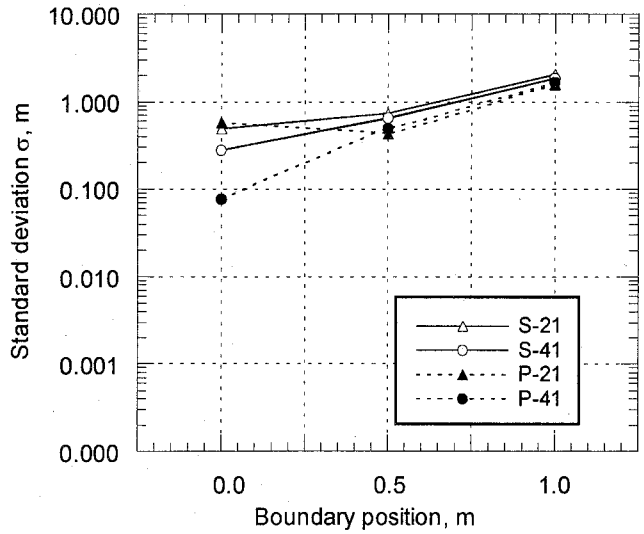

Fig. 3-22 Standard deviation at δ = 1.0m with ill assumption

be attributed to the fact that the estimated displacement for distribution E tends to be larger than the exact solution due to the positive distribution, and the ill assumption of 0.5m coincidentally adjusted the drift of the estimated displacement.

On the other hand, from **Fig.3-22**, it is found that when the maximum displacement is 1.0m, accuracy generally decreases as the ill assumption increases for all the arrangements, regardless of the calculation algorithms.

Thus when the boundary is assumed to be located 0.5m shallower than the exact boundary, if the maximum displacement is small, such as 0.5m, a significant change in the accuracy may not occur, but as the maximum displacement increases the accuracy may increase, regardless of the transformation algorithms. It can be said that if the maximum displacement increases, the influence of incorrect boundary assumption also become large, causing a decrease in the accuracy for both algorithms, spline and polynomial.

3.4.4 Summary

To attain the high accuracy of FODD, the displacement estimation is conducted using spline interpolation and polynomial approximation for the fitting, assuming 8 curvature distributions and 10 sensor arrangements for the 20m FODD.

As a result, for uniform arrangement, it is found that though there is no significant difference between two algorithms, the spline interpolation with many sensors may be preferable for random distribution.

In contrast, for non-uniform arrangement, the accuracy of the estimation may increase by installing more nodes in the former section, and also using the spline interpolation. But the uniform arrangement may give higher accuracy than the non-uniform arrangement.

Thus for higher accuracy, the uniform arrangement of as many sensors as possible may be preferable using the spline interpolation. Note that for almost all cases, an increase in maximum displacement may decrease the estimation accuracy if the accuracy is defined as a standard deviation.

Moreover, the influence of the ill boundary assumption on the accuracy also may increase as the maximum displacement increases.

3.5 Fundamental test for FODD

3.5.1 Element test

In order to evaluate the material for the main body of FODD, fundamental tests such as compression, bending, and temperature are conducted on vinyl chloride specimens. First, the compression tests are carried out on three vinyl chloride pipe specimens, which have an inner and outer diameter of 40.0 and 48.0mm, respectively. The loads are applied to the specimens on both end sections within the elastic regime, and the gauges are installed on the surface of the pipe to measure vertical and horizontal strains. **Table 3-3** shows the results of three specimens and their average. As a result, it is found that the average of elastic modulus and the Poisson ratio are 3.16×10^3N/mm^2 and 0.34, respectively.

Next the bending test is carried out on the vinyl chloride pipe, which also has an inner and outer diameter of 40 and 48mm, respectively, and is simple-supported as shown in **Fig. 3-23**. In this experiment, at the center of the pipe, the displacement and the applied loads are measured by a dial gauge and load cell, respectively. **Fig 3-24** shows the relationship between the load and displacement at the center of the pipe. It is found that the pipe subject to bending moment behaved elastically until the load reached about 500N, after the pipe showed some hardening behavior.

Now the curvature, ϕ, can be given by

$$\phi = \frac{M}{EI} \tag{3.10}$$

where M is the bending moment, E is the elastic modulus, and I is second-order inertia.

Let E and I be 3.16×10^3N/mm^2 and 1.35×10^5mm^4, respectively. When M is 2.25×10^5Nmm (= 500N×450mm), substituting those values into equation (3.10), the curvature ϕ becomes 500μ mm/mm. Thus it can be said that FODD should be applied to the deformation whose maximum curvature is less than 500μ mm/mm. Note that if FODD is applied to the deformation with more than 500μ mm/mm, even in that ground FODD can measure the deformation since the deformation is obtained using only curvature information, but accuracy may decrease because the partial plasticity may

cause local deformation, which distributes the stress non-uniformly.

Next, a temperature test is carried out on a small plate of the vinyl chloride plastic. The specimen piece for this test is 40mm long, 30mm wide, and 6mm thick, on the center of which three resistive gauges are installed. The specimen is cooled down step-by-step to about -10°C. **Fig. 3-25** illustrates the temperature-strain relationship of the specimen. The approximated equation obtained by the least-square method is also shown in this figure. Note that the strain is initialized to 0μ at 0°C in this figure. Finally it is found that the temperature sensitivity is 53.9μ/°C, which is almost five times as much as that of steel.

Table 3-3 Compression test results

Specimen #	1	2	3	Average
Elastic modulus $\times 10^3 N/mm^2$	3.12	3.34	3.02	3.16
Poisson ratio	0.43	0.28	0.31	0.34

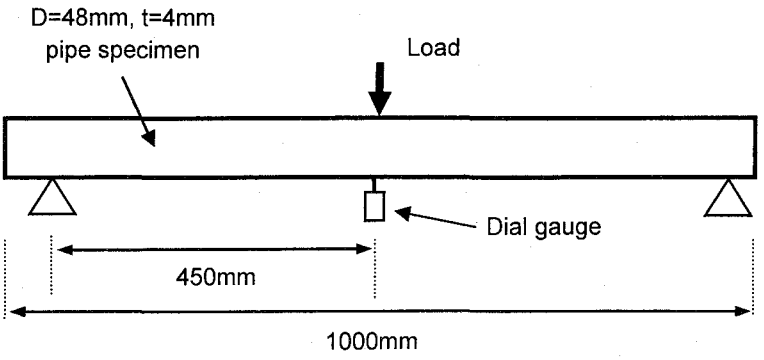

Fig. 3-23 Test setup of pipe bending test

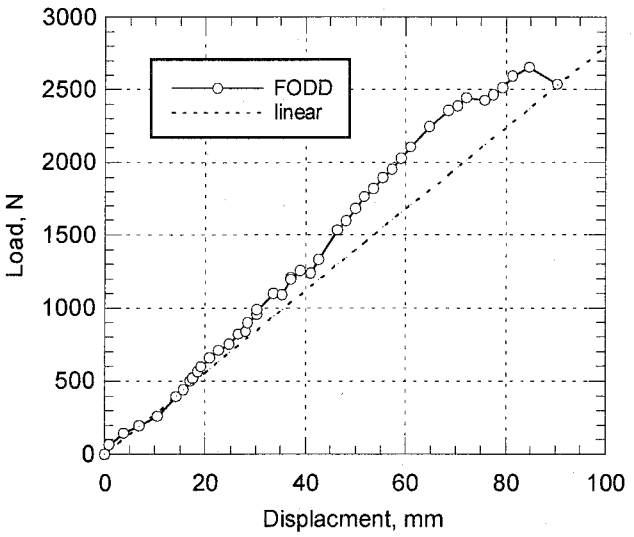

Fig. 3-24 Load-displacement relation of the pipe

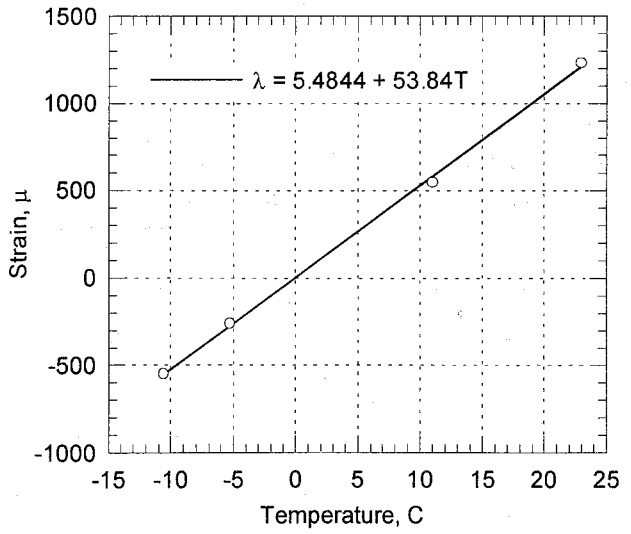

Fig. 3-25 Temperature-strain relationship of the vinyl material

3.5.2 Measurement test on FBG sensor

Two bending tests are carried out so as to evaluate the FBG sensor applied for a strain measurement of vinyl chloride material. First, an FBG sensor is installed on the center of the vinyl chloride plate, which is 400mm long, 100mm wide, and 19mm thick. The plate is simple-supported and loaded in the center span as shown in **Fig. 3-26**. For comparison, two strain gauges are also installed on the plate next to the FBG. The loads are applied by adding the 2kg weight step-by-step. Note that the measurement system in these tests, FBG-IS, can detect only the peak wavelength of a spectrum; strain is obtained by the peak shift. **Fig. 3-27** shows the relationship between load and strain of the gauge and the FBG sensor, respectively. Note that in this figure the values of the gauges are the average value of the two gauges. It is found that FBG and the gauges agreed well with each other, and the elastic modulus obtained by this test is close to that by elemental test.

Next, for the same purpose as the plate test, the bending test is carried out on the vinyl chloride pipe, on the center of which FBG sensors are installed, as shown in **Fig. 3-28**. Resistive gauges are also installed on the pipe for comparison. The pipe is simple-supported and subject to two-point loads. **Fig. 3-29** and **Fig. 3-30** show the relationship between the load and the negative and positive strain of the pipe by both instruments, respectively. The exact value in these figures means the strain obtained by the measured values of the load and displacement. From these figures, it is found that even for compression measurement, FBG sensors agreed well with the gauges. Note that the differences in this test may be attributed partly to incorrect sensor installation.

Thus it can be said that FBG can measure the strain of vinyl chloride material as well as the resistive gauges can.

3.5.3 FODD unit test

Before FODD is applied to practical measurement, calibration should be required. Thus to evaluate herein the accuracy of the FODD system, bending tests are conducted on the FODD unit, which has a length of 4m and 5 sensor sections. As shown in **Fig. 3-31**, the unit is set on the flat board and supported horizontally at the two points. **Fig. 3-32** shows the layout of the experiment setup. The displacements

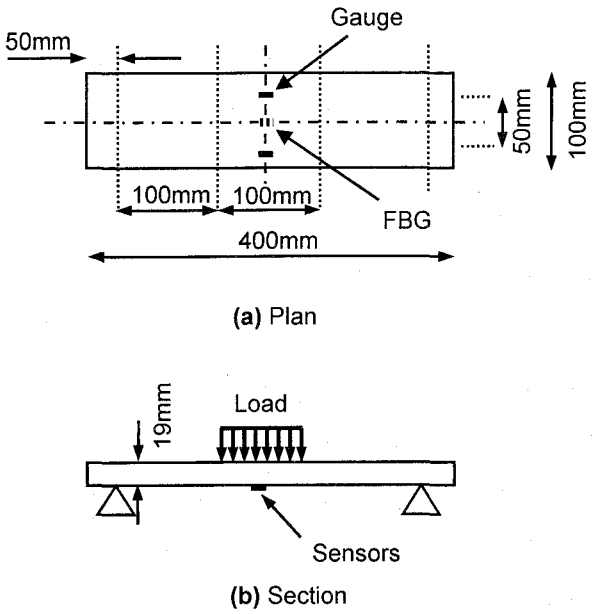

Fig. 3-26 Test setup of bending test on plate

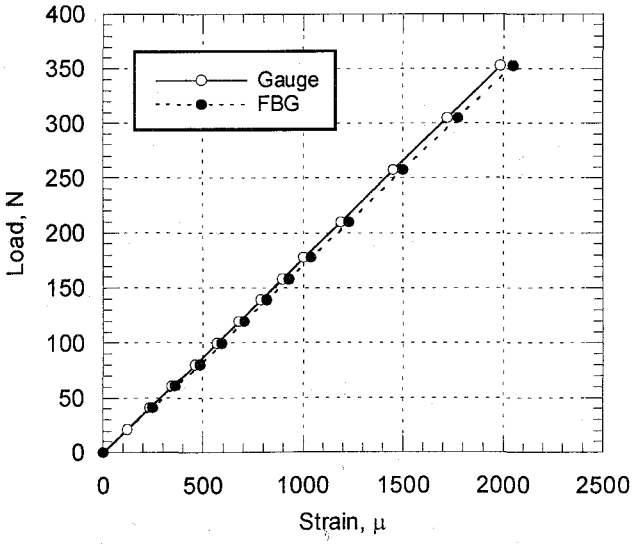

Fig. 3-27 Load-strain relation of the pipe by both sensors

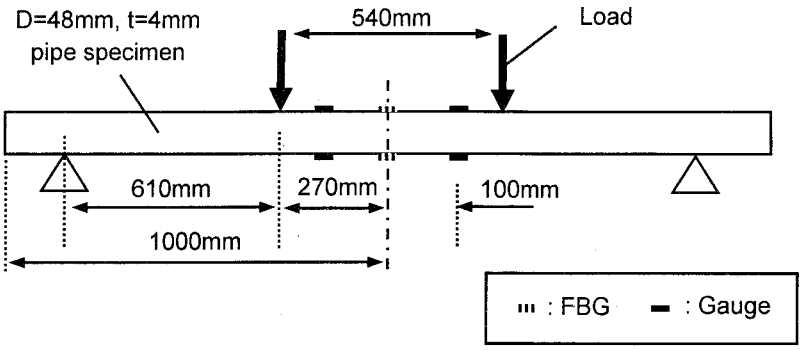

Fig. 3-28 Test setup of pipe bending test

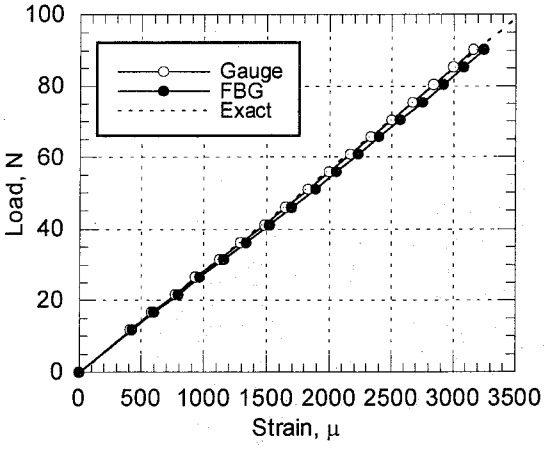

Fig. 3-29 Relationship between load and positive strain

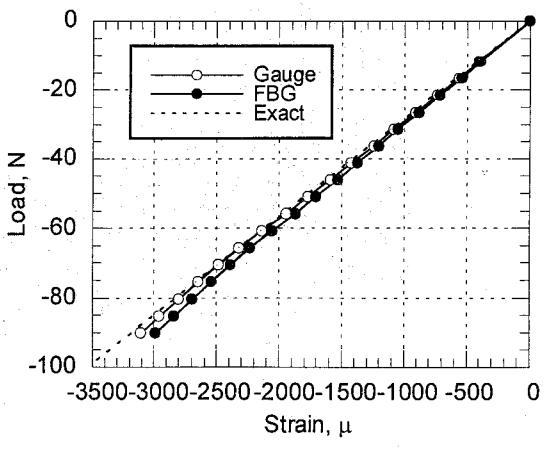

Fig. 3-30 Relationship between load and negative strain

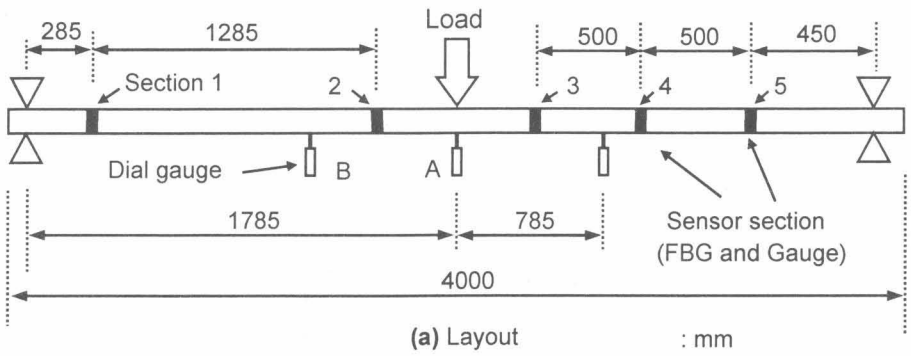

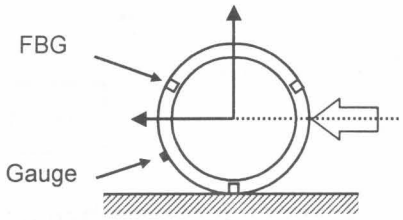

(b) Sensor section

Fig. 3-31 Test setup for unit test

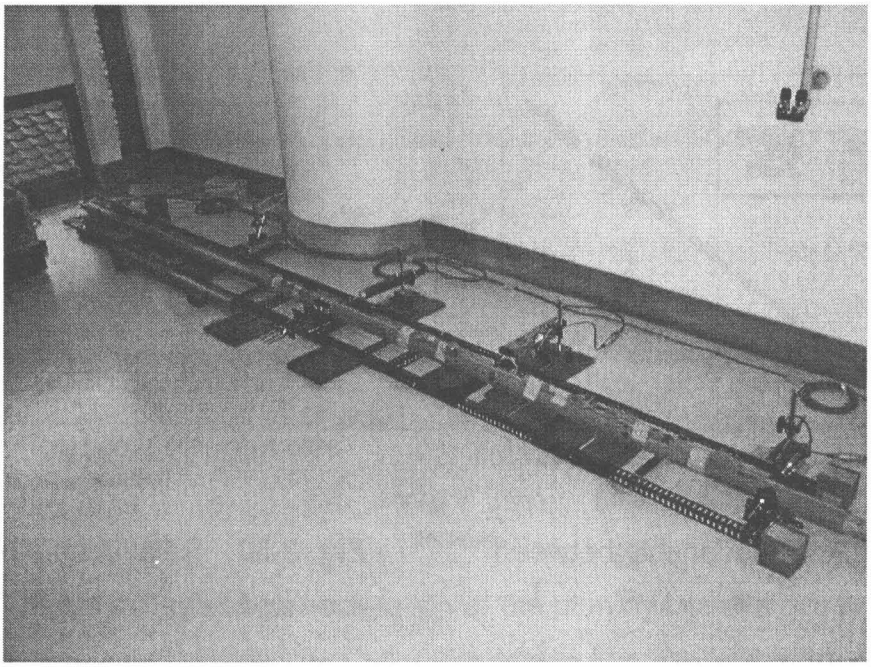

Fig. 5-32 Layout of the unit test

are measured at the center (A), and the two side points located apart 785mm from the center (B), respectively. The load applied at the center of the unit is controlled by displacement, adding 10mm in one step up to 50mm. Strain gauges are also installed on the unit with a rotation of 60 degrees in the same section where FBG sensors are installed. **Fig. 3-33** shows the strain values by FBG and gauges corresponding to FBG. From this figure, the values by FBG agreed well with those by gauges. Using these values, the displacement is estimated in each step. Note that in this test, the curvature distribution apparently formed a triangle, thus a triangle distribution is assumed for this curvature distribution. **Fig. 3-34** shows the estimated displacement at A and B for all steps. Note that the values of the dial gauge at B indicate the average displacements measured by two dial gauges at the symmetrical position. It is found that the difference between the measured values and the estimated values at the center is larger than those at the side, which may be caused by the accumulated errors proportional to the integral length. It is clear that using strain values by FBG allowed the displacement to be obtained within an accuracy of about 6.7%.

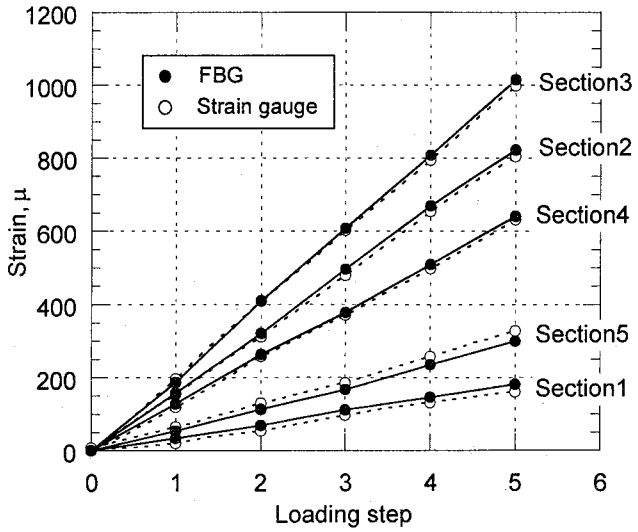

Fig. 3-33 Strain values by FBG and by gauges corresponding to FBG

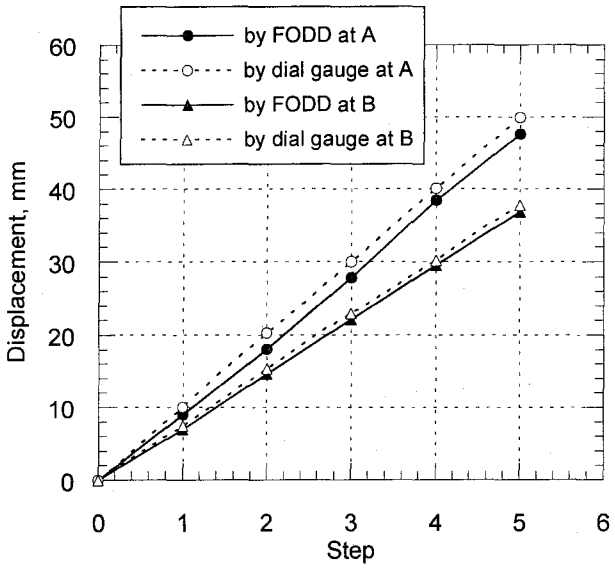

Fig. 3-34 Estimated displacement at the center and the sides for all steps

3.6 Site test

3.6.1 Test setup

To evaluate the measurement system, including installation and workability of FODD, the measurement test is conducted using embankment. For comparison, the vinyl chloride pipe with resistive gauges instead of FBG is also installed. **Fig. 3-35** shows the specimens used in this test. Although a FODD unit is designed to be 4m long, the specimen is 2m long and has a joint structure for the extension, to evaluate the joint structure as well. At most, the joint can connect three optical fibers because of the size of the optical connector. Note that this joint structure may become a weak point of the FODD system because the connector is a crump-style connector: easy to detach but vulnerable to impurities between the fibers.

For further development, the advanced model, which does not need the optical connection, is also proposed as shown in **Fig. 3-36**. The curvature radius of the optical fiber should not be less than 25mm because if the radius is less than 25mm, the light power rapidly decreases due to the bending loss. Thus in the advanced

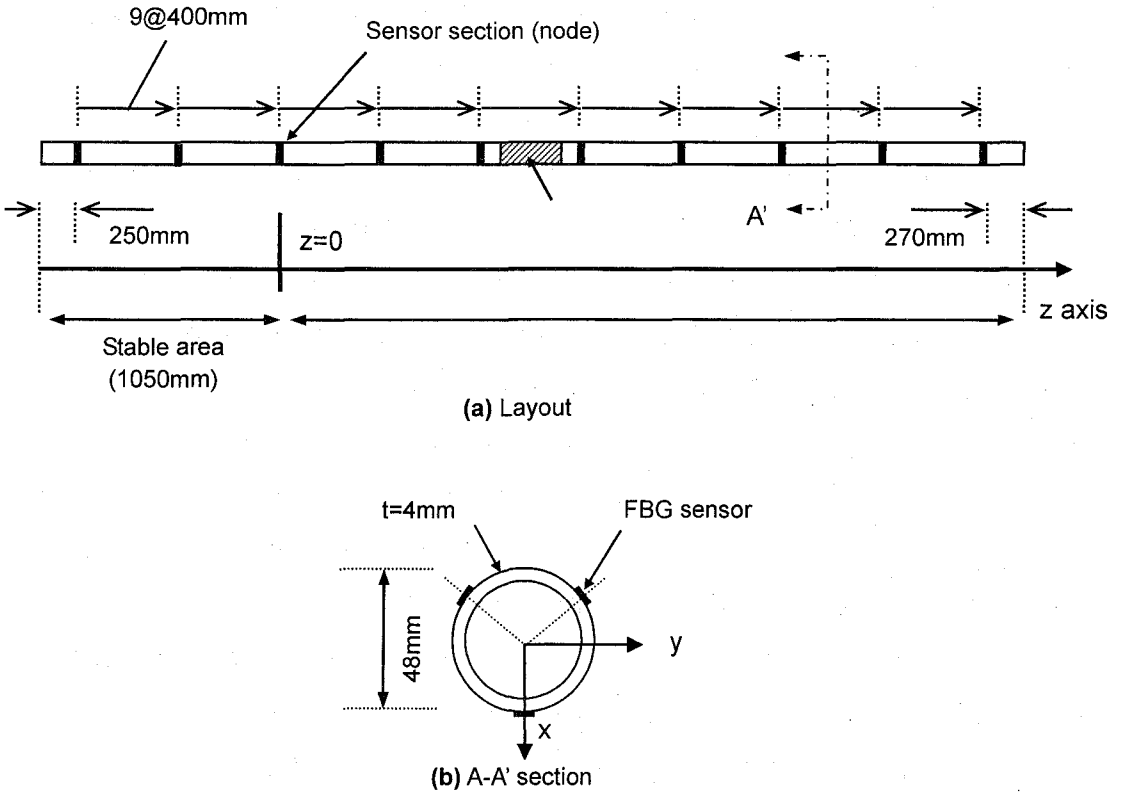

Fig. 3-35 FODD specimen used in site test

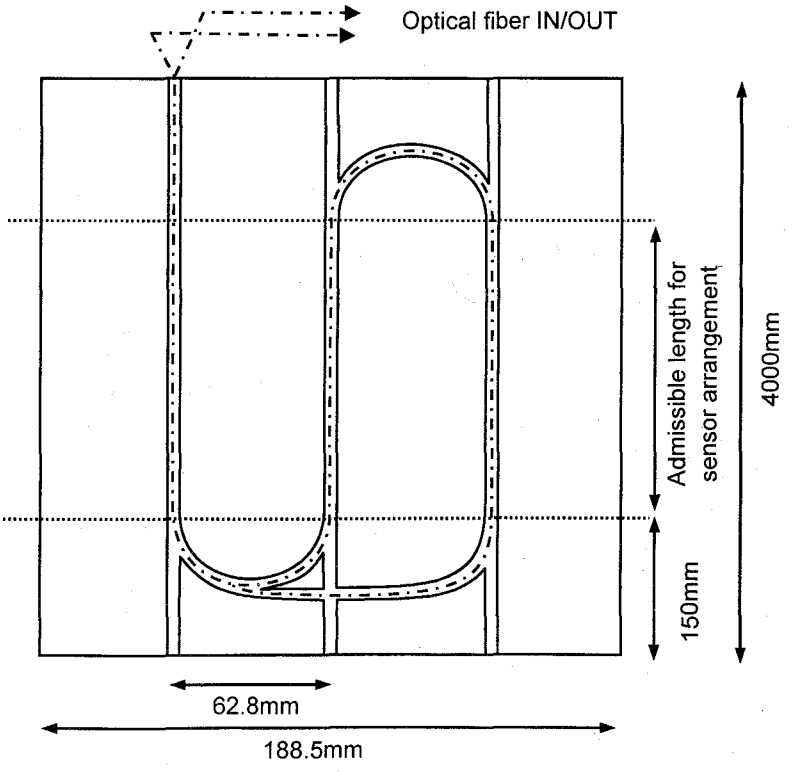

Fig. 3-36 Development elevation of FODD

model, for each unit only one fiber is installed so that the fiber is bent 3-dimensionally with a curvature radius of more than 25mm. Note that this advanced model is not fabricated and tested in practice.

Fig. 3-37 shows the embankment used in this test. FODD and the gauge pipe are installed in this embankment and fixed with 1m-long steel pipes. Local coordinates of each instrument are set so that the local x-axis has the same direction as the global X-axis. Vinyl sheet is also installed in the embankment to lead the movement of slope. The 10kN weight is loaded on top of the embankment as a one step; after 10 steps the slope is cut by a drag shovel, as shown in **Fig. 3-38**. In this figure the number indicates the step of cutting. **Fig. 3-39** and **Fig. 3-40** illustrate the layout of the embankment, the top of the embankment, and the installed instruments respectively. **Fig. 3-41** shows the cutting procedure after the loading.

For the wire extension, FODD used only 3 optical fibers; the gauge pipe needed many wires to install the same number of sensors as in FODD. Note that only one cable of the optical fibers is available in this experiment due to the capacity of the FBG-IS system because the optical switch is not installed. But in general, over 50 lines can be connected to one FBG-IS system if the optical fiber switch is installed.

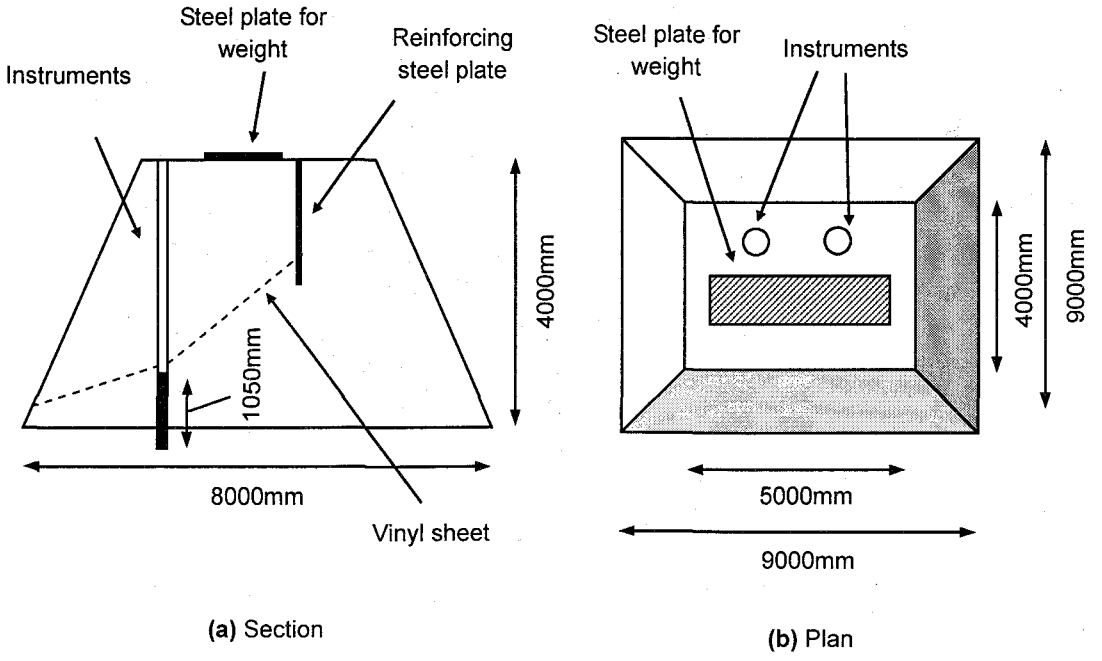

Fig. 3-37 Embankment section and plan

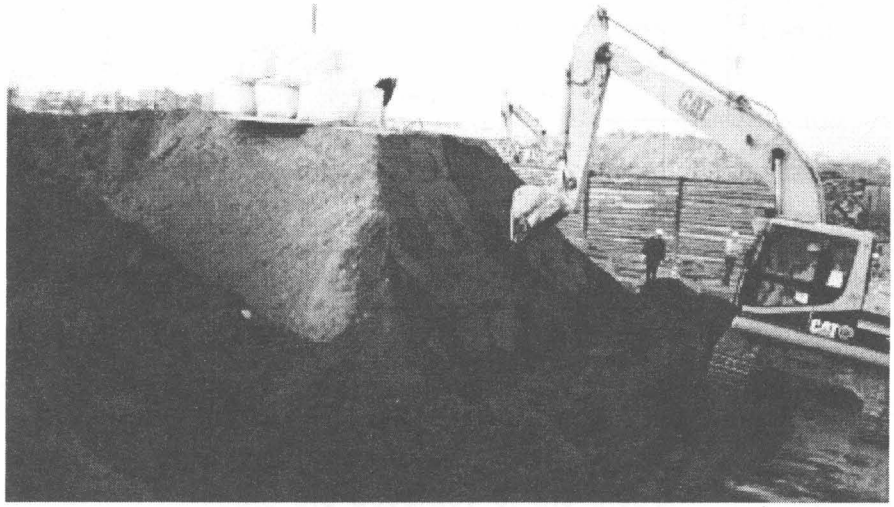

Fig. 3-38 Cut by Drag shovel

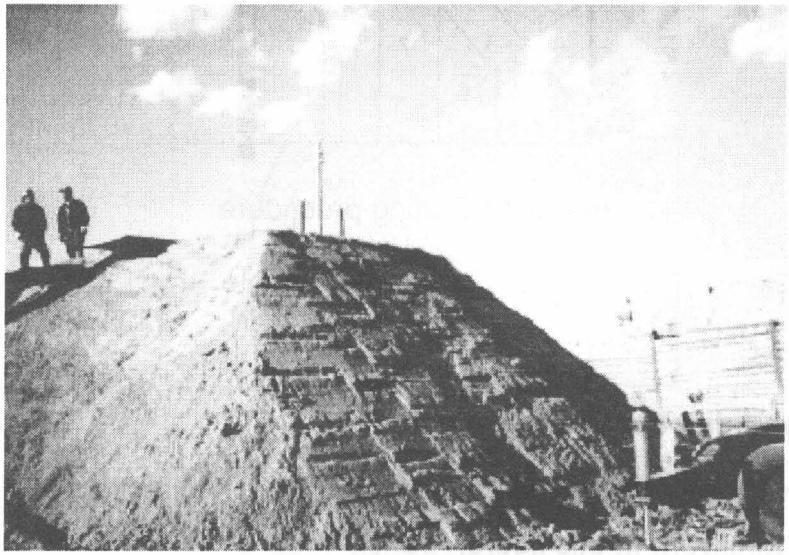

Fig. 3-39 Embankment layout

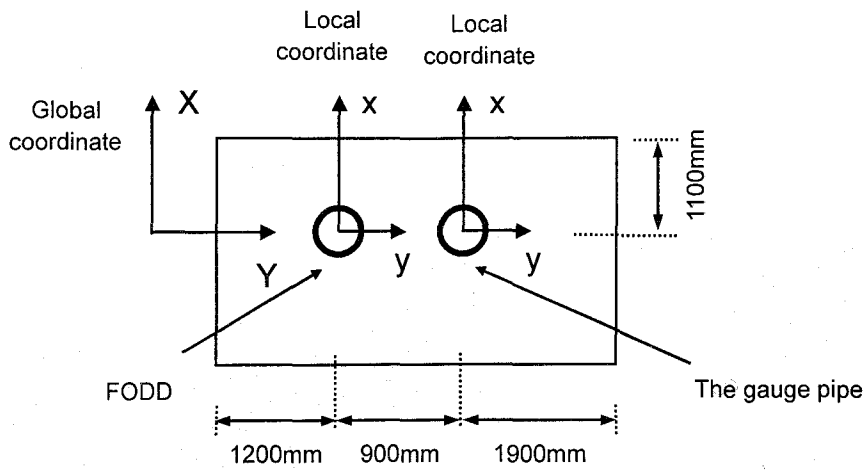

Fig. 3-40 Instruments arrangement on the embankment top

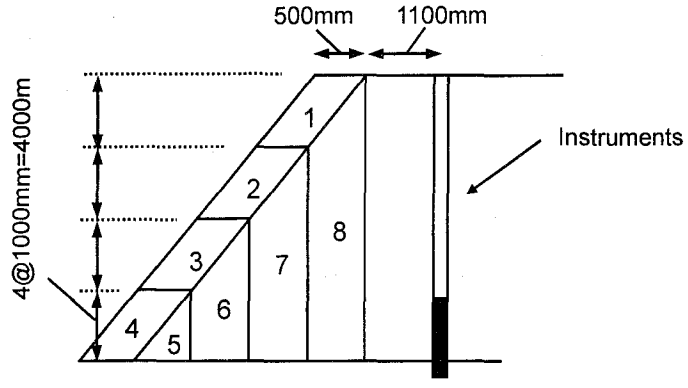

Fig. 3-41 Cutting procedure

3.6.2 Results and discussion

Fig. 3-42 shows the estimated displacement in the X direction by FODD and the gauge pipe, respectively. In this figure, "transit" means the displacement of the FODD head measured by the transit at step 8. Note that the displacements of only steps 7 and 8 are illustrated since the movement of the embankment did not occur clearly until step 6. Note also that both estimated displacements are obtained using polynomial approximation. It is found from this figure that at step 7, the displacement of FODD is

slightly smaller than that of the pipe, but at step 8 they agreed with each other as well as the value of transit. These observations may be attributed to the fact that at step 7 the occurred displacement is too small, such as 0.1 mm, to be detected but at step 8 the embankment moved up to 4mm, which can be detected. Finally, the drag shovel hit the instruments and broke them after step 8. FODD measured the displacement just before the incident, and **Fig. 3-43** shows the displacement after step 8. At this stage, cutting face is so close to the instruments that the ground movement around FODD is different from that around the pipe gauge. One can see that the displacements of the gauge pipe are larger than those of FODD and both displacements are independent. It can be also said that the FODD and the gauge pipe moved forward first, then is pushed backward at the top area by the shovel.

Although the movement of the embankment itself is quite small and could not be estimated exactly, FODD and the gauge pipe can estimate the displacement using FODD algorithms. To evaluate the accuracy of the instrument, further experiments using actual-sized ground movement are required.

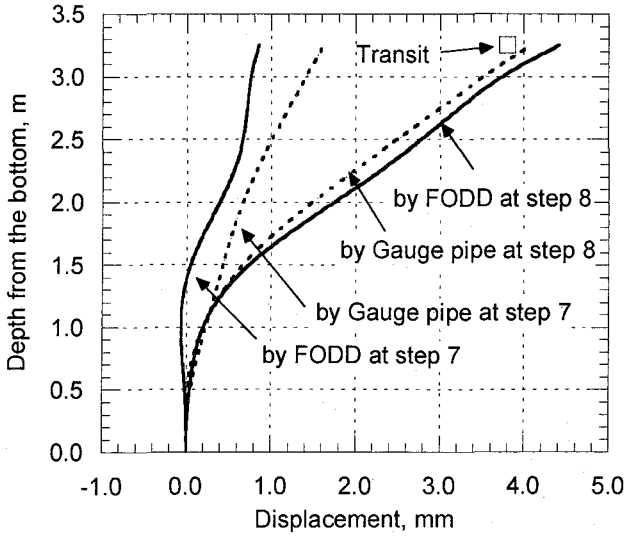

Fig. 3-42 Estimated displacement in the X direction by FODD and the gauge pipe

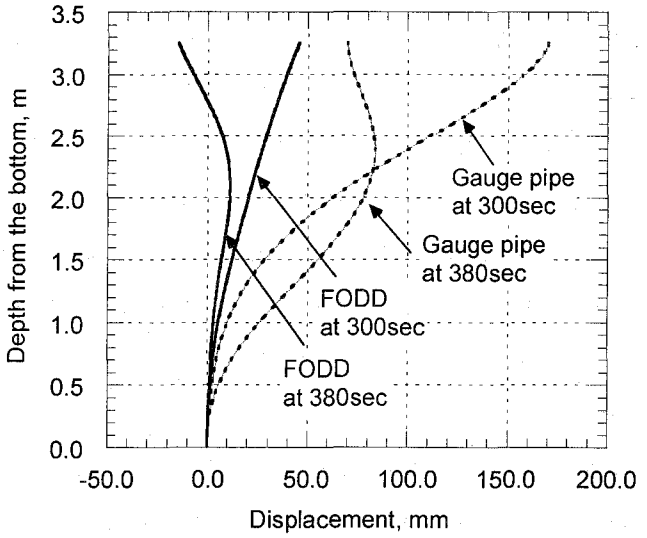

Fig. 3-43 Estimated the displacement after step 8

3.7 Summary of Chapter 3

To evaluate the FODD system, including the displacement transformation algorithm, the numerical analyses, material tests, and measurement test are conducted.

First, for the purpose of evaluating accuracy, the displacement estimation is conducted using spline interpolation and polynomial approximation for the fitting, assuming 8 curvature distributions and 10 sensor arrangements for the 20m FODD.

As a result, for uniform arrangement, it is found that though there is no significant difference between the two algorithms, the spline interpolation with many sensors may be preferable for random distribution.

For non-uniform arrangement, the accuracy of the estimation may increase by installing more nodes in the former section and also using the spline interpolation. But the uniform arrangement may give higher accuracy than the non-uniform arrangement.

Thus if FODD is applied to random curvature distribution, the uniform arrangement of as many sensors as possible may be preferable using the spline interpolation. Note that for almost all cases, an increase in maximum displacement may decrease the estimation accuracy if the accuracy is defined as standard

deviation.

Next, to calibrate FODD, fundamental and unit testing, including material test, bending test and site test, are carried out. From the fundamental test, FBG is found capable of measuring the strain of vinyl chloride material as well as resistive gauges. The unit test results showed that the FODD unit can estimate the displacement within about 6.7 % errors using strain data by FBG sensors. Finally, as a result of the site test, it is confirmed that although FODD system can estimate the displacement. But additional measurement tests should be required since the displacement is not large enough to evaluate the accuracy of FODD.

Chapter 4 Monitoring system configurations

4.1 General remarks

FBG sensors have been evaluated and applied for various measurements so far. The past researches on FBG sensor can be roughly divided into two categories; elemental and practical. The elemental researches in general focused on the sensor phenomena or the measurement principle without much consideration of practical problems. On the other hand, in practical researches, the applications of the sensors are reported but few of them described the system requirement in detail such as electricity, cable length, light intensity, transmission loss, etc. However, these essential properties should be evaluated when the monitoring systems using FBG sensors are practically applied. These requirements depend on the demodulation system for FBG sensors. Of course, there are various demodulation systems, but Fabry-Perot tunable filter demodulation system has been used widely and become one of the reliable systems for the FBG measurement. FBG-IS system is a commercial system based on the FFP tunable filter, produced by Micron Optics Inc. Though the stability of this system is guaranteed by the maker, the system may be used under harsh environment beyond the maker's expectations.

Thus in this chapter, the FBG-IS system (#3137 Version 3.3) is evaluated by several tests including voltage stability, temperature stability, transmission loss stability, multiplexing combination loss stability, etc. In addition, the influence of the bonding condition on the measurement is also evaluated. Then, considering the system requirements such as optical loss evaluation, an all-purpose monitoring system is configured.

Table 4-1 Specification of FBG-IS

Wavelength rang	1530-1570nm
Optical Power	-55dB
Dynamic range	12dB
Optical loss limit	6dB
Resolution	<1pm
Scan frequency	52.4Hz
Minimum FBG space	0.5nm
Power supply	95-135VAC
Operating temperature	10.0-40.0°C

4.2 Fabry-Perot tunable filter demodulation system (FBG-IS system)

Several approaches have been proposed for the demodulation system recently, including passive spectral ratiometric demodulation, tunable narrowband filter demodulation, interferometric-based demodulation, etc. Fabry-Perot tunable filter demodulation belongs to tunable narrowband filter demodulations which use tunable filter to detect the center wavelength of FBG. As shown in **Fig. 4-1**, the system scans the Fabry-Perot filter that moves the optical length periodically using PZE so as to find the peak intensity of the reflected light. The system can find the peak intensity at high frequency since it periodically applies the triangle voltage to the PZE, as shown in **Fig. 4-2**. The center wavelength corresponds to the optical length when detector finds the peak intensity. In the FBG-IS system, based on the FFP tunable filter, the system controls voltage and light source power to find the peak wavelength clearly.

Note that the system herein includes FBG-IS unit and control PC with NI-DAQ. **Table 4-1** shows the specification of FBG-IS system. The maker guarantees the stability under the condition as described in the table, but the detailed stability and performance must be clear for practical applications.

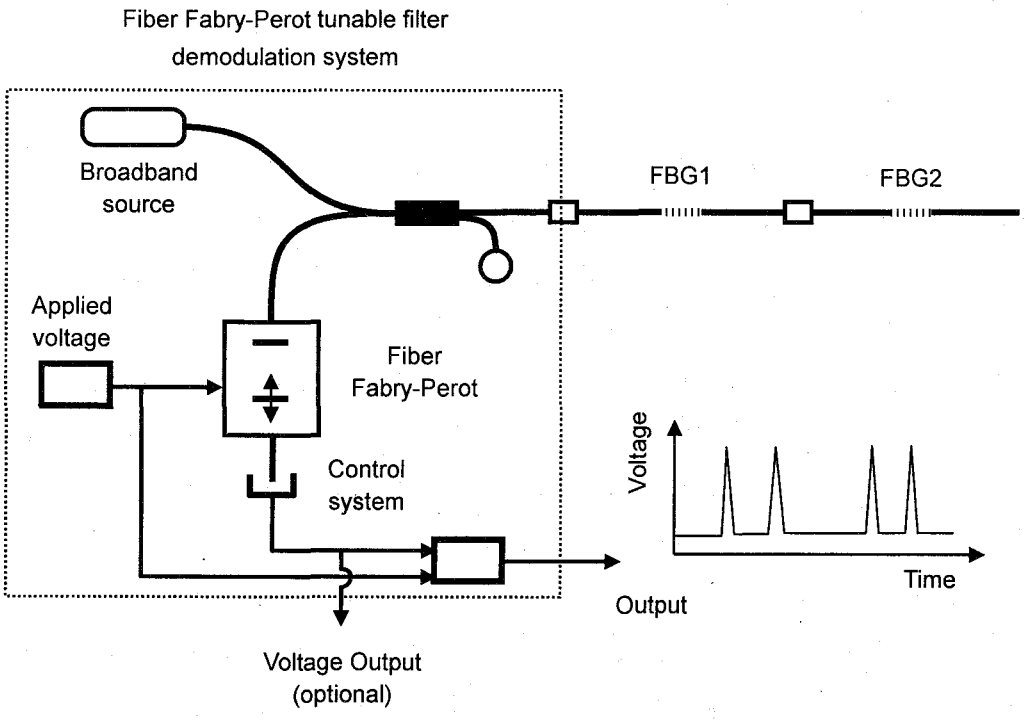

Fig. 4-1 Fiber Fabry-Perot tunable filter demodulation system

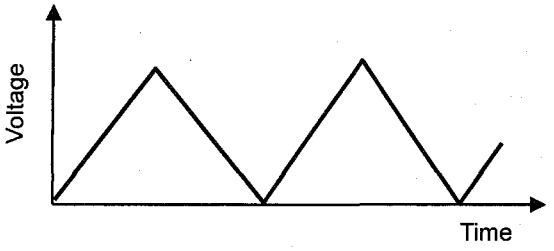

Fig. 4-2 Applied voltage

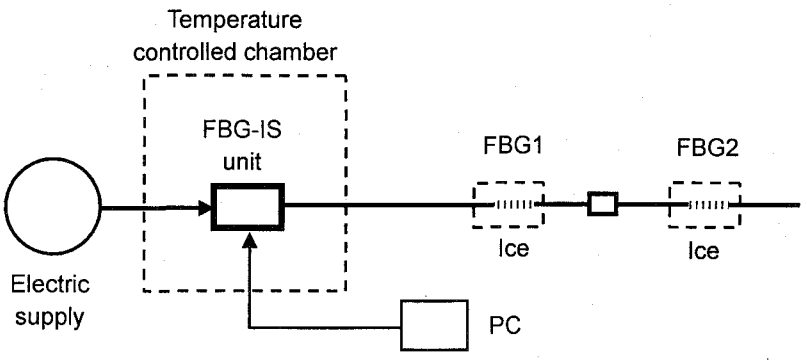

Fig. 4-3 Setup for environmental test

4.3 Environmental tests on FBG-IS unit

4.3.1 Test setup

First, the temperature and voltage stability of this unit is evaluated. In this test, two FBG sensors with a Bragg wavelength of 1533.5±1 (1533.4) and 1555.0±1 (1554.7) nm are used. Each of them is fabricated in one optical fiber having a cladding diameter of 125μm and a UV-coating of 250μm.

In the temperature stability test, FBG-IS unit is set in the chamber room and heated from 5.0 to 45.0°C, while the sensors are frozen in the ice so as to keep a temperature of 0.0°C, as shown in **Fig.4-3**. Note that the maker guarantees the stability under the temperature ranging from 10.0 to 40.0°C, but it is possible that the temperature may go down below 10.0°C due to the harsh environment of the site.

Next, to evaluate the stability against the fluctuation of supplied power, the unit is powered by the electricity ranging from 85.6 to 110.0VAC to detect five FBG sensors having a Bragg wavelength of 1533.5±1, 1541.5±1, 1551.0±1, 1557.5±1, and 1563.5±1nm, respectively. Note that the sensor element is free at a temperature of 23.0°C.

4.3.2 Results and discussion

Fig. 4-4 shows the output values of stain in temperature test ranging from 5.0 to 45.0°C. Note that each value denotes the average of 10 samplings at each condition and all data are initialized to 0μ at 25.0°C. From this figure, it is found that the fluctuation of the output strain is within 20μ, though the amplitude depended on the Bragg wavelength. This small fluctuation may be caused by the FBG installed inside the unit for the reference to determine the wavelength, which may be slightly influenced by the temperature change.

Accordingly, this FBG-IS system may have stability in a range from -10.0 to 45.0°C to some extend, but it is possible that about 20μ error will occur due to the temperature change of 50.0°C.

Fig. 4-5 shows the output strain while the power supply voltage varied from 85.6 to 110.0VAC. From this figure it is found that from 86.0 to 110.0V the fluctuation is quite small, though the output becomes unstable below a voltage of 85.6VAC. Note

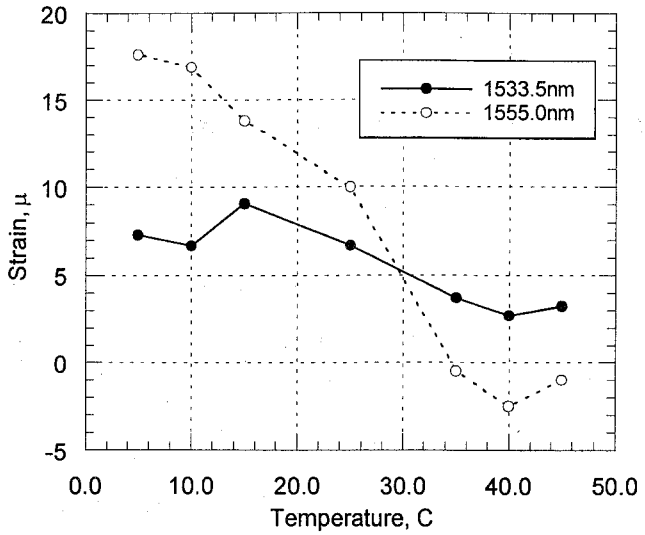

Fig. 4-4 Temperature stability of FBG-IS unit

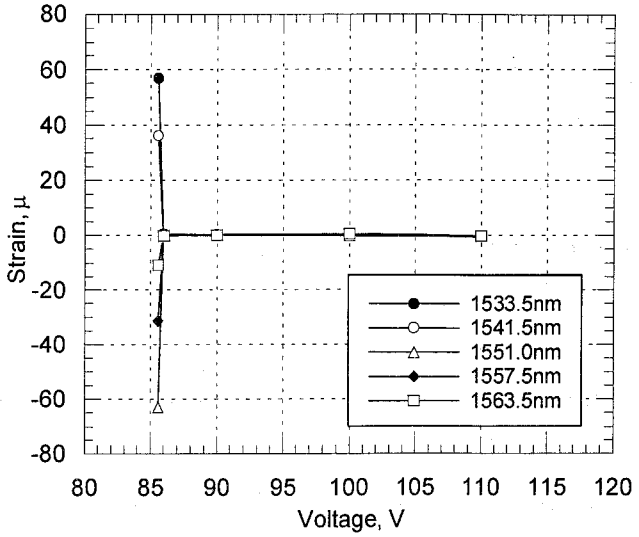

Fig. 4-5 Voltage stability of FBG-IS unit

that the unit still worked after the voltage went below a voltage of 86.0VAC. It can be said that the power supply should be kept from 90.0 to 130.0VAC for the stable measurement; otherwise the output becomes unstable thought the unit still works.

4.4 Stability evaluation against transmission loss

4.4.1 Test setup

In this section, the bending loss of a transmission optical fiber between FBG-IS and FBG sensor is evaluated. Two FBG sensors used in this test are fabricated in a single-mode fiber having a diameter of 125μm (cladding) and 250μm (UV-coating) respectively. Their Bragg wavelength are 1533.5±1 (1533.4) and 1550.0±1 (1554.7) nm, respectively, and two sensors are connected by splicing connector. The temperature around the sensors is set to 23.0°C and the tested length is 5.0m. Test series are shown in **Fig. 4-6**. In Series 1, in order to evaluate the bending influence, the optical fiber is rolled once in five different radiuses such as 6.5, 9.0, 10.0, 24.0, and 32.0mm. In Series 2, the optical fiber is rolled from once to 12 times in three different rotation radiuses such as 10.0, 24.0 and 32.0mm, respectively, in order to evaluate the influence of the loop number on the measurement. Finally, Series 3, the fiber is twisted from once to four times over 150.0mm long, to evaluate the influence of the twisting.

4.4.2 Results and discussions

(1) Series 1

Fig. 4-7 shows the values of output strain and output voltage of the unit, varying the curvature radius of the loop. Note that the output voltage herein can be thought to represent the light power of the reflected light from FBG sensor. Thus, for instance, if the voltage becomes lower, the power of the detected light may become lower. Unfortunately this voltage can not be described using dBm, i.e., absolute optical power, since the voltage is not designed to indicate the absolute optical power, but to intrinsically control the system.

From this figure, it is found that the output voltage of two wavelength are

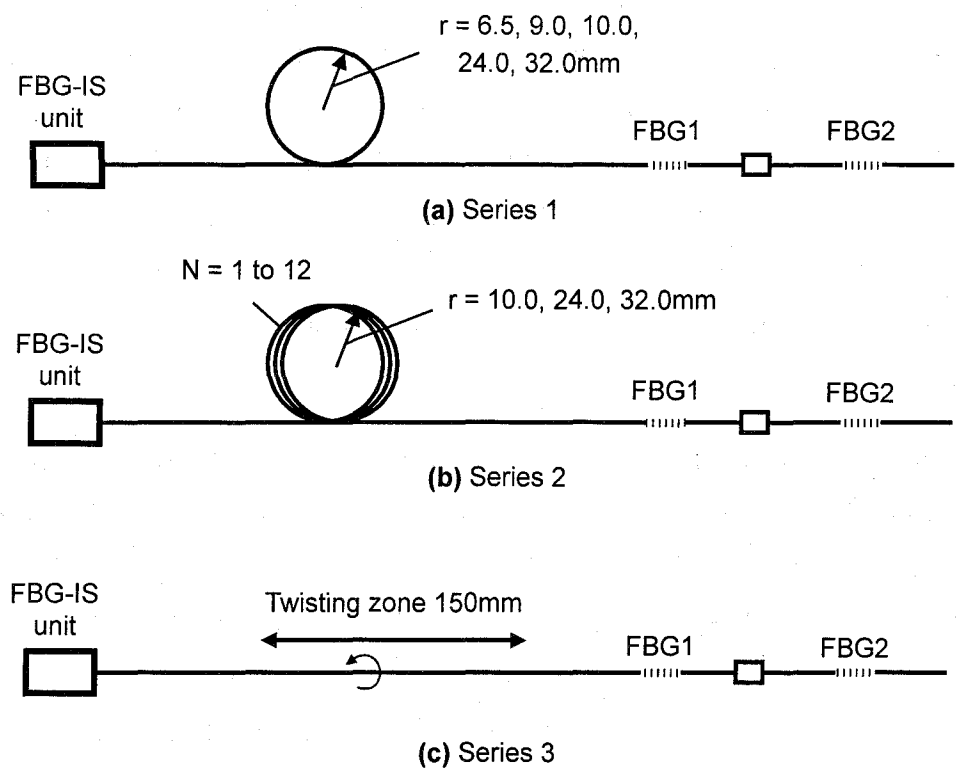

Fig. 4-6 Test series for transmission loss evaluation

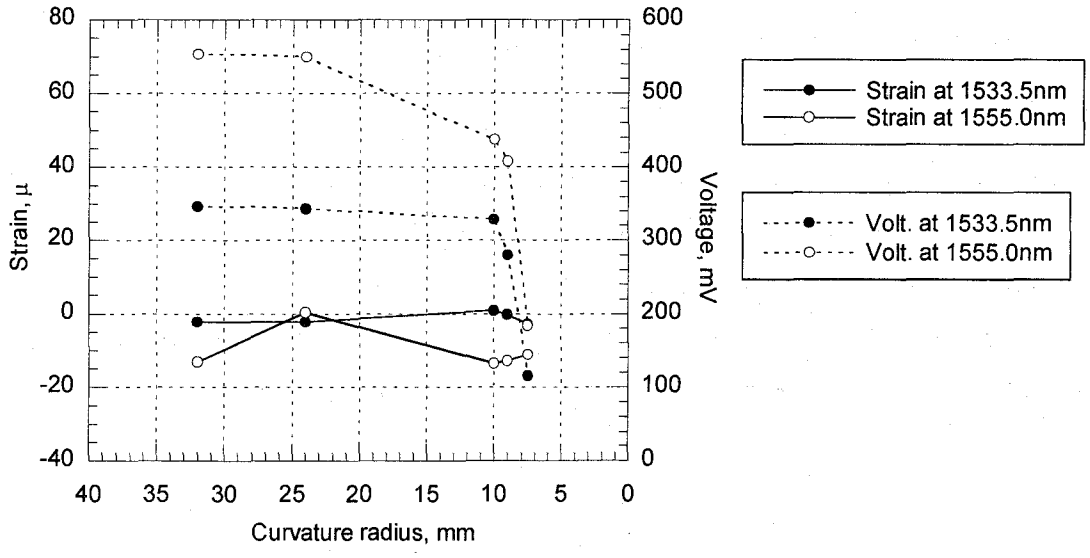

Fig. 4-7 Output vs. curvature radius

initially different from each other. This initial difference may be attributed to the connector loss between the sensors. Though the voltage went down rapidly after the curvature reached 10.0mm, the output strain remained stable. It can be said that the optical loss might be less than 6dB even when the light experienced a curvature radius of 6.5mm, because the loss limitation for the unit is 6dB. But it is possible that if the input power becomes lower, even the curvature radius of less than 20mm may cause the unstable measurement. Thus, the optical fiber should evade less than 20.0mm curvature radius for the stable measurement.

(2) Series 2

Second, in order to evaluate the influence of the number of loops of optical fibers on each output, the fibers are rolled up from once to 12 times with three different curvatures, respectively. The output strain and output voltage in 32.0, 24.0, and 10.0mm curvature radius are shown in **Fig. 4-8**, **Fig. 4-9** and **Fig. 4-10**, respectively. It is found from these figures that the output strain or output voltage remained stable if the fiber rolled with a curvature radius of 32.0 or 24.0mm. However, when the fiber is rolled up with a curvature radius of 10.0mm, the voltage decreases as the number of loop increases. Additionally, the decrease ratio depended on the wavelength; the output voltage at 1550.0nm decreases faster than that at 1533.5nm. In contrast to the output voltage, the output strain remained stable except at the loop number of 12. Thus it can be also said that the optical loss mainly depend on the curvature radius and on the wavelength, not on the loop number.

(3) Series 3

The influence of twisting number of the optical fiber on the output is evaluated. **Fig. 4-11** shows the each output of the unit when the fiber is twisted. Though the initial output voltage differed from each wavelength, the output strain remained stable. This may be attributed to the symmetric structure of the optical fiber. It can be said that the influence of the twisting fiber may be smaller than that of bending.

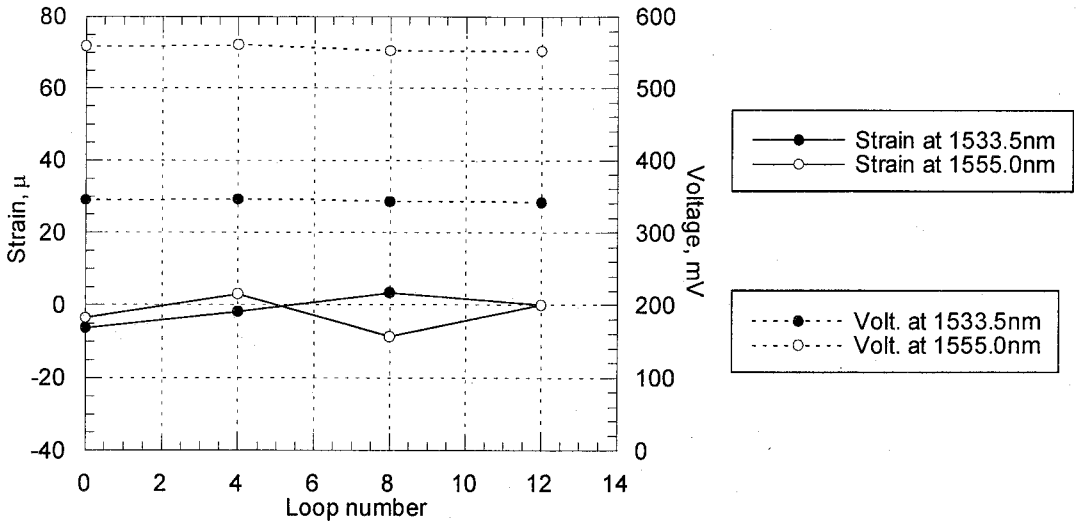

Fig. 4-8 Output vs. loop number at radius = 32mm

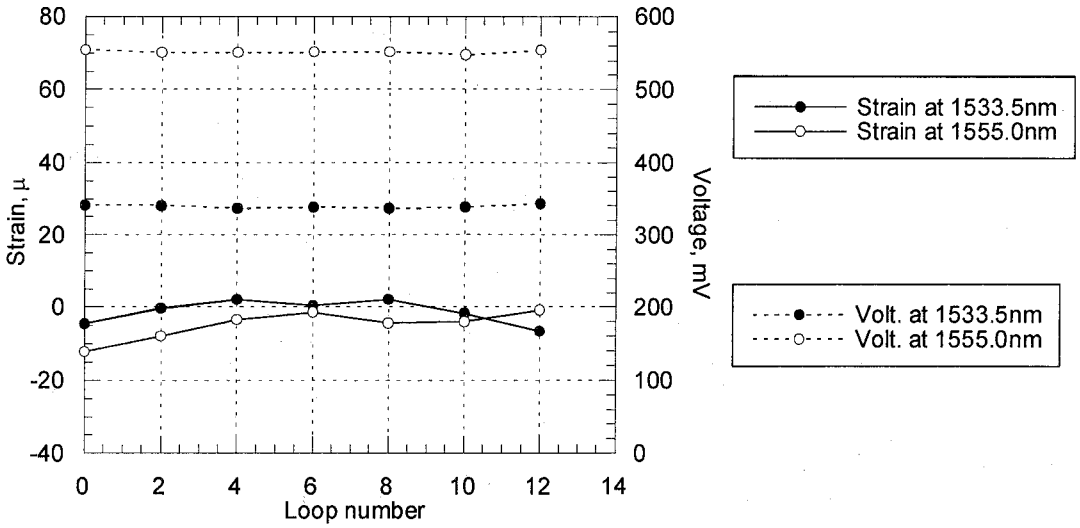

Fig. 4-9 Output vs. loop number at radius = 24mm

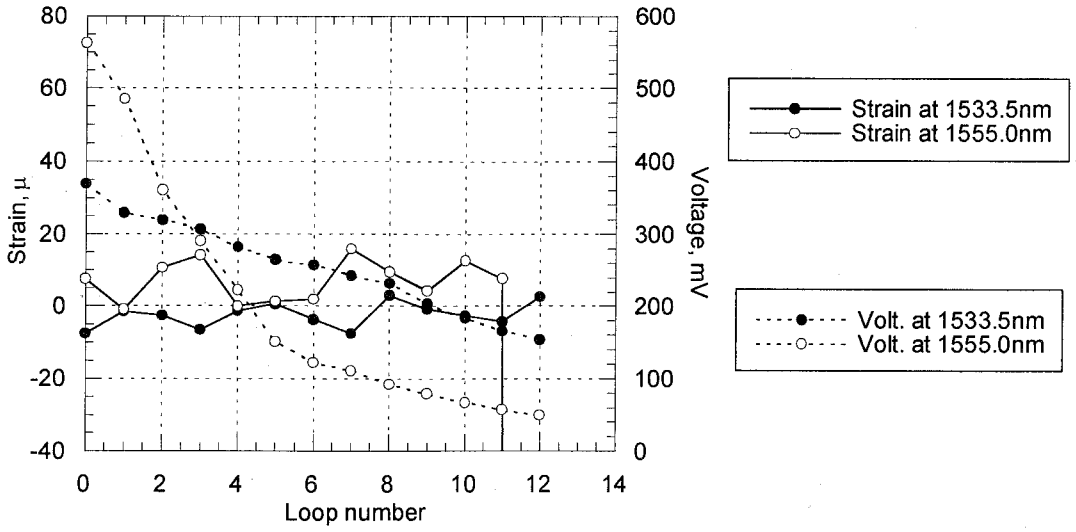

Fig. 4-10 Output vs. loop number at radius = 10mm

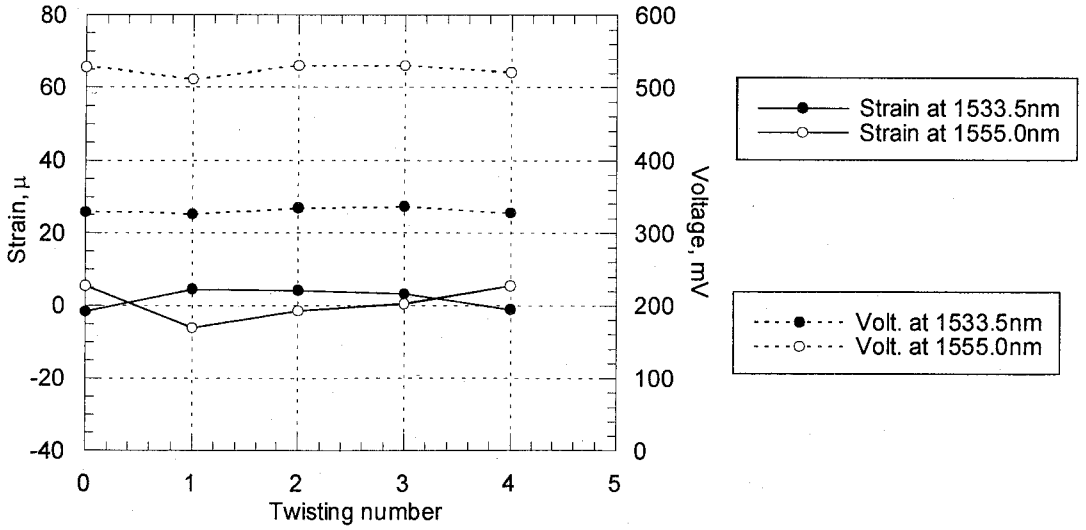

Fig. 4-11 Output vs. twisting number

4.5 Multiplexing loss evaluation

4.5.1 Target of this section

As mentioned before, FBG sensor can be arrayed in one optical fiber, which is called multiplexing. The optical fiber with sensors should be inevitably connected to each other using physical connectors or by splicing method. Once the FBG sensor is made within the fiber, the sensor can not be removed or reinstalled within the fiber. Moreover, it is difficult to determine the number or location of the sensors beforehand. From the point of view of economy or convenience for use, it should be better to fabricate one sensor within one fiber and then connect each other so as to make arrays of sensor. Therefore, in this section, the optical loss that may occur in multiplexing instruments such as connectors or light dump is evaluated.

4.5.2 Test setup

In this test, two FBG sensors with a wavelength of 1542.0nm (λ_1) and 1563.0nm (λ_2) are used. Light source equipment is FiberLabs ASE-FL7004 that can produce a broadband source in range of 1530.0nm to 1610.0nm, and the spectrum analyzer is ADVANTEST Q8384 as shown in **Fig. 4-12**. In this test, FC connector and two kinds

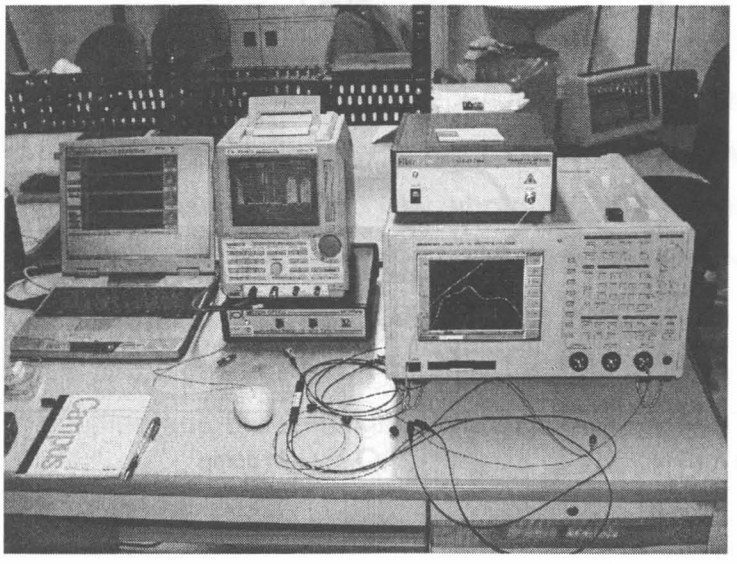

Fig. 4-12 Layout of the system used in the test

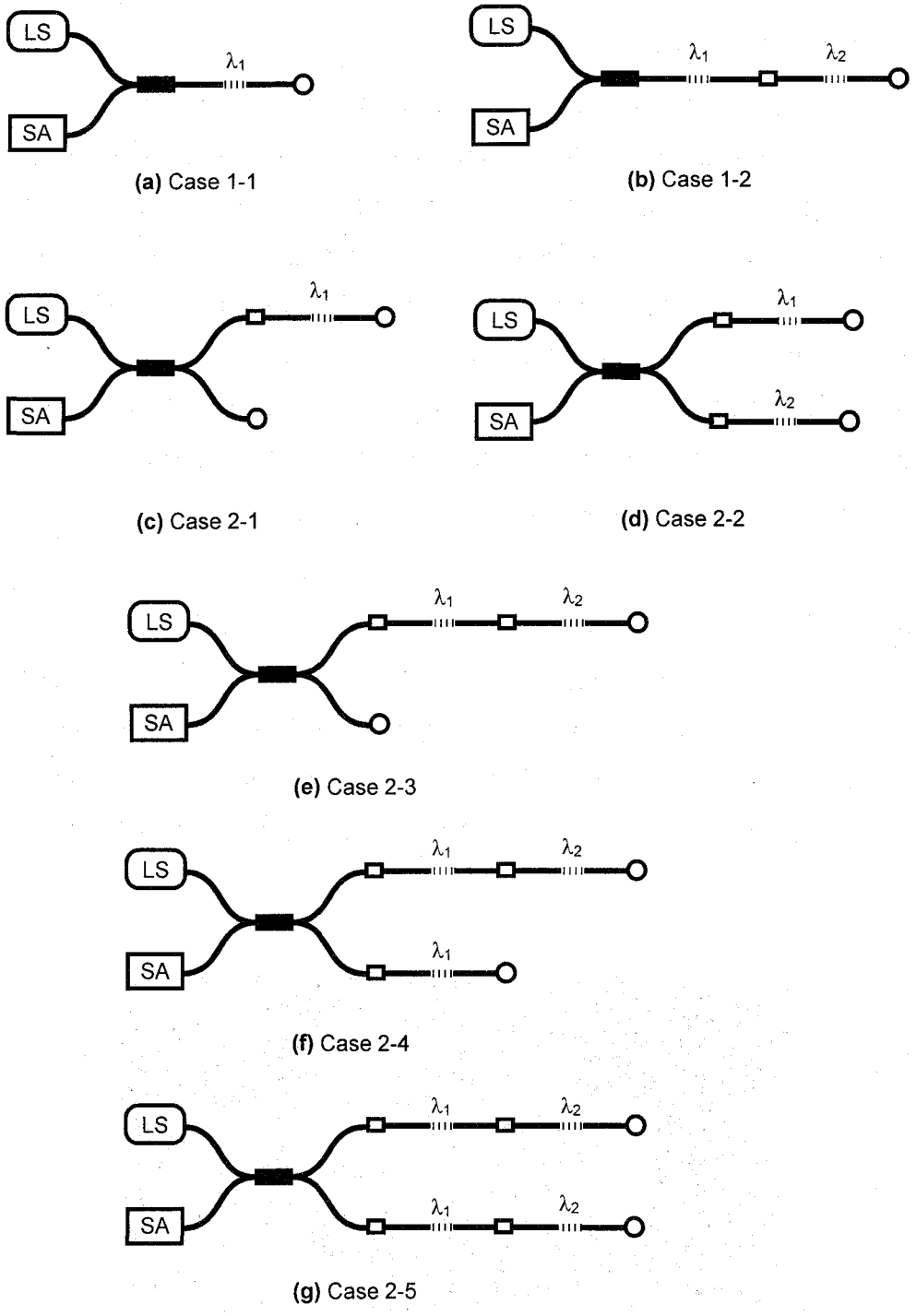

Fig. 4-13 Combination case

Table 4-2 Optical power of FBG reflective light (dBm)

Case	1542.0nm (λ_1)			1563.0nm (λ_2)		
	Dump	Non-dump	Difference	Dump	Non-dump	Difference
1-1	-25.498	-25.548	-0.050	-	-	-
1-2	-25.415	-25.466	-0.051	-28.750	-28.789	-0.039
2-1	-25.662	-25.454	+0.208	-	-	-
2-2	-25.814	-25.778	+0.036	-28.047	-27.933	+0.114
2-3	-25.587	-25.369	+0.218	-29.069	-28.887	+0.182

of 3dB coupler are used. **Fig. 4-13** shows the possible combinations using 2 sensors and one coupler. In case 1-x, a three-port coupler is used while in case 2-x a four-port coupler is used. Note that the light dump is intended to avoid the Fresnel reflection from the end of the optical fiber.

4.5.3 Results and discussion

Fig. 4-14 to **Fig. 4-21** shows the reflectivity of each sensor in Case 1-1 to 2-5 with or without dump, respectively. **Table 4-2** also shows the power level of the peak wavelengths in each spectrum. From these figures and table, it is found that though the dump did not have significant influence on the spectrum, it caused a quite small decrease in the reflectivity except the Bragg wavelengths. As for the reflectivity of Bragg wavelength, the effect of the dump depended on the wavelength and the coupler type; in case of 3-port coupler, the dump increases the power level at λ_1 by about 0.05dB, while it increases that at λ_2 by about 0.04dB. As opposed to those cases, in case of 4-port coupler, the dump decreases the power level at λ_1 by about 0.1dB, while it decreases that at λ_2 by about 0.2dB. This increase may be attributed to the fact that in contrast to the case of 3-port coupler, the light propagated and split into two fibers in 4-port coupler, and the split light including Bragg wavelength is reflected at the end of the other fiber with no sensor, and then detected. Thus, it can be said that the dump may improve in clear peak though the intensity may not increase.

On the other hand, from **Fig. 4-19** and **Fig. 4-21**, both of which describes the spectrum around λ_2 but differs in the presence of the connector, it is found that the

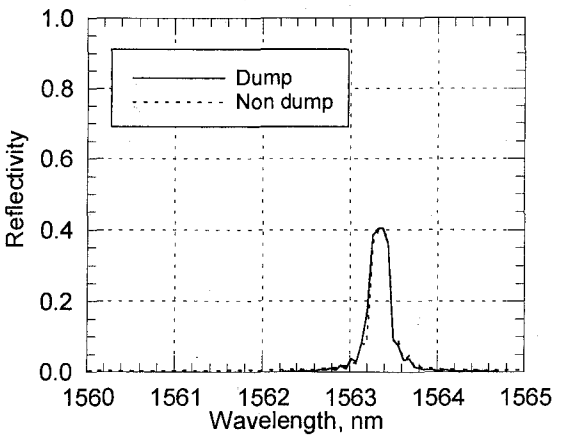

Fig. 4-14 Spectra of Case 1-1 around λ_1

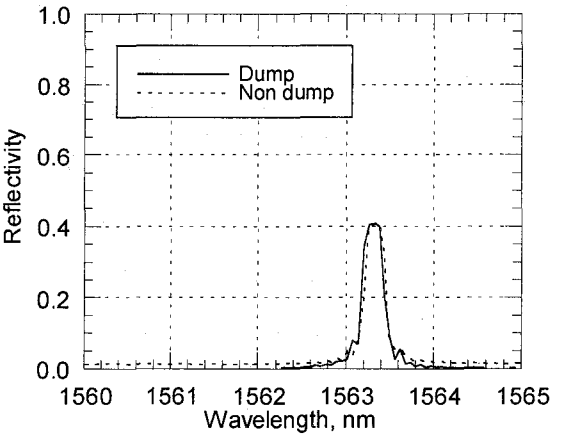

Fig. 4-15 Spectra of Case 1-2 around λ_1

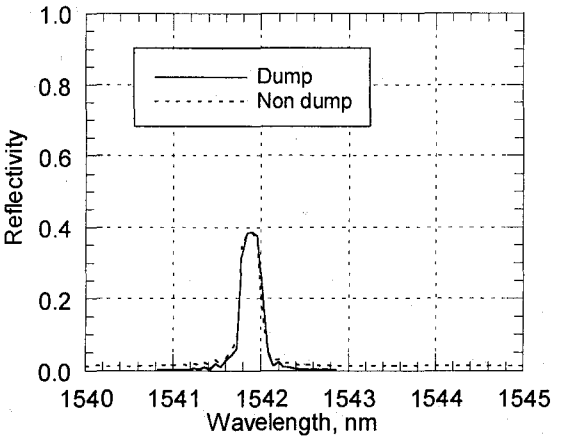

Fig. 4-16 Spectra of Case 1-2 around λ_2

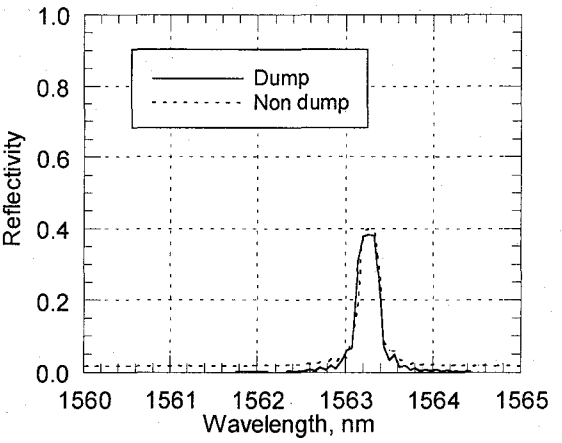

Fig. 4-17 Spectra of Case 2-1 around λ_1

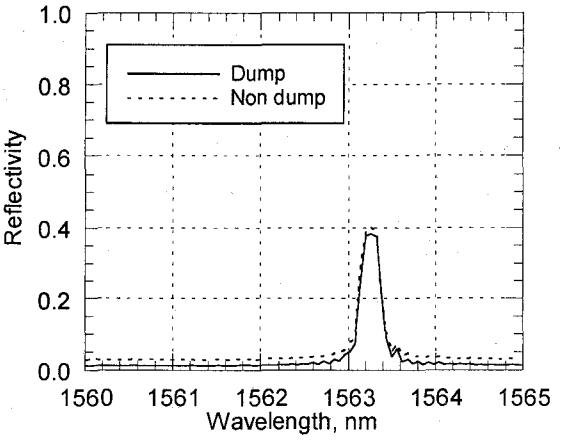

Fig. 4-18 Spectra of Case 2-2 around λ_1

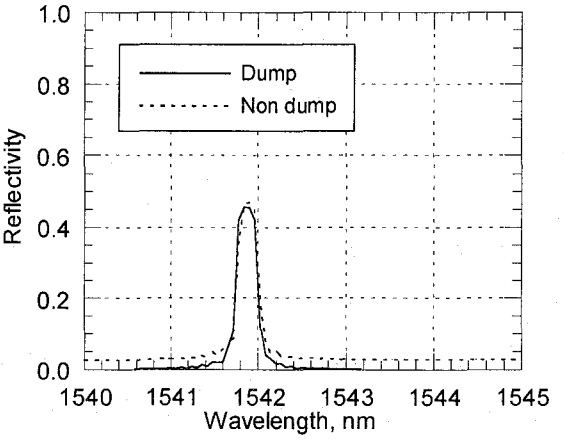

Fig. 4-19 Spectra of Case 2-2 around λ_2

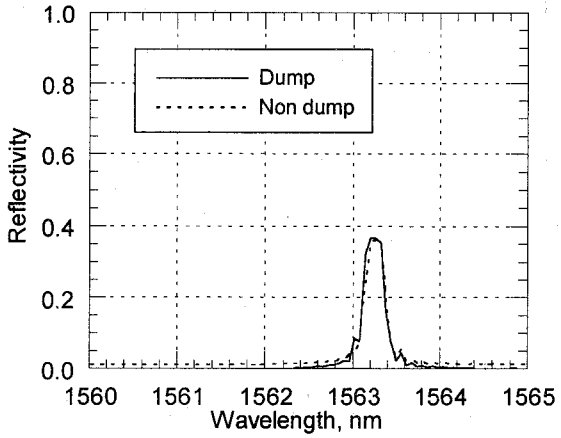

Fig. 4-20 Spectra of Case 2-3 around λ_1

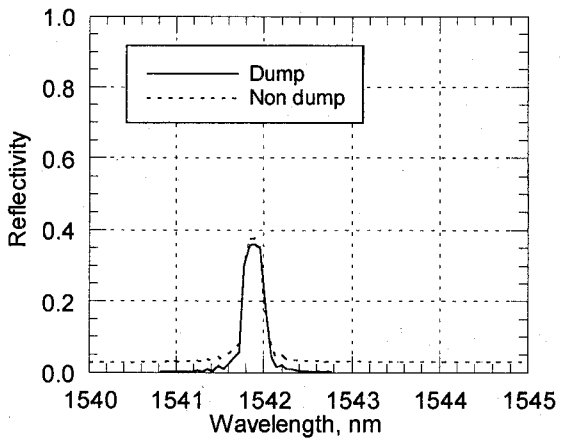

Fig. 4-21 Spectra of Case 2-3 around λ_2

presence of the connector decreases the reflectivity by 5.6%, which is almost equal to 0.23dB. Thus the optical loss of one connector may not be significant but too many connectors use such as 12 should be avoided since the loss limit becomes 6dB. Note that in general the connector loss may 0.5 -1.0dB.

4.6 Bonding test

4.6.1 Target of this section

As mentioned in Chapter 2, the accuracy of FBG sensors may depend on the strain distribution along the sensing part. In general, often the sensor may not completely be attached to the host structure. Thus in this section, in order to evaluate the influence of the bonding condition between the host structure and the sensor, a loading test is carried out on the cantilever that FBG sensor is attached on partially as well as perfectly.

4.6.2 Test setup

In this test, two kind of bond condition are assumed: partial bonding and total bonding. As shown in **Fig. 4-22**, the partial bonding indicates the case that a half sensing part

of FBG sensor, i.e. 5mm, is bonded on the host structure leaving the other part free, while the total bonding indicates the case that FBG sensor is bonded on the structure perfectly. In each case the aluminum plate having 250mm length, 30mm width and 3mm thickness, is used for the host structure. **Fig. 4-23** illustrates the host structure and the arrangement of the sensors including gauges. The load is applied at the end of the plate step by step; at each step 4.9N is applied and totally 14.7N is applied.

4.6.3 Results and discussion

Fig. 4-24 and **Fig. 4-25** illustrate the strain values of total bonding and partial bonding at each step, respectively. In these figures SA indicates the value of FBG sensor that is detected by spectrum analyzer, IS indicates the value of FBG sensor by FBG-IS system, and Gauge indicates the average value of five strain gauges. As for total bonding, the values of IS and Gauge agreed well with each other, while those of SA slightly differed from the others. This difference may be caused by the accuracy of spectrum analyzer that can detect the optical power with 10.0 pm accuracy, which is 10 times larger than that of IS. However as for partial bonding, both the values of IS and SA differed from those of Gauge, though they agreed with each other. It is found that the difference of the strain values between the gauge and FBG including IS and SA become about 100μ. Note that for partial bonding the spectrum is split into two peaks since the partial bonding resulted in the two grating parts as will be shown later, and thus the values of IS and SA are obtained by detecting the difference between two peaks.

Fig. 4-26 and **Fig. 4-27** show the spectra of reflected light in partial and total bonding, respectively. Note that these spectra are measured by spectrum analyzer. From **Fig. 4-26**, it is found that clear peaks existed in the spectra though the width of the peak becomes slightly wider as the load increases, which may be caused by the increase of strain gradient. The strain distribution in this case is not constant since the moment distribution formed triangle shape. On the other hand, from **Fig. 4-27**, it is found that the peak split as the load increases. The peak of shorter wavelength may represent the free section, while the other peak may represent the bonded section. Thus, as the load increases, the peak of longer wavelength shifts in the direction of long wavelength. Additionally, the reflectivity of the peak of longer wavelength decreases with the load. This may be attributed to the fact that the bonded part is

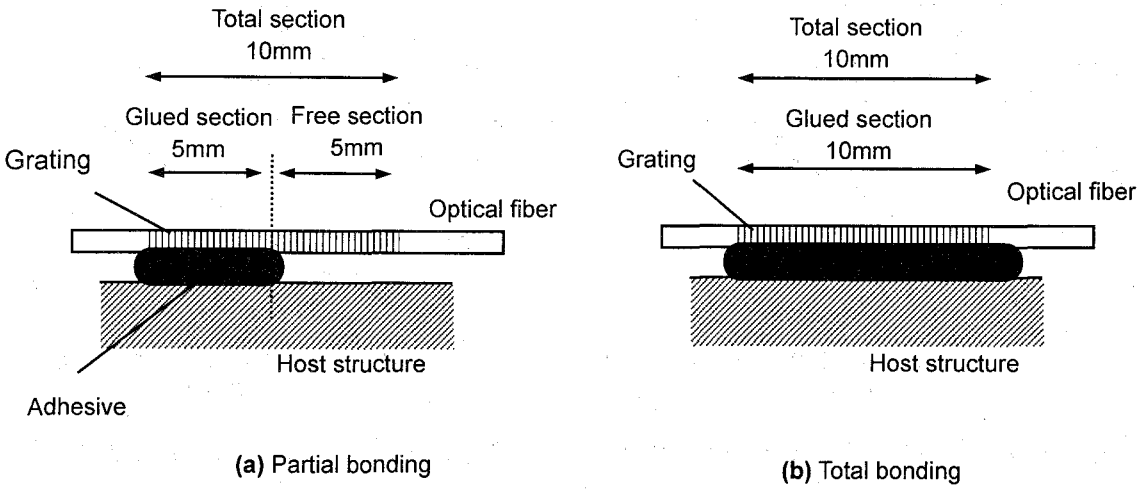

Fig. 4-22 Bond type assumed in the test

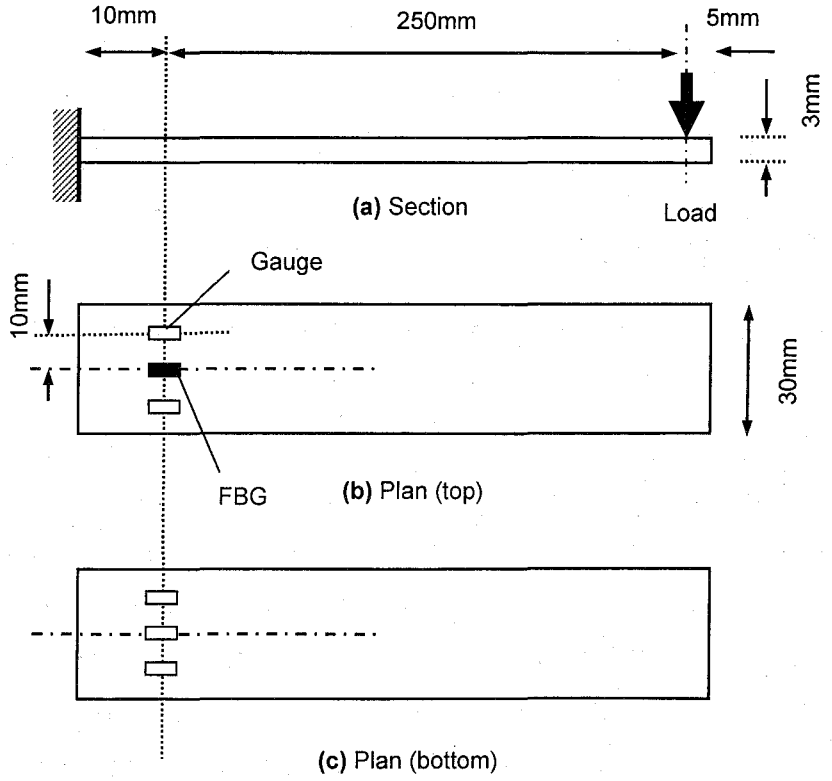

Fig. 4-23 Test setup for the bonding test

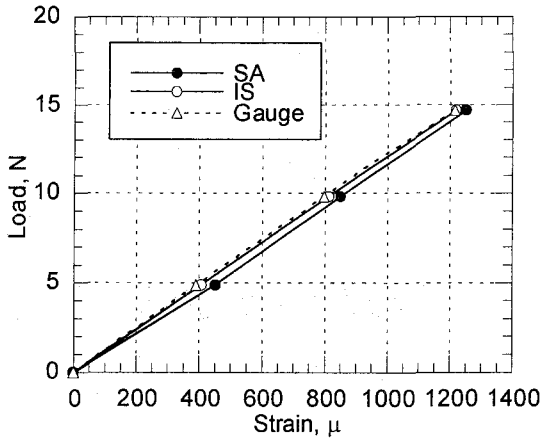

Fig. 4-24 Strain-load relationship of total bonding

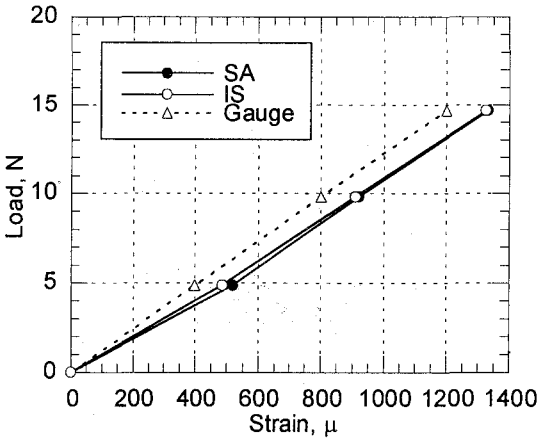

Fig. 4-25 Strain-load relationship of partial bonding

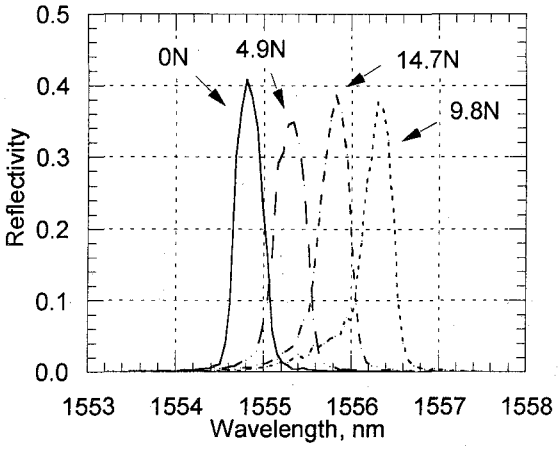

Fig. 4-26 Spectra of total bonding

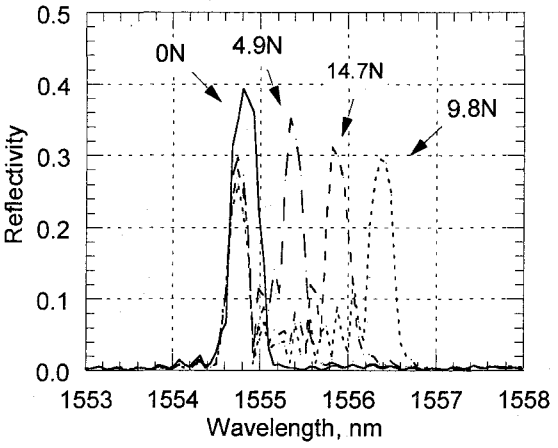

Fig. 4-27 Spectra of partial bonding

subject to the large strain gradient and the rapid strain change from free section to bonded section may cause a decrease in the reflectivity. Therefore, the partial bonding may cause significant errors in the measurement, and these errors can not be detected by FBG-IS system since it can not evaluate the shape of the spectrum.

Note that free section may be subject to only temperature change, while the bonded section may be subject to both strain and temperature change. Thus, by subtracting the value of longer wavelength peak from that of shorter one, the temperature compensation may be attained, as described in Chapter 1. However, in

this case if the half sensing section is used for temperature compensation, the reflectivity of the reflected light may decrease 50% comparing with the normal use, because the total length of sensing part is 10.0mm and the sensing part having a length of 5.0mm can produce only a half reflectivity. Moreover, if the strain change is small it is difficult to distinguish the values of shorter and longer wavelength peaks. Thus, this mechanism may not be appropriate for the temperature compensation method.

4.7 System configuration for monitoring

4.7.1 Target of this section

The transducers based on the FBG sensor such as gauge, inclinometer, pressure meter, displacement meter, etc., have been proposed recently and It becomes much important to build the practical configuration considering the optical loss associated with sensor arrays. If these FBG-based instruments are connected to the interrogation system without any consideration of optical loss, it is possible that the measurement becomes unstable due to the optical loss. FBG-IS system has some limitation in the sensor arrays and multiplexing due to the optical loss and dynamic range. Thus, in this section the system requirements for the stable measurement are estimated and the monitoring system using FBG sensors and FBG-IS system is configured.

4.7.2 Maximum number of multiplexing

Using the equations of (B-33), (B-42) and (B-43), the half width, the reflectivity and the Bragg wavelength of the reflection, becomes 0.095nm, 93.5% and 1550.0nm respectively, when the average refractive index is 1.5, the refractive index vibration is 1.0×10^{-4}, the grating period is 517.0nm, and the sensor length is 10.0mm. Therefore, in order to recognize the Bragg wavelength, at least, wavelengths range of 0.095nm × 2 = 0.19nm should be required for one sensor. Thus, considering that the measurement-range of the FBG-IS system is 40.0nm (=1570.0nm - 1530.0nm), let Δ be the measurement range of each sensor in wavelength and N be the number of the sensor; Δ can be given by the following equation:

$$\Delta \times N + 0.19 \times N = 40.0 + 0.19 \quad (4.1)$$

i.e.,

$$\Delta = 40.0/N + 0.19/N - 0.19. \quad (4.2)$$

For instance, if 30 sensors are fabricated in one array, each range becomes 40.0/30 + 0.19/30 - 0.19 = 1.1496nm, i.e. 958μ. On the other hand, if only one sensor is to be detected in the system, theoretical maximum range of the sensor becomes 40.0nm, i.e., 33,333μ. However, practically, the possible number of sensors installed in one fiber using the FBG-IS system can be at most 10 due to some optical loss, according to the maker. Note that if using optical switch and parallel multiplexing arrangement, the FBG-IS system can detect more than 500 sensors.

4.7.3 Optical loss calculation

On the other hand, in general the transmission loss of the optical fiber is about 2.0dB/km, and the connection loss of FC and SC connector is about 0.5 -1.0dB as mentioned before. Now letting P_0, P_λ, L, β, d_C, N_C and N_P be the optical power of light source, the optical power of the reflected light from FBG sensor, the distance from the source to the sensor, the reflectivity of FBG sensor, the connector loss, the number of connector, and the number of coupler between the detector and sensor, respectively, P_λ can be given by the following equation:

$$P_\lambda = P_0 \times \beta + 2 \times N_C \times d_C + 2 \times N_P \times (-3.0) + 2 \times L \times (-2.0) \text{ [dB]}. \quad (4.3)$$

Note that N_C is more than or equal to N_P since one coupler needs one connector at least, which yields

$$N_P \leq N_C . \quad (4.4)$$

Additionally, assuming that the dynamic range of IS system is 12dB, the maximum and minimum detected optical power of the sensors should satisfy the following equation:

$$| P_{max} - P_{min} | < 12 \text{ [dB]} \quad (4.5)$$

where P_{max} and P_{min} are the maximum and minimum optical power. At the same time, provided that FBG-IS system uses the light source of -45.0dB, the minimum optical power should satisfy the following equation:

$$P_{min} \geq -51.0 \text{ [dB]}. \quad (4.6)$$

Therefore, because FBG-IS system includes at least one coupler, when the light source having -20.0dB is assumed to be used, the maximum use of transmission length, coupler and connector, can be given as follows:

(1) Maximum transmission length

Maximum transmission length can be obtained when the sensor is directly connected to the system. Thus, substituting 1 for N_P and N_C, -0.5dB and 0.935 for d_c and β, respectively, equation (4.3) and (4.6) yields the maximum transmission length, L_{max}, expressed as

$$L_{max} = (51.0 - 20\times0.935 - 0.5\times1\times2 - 2\times3.0\times1) / 4.0 = 6.325 \text{ [km]}. \quad (4.7)$$

Thus, the length of the network should be less than 6.325km.

(2) Maximum coupler number

For 10.0m optical fiber, using the above values and equation (4.3) and (4.6), the maximum number of the possible coupler can be given by

$$N_P = (51.0 - 20\times0.935 - 2\times0.5\times10^{-2}) / 7.0 = 4.6 \approx 4. \quad (4.8)$$

Thus, only 4 couplers can be used in one system for 10.0m optical fiber.

(3) Maximum connector number

For 10m long optical fiber, the maximum number of the connector of FC or SC can be given by

$$N_C = (51.0 - 20\times0.935 - 2.0\times3 - 2\times0.5\times10^{-2}) / 1.0 = 26.3 \approx 26. \quad (4.9)$$

Thus, for 10m optical fiber, the maximum connector number becomes 26.

Note that optical loss estimation should be required for each sensor configuration since the maximum numbers and length depends on the light source or the fiber properties.

4.7.4 System configuration

The monitoring system using optical sensors for all purpose is configured. **Fig. 4-28** shows the system configuration for site monitoring using optical sensors. In this figure, solid lines denote light transmission within the optical fiber, while chain lines and double chain lines denote electrical data transmission and electrical power resource, respectively.

In general, the monitoring system can be divided into three sub systems: sensor system, data acquisition system, control system.

The sensor system is a sensor network that should be arranged according to the optical loss calculation as described in previous section, so that the minimum optical intensity of the light reflected from the sensors is more than -56dB.

The data acquisition system indicates the station to operate the FBG-IS system, optical power supply, and other control units, which sits between the sensor system and control center. In this station, UPS system is installed for the power supply; uninterruptible power supply (UPS) is a device that sits between a power supply and devices such as computer or measurement units to prevent undesired features of the power sources including outages, sags, surges, bad harmonics, etc., from the supply from adversely affecting the performance of devices.

The data from the station is send to the control center, which consists of the data-base server, analysis unit, and telecommunication unit. The data stored in the data-base should be filtered using some trigger or converted into the physical values so as to reduce the data size, since the raw data are enormous and the disk space of the server becomes rapidly full if they are stored without any trigger. Thus, it is necessary and important to interpret and evaluate the data so as to obtain significant information, which depends on the monitoring applications. The administrator must be in the control center to evaluate the history or real-time information from the site. If the

information tells serious hazard, warnings or alarms should be sent to the sites from the control center.

Basically, this system configuration can be applied to kinds of monitoring by adjusting functions, such as the optical power or telecommunication device etc., with the optical loss estimation.

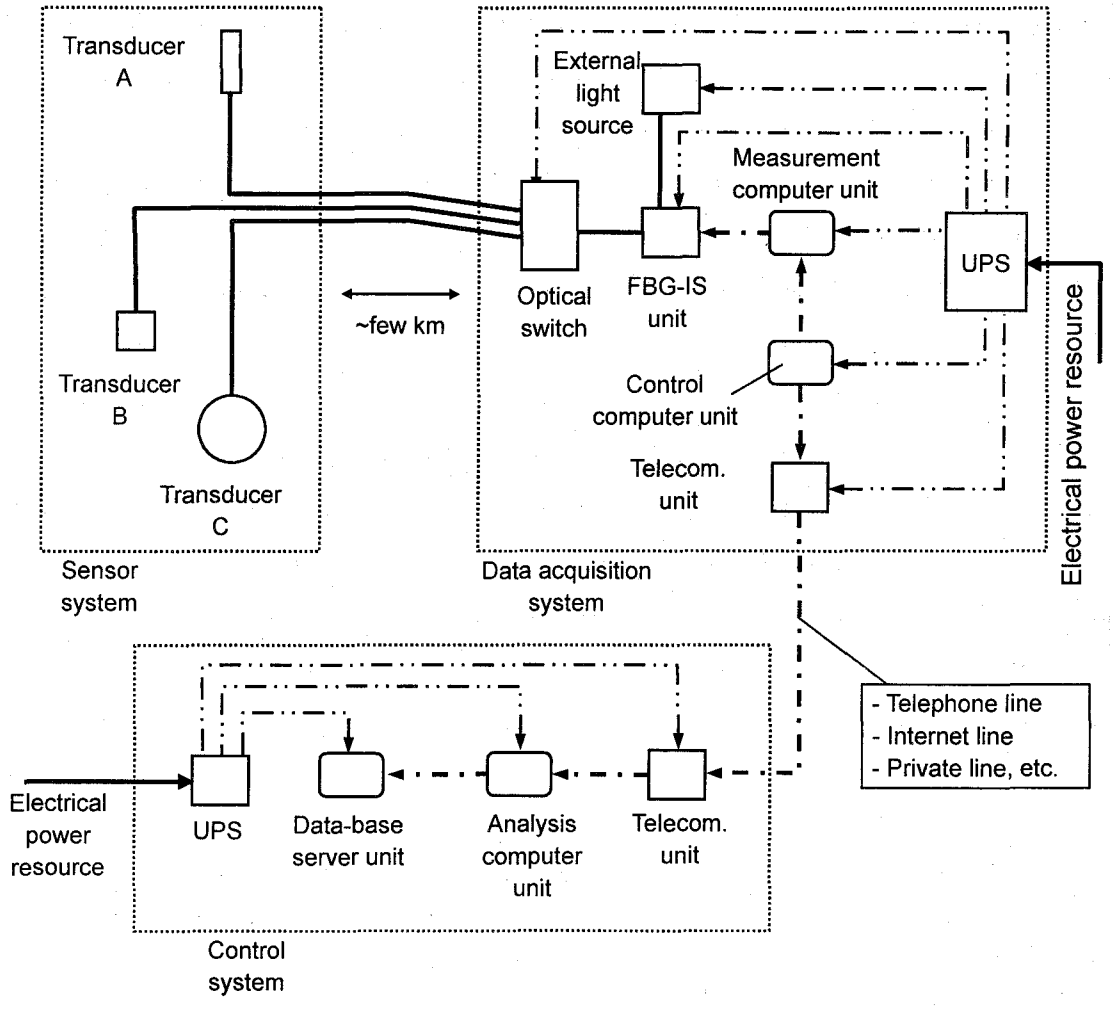

Fig. 4-28 All-purpose monitoring system configuration

4.8 Summary of Chapter 4

To evaluate the stability of FBG-IS system under harsh environment, several tests including temperature, voltage, optical loss and bonding test, are carried out. As a result, it is found that FBG-IS system requires stable power supply ranging from 86 to 110 V, and the temperature around the system should be constant, for the stable measurement. For the transmission fiber, it is found that the fiber should evade less than a curvature radius of 20mm and more than 12 loops, though the influence of the loop number on the measurement is smaller than that of curvature. In addition, twisting influence is quite small comparing with the other factors.

Next, the connection loss associated with multiplexing is evaluated. It is found that the light dump may sharpen the spectrum peak and the connection loss becomes 0.23dB. This connection loss should be considered when the sensors are arrayed in one fiber.

From the results of bonding test, it is found that the bond condition have quite large influence on the measurement. The imperfect bonding may cause multi-peaks in the spectrum that also may result in unstable measurement if using FBG-IS system.

Finally, considering the requirements for practical application, the monitoring system using optical fiber sensors is configured. When the system is configured, the optical loss evaluation such as connection loss and coupler loss should be required for each system configuration.

Chapter 5 Application study

5.1 General remarks

In this chapter, the applications of monitoring system using optical fiber sensors are described. First, the monitoring system, using FODD and FOG developed in Chapter 2 and 3, is practically applied to safety control monitoring of open cut excavation. Although FODD is originally designed for the land sliding measurement, the proposed system is applied to monitoring of the ground deformation behind retaining walls in an open cut excavation in order to calibrate the system. Then, the monitoring system on the pipeline control is designed, with the basis of the proposed system.

5.2 Application for open cut excavation control

5.2.1 Measurement planning for open cut excavation

The tunnel construction in a city area often requires neighboring construction. Thus, the impact on surrounding structures associated with the neighboring construction of the tunnel with the open cut method must be considered; the deformation of the ground around the tunnel should be restricted.

In general, the purpose of monitoring during construction is to confirm the safety of the construction as well as to adjust the structural properties at the design stage. **Fig. 5-1** shows the general monitoring procedure in the open excavation. **Table 5-1** also shows the instruments and items required for the monitoring. The instruments should be selected according to the frequency, time, size, and cost of the monitoring. The obtained data are used for improving the prediction accuracy as well as confirming the safety of the present state; the back analysis is conducted to adjust the initial information such as soil properties, while the measured data are compared with

the safety criteria to evaluate the present safety.

In this study, the horizontal displacement and strain of the wall are monitored by optical fiber sensors. Note that besides the proposed sensor systems the other objects are also monitored by conventional instruments such as resistive gauges.

5.2.2 Site

The construction site of Kita Suma tunnel is located in the north part of residential area of Hyogo prefecture, Japan. This site can be divided into two areas according to the tunnel construction method. As shown in **Fig. 5-2**, the tunnel excavation is executed mainly by NATM (New Austrian Tunnel Method). However, from the end of the tunnel to the pit for NATM, open cut method is adopted. The optic fiber sensors are located in this section and extended by optical fibers to the measurement controllers in the site office, about 500m apart from the sensors. In addition to the optical sensing system, other conventional measurements are also conducted to access the influence of construction to the surroundings.

The detail plan around the devices is shown in **Fig. 5-3**. The FODD is installed in the borehole 1m behind the retaining wall. For comparison, a conventional inclinometer is also set adjacent to the FODD. **Fig. 5-4** illustrates the sensor arrangement along the FODD. In addition, the resistive gauges are also installed on the surface of the FODD, indicated as G in this figure. In front of these two instruments, the FOG and foil gauge are also installed on the H-steel beam of retaining wall, as shown in **Fig. 5-5**. This excavation is executed by dividing the depth into 5 stages and installing anchors at 4 levels. The length of the wall is 18m and the excavation depth and width is 11.5m and about 23m, respectively. **Fig. 5-6** and **Fig. 5-7** show the installation of FODD and layout of the construction site, respectively.

Note that the proposed system does not include the conventional instruments installed in the site, but they can be replaced by the transducers based on the optical fiber sensors.

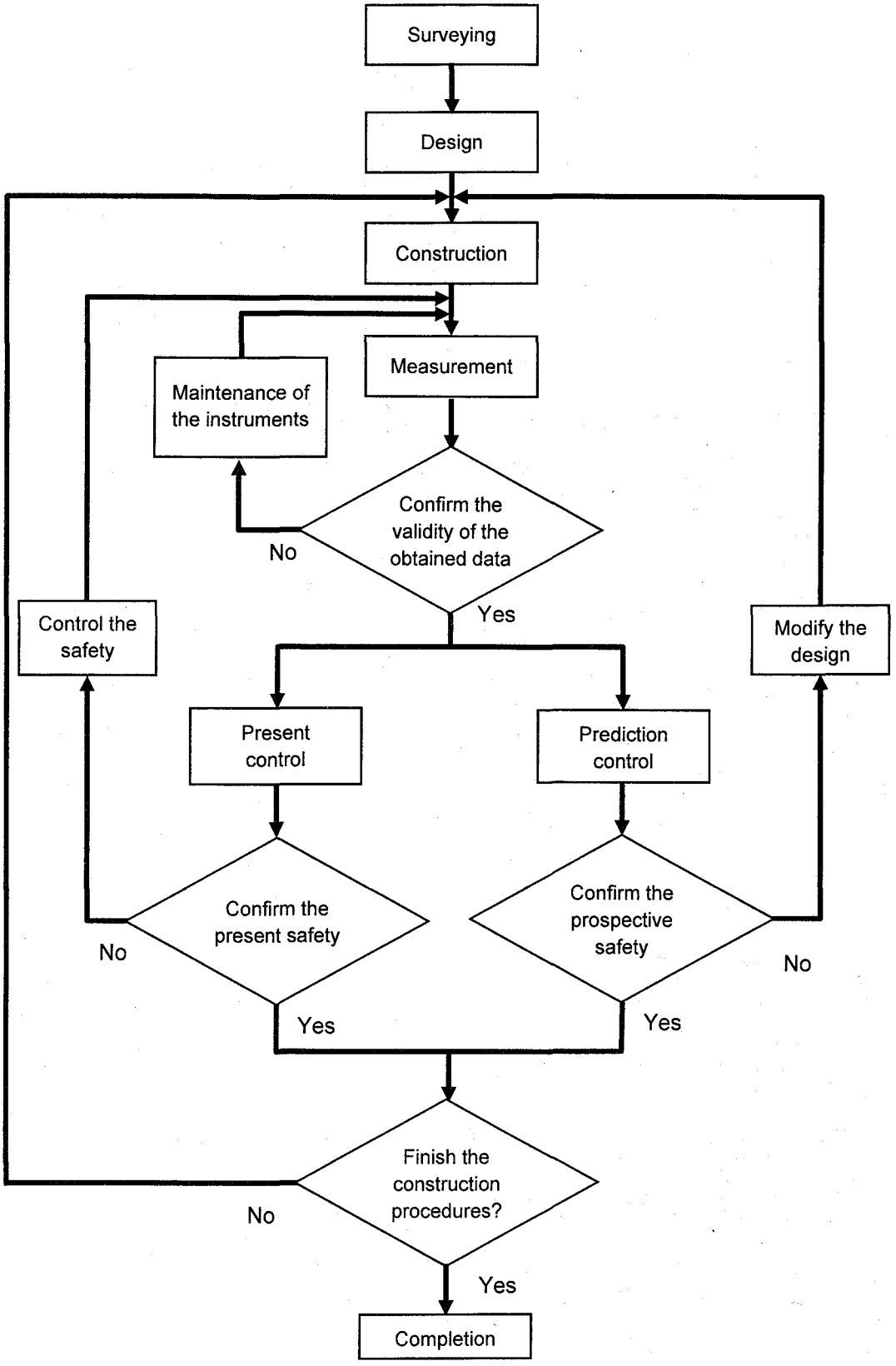

Fig. 5-1 Construction procedure with measurement control

Table 5-1 Instruments used in the excavation monitoring

Target	Item	instrument
Retaining wall	Horizontal displacement	Inclinometer
	Stress	Strain gauge (steel)
		Strain gauge (rebar)
		Stress gauge for concrete
	Lateral pressure	Soil pressure meter
	Water pressure	Piezometer
Strut	Axial force	Load cell
		Strain gauge
	Temperature	Thermo-couple
Anchor	Axial force	Load cell
Excavation base ground	Water pressure	Piezometer
	Vertical displacement	Settlement gauge
	Horizontal displacement	Inclinometer
Surrounding ground	Settlement	Settlement gauge
	Horizontal displacement	Inclinometer
	Ground water level	Piezometer
Surrounding structures	Settlement	Settlement gauge
	Incline	inclinometer
Main structure	Stress	Strain gauge (steel)
		Strain gauge (rebar)
		Stress gauge for concrete
	Temperature	Thermo-couple

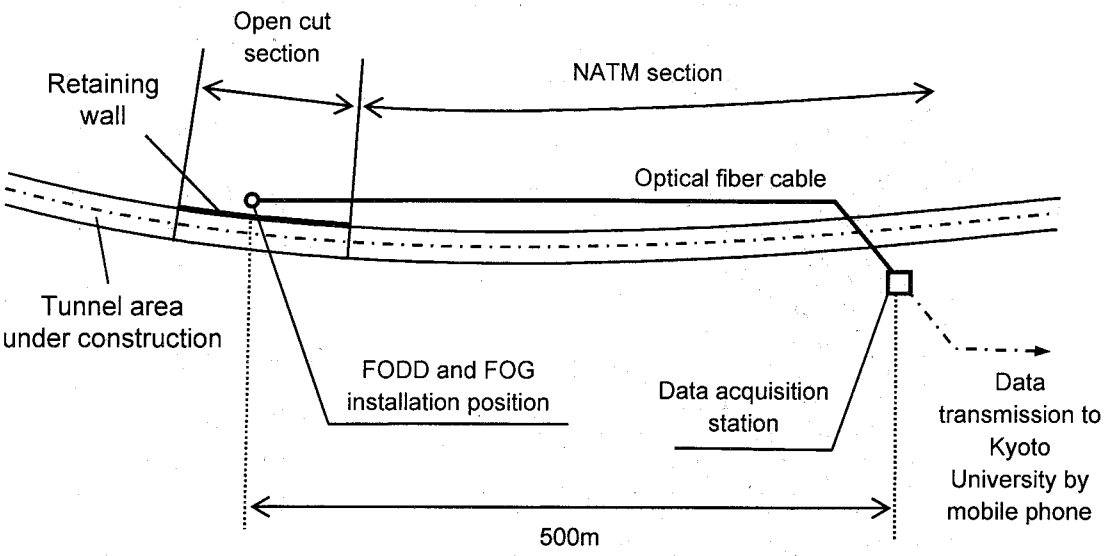

Fig. 5-2 Plan of tunnel construction site

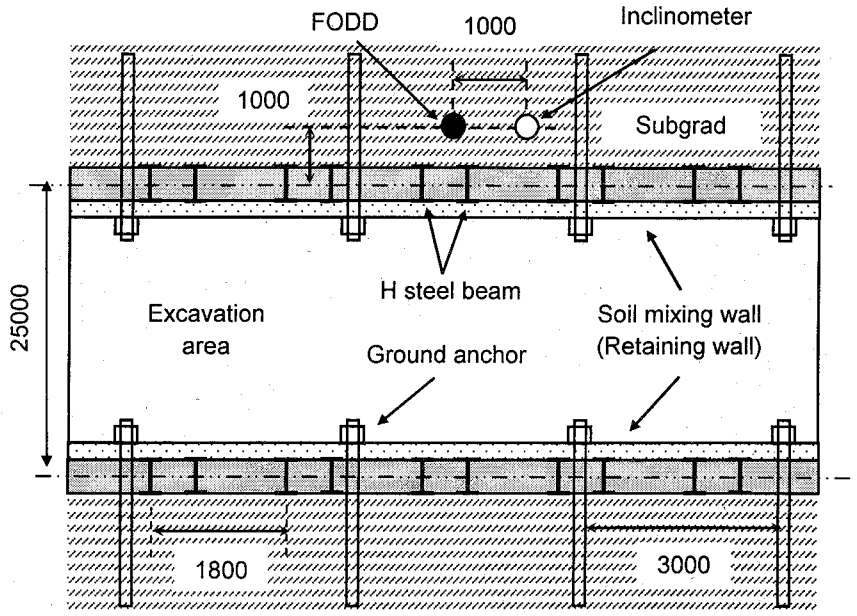

Fig. 5-3 Detail plan of the control area

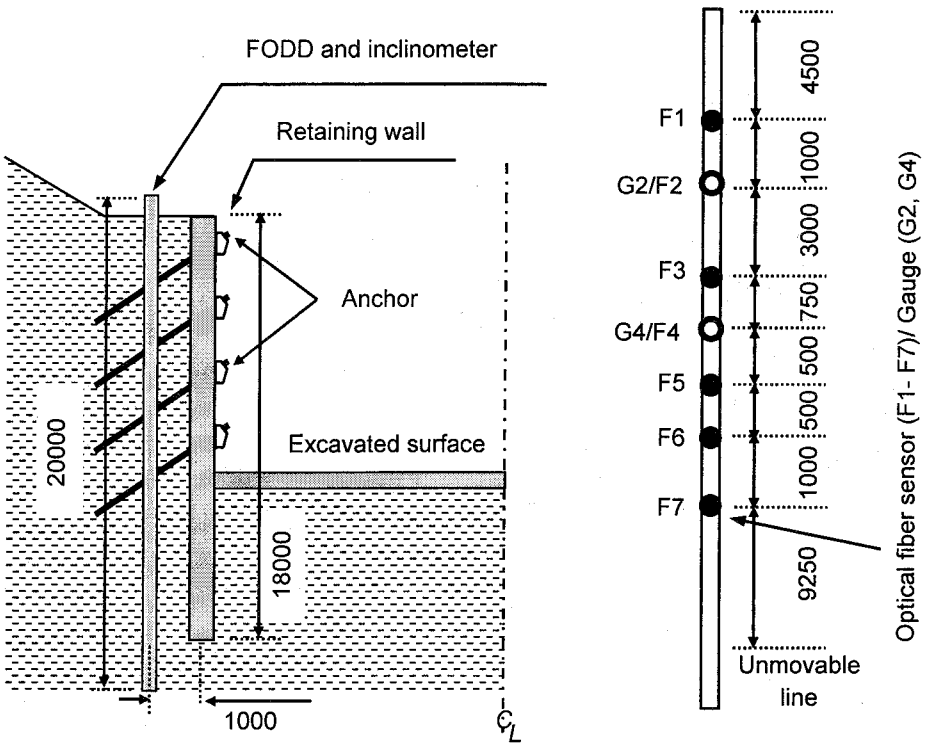

(a) Section, unit mm

(b) Sensor position, unit mm

Fig. 5-4 Section of the control area and sensor position of FODD

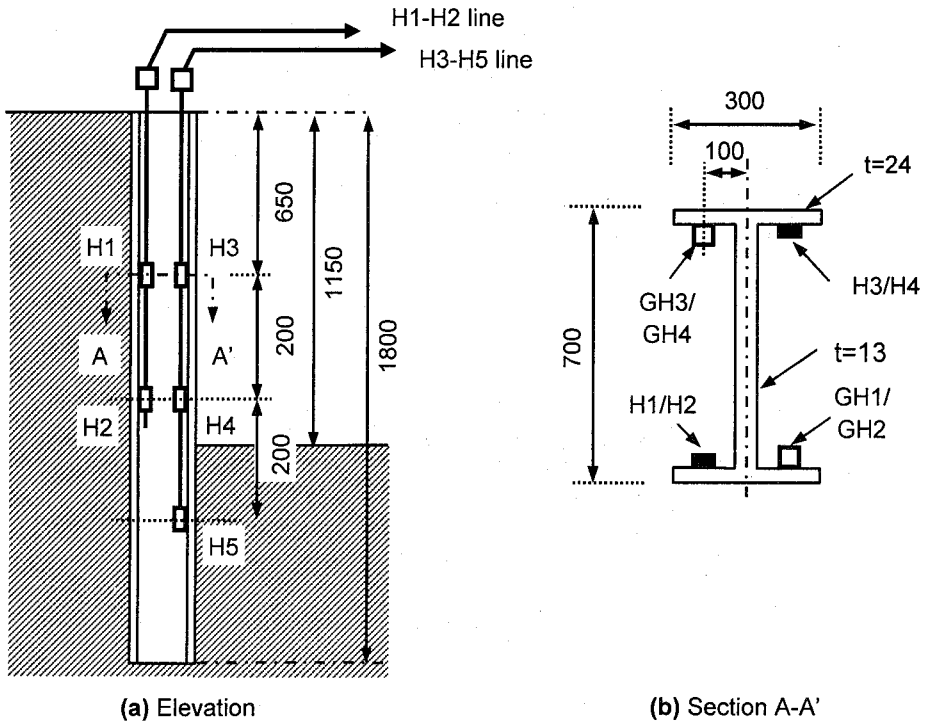

(a) Elevation

(b) Section A-A'

Fig. 5-5 Section of the control area and sensor position of FOG

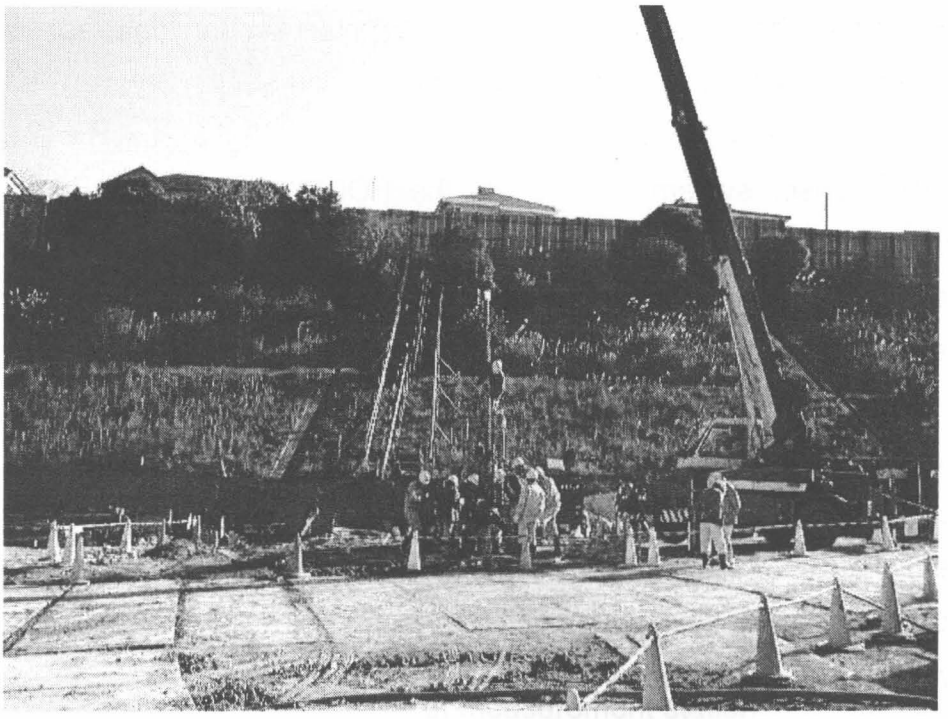

Fig. 5-6 Installation of FODD

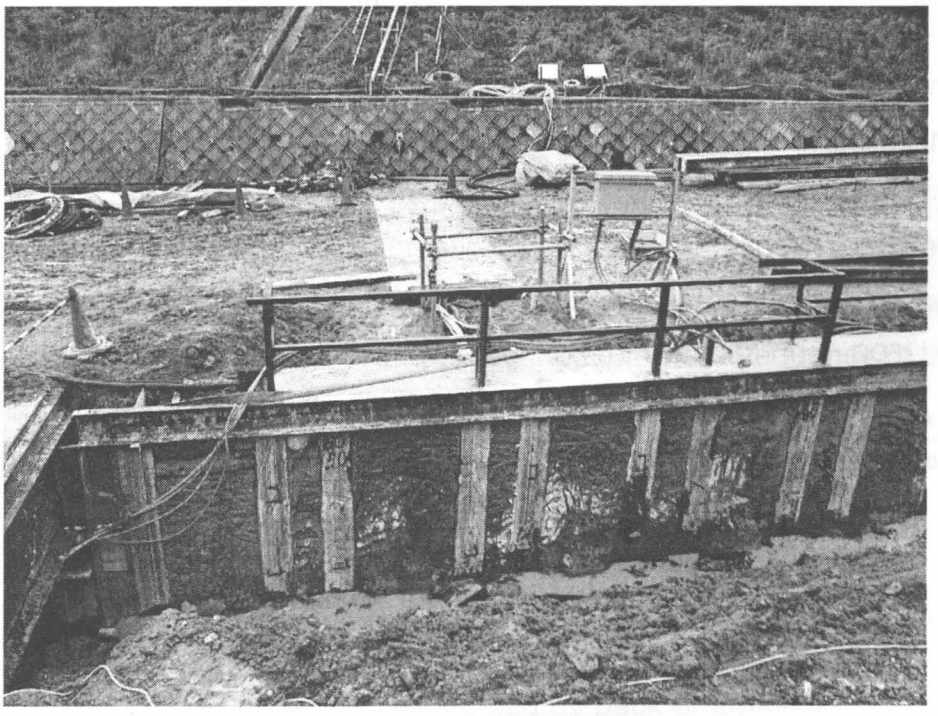

Fig. 5-7 Layout of control steel beam and retaining wall

5.2.3 System configuration

In this application, the monitoring system consists of sensor, data-acquisition, and control system; the sensor system and data-acquisition station (system) is located in the site, while the control system is in Kyoto University with the operator. As shown in **Fig. 5-8**, the sensor system consists of the FODD and FOG sensors, and the data-acquisition station consisted of FBG-IS system, optical switch, external light source, control PC, measurement PC and mobile phone. Since the distance between sensor elements (FBG sensors) and control unit (FBG-IS) is too large to transmit the light from the source to the detector, the external optical-power-source is used to strengthen the light power. Moreover, the optical switch should be connected between the sensors and the FBG-IS to extract the data of three lines. The measurement PC drives the FBG-IS unit to regulate the measurement every 4 seconds, while the control PC accumulates the data from the measurement PC once an hour. **Fig. 5-9** shows layout of the acquisition system.

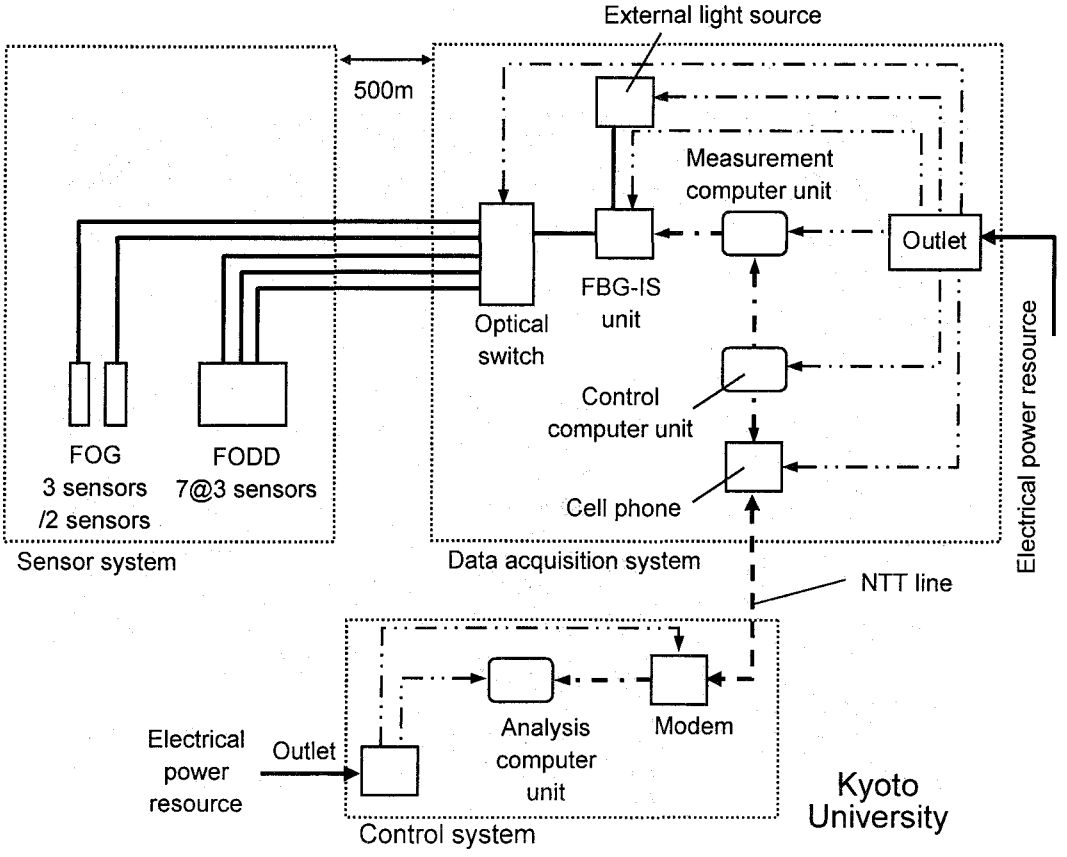

Fig. 5-8 System configuration

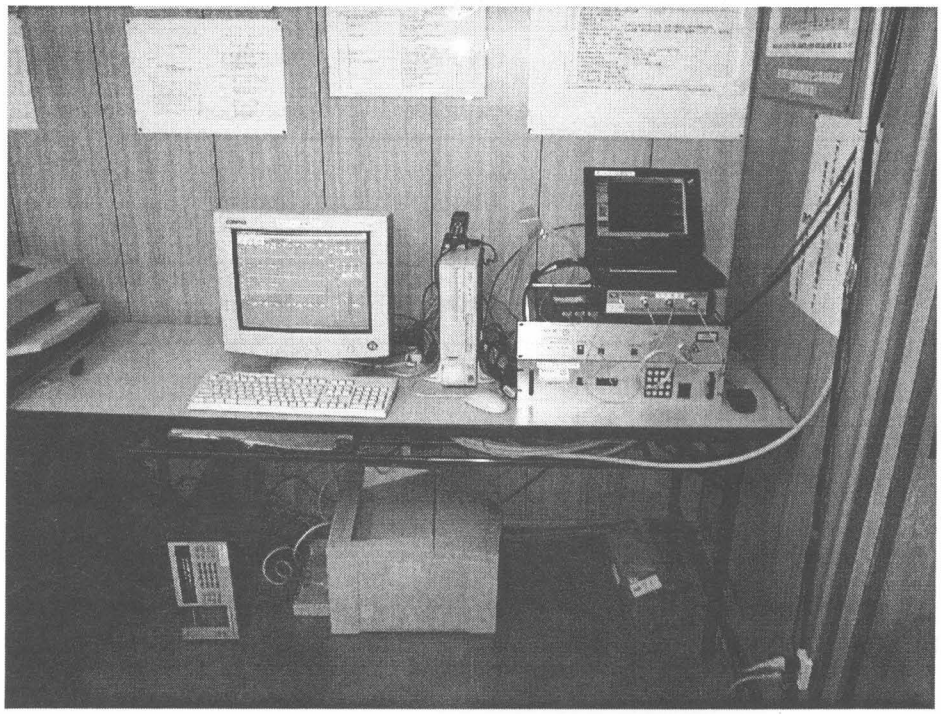

Fig. 5-9 Layout of measurement station

The control center with the operator is located in Kyoto University. The control PC of the data acquisition system transmitted the accumulated data to Kyoto University by telephone line using mobile phone: to obtain the data, first, the operator in Kyoto University makes a telephone call to the mobile phone of the data acquisition system, and then the data are automatically transmitted to the control system. Finally when the process is finished, the computer automatically hangs up the line. Thus the operator can extract the data from the acquisition system at any time, and can recognize the state of the site remotely. **Table 5-2** shows the measurement frequency of the FODD and the instruments adjacent to the FODD.

5.2.4 Construction-procedure control based on monitoring

As an analytical sequence to control the construction, two analyses are conducted: present state analysis and prediction analysis. In the present state analysis, the information on the ground properties is updated by back analysis using the obtained data besides the safety confirmation. In the prediction analysis, the deformation at next stage is predicted using updated information by conducting forward analysis. If

Table 5-2 Measurement frequency

Objective		Before excavation	During excavation	After excavation
Strain of the wall	FOG Strain gauge	1/hour	1/hour*	1/hour
Ground deformation behind the wall	FODD	1/hour	1/hour	1/hour
	Inclinometer	1/week	1/ ex. step	1/week

* When the measurement value exceeds the reference value (design value), the frequency will increase (1/10 min)

the estimated deformation is admissible, the next stage of construction can be feasible.

Note that though the proposed system is practically applied to measurement, the actual excavation procedures are not controlled by the proposed system.

(1) Analytical model

In this study, the back analysis model proposed by Ono (1993) is adopted. As shown in **Fig. 5-10**, the retaining wall is assumed to be a simple-supported beam with a length of 0.5m (H700×300×13/24) for each element, while ground anchor and subgrade reaction are assumed to be elastic spring and elasto-plastic spring, respectively. Additionally, the backward soil pressure is assumed to be a triangle distribution. The decrease of the lateral pressure from the excavation side due to the excavation is expressed by applying the equivalent force of excavation to the wall.

Note that a coefficient of subgrade reaction, K_h, is determined using N value according to the Japanese code of specifications for highway bridge (Nihon Doro Kyokai, 2002), as shown in **Table 5-3**. Note also that the spring constant of ground anchor is given by Japanese standard for tunnel (JSCE, 1996) in the form

$$K_S = \frac{A_S E_S}{L_S I_S} \cos^2 \alpha \tag{5.1}$$

where K_S is the spring constant of the anchor per 1m (kN/m/m), A_S is the area section

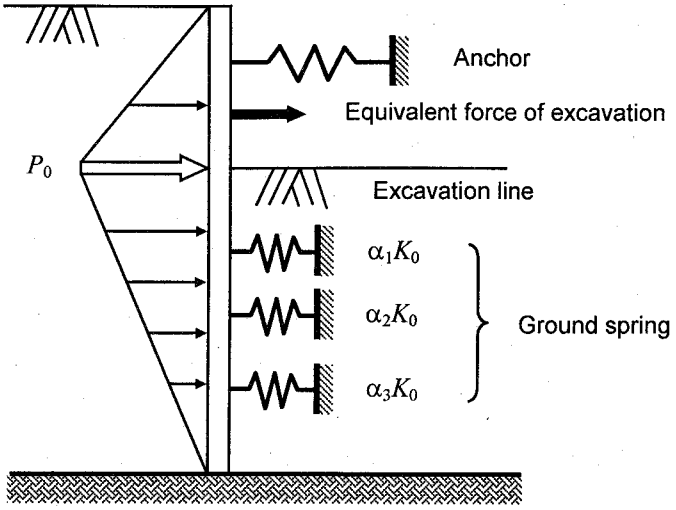

(a) Back analysis model

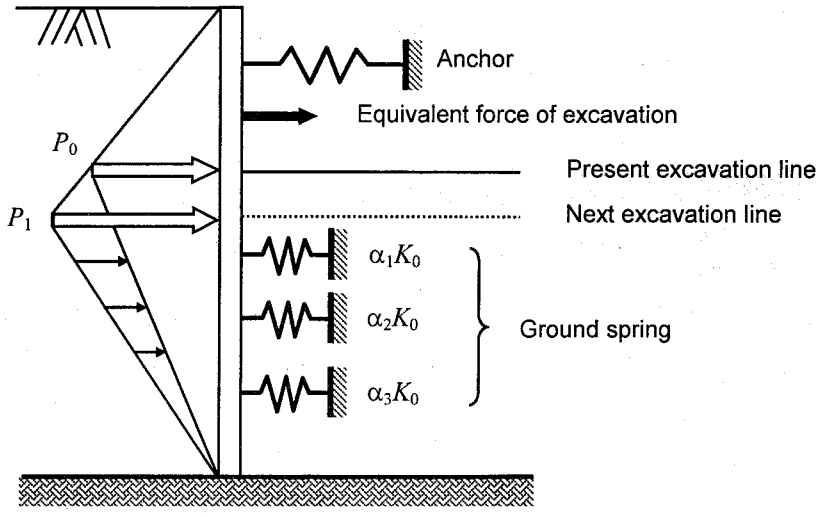

(b) Prediction of the next stage

Fig. 5-10 Analytical model for the retaining wall

Table 5-3 Geological profile and soil properties

Geological category	Type	N value	Unit weight [kN/m^3]	Internal friction angle	Cohesion [kPa]	Deformation modulus [MN/m^2]	K_h [MN/m^3]
Sandy soil	Bank (B)	7	18.6	25	0.0	7.85	7.54
Cohesive soil	Talus (Pt)	16	18.6	20	18.6	43.9	10.56
Soft rock	Sand stone (Ks)	60	19.6	45	0.0	98.1	23.57

Table 5-4 Spring constant of the ground anchor

step	Number of steel struts	A_S [mm^2]	E_S [kN/m^2]	L_S [m]	I_S [m]	α	K_S [kN/m/m]
1	4	394.8	2.0×10^8	16.5	3.0	30.0	1196.4
2	5	493.5	2.0×10^8	13.5	3.0	30.0	1827.8
3	6	592.2	2.0×10^8	10.7	3.0	30.0	2767.3
4	2	197.4	2.0×10^8	8.5	3.0	30.0	1161.2

of steel strand wire (m^2), E_S is the elastic modulus of the steel strand wire (kN/m^2), L_S is the anchor length (m), I_S is the horizontal interval, and α is the angel of the anchor. Input data of the spring constant is shown in **Table 5-4**. The equivalent force of excavation is determined using the passive soil pressure given by the following equation:

$$P = K_P(\gamma h - P_W) + 2c\sqrt{K_P} + P_W \qquad (5.2)$$

where P is the passive lateral soil pressure (tf/m^2), γ is the wet unit weight of soil (tf/m^3), P_W is the water pressure from the excavation side, h is the depth from the excavation base, c is cohesion of the soil, and K_P is the horizontal coefficient of the passive lateral soil pressure given by

$$K_P = \frac{\cos^2 \phi}{\left\{1 - \sqrt{\frac{\sin(\phi + \delta)\sin\phi}{\cos\delta}}\right\}^2} \tag{5.3}$$

where ϕ is the internal friction angle of the soil, and δ is the friction angle between the soil and the wall which is equal to $\phi/2$.

The coefficient of elastic spring of subgrad reaction in each geological layer can be expressed as $\alpha_i K_0$ where α_i is the ratio of each coefficient to the representative coefficient, K_0. In the ground spring assumption, the limitation force of the ground reaction is set to passive soil pressure.

(2) Back analysis

In the back analysis, the maximum lateral pressure, P, of assumed triangle distribution and the representative coefficient of subgard reaction, K, are estimated using the measured data by non-linear least square method.

In the forward analysis, the displacement of node i can be expressed as a function of P and K in the form

$$v_i = f_i(P, K). \tag{5.4}$$

Thus when the small increment of ΔP and ΔK occur to P and K, respectively, the displacement of node i can be given by

$$v_i = f_i(P + \Delta P, K + \Delta K). \tag{5.5}$$

Then equation (5.5) yields

$$v_i = f_i(P, K) + \frac{\partial f_i}{\partial P}\Delta P + \frac{\partial f_i}{\partial K}\Delta K. \tag{5.6}$$

Now the increment of ΔP and ΔK can be determined by minimizing the residual sum of squares, S, given by

$$S = \sum_i (v_i - m_i)^2 \tag{5.7}$$

where m_i is the measured data. Now by differentiating S with respect to ΔK and ΔP respectively, the following equations can be obtained:

$$\begin{Bmatrix} \Delta P \\ \Delta K \end{Bmatrix} = \begin{bmatrix} \sum_i \left(\frac{\partial f_i}{\partial P}\right)\left(\frac{\partial f_i}{\partial P}\right) & \sum_i \left(\frac{\partial f_i}{\partial P}\right)\left(\frac{\partial f_i}{\partial K}\right) \\ \sum_i \left(\frac{\partial f_i}{\partial K}\right)\left(\frac{\partial f_i}{\partial P}\right) & \sum_i \left(\frac{\partial f_i}{\partial K}\right)\left(\frac{\partial f_i}{\partial K}\right) \end{bmatrix}^{-1} \begin{Bmatrix} -\sum_i \left(\frac{\partial f_i}{\partial P}\right)(f_i - m_i) \\ -\sum_i \left(\frac{\partial f_i}{\partial K}\right)(f_i - m_i) \end{Bmatrix}. \tag{5.8}$$

Finally the optimum K and P will be found after several iterations by updating K and P. For the prediction analysis, the side of the pressure triangle is extended to the next excavation line, as shown in **Fig 5-10 (b)**. After next excavation completes, K and P will be updated using the data obtained in the next excavation stage.

5.2.5 Measurement results and discussion

(1) Measurement results

Monitoring using optical fibers is conducted during the tunnel construction. Unfortunately, during the installation of the FODD, one of the three optical fiber embedded in the pipe is cut at the first unit area. However, in this measurement, two fibers are enough to estimate the displacement because the direction of the deformation is clearly known. Therefore, the monitoring is carried out using two fibers.

Fig. 5-11 shows the axial strain history of sensor section F4, from the third excavation step to the fifth step. Note that the axial strain is defined as the average strain of two sensors on the same section. In this figure, G4 indicates the axial strain by the resistive gauges on the same section. From this figure, it is found that the strain by the gauges varied corresponding to the excavation steps as well as the anchor steps. However, as opposed to the gauge, the strain values by FBG sensor fluctuated periodically, though the trend of them is similar to those of the gauge. This fluctuation may be attributed to the periodical temperature change. **Fig. 5-12** illustrates the histories of the outside air temperature in Kobe area recorded by JMA (Japan

Meteorological Agency), the temperature measured by the thermo-couple installed on the outside of H-steel beam in the soil mixing wall, and the equivalent temperature obtained from the compensation FOG sensor installed on the inside the wall. From this figure, the values by JMA agreed with those by thermo-couple though the amplitude of them slightly differed from each other. In contrast, the amplitudes of FOG are similar to those of the thermo-couple, though the phase of temperature fluctuation is different from those of the others. This may be caused by heat conduction lag due to the location difference since the FOG is embedded within the wall while the thermo-couple is set outside and vulnerable to the temperature change. Thus the fluctuation in the axial stress history may be attributed to the temperature change.

On the other hand, **Fig. 5-13** shows the curvature history by both gauge and FODD. It is found that both of them agreed with each other and changed corresponding to the construction steps. It can be said that the temperature effect on the FBG sensor is cancelled during the curvature calculation. Therefore, the temperature effect cannot be taken into account when the displacement is derived from the curvature.

Fig. 5-14 shows the curvature distribution by FODD and inclinometer on the 70th day. In this figure, "Inc." indicates inclinometer. Note that the data of F6 and F7 are ignored since the data acquisition of them becomes unstable due to the optical loss in the connection structure between first and second unit. Note also that the curvature of inclinometer is obtained by dividing the difference of two adjacent angle values by a distance of 0.5m. It is found that the values by both instruments agreed with each other. Therefore, considering the results of fundamental test on the FODD as well as the agreement with the gauge, this result indicates that if the number of sensor increases the FODD may sufficiently measure the deformation; In that case, the required number of the sensor section should be clear.

Thus in this study, the values of the curvature obtained from the inclinometer are used to determine the required number of the sensor section. Now let us assume that the data are obtained at two different intervals of 1.0m and 0.5m, respectively. **Fig. 5-15** illustrates the estimated results using both spline and polynomial functions. The displacement distribution is obtained by inclinometer while the displacement at the head of FODD is obtained by distancemeter. Note that the values by inclinometer are directly obtained by the cumulative changes of the angle. Note also that before fitting

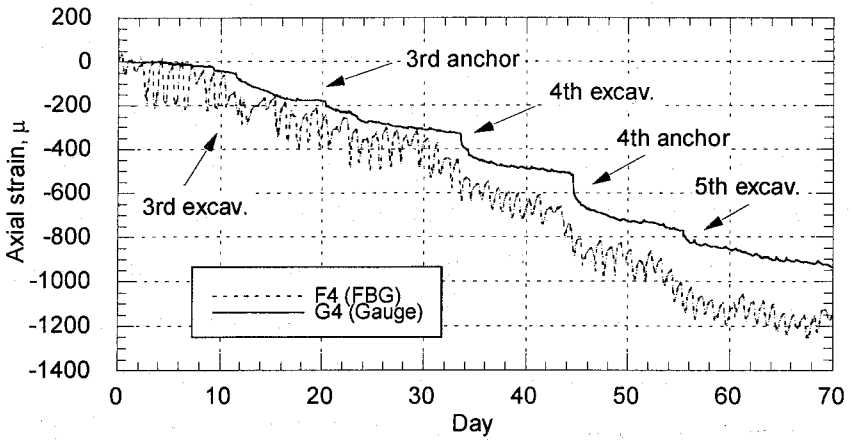

Fig. 5-12 Axial strain history

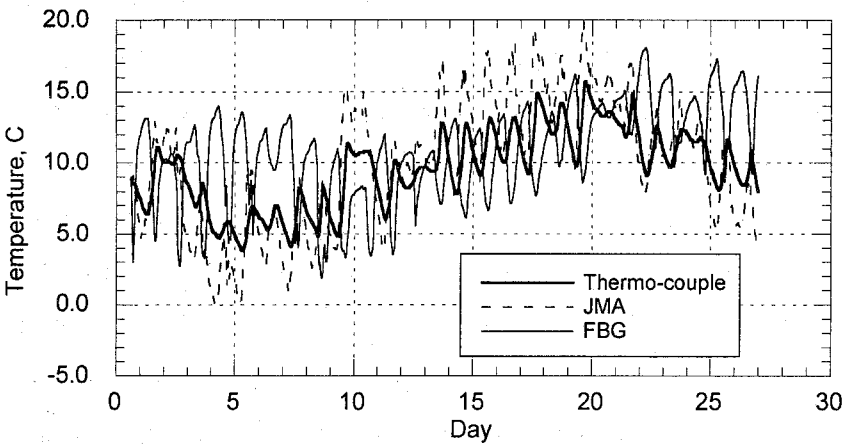

Fig. 5-13 Temperature history

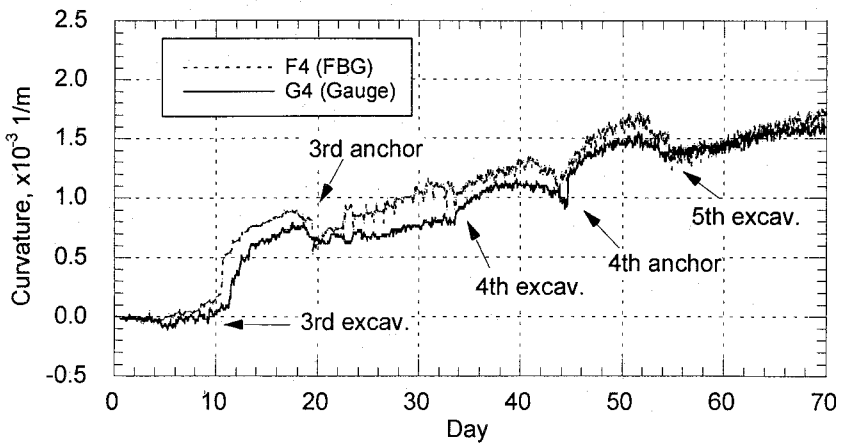

Fig. 5-14 Curvature history

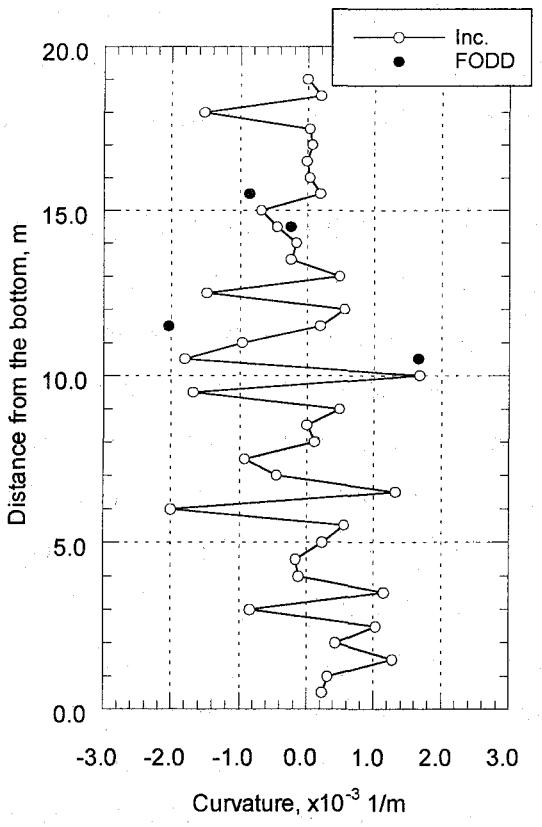

Fig. 5-15 Curvature distribution

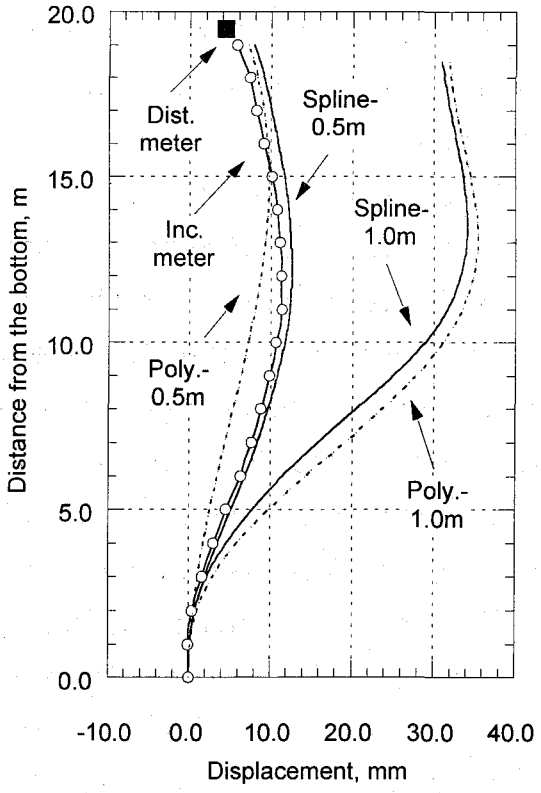

Fig. 5-16 Estimated displacement

the spline functions the data is smoothed three times since the fluctuation is too large to fit. According to the results of AIC, the degree of polynomial becomes first and fourth for the case with an interval of 0.5 and 1.0m, respectively.

First, from this figure, the displacement at the inclinometer head by inclinometer agreed with that at the FODD head by distancemeter. Thus the curvature values by inclinometer may be valid even for FODD. It is also found that when the data are obtained at an interval of 0.5m the distribution by spline agreed well with that by inclinometer. The standard deviation between the values by inclinometer and those by spline becomes 7.7mm. However, even for spline method, when the sensors are arranged at an interval of 1.0m, the estimated displacement by both methods is quite larger than that by inclinometer. Note that the maximum displacement occurred in this experiment is only about 10.0mm which is too small to compensate the errors by smoothing or least square method. Moreover, the ratio of the errors caused by only FBG-IS (4μ) to the maximum obtained curvature is more than 10%, which cannot be

neglected. Therefore, another experiment where large deformation will occur should be carried out. Finally it can be said that the sensor system of FODD can be available if many sensor sections are installed, but it should be confirmed through a practical experiment.

As for the strain history of the H steel beam by FOG, the data of H1 and H2 which are connected to the same transmission line becomes unstable after the maintenance day, while the sensors on the other line remained stable. On the maintenance day, both of the two transmission lines are replaced with new lines. After reconnection on that day, the connection loss may have increased in line of H1 and H2, due to the imperfection of the FC connection. Thus the connection between the optical fibers should be attained by fusion splicing which can connect them with small optical loss, not by FC or SC connection. **Fig. 5-17** shows the strain history by H3 on the stable line with temperature compensation, and that by strain gauge, GH3, installed on the same section as H3. From this figure, it is found that although both of the data do not agree well with each other, they changed with some time lag according to the construction steps. Especially, the strain by H3 increases rapidly after the anchor is installed close to the sensor. This means that H3 can detect the deformation after relatively large deformation occurs in the host structure. It may be attributed to the uncertain factors associated with the bolt anchorage which delay transmitting the deformation to the sensor, as mentioned in Chapter 2. Therefore, FOG should be installed on the host structure using complete anchorage such as welding.

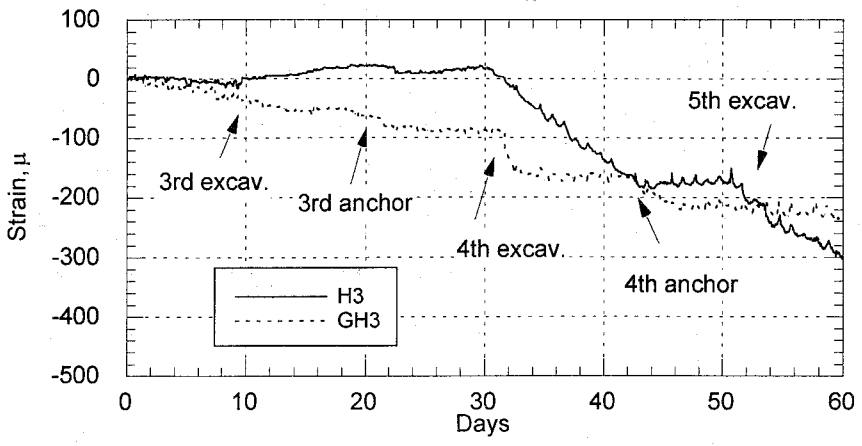

Fig. 5-17 Strain history of H-steel

(2) Back analysis

Next, the proposed back analysis system is calibrated by using the obtained displacements; the soil properties, P and K, of the first excavation stage are estimated. **Table 5-5** shows the initial and estimated properties of the soil. The initial value of P is set to the passive soil pressure. It is found that the estimated P is much smaller than the initial, while the estimated K is larger than the initial. This means that the values assumed in the design may include much safety margin. Then using the updated K and P, the deformation of the next excavation stage is estimated. **Fig. 5-18** shows the estimated deformation and the real displacement obtained by the inclinometer in the next excavation. Both of the displacements agreed with each other, which means that the estimated properties are enough valid to estimate the deformation in the next step. Judging from the estimated deformation, the anchors for the next excavations may be diminished, which leads to cost reduction.

5.2.6 System configuration for land-sliding control

Basically, the system excluding FOG can be applied to the land-sliding monitoring without major changes. In the land-sliding monitoring, FODD detects the deformation to send the information to the control center. **Fig. 5-19** shows the monitoring system designed for the land-sliding control. The data-acquisition station is located few km apart from the sensor systems, and the administrator can obtain the data from the several stations using satellite or internet in the control center. Naturally, the sensor system can include the other instruments including an extension meter, a water-level gauge, etc., based the optical sensors. When the obtained data transcends the control criteria, the administrator can remotely give some instructions to the measurement site, such as warning or emergency evacuation.

Table 5-5 The initial and estimated properties

	Initial	Estimated
P	94.86 kN/m^2	11.37 kN/m^2
K	7.54 MN/m^3	13.57 MN/m^3

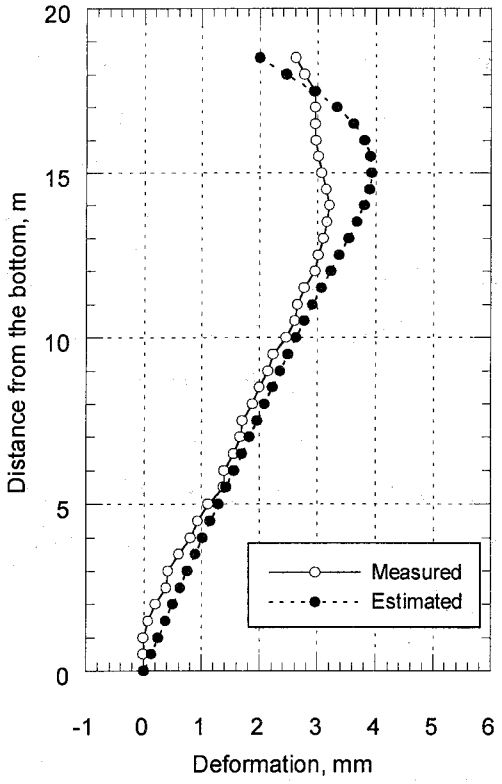

Fig. 5-18 Estimated and measured deformation

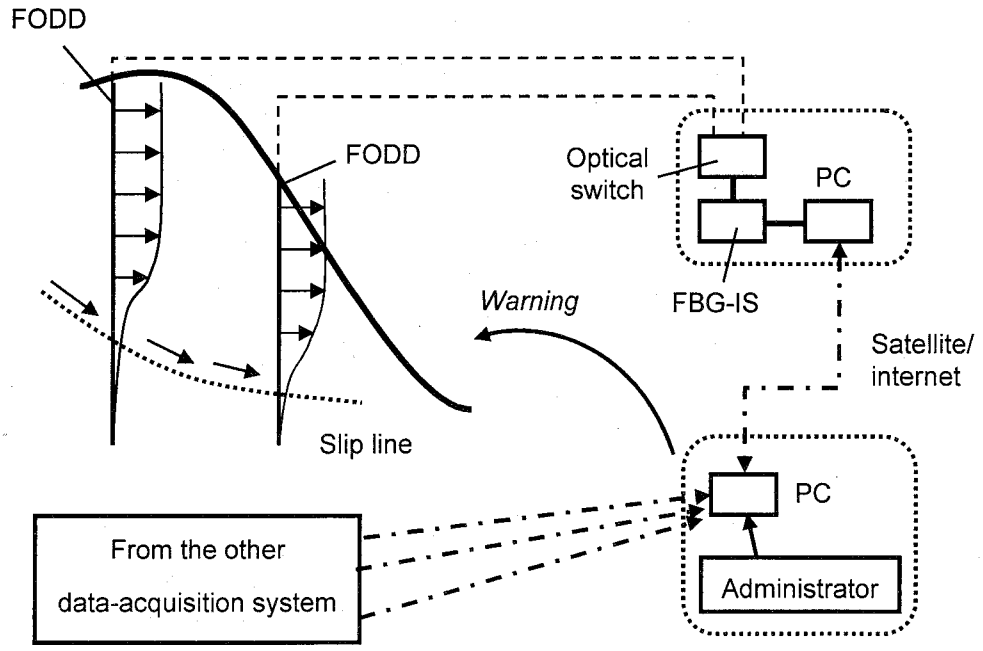

Fig. 5-19 System configuration for the land-sliding control

5.2.7 Summary

The monitoring by the proposed system is conducted on the excavation site, so as to confirm the system stability and feasibility. It is found that in the proposed system, the control system, including back analysis and remote control, and data-acquisition system are sufficiently feasible. As for the sensor system, though some of the sensors become unstable due to the connection loss of the optical fiber, the FODD may be available if many sensor sections are installed, for instance, with an interval of 0.5m for 20m FODD. However, the FOG does not agree with the strain gauges and should be improved to apply a practical measurement. In addition, the evaluation of the accuracy of FODD cannot be made because the deformation was small and the installed sensors are not enough. Thus, for further investigation, the proposed system should be evaluated using the larger deformation enough to estimate the deformation.

5.4 Application for pipeline control

5.4.1 Target of this section

In pipeline construction, trees on the pipeline route are cut and planted after the installation. However, the trees cannot be grown up enough to protect the permafrost from the sunshine during summer, thus some part of the permafrost may thaw in summer. In addition the heat scattered from the operating pipe may also cause the thaw settlement. After all, the melted ground may freeze again in winter. These areas become unstable, where the ground thaws and freezes cyclically, as shown in **Fig. 5-20**. These unstable areas exist along the pipeline sporadically and may cause the local buckling (Fukushima et al, 1999).

On the other hand Suzuki et al. (1995) reported that the pressure due to frost heave may reach 570 to 2160kPa and frost heave may be grown up to 100mm, in the ground having the frost thickness of 600mm. Since the soil under the buried pipe may thaw more than 600mmm in some case (O'Hashi, 1997), the pipe may be subject to quite large pressure locally due to the frost heave. Conventional monitoring systems for the pipeline are mainly based on the leakage detection or inner pressure control (O'Hashi, 1997). These systems intend to negatively detect the damage after the

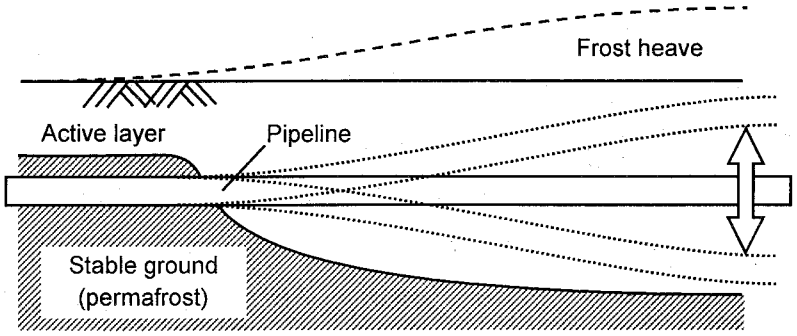

Fig. 5-20 Cyclic movement due to the frost heave and thaw settlement

fracture, since it is difficult to monitor the mechanical behavior of the pipe for long distance. But considering the repair cost and the damage for the ambient environment, the damage should be detected actively before the fracture.

Conversely, optic fiber sensors open up the possibility to control the mechanical behavior of the pipe since they can monitor the pipe over a distance of few kilometers. Taking advantage of this characteristic, H. Chen et al. (1998) proposed the pipeline monitoring configuration using optic fiber sensors, but for leakage detection.

Thus in this section, the monitoring system using FBG (Fiber Bragg Grating) sensors for the gas pipeline in the permafrost is designed. First, the finite deformation analysis is conducted on the thin shell pipe subject to bending as well as inner pressure to evaluate the pipe strength. Then, the admissible length of the pipe to cross the unstable area is evaluated, assuming that the pipeline in the unstable permafrost area is the line structure subject to distributed load and clumped at both the ends. Finally the monitoring configuration based on FBG sensors is designed according to the requirements such as the admissible length and the optical loss and range for both the sensors.

5.4.2 Finite deformation analysis

(1) Model

In order to estimate the strength of the pipe, the finite deformation analysis, using FEM code of ABAQUS, is conducted on the thin shell pipe subject to uniform bending

and inner pressure, having two times longer length than diameter. Considering the symmetry of the pipe, four nodes thin shell elements are applied to the half pipe model as shown in **Fig. 5-21**. The assumed pipe specifications are shown in **Table 5-6**. The strain-stress curve is assumed to be bilinear where plastic modulus is 0.01 times smaller than elastic modulus. According to the standard specification of the pipeline in Japan, a pressure of 7.35 N/mm^2 is applied to the inside of the pipe, which is equal to 50 to 70% of the yielding stress of the pipe. In the analysis procedures, first, the pressure is applied uniformly and then the bending is applied at the rigid rings located in the both ends of the pipe. Note that the curvature used in this study is the relative angle of the both ends divided by the pipe length.

Table 5-6 Specifications of the assumed pipe

Model name		A	B	C	D
Diameter, D	(mm)	1400	1400	1800	1800
Thickness, t	(mm)	16	22	25	30
Poission ratio, ν		0.3	0.3	0.3	0.3
Elastic modulus, E	($\times 10^5$ MPa)	2.06	2.06	2.06	2.06
Density of the pipe, ρ	($\times 10^{-5}$ N/mm^3)	7.7	7.7	7.7	7.7
Yielding stress, σ_t	($\times 10^2$ MPa)	4.214	4.214	4.214	4.214
Plastic coefficient, $E_P = 0.01E$	($\times 10^3$ MPa)	2.06	2.06	2.06	2.06
Moment of second order, I	($\times 10^{10}$ mm^4)	1.67	2.26	5.49	6.53
Area, A	($\times 10^4$ mm^2)	6.95	9.52	13.93	16.67
Full plastic moment, M_P	($\times 10^9$ Nmm)	12.92	17.61	33.19	39.61
Yielding moment, M_Y	($\times 10^9$ Nmm)	10.02	13.61	25.70	30.58
Stress level due to inner pressure, σ_H/σ_Y		0.746	0.538	0.610	0.506

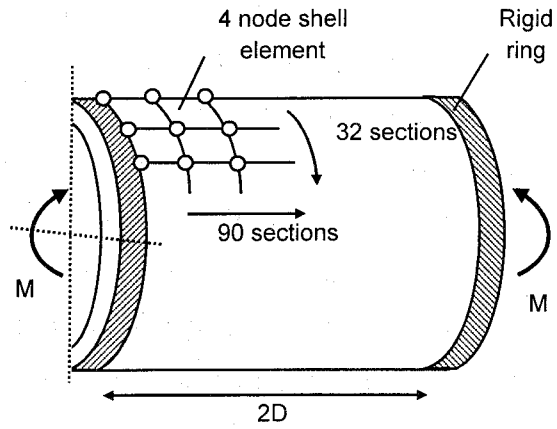

Fig. 5-21 FEM model for the pipe subject to bending and inner pressure

(2) Results and discussions

Fig. 5-22 to **Fig. 5-25** show the relationship between the bending moment and the average curvature of the case A to D, respectively. In these figures, the longitudinal and horizontal axes are the non-dimensional moment and curvature, respectively, which are the moment and curvature divided by the yielding moment and curvature of each case without consideration of the inner pressure.

From **Fig. 5-22**, it is found that in the case of the pipe A having a diameter of 1400mm and a thickness of 16mm, with inner pressure, the maximum strength is about 60% of that without inner pressure. After reaching the maximum strength, the strength decreases slowly as the curvature increases. In contrast, without inner pressure, the strength drops rapidly due to the buckling as the curvature increases, though the maximum strength is larger than that of the case with inner pressure.

However, from **Fig. 5-23**, when it comes to the pipe B having a thickness of 20mm, with inner pressure, the maximum strength is found to be almost 80% less than the yielding moment without inner pressure. Thus if inner pressure is applied to the pipe, the increase in the pipe thickness may cause the increase in the maximum strength due to the decrease in the circumferential stress. Even if inner pressure is not applied, the increase in the thickness may diminish the rapid decrease after reaching the maximum strength.

On the other hand, as for the pipe having a diameter of 1800mm, it is found from **Fig. 5-24** that in the case of pipe C having a thickness of 25mm, with inner pressure the maximum strength is about 70% less than the yielding moment without pressure. In addition, after reaching the maximum strength, the strength decreases slowly as curvature increases. Without inner pressure, the strength rapidly decreases after reaching the maximum strength. As for the pipe D having a thickness 30mm, as can be seen in **Fig. 5-25**, thought the maximum strength of the case with inner pressure is smaller than that without inner pressure, the strength of both cases decreases similarly, after reaching the maximum strength.

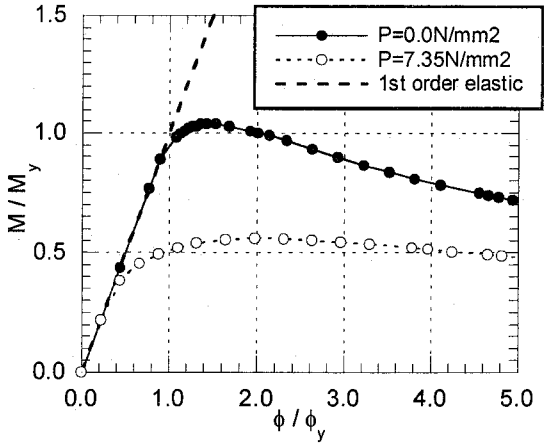

Fig. 5-22 M-ϕ curve of pipe A

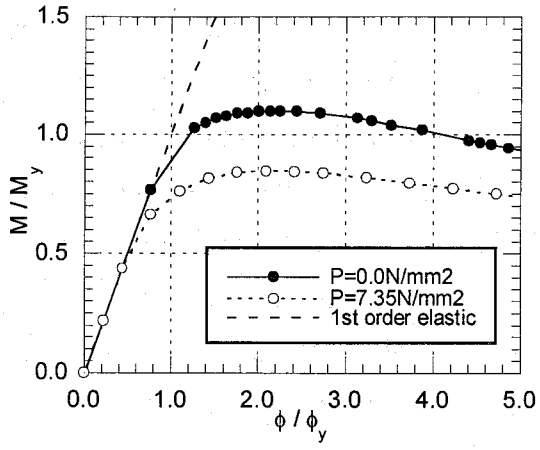

Fig. 5-23 M-ϕ curve of pipe B

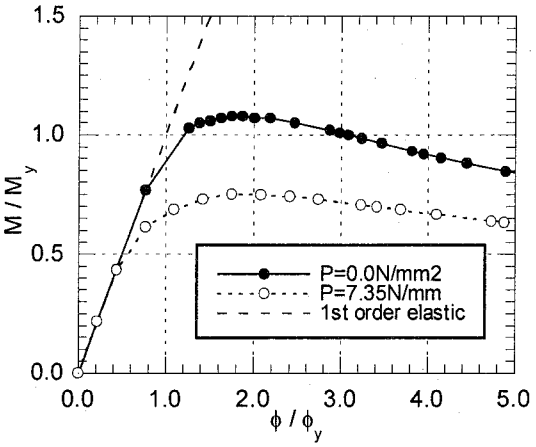

Fig. 5-24 M-ϕ curve of pipe C

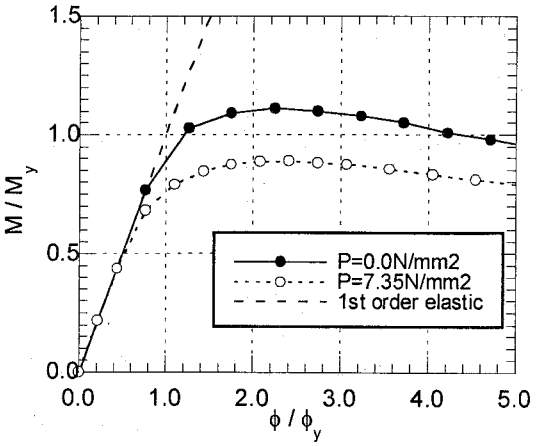

Fig. 5-25 M-ϕ curve of pipe D

Thus it can be said that the inner pressure may diminish the rapid decrease in the strength due to the buckling after reaching the maximum strength, but also may cause the decrease in the strength. Consequently, the inner pressure should be considered for safety control as well as the design of the gas pipe because they may diminish the pipe strength against bending.

5.4.3 Admissible length for the pipeline to cross the unstable ground

To estimate the admissible length of the pipeline crossing the unstable area, the pipeline is assumed to be a beam clumped at both the ends by the stable permafrost, as shown in **Fig. 5-26**. In this study, the frost heave movement is assumed to be upward distributed load, while in the thaw settlement, the pipe is assumed to be subject to the self weight and the pressure of soil having a thickness of 1m and a density of 1.57kN/mm^3. In case with consideration of the buckling, when the moment reaches the yielding moment at both the ends, the pipe structure is assumed to collapse. In case without consideration of the buckling, after the moment reaches the full plastic moment at the ends, the ends will form the plastic hinges and then the structure will collapse at the time that the moment of the center reaches the full plastic moment. Note that the inner pressure is not considered either in the case without consideration of the buckling.

Fig. 5-27 and **Fig. 5-28** shows the relationships between the admissible length of the pipe having a diameter of 1400mm and 1800mm and the frost heave pressure, required for the plastic failure with consideration of the buckling. **Fig. 5-29** also shows the relation between the admissible length and the frost heave pressure without consideration of the buckling. The frost heave may depend on the depth and width of the thawed soil as well as the water content. Suzuki et al. (1995) reported that the

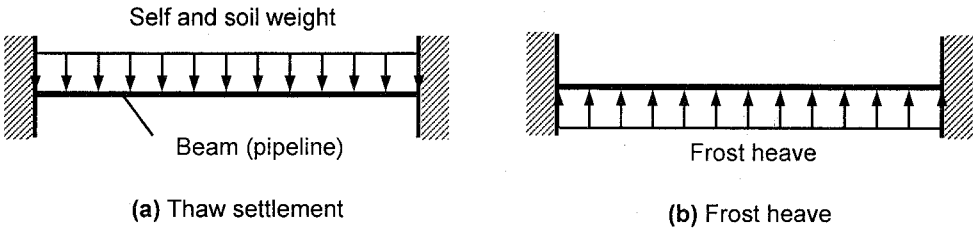

(a) Thaw settlement **(b)** Frost heave

Fig. 5-26 Simple beam models

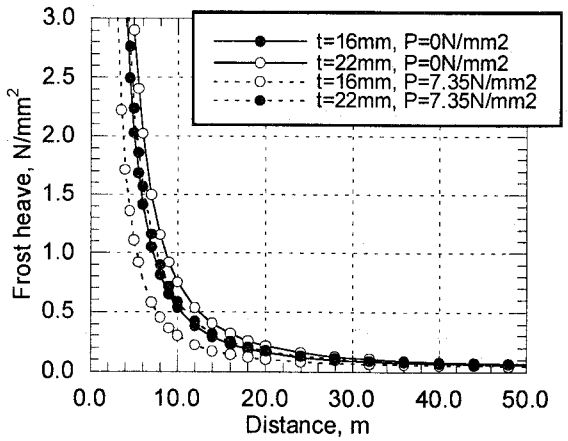

Fig. 5-27 Admissible length for frost heave (A and B: D=1400mm)

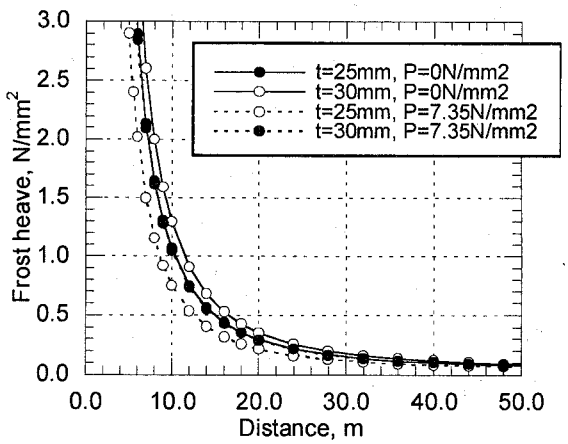

Fig. 5-28 Admissible length for frost heave (C and D: D=1800mm)

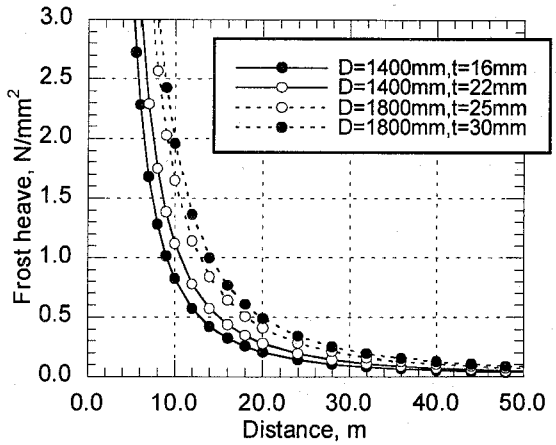

Fig. 5-29 Admissible length for frost heave without buckling

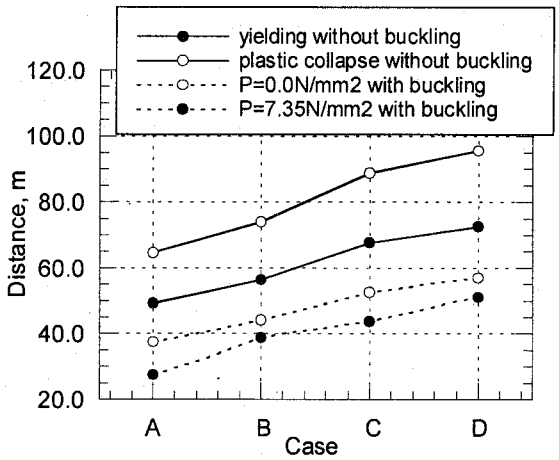

Fig. 5-30 Admissible length for thaw settlement

pressure due to the frost heave may reach 2.0N/mm^2 in the soil having a thickness of 600mm. Now provided that the frost heave pressure is not over 2.0N/mm^2, if the pipe D crosses less than 7m unstable area, the buckling may not occur even with consideration of inner pressure. Even if the unstable area grows up over 7m, the pipe may not collapse until the pressure reaches the limit determined by the curve in the figure. Thus the pressure should be monitored for over 7m unstable area.

On the other hand, **Fig. 5-30** illustrates the admissible length of the pipe crossing the thaw settlement area. From this figure, if the pipe D is used for the pipeline, the

maximum length of the pipe crossing the thaw settlement without any failure becomes about 50m. However, if the ground thaws over 50m in summer, in winter the pipe may collapse due to the frost heave pressure of only about 0.1N/mm^2. Thus, when the thaw settlement grows from 7m up to 50m, the soil pressure monitoring should be required in winter to keep the pressure less than the limit.

Therefore, provided that the pipe D is used for the pipeline, the minimum and maximum admissible length of the pipe to cross the unstable area is found to be 7.0m and 50m, respectively.

5.4.4 Requirements in pipeline monitoring in permafrost area

(1) Monitoring requirements

Fig. 5-31 shows the proposed monitoring configuration for the pipeline in the permafrost area. In order to detect the unstable area for a distance of at least 7m, the temperature sensors are installed every 2m: the area having the temperature below 0°C can be considered to be stable while the area having the temperature above 0°C can be considered to be unstable. At every 4m, the soil pressure sensors are installed on the bottom surface of the pipe to observe the pressure of the frost heave. In summer, the unstable area should be controlled to be less than 10m, where safety factor for thaw settlement is about 10.0, by covering the heat insulator on the controlled area as well as soil improvement. If the unstable area exceeds more than 50m, urgent improvement should be taken such as jack up. In winter, though the unstable area is controlled not to exceed 7m in summer, if the unstable area exceeds 7m, the soil pressure should be monitored. When the soil pressure exceeds the limitation, the gas operation must be stopped and the large scale improvement should be taken for that area.

(2) Sensor requirements

In this configuration, each sensor is based on FBG sensor: FBG sensor is one of the optical fiber sensors and can measure the strain along the fiber as well as the temperature at the designated points. In general the sensor properties such as sensor range, accuracy, maximum number of the arrayed sensors, etc., depends on the demodulation system. In this study, the demodulation system is assumed to have an accuracy of 4pm, a limit optical loss of 12dB, and a total wavelength range of 40nm

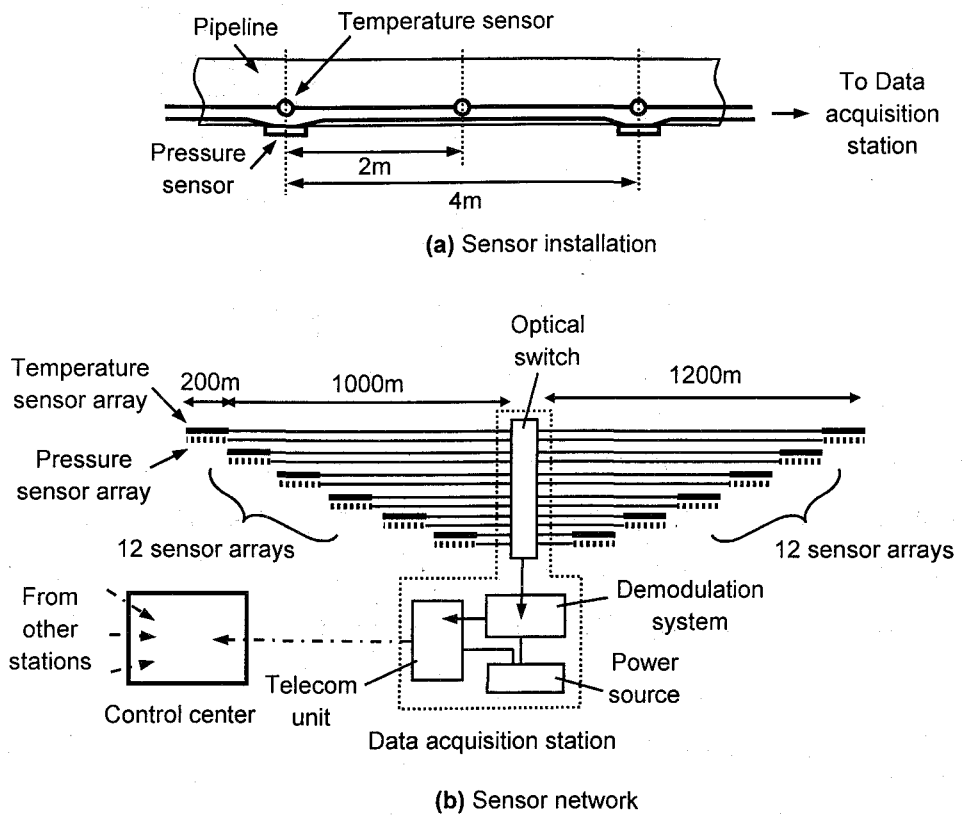

Fig. 5-31 Monitoring configuration

using WDM (wavelength division multiplexing), where the total wavelength range should be divided into all individual sensor ranges. Now assuming that the control temperature ranges from -15 to 25°C, each sensor may require a wavelength range of 0.372nm, since the temperature sensitivity of FBG is 9.3×10^{-3}nm/°C (Measure, 2000). Thus almost 100 sensors can be installed on one fiber, which can cover 200m if the sensors are installed at an interval of 2m. In this case assuming that each sensor requires two fusion splicing connection having loss of 0.1dB, totally 10dB loss may occurs, which is acceptable for the proposed system. The optical fiber having one sensor array can extend up to 1km since optical transmission loss is 2.0dB/km generally (Measure, 2000), thus 6 arrays can be installed within 1.2km.

The soil pressure sensor is also based on FBG sensors proposed by Chang, et al (2000) as shown in **Fig. 5-32**: the FBG sensor is installed on the circular diaphragm of

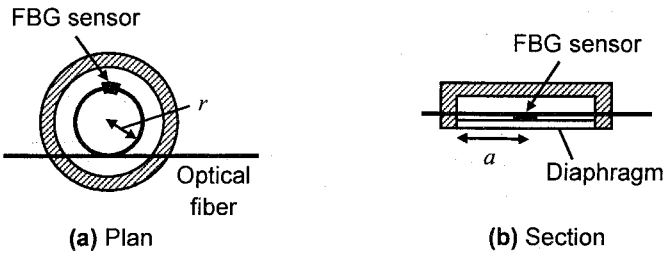

Fig. 5-32 Soil pressure transducer

the pressure transducer circumferentially to yield uniform strain for accurate measurement. Now assuming that the pressure transducer is subject to the distributed load, q, over the entire surface, the strain along the fiber at a distance r from the center of the diaphragm can be expressed as

$$\varepsilon = \frac{3q}{8E_A h^2}\left\{a^2(3+\nu) - r^2(1+3\nu)\right\} \tag{5.9}$$

where E_A, h, a and ν is the elastic modulus, thickness, radius and Poisson's ratio of the diaphragm, respectively.

In this study, aluminum plate is adopted for the diaphragm and the assumed properties are shown in **Table 5-7**. Note that sensor position of 50mm is determined according to the minimum curvature radius of the optical fiber. Then assuming that the control pressure range is 2.00N/mm^2, the dynamic wavelength range becomes 0.8nm, since the strain sensitivity of FBG sensor is 1.24×10^{-4}nm/μ (Measure, 2000). Using this sensor range, the pressure sensors can be installed at an interval of 4m over a distance of 200m, which may yield the total optical loss of 5.0dB if each sensor is connected by fusion splicing. Though this sensor array can extend up to 3.5km, 6 arrays are installed within 1km as well as the temperature sensor.

The data acquisition station consists of the demodulation system for FBG, optical switch, telecommunication unit and power source. The demodulation system can detect two pairs of 6 sensor arrays, i.e. total 24 arrays, using optical switch, thus the station should be installed every 2km along the pipeline. The telecommunication unit

can send the data to the control center that can gather the data from several stations. The power source should be the independent generator such as solar system since it is difficult to transfer the electricity to every station.

Finally, if the proposed system is applied to the pipeline monitoring, the sensor network can cover 2km using one optical fiber for each sensor, as shown in **Fig. 5-33**. Therefore, though a data acquisition station should be installed along the pipeline at every 2km, the wide range control of the pipeline over hundreds km can be attained by using the proposed system configuration. Note that the system configuration should be modified if it is applied practically, since the modulation system may be upgraded and another optical loss may occur due to some bending or other reasons.

Table 5-7 Properties of the assume aluminum plate

Elastic modulus, E_A	6.63×10^{-4} N/mm^2
Poisson ratio, ν	0.345
Radius of the diaphragm, a	100mm
Thickness of the diaphragm, h	22mm
Sensor position, r	50mm

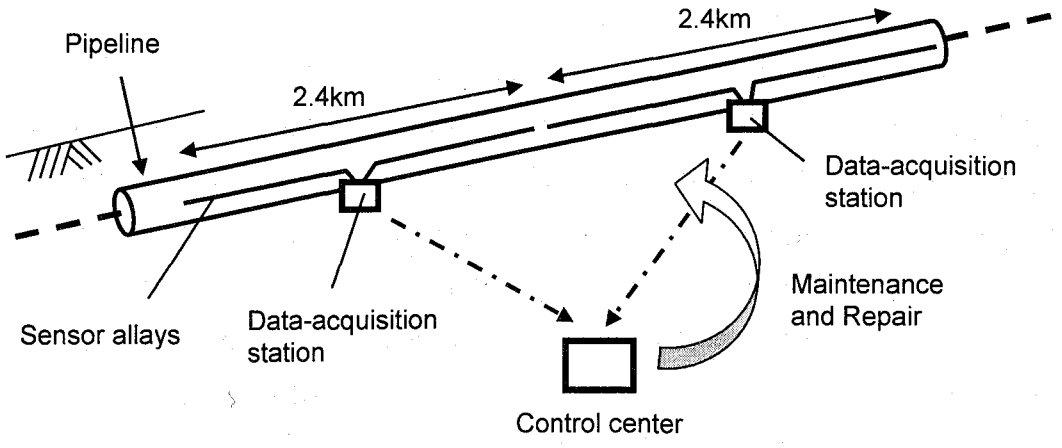

Fig. 5-33 General scheme of pipeline monitoring

5.4.5 Summary

In order to monitor the pipeline in the permafrost area, the monitoring system using optical fiber sensors is designed. First, finite deformation analysis is conducted to evaluate the pipe strength subject to bending as well as inner pressure. As a result, it is found that though the inner pressure may diminish the rapid decrease in the strength due to the buckling after reaching the maximum strength, the pressure may decrease the maximum strength. The pipe having a diameter of 1800mm and a thickness of 30mm is found to have the highest strength even with consideration of inner pressure as well as local buckling. Then assuming that the pipeline in the permafrost is a beam clumped at the ends subject to the distributed load, safety conditions for the pipe in the permafrost are evaluated. It is found that the unstable area should not exceed 50m for thaw settlement, and the frost heave pressure control should be required for the unstable area ranging from 7m to 50m. In order to detect the unstable area as well as soil pressure, the monitoring system is configured: by installing the temperature sensor every 2m and the soil pressure sensor every 4m, the pipeline behavior can be detected. Finally though the data acquisition station should be installed every 2km, the wide range monitoring can be attained by the proposed monitoring configuration.

5.5 Summary of Chapter 5

In this chapter, the applicability of the proposed system is evaluated. First of all, the system is applied to the deformation measurement behind the retaining wall in a tunnel excavation. In this application, FODD and FOG are installed on and behind the retaining wall. It is found that in the proposed system, the control and data-acquisition system including remote control are sufficiently feasible to a practical monitoring. As for the sensor system, though some of the sensors become unstable due to the connection loss of the optical fiber, the FODD may be available if many sensor sections are installed, for instance, with an interval of 0.5m for 20m FODD. However, the FOG does not agree with the strain gauges and should be improved to apply a practical measurement. In addition, the evaluation of the accuracy of FODD cannot be made because the deformation was small and the installed sensors are not enough.

Thus, for further investigation, the proposed system should be evaluated using the larger deformation enough to estimate the deformation.

Next, the monitoring system is designed for the pipeline control in the permafrost area. First, finite deformation analysis is conducted to evaluate the pipe strength subject to bending as well as inner pressure. As a result, it is found that though the inner pressure may diminish the rapid decrease in the strength due to the buckling after reaching the maximum strength, the pressure may decrease the maximum strength. The pipe with a diameter of 1800mm and a thickness of 30mm is found to have the highest strength even with consideration of inner pressure as well as local buckling. Then, assuming that the pipeline in the permafrost is a beam clumped at both the ends subject to the distributed load, safety conditions for the pipe in the permafrost are evaluated. It is found that the unstable area should not exceed 50m for thaw settlement, and the frost heave pressure control should be required for the unstable area ranging from 7m to 50m. In this study, the unstable area is detected by the temperature monitoring; by installing the temperature sensor every 2m and the soil pressure sensor every 4m, the pipeline behavior can be detected. Finally, though the data acquisition station should be installed every 2km, a wide-range monitoring can be attained by the proposed monitoring configuration.

Chapter 6 Conclusions

The intention in this study is the development and application of a monitoring system using optical fiber sensors. Transducers based on FBG sensors are developed and their applicability is evaluated in Chapter 2 and 3. In Chapter 4, the system is established and extended to a general objective. In Chapter 5, the proposed monitoring system is applied to an actual monitoring and several applications are designed. The following conclusions are obtained in this study:

In Chapter 2, the strain measurement module using the FBG sensor was proposed and evaluated experimentally and analytically.

As the result of the tension test, the proposed module showed elastic behavior within a strain of about 2000μ. But in this test, some bending may have occurred due to the incomplete bolt anchorage, developing non-uniform strain gradient along the fiber, thus the spectrum contained multi-peaks. It can be said that once some excessive force is applied to the module beyond the elastic regime to develop non-uniform strain gradient, the module maintains the deformation history affecting the measurement stability. Therefore, the proposed module should be applied to the strain measurement within its elastic regime, i.e., up to around 2000μ.

In the bending test, although the output of the FBG and the strain of the host structure obtained by the gauge were found to be proportional to the applied load, these two values did not agree with each other. Because of uncertain factors such as bolt anchorage, the ratio of these two values can not be determined. Thus, at the least, some complete anchoring such as welding should be required to determine the calibration coefficient.

Temperature sensitivity, obtained by the temperature test, showed that the wavelength shift was proportional to the temperature change, and the sensitivity was found to be 18.77×10^{-6}/°C. However this sensitivity is quite large; temperature compensation must be required for practical applications such as in situ monitoring.

To evaluate the FBG spectrum subject to non-uniform gradient, linear, quadric, and cubic distributions were assumed and converted into the spectrum by the

T-matrix method. Consequently, as the gradient or gradient change of the distribution increased, the bandwidth of the spectrum increased and the reflectivity decreased. Moreover, the peak wavelength does not always correspond to the average of the strain distribution and the difference between the peak and the average may increase as the gradient increases.

FEM analysis was conducted to obtain the strain distribution of the module subject to tension, compression, and bending. The spectra of FBG on the module were also obtained by the T-matrix method. As a result, it can be said that the sensitivity of the module strongly depends on the z-axial rotations and non-uniform distribution may occur because of the pure tension force. Thus the module should be modified so that it has no geometrical eccentricity and the z-axial rotation is perfectly constrained so as to have constant sensitivity.

Finally, the temperature independent module was proposed in order to overcome the problems associated with the old module: high temperature sensitivity and vulnerability to the deformation history. The new module was analytically evaluated. Consequently, the mechanism of the new module can compensate the temperature effect, but the sensitivity of the dimension to the mechanical strain applying to the FBG for the compensation was found to be quite high. Thus, high fabrication accuracy should be required for accurate compensation. Moreover, the output of the FBG did not agree with the applied strain, but there was a linear relationship between them. Thus, some calibration tests are needed for this new module, even if it is attached to the host by welding.

In Chapter 3, the displacement transducer based on the FBG sensor, named FODD, was proposed. To evaluate the FODD system, including the displacement transformation algorithm, the numerical analyses, material test, and measurement test were conducted. As for the transformation algorithm, 8 curvature distributions and 10 sensor arrangements were assumed for the 20m FODD. As a result, polynomial approximation may provide higher accuracy than spline interpolation when the nodes are arranged uniformly, while spline may provide higher accuracy when the nodes are arranged non-uniformly. In general, it was found that for both algorithms, higher accuracy may be attained by installing more nodes, especially in the former section, and that an increase in maximum displacement may cause a decrease in accuracy. Moreover, the influence of the incorrect boundary assumption on accuracy also may increase as the maximum displacement increases.

Next, to calibrate the FODD, fundamental and unit testing, including material, bending, and site, were carried out. From the fundamental test, FBG was found to be

able to measure the strain of vinyl chloride material as well as resistive gauges. The unit test results showed that the FODD unit can estimate the displacement within about 6.7 % errors using strain data by FBG sensors. Finally, as a result of the site test, it was found that although the FODD system can estimate the displacement, additional measurement tests should be required since the displacement was not large enough to evaluate the accuracy of FODD.

In Chapter 4, to evaluate the stability of the FBG-IS system under harsh environments, several tests including temperature, voltage, optical loss, and bonding, were carried out. As a result, it was found that for stable measurement the FBG-IS system requires a stable power supply ranging from 86 to 110 V, and that the temperature throughout the system should be constant. For the transmission fiber, it was found that the fiber should avoid less than 20mm curvature and more than 12 loops, though the influence of the loop number on the measurement was smaller than that of curvature. In addition, twisting influence was quite small in comparison with the other factors.

The connection loss associated with multiplexing was also evaluated. It was found from this evaluation that the light dump may sharpen the spectrum peak, and the connection loss became 0.23dB. This connection loss should be considered when the sensors are arrayed in one fiber.

From the results of the bonding test, it was found that the bond condition greatly influences the measurement. The imperfect bonding may cause multi-peaks in the spectrum that also may result in unstable measurement when using the FBG-IS system.

It was also found that for practical application, optical loss evaluation such as connection and coupler loss should be required for each system configuration. Considering their results, the all-purpose monitoring system was configured.

In Chapter 5, the applicability of the proposed system is evaluated. First of all, the system is applied to the deformation measurement behind the retaining wall in a tunnel excavation. In this application, FODD and FOG are installed on and behind the retaining wall. It is found that in the proposed system, the control and data-acquisition system including remote control are sufficiently feasible to a practical monitoring. As for the sensor system, though some of the sensors became unstable due to the connection loss of the optical fiber, the FODD may be available if many sensor sections are installed, for instance, with an interval of 0.5m for 20m FODD. However, the FOG does not agree with the strain gauges and should be improved to apply a

practical measurement. In addition, the evaluation of the accuracy of FODD cannot be made because the deformation was small and the installed sensors are not enough. Thus, for further investigation, the proposed system should be evaluated using the larger deformation enough to estimate the deformation.

Next, the monitoring system is designed for the pipeline control in the permafrost area. First, finite deformation analysis is conducted to evaluate the pipe strength subject to bending as well as inner pressure. As a result, it is found that though the inner pressure may diminish the rapid decrease in the strength due to the buckling after reaching the maximum strength, the pressure may decrease the maximum strength. The pipe with a diameter of 1800mm and a thickness of 30mm is found to have the highest strength even with consideration of inner pressure as well as local buckling. Then, assuming that the pipeline in the permafrost is a beam clumped at both the ends subject to the distributed load, safety conditions for the pipe in the permafrost are evaluated. It is found that the unstable area should not exceed 50m for thaw settlement, and the frost heave pressure control should be required for the unstable area ranging from 7m to 50m. In this study, the unstable area is detected by the temperature monitoring; by installing the temperature sensor every 2m and the soil pressure sensor every 4m, the pipeline behavior can be detected. Finally, though the data acquisition station should be installed every 2km, a wide-range monitoring can be attained by the proposed monitoring configuration.

Through the several examinations and evaluations for the proposed system and FBG sensors in this study, both merits and demerits of the proposed system including the FBG sensor become clear. Thus this study may be a guide for practical applications of the FBG sensor. But further investigations are required for practical applications since the durability of the sensor and the system cannot be sufficiently evaluated.

Reference

- Akaike, H., (1974). "A new look at the statistical model identification," *IEEE tans. on automatic control*, AC-19, 716-723.
- Banks, H. T., Smith, R. C. and Wang, Y. (1996). *Smart Material Structures -modeling, estimation and control*, Paris, Masson.
- Bao, X., DeMerchant, M., Brown, A. and Bremner, T. (2001). "Tensile and compressive strain measurement in the lab and filed with the distributed Brillouin scattering sensor," *J. Lightwave Tec.*, Vol.19 No.11, 1698-1704.
- Belleville, C. and Duplain, G. (1993). "White-light interferometric Multimode fiber-optic strain sensor," *Opt. Lett.*, Vol.18, 78-80.
- Berthold, J. W. (1997). "Sensors in Industrial Systems," in *Optical Fiber Sensors*, Vol.4 (Dakin, J., and Cushaw, B, Eds.), 261-308, Artech House.
- Bhatia, V., D'Alberto, T., Zabaronick, N. and Claus, R.O. (1997). "Temperature-Insensitive Long-Period Gratings for strain and refractive index," *Proc. SPIE*, Vol.3042, 194-202.
- Black, C., Udd, E., Schulz, W. and Kreger, S. (2002). "Using Multi-Axis Fiber Grating Strain Sensors to Measure Transverse Strain and Transverse Strain Gradients in Composite Materials with Complex Weave Structures," *Proc. SPIE*, Vol. 1694, 162-167.
- Bosia, F., Giaccari, P., Facchini, M., Botsis, J., Limberger, H.G., and Salathe, P. (2002). "Characteristics of embedded fiber Bragg grating sensors written in high-birefringent optical fibers subjected to transverse loading," *Proc. SPIE*, Vol.4694, 175-186.
- Chang, C., Jhonson, G., Vohra, S. and Althouse, B. (2000). "Development of Fiber Bragg Grating Based Soil Pressure Transducer for measuring Pavement Response," *Proc. SPIE*, Vol.3986, 480-488.
- Dakin, J.P. (1995). "Distributed Optical Fiber Sensor," in *Fiber Optic Smart Structures* (Eric Udd, Ed.), Wiley, 373-408.
- Dakin, J. P., Mackenzie, Steven J. and Hodgkinson, J. (1997). "Optical Fiber

–Chemical Sensing using direct spectroscopy," in *Optical Fiber Sensors*, Vol.4 (Dakin, J., and Cushaw, B, Eds.), 1-51, Artech House.

- Davis, M.A. and Kersey, A.D. (1996). "Separating the temperature and strain effects on Fiber Bragg Grating Sensors using Stimulated Brillouin Scattering," *Proc. SPIE*, Vol.2718, 270-278.
- Davis, M.A., Bellemore, D.G., and Kersey, A.D. (1997). "Distributed fiber Bragg Grating strain sensing in reinforced concrete structural components," *Cement and Concrete Components*, Elsevier Science, Vol.19, 45-57.
- Dignath, F., Hermle, M. and Schiehlen, W. (2000). "Smat structures in Robotics," in *IUTAM Symposium on Smart Structures and Structronic Systems* (Gabbert, U. ed.), 33-40, Kluwer academic publishers.
- Doyle, C. and Fernando, G.F. (2000). "Biaxial Fiber-Optic Accelerometers," *Proc. SPIE*, Vol.3986, 389-396.
- Fields, J. N., and Cole, J. H. (1980). "Fiber microbend acoustic sensor," *Applied Optics*. 19, 3265-3267.
- Fukuoka, H., Ezaki, T., and Kodama, N. (1997). "Observation of Landslide Movement by GPS Static Survey," *Soils and Foundations the Japanese Geotechnical Society*, Vol.45 No.6 (473), 29-31 (in Japanese).
- Fukushima, H., Oshima, Y., Sugiura, K., Ono, K., and Ohashi, K. (1999). "Behavior of pipeline in permafrost and its design consideration," *J. Constructional Steel JSSC*, Vol.7, 483-488.
- Glisic, B., Inaudi, D., Kronenberg, P., LLoret, S. and Vurpillot, S. (1999). "Special sensors for deformation measurements of different construction material and structures," *Proc. SPIE*, Vol. 3670, 505-513.
- Hartog, A.H. (1983). "A distributed temperature sensor based on liquid-core optical fibers," *J. Lightwave Tech.* LT-1 No.3, 498-509.
- Hasui, A. (2002) "Displacement Monitoring System with Optical Sensors," *Inspection Engineering*, No.4, 47-51 (in Japanese).
- Horiguchi,T., Rogers, A., Graig Michie, W., Stewart, G. and Culshaw, B. (1997). "Distributed sensors: recent developments," in *Optical Fiber Sensors*, Vol.4 (Dakin, J., and Cushaw, B, Eds.), 309-368, Artech House.
- Huang, S., LeBlanc, M., Ohn, M. M., and Measures, R. M. (1995). "Bragg intragrating structural sensing," *Appl. Opt.*, Vol.34 No.22, 5003-5009.

- Idriss, R.L., White, K.R., Pater, J.W., Vohra, S.T., Chang, C.C., Danver, B.A., and Davis, M.A. (1998). "Monitoring and Evaluation of an Interstate Highway Bridge using a network of optical fiber sensors," in *Fiber Optic Sensors for Construction Materials and Bridges*, F. Ansari (Ed.), Technomic Publishing Co. Inc.,159-167.
- Inaudi, D., Cananova, N., Kronenberg, P. and Vurpillot, S. (1997). "Railway bridge monitoring during construction and sliding," *Proc. SPIE*, Vol.3043, 58-64.
- Inaudi, D. (2001). "Application of Optical Fiber Sensor in Civil Structural Monitoring," *Proc. SPIE*, Vol. 4328, 1-10.
- Inman, D. J., Ahmadian, M. and Claus, R. O. (2000). "Simultaneous Active Damping and Health monitoring of Aircraft Panels," in *IUTAM Symposium on Smart Structures and Structronic Systems* (Gabbert, U. ed.), 1-8, Kluwer academic publishers.
- Ishikawa, S. (2000). "High resolution seining method using optical fiber gratings," *OYO BUTURI The Japan Society of Applied Physics*, Vol.69 No.6, 648-654.
- Jin, X. D., and Sirkis, J. S. (1997). "Optical fiber sensors for simultaneous measurement of strain and temperature," *Proc. SPIE*, Vol.3042, 120-127.
- Jones, R.T., Berkoff, T.A., Bellemore, G., Early, D.A., Sirkis, J.S., Putnam, M.A., Friebele, E.J., and Kersey, A.D. (1996). "Cantilever plate deformation monitoring using wavelength division multiplexed fiber Bragg grating sensors," *Proc. SPIE*, Vol.2718, 258-267.
- JSCE, (2002). *Japanese standard for open cut tunneling*, JSCE, Tokyo (in Japanese).
- Kimura, K., Tanaka, S., Furuta, K., and Kitagawa, E. (1999). "A study acquiring for disaster prevention information by 3 dimension measurement method using digital camera and GPS," *Proc. the 54th Annual Conf. JSCE*, 62-63 (in Japanese).
- Kodindouma, M.B., and Idriss, R.L. (1996a)."An integrated sensing system for Highway Bridge monitoring," *Proc. SPIE*, Vol.2719, 132-140.
- Kodinduma, M., Idriss, R.L., Kersey, A.D., Davis, M.A., Bellemore, D.G., Friebele, E.J., and Putnam, M.A. (1996b). "Damage assessment of a full scale bridge using an optical fiber monitoring system," *Proc. SPIE*, Vol.2791, 265-275.
- Kojima, K., Hirayama, Y., Itou, H., Yamamura, T., Ohta, H. and Yokota, Y. (2002). "A measurement of embankment used an optical fiber sensor," *the 37th Japan National Conf. on Geotech. Eng.*, Osaka, 167-168.

- Kojima, S., Satori, K., Fukuchi, K., Hongo, A., and Takeda, N. (2002). "Development of multipoint strain measurement systems using small-diamter fiber Bragg gratings," *Proc. SPIE*, Vol.4694, 202-209.
- Kronenberg, P., Casanova, N., Inaudi, D. and Vurpillot, S. (1997). "Dam monitoring with fiber optic deformation sensor," *Proc. SPIE*, Vol.3043, 65-71.
- Kumagai, H., Mita A. and Ohno, H. (2000). "Development and verification of the optical fiber sensor for concrete structures," *JCI Concrete J.*, Vol.38 No.7, 17-21 (in Japanese).
- Kurashima, T., Usu, T., Tanaka, K., Nobiki, A., Sato, M. and Nakai, K. (1997). "Application of fiber optic distributed sensor for strain measurements in civil engineering," *Proc. SPIE*, Vol.3241, 247-258.
- Lawrence, C.M., Nelson, D.V., Benett, T.E. and Spingarn, J.R. (1997). "Determination of process-induced residual stress in composite materials using embedded fiber optic sensors," *Proc. SPIE*, Vol.3042, 154-167.
- Lopez-Higuera, J.M., Echevarria, J., Quintela, A. Jauregui, C. and Cobo, A. (2001). "Strain and temperature transducer on one fiber Bragg Grating," *Proc. SPIE*, Vol.4328, 192-198.
- Lo, Y. L., and Sirkis, J. S. (1997). "Simple method to measure temperature and axial strain simultaneously using one in-fiber Bragg grating sensor," *Proc. SPIE*, Vol.3042, 237-243.
- Marcus, D. (1989). "Fiber-Coupled Short Fabry-Perot Resonance," *J. Lightwave Tech.*, Vol.7 No.5, 869-876.
- Mason, B., Hogg, D., and Measures, R.M. (1992). "Fiber optic strain sensing for smart adaptive structure," *Proc. SPIE*, Vol.1777, 135-138.
- Matrat, J., Levin, K., and Jarlas, R. (2001). "Implementation of a Bragg Grating Strain Rosette embedded in composites," *Proc. SPIE*, Vol.4328, 168-179.
- Matrat, J. and Levin, K. (2002). "An embedded optical fiber strain rosette for in-plane measurements," *Proc. SPIE*, Vol.4694, 187-194.
- Matsushita, A., Kamada, T., Okuno, M., Seki, K. and Tanaka, R. (2002). "Tunnel monitoring system by using optical fiber sensor (BOTDR)," *the 37th Japan National Conf. on Geotech. Eng.*, Osaka, 1663-1664 (in Japanese).
- Measures, R.M. (2001). *Structural monitoring with fiber optic technology*, San Diego, Academic Press.

- Menendez, J. M., Guemes, J. A. (2000). "Bragg grating-based multiaxial strain sensing: its application to residual strain measurement in composite laminates," *Proc. SPIE*, Vol.3986, 271-281.
- Mizutani, T., Okabe, Y., and Takeda, N. (2002). "Crack identification in CFRP laminates using small-diameter FBG sensors," *Proc. SPIE*, Vol.4694, 330-340.
- Miki, C. and Mizunoue, T. (2000). "The applicability to monitoring for the steel bridge of BOTDR with optical new optical fiber," *Proc. the 55th Annual Conf. JSCE*, 634-635 (in Japanese).
- Morin, A., Caron, S., Van Neste, R. and Edgecombe, M.H. (1996). "Field monitoring of the ice load of an icebreaker propeller blade using fiber optic strain gauge," *Proc. SPIE*, Vol.2718, 427-438.
- Nellen, P.M., Frank, A., Bronnimann, R., Meier, U., and Sennhauser, U. (1999). "Fiber optical Bragg grating sensors embedded in CFRP wires," *Proc. SPIE*, Vol.3670, 440-449.
- Nihon Doro Kyokai, (1996). *Design specifications for highway bridges, part 4 substructure*, Nihon Doro Kyokai, Tokyo (in Japanese).
- Okumura, I. and Kawano, M. (2002). "Falling rocks detection system using optical fiber sensor (OTDR)," *the 37th Japan National Conf. on Geotech. Eng.*, Osaka, 2257-2258 (in Japanese).
- Ono, K., (1993). "Design and Practice of Open Excavation," *Excavation in Urban Areas*, KIG Forum '93, (Adachi, T. ed.), 1-22.
- Ono, K., Oshima, Y., and Sugiura, K. (2002). "Development of a strain measurement module using FBG sensor," *J. Appl. Mech. JSCE*, Vol.5, 863-872 (in Japanese).
- Ota, I., Tsuda, T., Shinozaki, A., Yodo, S., Ota, T., Shigematsu, T., Koyanagi, S., Ibusuki, Y., and Mugino, A. (1999). "Development of optical fiber gratings for WDM systems," *Furukawa Review*, the Furukawa Electric Co. Ltd., No.104, 63-68 (in Japanese).
- Patrick, H.J., Williams, G.M., Kersey, A.D., Pedrazzani, J.R. and Vengsarkar, A. (1996). "Hybrid Fiber Bragg Grating/ Long Period Fiber Grating Sensor for Strain/ Temperature Discrimination," *IEEE Photonics Tech. Lett.*, Vol.8, 1223-1225.
- Rao, Y., Zeng, X., Wang, Y., Zhu, T. and Ran, Z. (2001a). "Temperature-strain discrimination using a wavelength-division-multiplexed chirped-FBG/EFPI sensor

system," *Proc. SPIE*, Vol.4596, 97-103.

- Rao, Y., Yuan, S., Zeng, X., Lian, D., Wang, Y. and Huang, S. (2001b). "Application of an improved EFPI/FBG system to simultaneous strain/temperature measurement of advanced 3-D braided composite materials," *Proc. SPIE*, Vol.4596, 110-118.
- Sato, T., Honda, R., Shibata, S., and Takegawa, N. (2001). "Ground strain measuring system using optical fiber sensors," *Proc. SPIE*, Vol.4328, 35-46.
- Suzuki, T., Shun, S., and Sawada, S. (1995). "Experimental study on heaving force on natural ground," *J. JSCE*, 523 III-32, 133-140 (in Japanese).
- Takeda, N., Okabe, Y., Tsuji, R. and Takeda, S. (2002). "Application of chirped fiber Bragg grating sensors for damage identification in composites," *Proc. SPIE*, Vol. 4694, 106-117.
- Takeda, S., Okabe, R. and Takeda, N. (2002). "Detection of delamination in composite laminates using small-diameter FBG sensor," *Proc. SPIE*, Vol.4649, 138-148.
- Tanaka, N., Okabe, Y., and Takeda, N. (2002). "Temperature-compensated strain measurement using FBG sensors embedded in composite laminates," *Proc. SPIE*, Vol.4694, 304-313.
- Tuck, C.J. and Fernando, G.F. (2002). "New techniques for manufacturing optical fiber-based fiber Fabry-Perot sensors," *Proc. SPIE*, Vol.4694, 43-52.
- Wakabayashi, N., Watanabe, K, and Kumagai, H. (2002). "Monitoring of tunnel supports with optical fiber senosrs," *Soils and Foundations the Japanese Geotechnical Society*, Vol.50 No.6 (533), 16-18. (in Japanese)
- Wu, Z., Takahashi, T. and Sudo, K. (2002). "An experimental investigation on continuous strain and crack monitoring with fiber optic sensors," *JCI Concrete Research and Technology*, Vol.13 No.2, 139-148.
- Wolfbeis, O. S. (1997). "Chemical Sensing Using Indicator Dyes," in *Optical Fiber Sensors*, Vol.4 (Dakin, J., and Cushaw, B, Eds.), 53-107, Artech House.
- Varis, T. and Measures, R.M. (1990). "Fiber optic Fabry-Perot gauge," *IEEE Photonics Tech. Lett.*, Vol.2 No.3, 227-228.
- Vogel, B., Cassens, C., Graupner, A. and Trostel, A. (2001). "Leakage detection systems by using distributed fiber optical temperature measurement," *Proc. SPIE*, Vol.4328, 23-34.

- Vurpillot, S., Casanova, N., Inaudi, D. and Kronenberg, P. (1997). "Bridge spatial displacement monitoring with 100 fiber optic sensors deformations: sensors network and preliminary results," *Proc. SPIE*, Vol. 3043, 51-57.
- Xu, M. G., Dong, L., Reekie, L., Tucknott, J. A., and Crzu, J. L. (1995). "Temperature-independent strain sensor using a chirped Bragg gating in tapered optical fiber," *Electron. Lett.*, 31, 823-825.
- Yamaga, I., Aoki, T., Yoshida, K., Sugai, E., Endo, T., and Nishimura, Y. (2002). "Report on the temperature compensation method of civil engineering transducers using FBG sensors," *Proc. the 56th Annual Conf. JSCE*, III-727 (in Japanese).
- Yamanabe, S., Tuneoka, S., Nakano, J., Kato, S., and Mori, T. (2001). "The filed test on the monitoring system of a surface layer collapse of the slope by mean of optical fiber sensors," *Proc. the 56th Annual Conf. JSCE*, 684-685 (in Japanese).
- Yariv, A. and Nakamura, M. (1977). "Periodic structures for intergrated optics," *IEEE Quantum Electron*, Vol.13 No.4, 233-253.
- Ye, C., Staines, S. E., James, S.W. and Tatam, R. P. (2002). "A polarization maintaining fiber Bragg grating interrogation system for multi-axis strain sensing," *Proc. SPIE*, Vol.4694, 195-201.
- Yoshida, Y., Kashiwai, Y., and Murakami, E. (2002). "Development of the monitoring system for slope deformation with fiber Bragg grating arrays," *Proc. SPIE*, Vol.4694, 296-303.

Appendix A

Fundamentals of optic fiber technology

A.1 Structure of an optical fiber

Basically, an optical fiber consists of core and cladding. As shown in **Fig. A-1**, the core of the optical fiber, which serves as a guide of incident light, is surrounded by the cladding. They are usually covered by the jacket only for the protection. A representative fiber used in industries has a 5μm-core diameter and 125μm-cladding diameter. Optical fibers in the telecommunication field operate over a wide range of wavelengths. However, the 1.55μm wavelength is mostly employed because of its minimal transmission loss. The cladding region has a slightly lower index of refraction n_2 than that of the core region n_1 as shown in **Fig. A-2**. Thus, the incident light runs in the core region reflecting at the boundary between the core and cladding. In order to make the light reflected completely at the boundary, the incident angle of the light θ_A should be satisfied with the following equation.

$$0 \le \theta_A \le \sin^{-1}\sqrt{n_1^2 - n_2^2} \equiv \theta_{\max} \qquad \text{(A.1)}$$

The maximum angle $\theta_{\max}$ indicates the maximum acceptable angle, called Numerical Aperture (NA). Representative values for NA range from 0.1 to 0.2.

A.2 Concept of wave mode

The light in the fiber can travel only with the restricted angle because of the interference. Let us assume the transmission of the light shown in **Fig. A-3**. Now the transmitting light is assumed to be a plane wave that has the angle φ with respect to the axial direction, a wave front (equiphase wave surface) is vertical to the moving

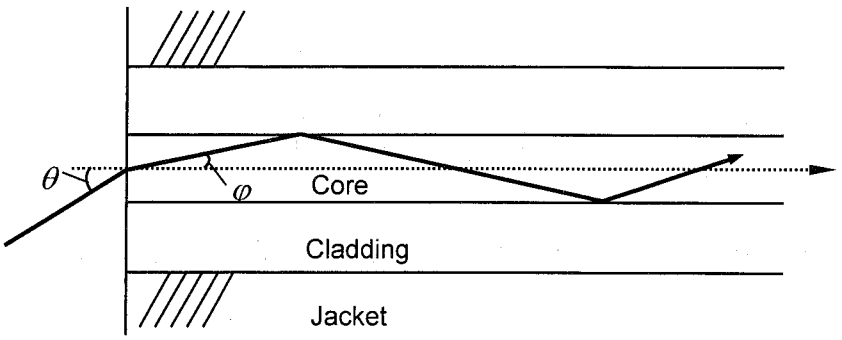

Fig. A-1 Primary constituents of an optical fiber

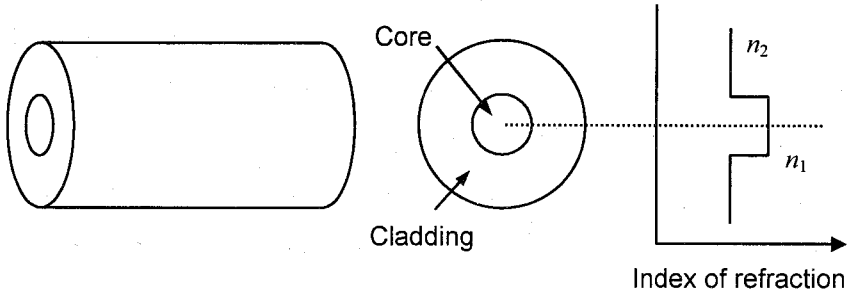

Fig. A-2 the index of refraction of an optical fiber

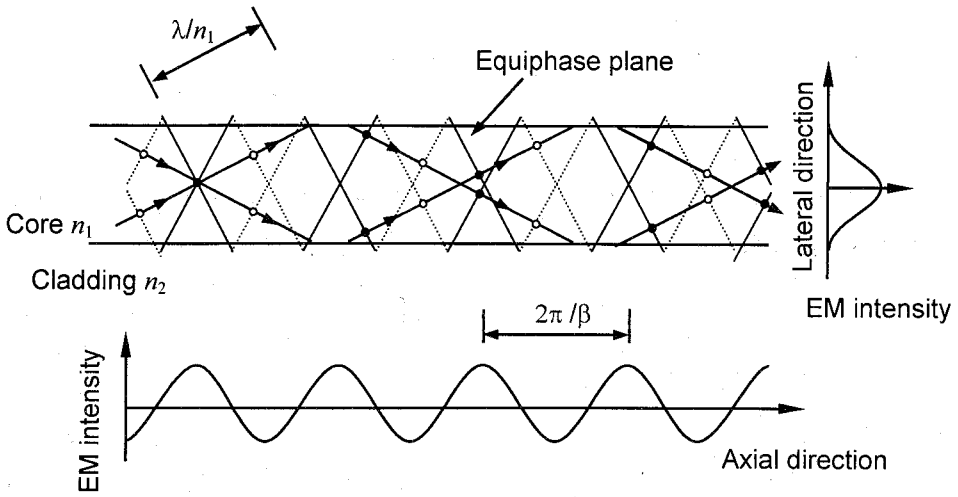

Fig. A-3 Trace of light wave and the corresponding mode

direction of the light. Assuming that the wavelength of the light in the vacuum is λ, the wavelength in the core decreases to λ/n_1 and the axial propagation constant β is given by

$$\beta = \frac{2\pi}{\lambda} n_1 \cos\varphi . \qquad \text{(A.2)}$$

In **Fig. A-3**, the dotted lines indicate a node of the wave; the solid lines indicate a loop of the wave. The highest wavelength intensity occurs in the center of the core because of the superposition, while the lowest intensity occurs at the boundary. The loop repeats periodically at a interval of $\lambda_p = 2\pi / \beta$, and this state of light is called mode, only where the light can keep steady.

Standardized frequency indicating the number of the acceptable modes in the fiber is given by the following equation.

$$v = \frac{2\pi a}{\lambda} \theta_{\max} \qquad \text{(A.3)}$$

where a is the radius of the core. As shown in **Fig. A-2**, for a step-index optical fiber, when the value of v is smaller than 2.405, only the first mode is transmittable, and this fiber is called single mode fiber. In order to make the standardized frequency less than 2.4, single mode optical fiber must have quite small core (5 to 10 mm diameter) and the ratio of the refraction difference of about 0.3%.

On the contrary, multi mode fiber can transmit the light in several modes. However, in multi mode fiber, the time to transmit the light is different in each mode, making the bandwidth narrow, as opposed to single mode fiber that permits a wide bandwidth. As shown in **Fig. A-4**, the pulse light transmitted in the multi mode fiber is converted into wider pulse. Thus, the bandwidth, i.e., the frequency of transmission of the light, becomes narrow.

Another advantage of single mode fiber is to preserve the polarization and phase of the light during the transmission. Therefore, single mode fiber is widely used in the telecommunication technology as well as optical fiber sensors.

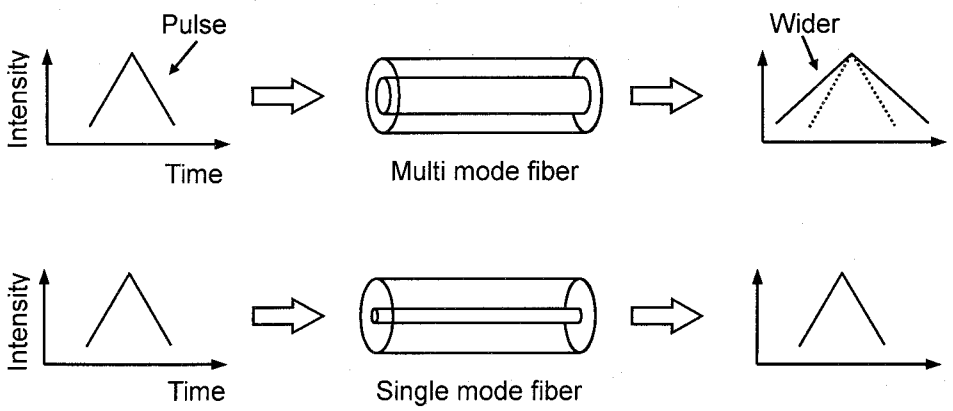

Fig. A-4 Conversion of pulse light in each mode fiber

A.3 Optical transmission loss

Transmission loss of the light in the single mode fiber is caused by both intrinsic and extrinsic reasons as shown in **Fig. A-5**. A bending loss and a coupling loss are representative extrinsic loss. The intrinsic loss is divided into two phenomena, scattering and absorption loss. The scattering loss includes Rayleigh, Raman, and Brillouin, and an absorption loss includes ultraviolet (UV) and infrared (IR). **Fig. A-6** shows the intrinsic loss of light with respect to wavelength. The spike in attenuation seen at about 1.4μm arises from the presence of hydroxyl (OH^-) group in silica. The attenuation of light in optical fiber is strong function of wavelength with two local minima, one at 1.3μm, and the other at 1.55μm. Thus these two wavelengths are main wavelength in the telecommunication technology.

(1) Scattering loss

The Rayleigh scattering arises from small optical inhomogeneities in the index of refraction of the glass formed during the manufacture. This loss, the strongest scattering among the scattering lights, increases with the glass temperature and is inversely proportional to λ^4.

The Raman scattering is an inelastic scattering where the incident light is converted into other wavelength light as shown in **Fig. A-7**. When some strong electric field is added into the transmission medium such as glass, atoms of the medium is excited and they emit different wavelength light. The emitted lights that

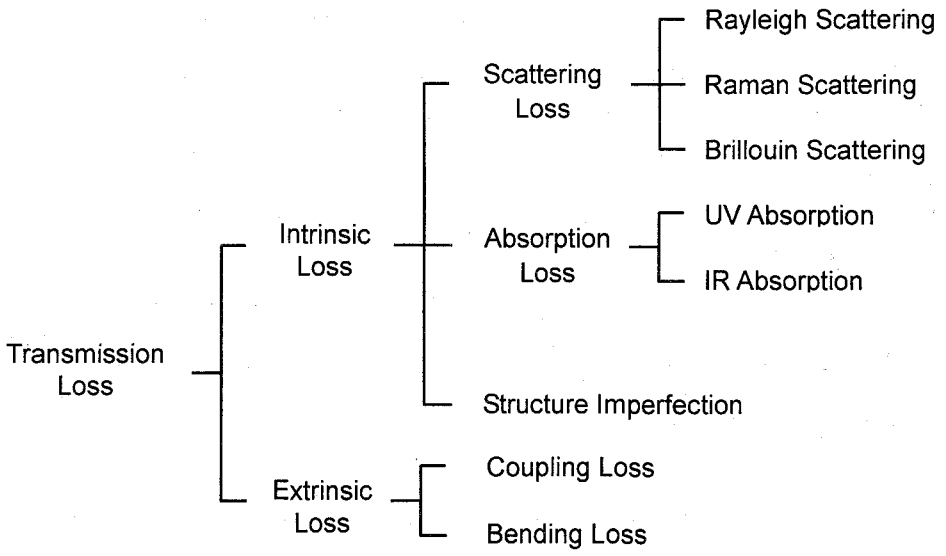

Fig. A-5 Transmission loss of an optical fiber

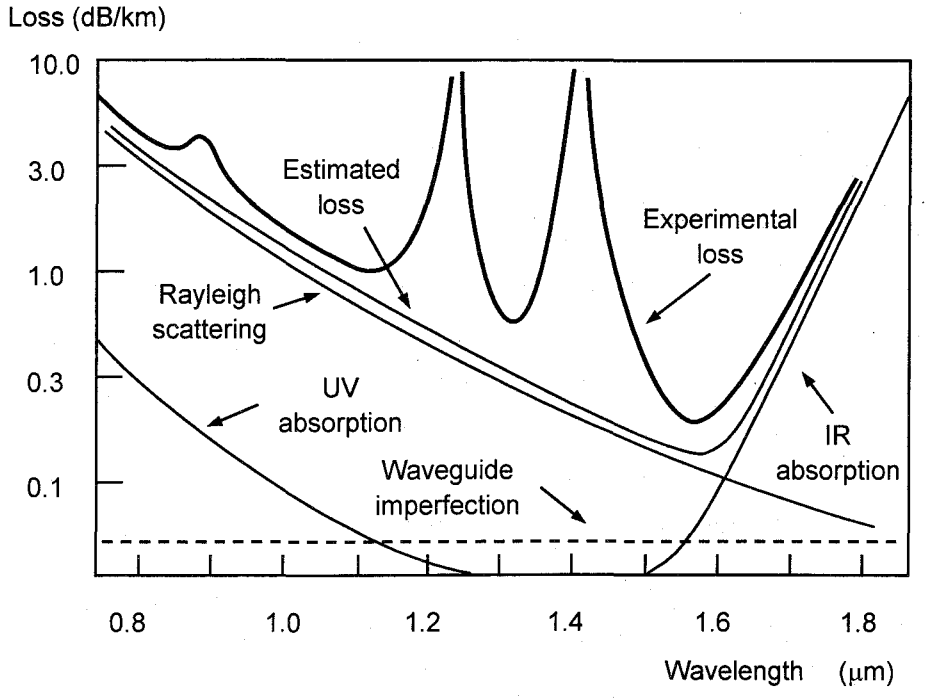

Fig. A-6 Intrinsic loss of an optical fiber as a function of wavelength

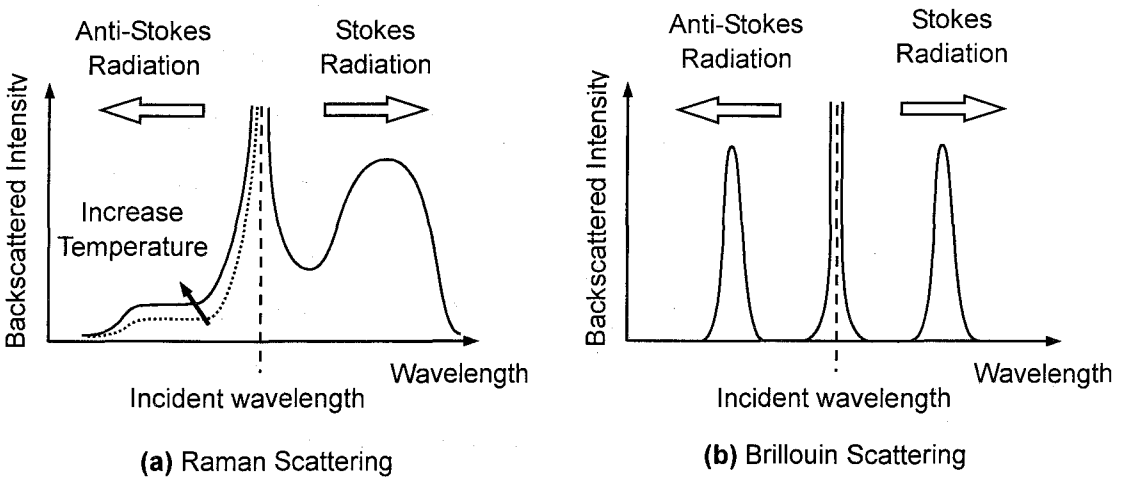

Fig. A-7 Spectra of Raman and Brillouin scattering with wavelength

have longer wavelength than the incident light are called Stokes light, as opposed to the anti-Stokes light that have shorter wavelength. Raman scattering intensity of anti-Stokes light strongly depends on temperature of the fiber, as opposed to Stokes light or Rayleigh scattering. Thus by emitting the pulse light into the fiber and detecting the spectrum ratio of Stokes to anti-Stokes, the temperature distribution is acquired. The ratio of intensities, r_R, at the anti-Stokes and Stokes wavelength, λ_a and λ_s, respectively, is given by

$$r_R = \left[\frac{\lambda_s}{\lambda_a}\right]^4 e^{-\frac{hc\Delta\nu}{kT}} \qquad \text{(A.4)}$$

where h is Planck's constant, c is the free-space velocity of light, k is Boltzmann's constant, $\Delta\nu$ is the frequency shift of the Stokes (or anti-Stokes) line from the optical laser frequency, ant T is the temperature in Kelvin.

The Brillouin scattering is also inelastic scattering arising due to the interaction of light with phonons (quantized acoustic waves). The light in the fiber is essentially scattered because of the variations in the index of refraction associated with acoustic waves. The energy of the light is partly converted into the acoustic waves that produce the scattered light. This scattered light has frequency shifted by the amount of the

acoustic velocity of the phonons, which in turn depends on the density of the glass and thus the material temperature. This Brillouin frequency shift, ν_B, is much smaller than that experienced in Raman scattering, and the bandwidth of Brillouin scattered light is much narrower than that of Raman scattered light. The Brillouin frequency shift in an optical fiber is given by

$$\nu_B = \frac{2nV_a}{\lambda} \tag{A.5}$$

where V_a is the velocity of sound in glass, n is the effective index of refraction of the optical fiber, and λ is the free-space wavelength of incident light.

(2) Bending loss

The guided light within the fiber tends to propagate straight. If the optical fiber is bent, the light also should propagate in the winding guide. Some of the light can not be curved and leaks out of the guiding fiber. Bending losses are associated with radiation of power from the cladding due to bending of the fiber (Measure, 2001).

(3) Coupling loss

Because of the small core of the single mode fiber, the coupling between two fibers easily happens to make misalignment, which can lead significant loss. The three primary types of misalignment: longitudinal, lateral offset, and angular, are schematically seen illustrated in **Fig. A-8**.

Longitudinal misalignment is of the axial gap between two ends of the fiber, lateral offset misalignment is of the offset vertical to the axes of two fibers, and angular misalignment accounts for the angle between the core axes. **Fig. A-9** shows the coupling loss of the two single mode fibers with a mode field diameter of 10 μm. This fact suggests that the fiber connection may yield serious problems in the practical measurement.

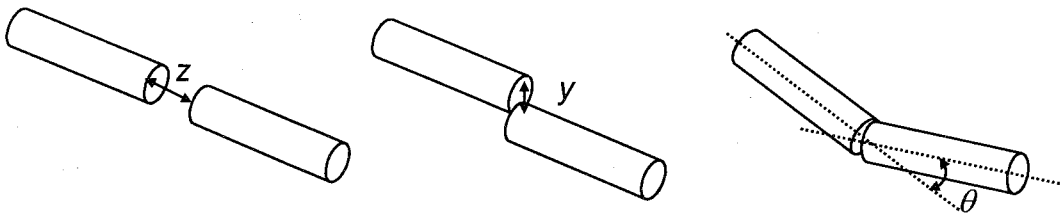

(a) Axial or longitudinal misalignment

(b) Transverse or lateral misalignment

(c) Angular misalignment

Fig. A-8 Three types of optical fiber misalignment

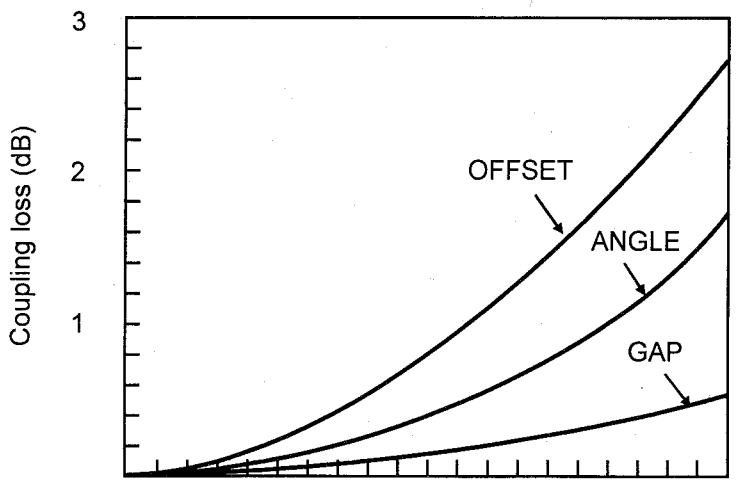

OFFSET (μm)	1	2	3	4
GAP (μm)	10	20	30	40
ANGLE (Degree)	0.5	1.0	1.5	2.0

Fig. A-9 Coupling loss of the two single mode fibers

Appendix B

Bragg Grating Reflection

B.1 Bragg grating reflection

The light is known to act as a wave and a particle at the same time. Regarding the light as a wave, i.e., the electromagnetic radiation, the propagation of the light is governed by the Maxwell equation, which in a material takes the form

$$\nabla^2 F = \frac{1}{v^2}\frac{\partial^2 F}{\partial t^2} \tag{B.1}$$

where v is the velocity of light in a material and F represents either electric field **E** and magnetic field **B**, as both satisfy this wave equation. Although **E** and **B** are the vectors respectively, each of the components satisfies equation (B.1), so **E** generally represents either of these components from now on.

For a monochromatic (i.e. single frequency) plane wave traveling in the direction z, the **E**-field solution of (B.1) can be expressed as

$$E(z,t) = E(z)e^{i\omega t} \tag{B.2}$$

where ω is the angular frequency of the light. By substituting equation (B.2) into (B.1), we obtain the one-dimensional form of the Helmholtz wave equation:

$$\frac{d^2 E(z)}{dz^2} = -\frac{\omega^2}{v^2}E(z). \tag{B.3}$$

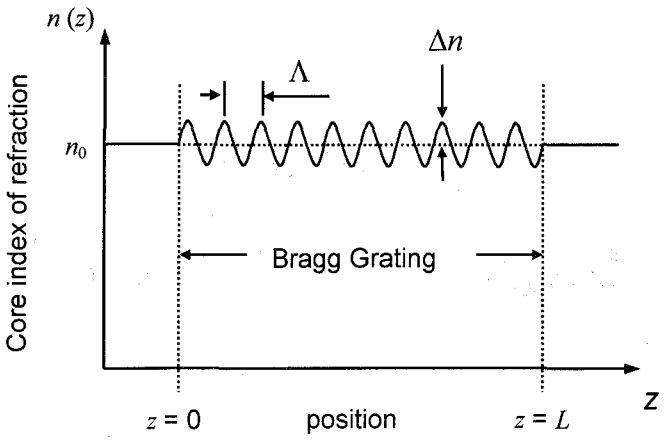

Fig. B-1 Modulation of the refraction index

Lawrence Bragg found that the light traveling through a region, in which the index of refraction has a periodic vibration, is strongly reflected only if the phase match condition is satisfied. In this grating, let the index of refraction have a sinusoidal vibration, as shown in **Fig. B-1**, described by the relation

$$n(z) = n_0 + \Delta n \cos(2pz) \tag{B.4}$$

where n_0 is the mean value of the core index of refraction, and Δn is the amplitude of the refractive index vibration, and

$$p \equiv \frac{\pi}{\Lambda} \tag{B.5}$$

where Λ is the period of the vibration.

On the other hand, the index of refraction expressed as

$$n \equiv \frac{c}{v} \tag{B.6}$$

where c is the velocity of light in free space.

We introduce the general propagating constant β expressed as

$$\beta^2 \equiv \frac{\omega^2}{v^2} \tag{B.7}$$

and the free space propagation k expressed as

$$k = \frac{2\pi}{\lambda} \tag{B.8}$$

where λ is the wavelength of light in free space. Finally, combining these two values, we see that

$$\beta = nk\,. \tag{B.9}$$

Using equations (B.7) and (B.9), then substituting equation (B.4) into (B.3), we arrive the equation

$$\frac{d^2E(z)}{dz^2} = -k^2\{n_0 + \Delta n\cos(2pz)\}^2 E(z). \tag{B.10}$$

If the vibration of the index of refraction Δn is much smaller than n_0, we can expand the square within the bracket in equation (B.10), drop the term proportional to Δn^2 and use the relation

$$\cos(2pz) = \frac{e^{2ipz} + e^{-2ipz}}{2} \tag{B.11}$$

to write the equation

$$\frac{d^2E(z)}{dz^2} = -\left\{\beta^2 + \xi\left(e^{2ipz} + e^{-2ipz}\right)\right\}E(z) \tag{B.12}$$

where we have introduced the propagation constant

$$\beta = n_0 k \tag{B.13}$$

and the coupling factor

$$\xi = n_0 \Delta n k^2 . \tag{B.14}$$

Noting that **E** represents the wave propagation, we can now assume the solution for equation (B.12) takes the form

$$E(z) = a_f(z) e^{-ipz} + a_b(z) e^{ipz} \tag{B.15}$$

where $a_f(z)$ is "forward" wave amplitude and $a_b(z)$ is "backward" wave amplitude, because e^{-ipz} and e^{ipz} represents forward and backward wave, respectively.

Substituting equation (B.15) into (B.12), and collecting the terms with the factor e^{-ipz} and the terms with e^{ipz}, respectively, then we obtain the following two equations:

$$\frac{d^2 a_f}{dz^2} - 2ip\frac{da_f}{dz} + (\beta^2 - p^2) a_f - \xi a_b = 0 \tag{B.16}$$

$$\frac{d^2 a_b}{dz^2} + 2ip\frac{da_b}{dz} + (\beta^2 - p^2) a_b - \xi a_f = 0 . \tag{B.17}$$

Moreover, assuming that second derivative terms are negligible, those two equations yield a pair of first-order coupled differential equations:

$$2ip\frac{da_f}{dz} - (\beta^2 - p^2) a_f + \xi a_b = 0 \tag{B.18}$$

$$2ip\frac{da_b}{dz} + (\beta^2 - p^2) a_b - \xi a_f = 0 . \tag{B.19}$$

Eliminating a_f from the second equation using the first, we obtain second-order differential:

$$\frac{d^2 a_b}{dz^2} - \kappa^2 a_b = 0 \tag{B.20}$$

where κ is grating coupling coefficient:

$$\kappa^2 \equiv \frac{\xi^2}{4p^2} - \frac{\left(\beta^2 - p^2\right)^2}{4p^2}. \tag{B.21}$$

In case that κ is real, we can introduce solutions of the form

$$a_b(z) = b_1 e^{\kappa z} + b_2 e^{-\kappa z}. \tag{B.22}$$

Now let us assume that the incident light wave will reach the grating at z = 0, and the power of forward wave is partly transformed into the backward wave through the grating. These assumptions yield the boundary conditions:

$$a_b(L) = 0 \tag{B.23}$$

$$P_f(0) = P_0 \tag{B.24}$$

where L is the grating length and P_0 is the value of the optical power in the forward wave $P_f(z)$ at z = 0. The first condition with equation (B.22) yields the back ward wave amplitude in the form

$$a_b(z) = 2b_1 e^{\kappa L} \sinh\{\kappa(z - L)\}, \tag{B.25}$$

and substituting this equation (B.25) into (B.16) yields an expression for the forward wave amplitude:

$$a_f(z) = \frac{2b_1 e^{\kappa L}}{\xi}\left[\left(\beta^2 - p^2\right)\sinh\{\kappa(z - L)\} + 2ip\kappa\cosh\{\kappa(z - L)\}\right]. \tag{B.26}$$

Note the intensity of the light is proportional to the square of the **E**-filed, the power of the each wave can be expressed as

$$P_f(z) = \alpha a_f^2(z) \tag{B.27}$$

$$P_b(z) = \alpha a_b^2(z). \tag{B.28}$$

Using the second boundary condition, we arrive at the optical power in backward wave at z = 0:

$$P_b(0) = \frac{P_0 \xi^2 \sinh^2\{\kappa L\}}{\left(\beta^2 - p^2\right)^2 \sinh^2\{\kappa L\} + 4p^2\kappa^2 \cosh^2\{\kappa L\}}. \tag{B.29}$$

Then, the reflectivity of the Bragg grating, $R(\kappa L)$, is defined as

$$R(\kappa L) \equiv \frac{P_b(0)}{P_0} \tag{B.30}$$

which can be seen to take the form

$$R(\kappa L) = \frac{\xi^2 \sinh^2\{\kappa L\}}{\left(\beta^2 - p^2\right)^2 \sinh^2\{\kappa L\} + 4p^2\kappa^2 \cosh^2\{\kappa L\}}. \tag{B.31}$$

From equation (B.21), κ becomes real, provided

$$\xi^2 - \left(\beta^2 - p^2\right)^2 \geq 0. \tag{B.32}$$

Now let the Bragg wavelength λ_B defined as

$$\lambda_B \equiv 2n_0\Lambda, \tag{B.33}$$

which corresponding to the phase-matched condition:

$$\frac{2\pi n_0}{\lambda_B} = \frac{\pi}{\Lambda} \qquad \text{i.e.,} \qquad \beta = p. \tag{B.34}$$

Under the phase-matched condition, equation (B.32) is valid and the grating couple coefficient takes the form

$$\kappa = \frac{\pi \Delta n}{\lambda_B}. \tag{B.35}$$

Finally, we see from (B.31) the peak reflectivity of Bragg grating,

$$R_{\max}(\kappa L) = \tanh^2\{\kappa L\}, \tag{B.36}$$

where κL is called the grating strength.

The reflection spectrum from the Bragg grating can be determined from equation (B.31). Practically, the peak in the reflection spectrum arises at the Bragg wavelength, which is given by (B.36). Considering (B.32), expression (B.31) can describe the spectrum for the wavelengths around Bragg wavelength. For the wavelengths much different from Bragg wavelength, κ becomes imaginary. We introduce

$$\kappa^* \equiv i\kappa = \sqrt{\frac{\left(\beta^2 - p^2\right)^2}{4p^2} - \frac{\xi^2}{4p^2}} \tag{B.37}$$

and the reflection spectrum in this part is given by

$$R(\kappa^* L) = \frac{\xi^2 \sin^2\{\kappa^* L\}}{\left(\beta^2 - p^2\right)^2 \sin^2\{\kappa^* L\} + 4p^2\kappa^{*2}\cos^2\{\kappa^* L\}}. \tag{B.38}$$

In order to evaluate the spectral width around the Bragg wavelength, we focus on the two null points on either side of the peak reflection. First null points in (B.38) arise when

$$\kappa^* L = \pi. \tag{B.39}$$

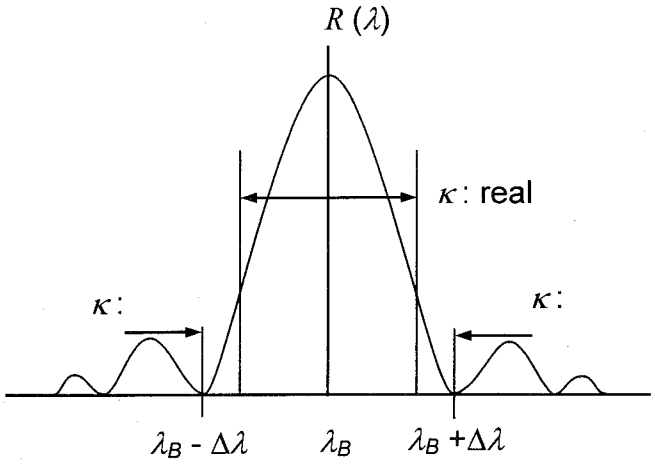

Fig. B-2 Bragg grating reflectivity spectrum

The wavelength corresponding to this first null λ_0 can be expressed as

$$\lambda_0 = \lambda_B + \Delta\lambda \tag{B.40}$$

where $\Delta\lambda$ is the displacement from λ_B as shown in **Fig. B-2**. Assuming that this displacement is much smaller than Bragg wavelength, (B.39) is approximated by the form

$$\frac{\pi L}{\Lambda}\sqrt{\left\{\frac{\Delta\lambda}{\lambda_B}\right\}^2 - \left\{\frac{\Delta n}{2n_0}\right\}^2} = \pi . \tag{B.41}$$

Thus, the half-spectral width of the Bragg grating reflection is given by

$$\Delta\lambda = \lambda_B\sqrt{\left\{\frac{\Lambda}{L}\right\}^2 + \left\{\frac{\Delta n}{2n_0}\right\}^2} . \tag{B.42}$$

It can be seen that the width decrease with longer gratings for a give period and with smaller index modulation of refraction for a given mean index. Substitution of

(B.33) and (B.35) into (B.36) yields

$$R_{\max}(\kappa L) = \tanh^2\left\{\pi\left(\frac{\Delta n}{2n_0}\right)\left(\frac{L}{\Lambda}\right)\right\}. \qquad \text{(B.43)}$$

As opposed to (B.42), we see from (B.43) that the reflectivity increases with the smaller modulation of the index of refraction. In order to acquire both a narrow spectral width and high reflectivity of the grating, some trade-off must be required in the decision of the index modulation.

For example, we assume a Bragg grating in the fiber used for sensors, which has the following parameters: n_0 = 1.5, Δn = 10^{-4}, Λ = 0.517 μm, and L = 10.0 mm. Then,

$\lambda_B = 2n_0\Lambda$ = 1.55 μm,

$$R_{\max} = \tanh^2\left\{\pi\left(\frac{\Delta n}{2n_0}\right)\left(\frac{L}{\Lambda}\right)\right\} = 93.5\%$$

and $\Delta\lambda = \lambda_B\sqrt{\left\{\frac{\Lambda}{L}\right\}^2 + \left\{\frac{\Delta n}{2n_0}\right\}^2} = 0.095\,\text{nm}$.

B.2 Temperature and strain sensitivity

FBG sensor requires temperature compensation because it is more sensitive to the temperature than the strain. Moreover, the wavelength shift, which comes from the temperature, depends more strongly on the change in refractive index than on the expansion of the fiber. Under uniform conditions, the sensor optical path length,

$$\varsigma_L = nL \qquad \text{(B.44)}$$

is just the product of the core index of refraction, n, and the gauge length of optical fiber, L. For FBG sensor, this length corresponds to the grating length. In general, the path length is a function of the applied stress, σ, and temperature, T, and can be expressed in the form

$$\varsigma_L = \varsigma_L(\sigma, T). \tag{B.45}$$

The incremental change in this path can be expressed by Taylor expansion, which results in

$$\Delta\varsigma_L = \left[\frac{\partial\varsigma_L}{\partial\sigma}\right]\Delta\sigma + \left[\frac{\partial\varsigma_L}{\partial T}\right]\Delta T \tag{B.46}$$

where $\Delta\sigma$ and ΔT are the representative incremental changes, respectively. Submitting the equation (B.10) into (B.12), this equation takes the form,

$$\Delta\varsigma_L = nL\left[\left\{1+\frac{1}{n}\left[\frac{\partial n}{\partial\varepsilon}\right]_T\right\}\frac{\Delta\sigma}{E} + \left\{\alpha_F + \frac{1}{n}\left[\frac{\partial n}{\partial T}\right]_\sigma\right\}\Delta T\right]. \tag{B.47}$$

Then, introduced are the strain and temperature sensitivities, S_ε and S_T, defined by the relations

$$S_\varepsilon = 1+\frac{1}{n}\left[\frac{\partial n}{\partial\varepsilon}\right]_T \tag{B.48}$$

and

$$S_T = \alpha_F + \frac{1}{n}\left[\frac{\partial n}{\partial T}\right]_\sigma \tag{B.49}$$

Then equation (B.13) can be rewritten

$$\frac{\Delta\varsigma}{\varsigma} = S_\varepsilon\Delta\varepsilon + S_T\Delta T\,. \tag{B.50}$$

Representative values for the fiber optic strain and temperature sensitivities at a wave length of 1550 nm are almost $S\varepsilon$= 0.8x10^{-6} and S_T= 6.0x10^{-6}/°C. If temperature

change does not occur, the wavelength shift in case of axial strain can be expressed by

$$\Delta\varsigma = \varsigma G \Delta\varepsilon \tag{B.51}$$

where G is the strain gauge factor in case of axial strain. For FBG sensor, wavelength shift takes the form

$$\Delta\lambda_B = \lambda_B G \Delta\varepsilon \,. \tag{B.52}$$

When the grating was operated at about 1550nm, and gain G is set to 0.8, then

$$\Delta\lambda_B = 1550 \times 10^{-9} \times 0.8 \Delta\varepsilon = 1.24 \text{ pm/}\mu. \tag{B.53}$$

Therefore, accurate measurement of wavelength is a key to obtain strain by FBG sensor and the resolution of spectrum analyzer currently available is about 10pm, which is equivalent to about 12μ.

On the other hand, if the only temperature changes from the initial state, apparent thermal strain that comes from the thermal expansion of the fiber is given by

$$\Delta\varepsilon = \frac{S_T}{S_\varepsilon} \Delta T = 7.5\mu \Delta T \,. \tag{B.54}$$

Note that thermal expansion coefficient of the fiber is only 0.5 μ/°C which is much smaller comparing the effective of the refractive index change, which is 5.5 μ/°C. Thus, even if the expansion of the fiber is restricted, the wavelength shift will occur by the temperature. In order to compensate the temperature effect in the strain measurement, other mechanisms must be required.

Appendix C

Optical Fiber Sensor Multiplexing Techniques

C.1 Multiplexing techniques

One of the most attractive characteristics of optical fiber sensors is the ability of making the arrays of sensors. If many sensors are to be applied, the multiplexing technique must be required. There are a number of multiplexing schemes, but in general this technique can be divided into two big categories: parallel and serial, as shown in **Fig. C-1**. Now we shall focus on the most common use in fiber optic structural monitoring and its schemes where each method includes parallel and serial arrays:

- Time Division Multiplexing
- Wavelength Division Multiplexing
- Coherence Division Multiplexing
- Frequency Division Multiplexing
- Spatial Division Multiplexing

Time Division Multiplexing (TDM): Short light pulses are used to identify the relevant sensor by means of light traveling time measurement. This technique is known as Optical Time Domain Reflectometry (OTDR) as will be mentioned below.

Wavelength Division Multiplexing (WDM): Each sensor operates at different wavelength. The information of each sensor can be detected by means of spectrum analyzing. FBG sensor belongs to this group.

Coherence Division Multiplexing (CDM): A reference interferometer is used to path-match one of a number of sensing interferometers. But this technique is restricted by the coherence length of the source and can require sophisticated signal processing.

Frequency Division Multiplexing (FDM): Each interferometric sensor operates with a signal that is modulated at a different frequency. Detecting the signals is achieved by means of appropriate bandpass filters to ensure that each detector only receives signals from a specific sensor.

Spatial Division Multiplexing (SDM): Each sensor, in turn, is connected physically to the data link and a detector by means of optical switching.

OTDR technique: Optical time domain Reflectometry (OTDR) technique is to detect the location of fracture of the fibers from the backscattering by means of a time-of-flight measurement using a very short laser.

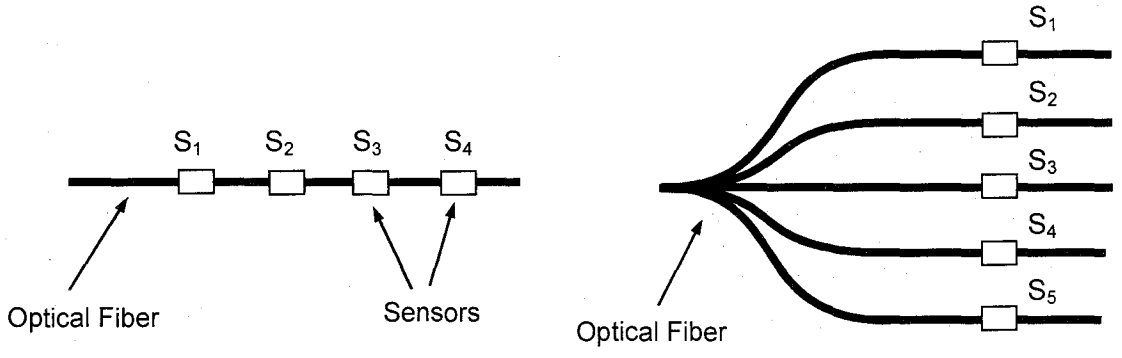

(a) Serial multiplexing

(b) Parallel multiplexing

Fig. C-1 Multiplexing techniques